UNIVERSIDAD AUTÓNOMA DE MADRID
Facultad de Ciencias
Departamento de Física Teórica

On the Nature of Distant Luminous Compact Blue Galaxies.

Memoria de tesis doctoral presentada por

Carlos de Hoyos Fernández de Córdova.

para optar al grado de doctor en Ciencias Físicas.

Dirigida por

Dr. Ángeles I. Díaz Beltrán.
(UAM)

y

Dr. Rafael Guzmán Llorente.
(University of Florida.)

11th May 2006

A mi familia,
por su apoyo.

He who knows, why should he keep it hidden?
-Sumerian saying.

With dreams to be a king, first one should be a man.
-Eric Adams, philosopher.

Acknowledgements.

This work would not have been possible without the help of many people and institutions.

I am of course indebted to my thesis directors, Ángeles Díaz and Rafael Guzmán for their guide, friendship and support, as well as for their forgiving attitude towards my numerous failings. I owe to them way too many things to be written in the handful of pages of the "Acknowlegements" chapter of a thesis book.

I am also grateful to the Grupo de Astrofísica de la Universidad Autónoma de Madrid. In particular, I give many thanks to Carlos Eiroa for many useful discussions/conversations and material support.

I also want to acknowledge the institutional support provided by the Departamento de Física Teórica de la Universidad Autónoma de Madrid. I value very much the teaching experience I have acquired during the two years I have spent as an Assistant Professor during the final years of my PhD.

I also have enjoyed the hospitality and institutional support of the Astronomy Department of the University of Florida, and of the Department of Astronomy of the University of California Santa Cruz and Lick Observatories

I am most grateful to David C. Koo for having allowed me to access the wondeful DEEP2 database. It's been thanks to him that I have had the privilege of observing in the W.M. Keck observatories, too.

I would also like to thank Matthew A. Bershady for helping me gain a more detailed understanding of the HST data.

I should not forget Roberto and Elena Terlevich for many useful discussions, and for their help during the final writing of this PhD thesis.

I am also in debt with Marcelo Castellanos first and foremost for his friendship and moral support, and then for the many discussions on scientific topics we've had.

I also have to transmit my gratitude towards Christopher N.A. Willmer, Drew Phillips, Kai G. Noeske and Enrique Pérez Montero for their scientific help during the realization of this work.

Some of the data presented in this work are based on observations made with the NASA/ESA Hubble Space Telescope and obtained from the data archive at the Space Telescope Institute. STScI is operated by the association of Universities for Research in Astronomy, Inc. under the NASA contract NAS 5-26555.

Some of the data presented in this work were obtained at the W.M. Keck Observatory, which is operated as a scientific partnership among the California Institute of Technology, the University of California and the National Aeronautics and Space Administration. The Observatory was made possible by the generous financial support of the W.M. Keck Foundation. I wish to recognize and acknowledge the very significant cultural role and reverence that the summit of Mauna Kea has always had within the indigenous Hawaiian community. I am most fortunate to have had the opportunity to conduct scientific observations from this mountain.

This work has also made extensive use of the NASA/IPAC Extragalactic Database (NED) which is operated by the Jet Propulsion Laboratory, California Institute of Technology, under contract with the National Aeronautics and Space Administration. I also used the HyperLeda database, which can be reached at `http://www-obs.univ-lyon1.fr/hypercat/intro.html`

Finally, I have to acknowledge the finantial support provided by the Formación de Profesorado Universitario grant (AP2000-1389), funded by the Ministerio de Educación Cultura y Deporte. I have also had the financial support of the AYA-2000-0973 and AYA-2004-08260-CO3-03 grants. I have also enjoyed the support of the following NASA/STScI grants HST-GO-08678.04-A and HST-GO-9126. This work was also supported by the NASA/LTSA NAG5-11635 and NASA/LTSA NAG5-6032 grants, as well as the NASA grant AR-07532.01-96. This work was also funded by the American NSF grants AST 95-29028 and AST 00-71198. The Del Amo grant program also provided financial support.

Now, it's time to switch to Spanish, for the personal acknowledgements.

Quiero agradecerle a mi familia toda su ayuda y colaboración. La vida sería más difícil sin vosotros. Gracias.

También debo agradecer su ayuda, y las veces que hemos arreglado el mundo, a los amigos: Nacho, Felipe, Marcos, Popi, Elena, Juan Carlos, Pablo, Julián, Toño, Oscar, Edu, Rubén , J, Mafer, Dani, Carlos (L), Guillermo, Carlos (A), Juan, Tomás, Félix, Miguel, Luis, Miguel Cárdenas, Jaime, Mariano, Beatriz, Manuel, Cotolo, Hubert, Jesús, Antonio y Emi.

Y familiares: María Victoria, Ángela, Enrique, Carmen, Rocío, Félix, Victoria, Astrid, Luis, Juan y Mary Ann.

Y los que ya no están: Alfonso, Luis, Andrés, Nicolás y Carlitos.

Termino agradeciendo su presencia y ayuda a los compañeros de trabajo que he tenido, en Madrid y en Estados Unidos: Alcione Mora, Alejandro Saiz, Luis Jiménez, Víctor Casanova, Héctor Artal, José Oñorbe, Mercedes Mollá, Marta Gavilán, Guillermo Hägele, Mónica Cardaci, Rubén, Chiqui, Raúl, Mike Taylor, Anthony Gonzalez, Ana Matkovich, Cynthia Gómez, Carlos Román, Eric McKenzie, Jorge Pérez Gallego, Ileana Vass, Susmita Datta, Ian Dobbs-Dixon, Sarah Martell, Jason Melbourne y Justin Harker.

Contents

List of Tables

List of Figures

Abstract.

This work deals with the nature of intermediate redshift Luminous Compact Blue Galaxies (LCBGs). LCBGs are small starburst systems that dominate the star formation density of galaxies at intermediate redshifts. Despite the key role LCBGs may play in galaxy evolution, their main properties are still largely unknown and the nature of the descendants of this galaxy class is still under discussion. Due to their narrow emission line-widths and number density, it's been suggested that LCBGs might be the progenitors of today's lower-mass spheroidal (Sphs) galaxies like NGC205 or NGC147. LCBGs have also been proposed as the progenitors of bulges of primeval spiral galaxies due to their high gas phase metallicities.

The first chapter presents a brief introduction of the basic properties of LCBGs, and their relevance for galactic evolution studies. It presents a historical overview of other studies of faint, blue, starforming galaxies that have had a historical impact on the topic of galactic evolution. The introduction also presents the main motivations of this work. Among these, the evolution of the luminosity function and the study of galactic evolution are the most important motivations. LCBGs are the most rapidly evolving galaxy population since $z = 1$, and they are very important contributors to the global star formation rate of the young Universe. It is therefore critical to establish the nature of this population if we are to give an answer to the aforementioned issues.

The second chapter presents a statistical study of a very large sample of HII galaxies taken from the literature. HII galaxies are also blue and compact objects undergoing a major burst of star formation. They are thought to be similar to many intermediate redshift LCBGs, the remaining LCBGs bearing a closer resemblance to local Starburst Nuclei galaxies. This latter subtype represents around 40% of the LCBGs in the distant universe. The study of local HII galaxies should provide us with a comparison control sample, in order to find out what properties and biases can be expected when studying the intermediate redshift LCBGs. For this reason, we study the subsample of HII galaxies whose properties most closely re-

semble the properties of the intermediate-redshift population of LCBGs. We also focus on the differences in several properties between galaxies that show the auroral line [OIII]λ4363 and those that do not present this feature in their spectra. LCBG-like HII galaxies are more similar to the objects not showing the [OIII]λ4363 line. It is also the case that objects without the auroral line are more luminous, more metal-rich and present a lower ionization degree. The underlying population is found to be much more important for objects without the [OIII]λ4363 line, and the effective temperature of the ionizing star clusters of galaxies not showing the auroral line is probably lower. It might therefore be expected that the intermediate-redshift population of LCBGs is powered by very massive, yet somewhat aged star clusters. The oxygen abundance of the ionizing clusters found in LCBGs would then be greater than the average oxygen abundance of local HII galaxies. This chapter appeared in print in the Monthly Notices of the Royal Astronomical Society. The bibliographic reference is:

Hoyos C., Díaz A. I., 2006, MNRAS, 365, 454.

Chapters three through five present the results of a high spatial resolution study of intermediate redshift LCBGs. This study targets the main properties of distant LCBGs. In particular, we focus on the basic star formation properties and structure of LCBGs, their spatially resolved kinematics and the stellar populations found in these systems. All these issues are of critical importance in the study of the evolution of this population of galaxies. The observational data used were obtained using the no longer operational STIS spectrograph and the WF/PC-2 and WF/PC-1 cameras, all these instruments are on board the HST telescope. The obtained spectra show prominent emission lines whose spatial profiles reveal, at least in some cases, the existence of various star-forming regions. This is confirmed in the WF/PC-1 and WF/PC-2 images. The observed objects exhibit a variety of morphologies.

The study of the kinematical properties which may be inferred from the HST/STIS spectroscopic observations of LCBGs confirms that these systems are low mass, dynamically hot systems in which random motions dominate over rotation, at least in the gaseous phase. This proves the accuracy of dynamical mass and mass-to-light ratios estimates from previously obtained integrated line-widths using the HIRES instrument in the ground-based W.M. Keck telescopes. The resolved kinematics indicates that the observed LCBGs are unlikely to be embedded in large, low surface brightness, disk systems. We have also used these obser-

vations to study in greater detail two of the observed LCBGs that merit special attention. One of them is the only dynamically cold member of the sample and the other one has a very high areal star formation rate. Mass-to-Light (M/L) ratios are derived for these two particular sources, and are used to constrain the stellar populations present in the central regions of these objects. It turns out that the stellar populations found in both systems are bound to be very different from one another, highlighting that the population of LCBGs is inhomogeneous.

We also find evidence for various stellar populations. One of them is identified as the ionizing population that makes the galaxy visible from such large distances, and the other one is the underlying, older stellar generation. Our models indicate that the first episodes of star formation the presented LCBGs underwent happened $\sim$ 7 Gyr ago ($z \sim 0.7$), and that their underlying stellar populations are very similar to those of local HII galaxies although they probably have a lower number of red giant stars. The estimated masses of the inferred stellar populations are compatible with their dynamical masses, and the HI content is thought to be small. The derived Star Formation Rates from Hα luminosities in these galaxies range between 0.5 and 7 $M_{\odot} yr^{-1}$. These star forming regions found in LCBGs are typically ten times more luminous than and approximately twice as large as the well known giant HII region 30-Doradus in the LMC. When compared to local star bursting galaxies, the LCBGs studied here turn out to be very similar to the brightest HII galaxies in terms of the areal star formation rate and in the ratio between the *galaxy* half light diameter to the *line-emitting* region half light diameter (D_{eff}/D_0). Some of the results from these chapters were published by The Astronomical Journal, as well as in a number of conferences and meetings. The bibliographic references are:

Hoyos C., Guzmán R., Bershady M. A., Koo D. C., Díaz A. I., 2004, AJ, 128, 1541.

Bershady, M. A., Vils, M., Hoyos, C., Guzmán, R., Koo, D. C., 2004, astro-ph/0411597.

Hoyos C., Guzmán R., Díaz A. I., Bershady M. A., Koo D. C., 2003, RMxAC, 16, 283.

Hoyos C., Guzmán R., Díaz A. I., Koo D., Bershady M., 2005, in "Starbursts: From 30 Doradus to Lyman Break Galaxies", Edited by R. de Grijs and R.M. González Delgado. Astrophysics & Space Science Library, Vol. 329. Dordrecht: Springer, 2005, p.P26.

Finally, chapter 6 presents the discovery of a rare sample of 17 metal-poor yet luminous star-forming galaxies at redshifts $z \sim 0.7$. These galaxies have blue luminosities close to

L^*, high star formation rates, and oxygen abundances of 1/3 to 1/10 solar. They thus lie significantly off the luminosity-metallicity relation found previously for field galaxies with strong emission lines at redshifts $z \sim 0.7$, and thus pose a challenge to galactic evolution theories. The prior works devoted to determine the metallicity of distant star forming objects relied on indirect, empirical calibrations of the diagnostics used to calculate oxygen abundances and the *assumption* that luminous galaxies are *not* metal-poor. Our discovery shows that this assumption is sometimes invalid. As a class, these galaxies are: (1) more metal-poor than common classes of bright emission-line galaxies at $z \sim 0.7$ or at the present epoch; (2) comparable in metallicity to $z \sim 3$ Lyman Break Galaxies but less luminous; and (3) comparable in metallicity to local metal-poor extreme Blue Compact Galaxies, but more luminous. Together, the three samples suggest that the most-luminous, metal-poor, compact galaxies become fainter over time. The main results of this chapter were published by The Astrophysical Journal, the complete reference is:

Hoyos C., Koo D. C., Phillips A. C., Willmer C. N. A., Guhathakurta P., 2005, ApJ, 635, L21.

Key words. galaxies:abundances. — galaxies:evolution. — galaxies:stellar content. — galaxies: ISM — galaxies: starburst — galaxies:high-redshift — galaxies:LCBGs. — galaxies: kinematics.

Resumen.

Esta tesis doctoral trata acerca de la naturaleza de las Galaxias Luminosas Compactas y Azules (GLCA) a desplazamientos al rojo intermedios más parecidas a las galaxias HII del universo local. Las GLCA son galaxias pequeñas, con un brote de formación estelar muy activo. Estos objectos dominan la densidad de formación estelar en galaxias a desplazamientos al rojo intermedios. A pesar de su papel fundamental que esta clase de objetos tienen en la evolución de las galaxias, sus principales propiedades son desconocidas en gran medida, ni tampoco se conoce muy bien cual es su relación con las poblaciones locales de galaxias. Debido a la estrechez de sus líneas de emisión y densidad numérica, se ha sugerido que las GLCA podrían dar lugar a las galaixas esferoidales del universo cercano como NGC205 o NGC147. También se ha propuesto que las GLCA darían lugar a los bulbos de las primeras galaxias espirales, debido a las altas abundancias metálicas de algunas GLCA.

El primer capítulo presenta una breve introducción a las propiedades más básicas de las GLCA, y su importancia desde el punto de vista de los estudios de evolución galáctica. Se presenta un breve apunte histórico acerca de otros estudios de galaxias débiles, azules y con un brote de formación estelar que han tenido un impacto histórico en la materia de evolución de galaxias. La introducción también presenta las principales motivaciones del presente trabajo. Entre las motivaciones, las más importantes son la evolución de la función de luminosidad y el estudio de la evolución de galaxias. Las GLCA son la población de galaxias que más rápidamente han evolucionado desde $z = 1.0$, y contribuyen muy apreciablemente a la tasa global de formación estelar del Universo joven. Es por lo tanto crítico conocer la naturaleza de la poblacion de GLCA si queremos responder a estas cuestiones.

El segundo capítulo de este trabajo presenta un estudio estadístico sobre una muestra de galaxias HII muy grande, tomado de la literatura. Las galaxias HII son también sistemas azules y compactos que están sufriendo un importante brote de formación estelar. Se piensa que muchas GLCA a desplazamientos al rojo intermedios son parecidas a estas galaxias HII.

El resto de las GLCA se parecen más a otra poblacion de galaxias con brotes de formación nucleares. Este segundo subtipo es menos numeroso en el universo distante que el primero, siendo tan sólo el 40% de todas las GLCA del universo a desplazamientos al rojo intermedios. El estudio de las galaxias HII locales nos proporcionaría una muestra de control con la que comparar las GLCA a desplazamientos al rojo intermedios para averiguar qué propiedades y sesgos se pueden esperar. Por estos motivos, se estudia la submuestra de galaxias HII más parecidas a las GLCAs a desplazamientos al rojo intermedio. El estudio también se ocupa de estudiar las diferencias entre aquellas galaxias que presentan la línea de emisión auroral [OIII]λ4363 y las que no muestran esta característica en su espectro. Las galaxias HII más parecidas a las GLCA tienen más puntos en común con la submuestra que no presenta la antedicha línea auroral. También se encuentra que los objetos sin esta línea son más luminosos, más ricos en metales y presentan un grado de ionización más bajo. Su poblacion subyacente es asimismo mucho más importante y las temperaturas efectivas de sus cúmulos ionizantes son probablemente menores. Sería pues lógicamente esperable que las GLCAs a desplazamientos al rojo intermedios poseyeran cúmulos ionizantes muy masivos, aunque algo envejecidos. La abundancia de oxígeno de las GLCAs sería entonces mayor que la del promedio de las galaxias HII locales. Este capítulo se publicó en "Monthly Notices of the Royal Astronomical Society." La referencia bibliográfica es:

Hoyos C., Díaz A. I., 2006, MNRAS, 365, 454.

Los capítulos 3, 4 y 5 muestran los resultados de un estudio de alta resolución espacial acerca de la naturaleza de las GLCA a desplazamientos al rojo intermedios. In particular, se estudian las propiedades básicas de formación estelar, la estructura, la cinemática espacialmente resuelta y las poblaciones estelares existentes en estos objetos. Todos estos puntos son necesarios para establecer la evolución de esta población de galaxias.

Las observaciones utilizadas fueron obtenidas usando el telescopio espacial Hubble, en concreto las cámaras WF/PC-2, WF/PC-1 y el espectrógrafo STIS. Tanto este último instrumento como la cámara WF/PC-1 ya no se encuentran operativos. Los espectros obtenidos presentan líneas de emisión muy conspícuas cuyos perfiles espaciales revelan, al menos en algunos casos, la existencia de varias regiones de formación estelar. Esto se confirma con las imágenes directas obtenidas, que también muestran una gran variedad morfológica.

El estudio de las propiedades cinemáticas que se pueden deducir a partir de las observa-

ciones del telescopio espacial demuestra que se trata de sistemas cinemáticamente calientes, en los cuales los movimientos aleatorios dominan sobre la rotación, al menos en la fase gaseosa. Estos resultados confirman las bajas masas dinámicas y los cocientes masa-luminosidad obtenidos previamente a partir de las medidas cinemáticas llevadas a cabo utilizando el intrumento HIRES en el telescopio W.M. Keck. Los datos cinemáticos, obtenidos con alta resolución espacial, muestran que esta pequeña muestra de GLCA es dinámicamente caliente y que los objetos no se encuentran sumergidos en un gran disco de bajo brillo superficial. Se han estudiado en mayor detalle dos de estas GLCA, una de ellas es el único miembro de la muestra que es dinámicamente frío, y el otro tiene una tasa de formación estelar por unidad de área muy elevada. Los valores de los cocientes masa–luminosidad, derivados de estos datos, se usan para perfilar las poblaciones estelares presentes en estos dos sistemas. Se encuentra que las poblaciones estelares presentes en estos dos sistemas son muy diferentes, subrayando la falta de homogenidad de la población de GLCA.

También hay evidencia de la existencia de varias generaciones estelares. Una de ellas se identifica con la población responsable de la ionización, que hace posible ver la galaxia desde distancias tan grandes. La otra es la población subyacente, más vieja. Nuestros modelos indican que los primeros episodios de formación estelar tuvieron lugar a desplazamientos al rojo de 0.7, hace aproximadamente 8×10^9 años. Las poblaciones estelares subyacentes son muy similares a las de las galaxias HII locales, aunque posiblemente tengan una menor cantidad relativa de estrellas gigantes rojas. Además, las masas que se estiman para las poblaciones estelares son compatibles con las masas dinámicas, y el contenido de hidrógeno neutro se piensa que es pequeño. Las tasas de formación estelar obtenidas a partir de las luminosidades en Hα van de 0.5 hasta 7 $M_{\odot} yr^{-1}$. Las regiones de formación estelar de las GLCAs son típicamente diez veces más luminosas y el doble de grandes que la muy conocida región 30-Doradus en la Gran Nube de Magallanes. Por otra parte, si las propiedades de formación estelar de las GLCAs se comparan con las de las galaxias HII más brillantes, resulta que las GLCAs estudiadas son muy parecidas a las galaxias HII más brillantes en términos de su tasa de formación estelar por unidad de área y en el tamaño relativo de las regiones de gas ionizado frente al tamaño global de las galaxias (D_{eff}/D_0). Algunos de los resultados presentados en estos capítulos fueron publicados en "The Astronomical Journal" y en conferencias y congresos. Las referencias bibliográficas son:

Hoyos C., Guzmán R., Bershady M. A., Koo D. C., Díaz A. I., 2004, AJ, 128, 1541.

Bershady, M. A., Vils, M., Hoyos, C., Guzmán, R., Koo, D. C., 2004, astro-ph/0411597.

Hoyos C., Guzmán R., Díaz A. I., Bershady M. A., Koo D. C., 2003, RMxAC, 16, 283.

Hoyos C., Guzmán R., Díaz A. I., Koo D., Bershady M., 2005, in "Starbursts: From 30 Doradus to Lyman Break Galaxies", Edited by R. de Grijs and R.M. González Delgado. Astrophysics & Space Science Library, Vol. 329. Dordrecht: Springer, 2005, p.P26.

En el último capítulo se presenta el estudio de una muestra de 17 galaxias con formación estelar pobres en metales aunque luminosas, a desplazamientos al rojo de $z \sim 0.7$. Las galaxias de esta muestra tan inusual tienen luminosidades cercanas a L^*, altas tasas de formación estelar y abundancias metálicas entre 1/3 y 1/10 solares. Se encuentran por lo tanto muy separadas de la relacion entre la luminosidad y la metalicidad que ha sido encontrada usando otras muestras de galaxias de campo a $z \sim 0.7$, su existencia es entonces problemática para los modelos de evolución de galaxias. Sin embargo, los trabajos anteriores usaron determinaciones indirectas y empíricas de la abundancia de oxígeno, y la *suposición* de que las galaxias observadas no son pobres en metales. El descubrimiento que se presenta en este capítulo implica que este supuesto no es válido en todos los casos. Las galaxias que presentamos son: (1) más pobres en metales que otras galaxias con líneas de emisión fuertes tanto en el universo remoto como locales;(2) comparables en metalicidad con las mucho más lejanas ($z \sim 3.0$) galaxias del corte de Lyman pero menos luminosas y (3) de metalicidad comparable a la poblacion de galaxias azules compactas extremas, pero más luminosas. El resultado general sugiere que las galaxias compactas pobres en metales más luminosas con brotes de formación estelar son cada vez más débiles. Los resultados principales de este capítulo se han publicado en "The Astrophysical Journal". La referencia es:

Hoyos C., Koo D. C., Phillips A. C., Willmer C. N. A., Guhathakurta P., 2005, ApJ, 635, L21.

Palabras Clave. galaxias:abundancias. — galaxias:evolución. — galaxias:brotes de formación estelar. — galaxias:contenido estelar. — galaxias: medio interestelar — galaxias:alto redshift. — galaxias:GLCAs. — galaxias: cinemática.

Chapter 1

Introduction.

Short Presentation of the Galaxy Class Studied. Luminous Compact Blue Galaxies (LCBGs) are small ($R_e \leq 3.0$kpc) starburst systems that dominate the number density of galaxies at intermediate redshifts. LBCGs have evolved more than any other galaxy class in the last 8 Gyrs (Mallén-Ornelas et al., 1999; Phillips et al., 1997; Guzmán et al., 1997; Guzmán et al., 2003) and are a major contributor to the observed enhancement of the UV luminosity density of the universe at $z < 1$, their number density decline being in concert with the rapid drop in the global Star Formation Rate since $z = 1$. Despite the key role LCBGs may play in galaxy evolution, their statistical properties are still largely unknown. They appear to form a bridge in redshift, size, and luminosity between Lyman-break galaxies and local HII galaxies today. However, the nature of the descendants of this galaxy class is still under discussion. Due to their narrow emission line-widths and number density, Koo et al. (1995) and Guzmán et al. (1998) suggested LCBGs might father today's lower-mass spheroidal (Sphs), also called dwarf elliptical (dEs) galaxies like NGC205. LCBGs have also been proposed as the progenitors of bulges of primeval spiral galaxies due to their high gas phase metallicities (Hammer et al., 2001; Kobulnicky & Zaritsky, 1999; Guzmán et al., 1998; Phillips et al., 1997). In this picture, the bright blue compact regions are embedded within a lower-surface brightness disk of larger size.

1.1 Main Drivers of this Study.

1.1.1 Historical Perspective.

One of the main lines of work in astrophysics is the nature of the faintest galaxies detected with the available telescopes. In fact, this has always been one of the main motivations to build larger telescopes. Although originally these galaxies were used as probes of the cosmological expansion with the main aim of discriminating between the different cosmological models, the motivations of these studies gradually changed with the first accurate measurements of the star formation history in normal galaxies (Tinsley, 1972a,b,c).

The properties of these faint galaxies have always been a problem since their detection (Koo, 1986; Tyson, 1988; Cowie et al., 1988). However, the first accumulated data point towards a very intense evolution of the galaxy population during the last 5–7 Gyr. The observations show a numerous galaxy population that can be observed at $B_{AB} = 23.0$ and $z \sim 1.0$. These galaxies are as blue as the bluest objects of the local universe. This is indeed indicative of important star forming episodes, although the precise connection of these galaxies with their local counterparts is still poorly known.

In order to search for these young galaxies still in their formation process, many galaxy counts have been carried out, together with color measurements in the hope of finding faint (faint meaning low observed flux, not low luminosity) blue galaxies. During the last two decades, several galaxies have claimed to be the "holy grial" of galaxy formation.

The first galaxy population that drew the attention of the astronomical community were the "Butcher-Oemler" galaxy clusters. These galaxies attracted the attention because it was found (Butcher & Oemler, 1984) that in these distant $z = 0.4$ clusters, the fraction of blue galaxies was higher than the fraction of blue galaxies in local clusters. However, the Hubble Space Telescope soon revealed that these galaxies are in most cases well formed spiral galaxies, and not young galaxies still under construction (Dressler et al., 1994). It was also found that the number of spiral galaxies was four times larger than the number of spirals in local clusters. It was also noted that only in the innermost regions of these clusters the galaxy inventory approached the galaxy mixture found in nearby clusters (Thompson, 1986). The cluster members with activated star formation similar to that observed in present-day spiral galaxies are late Hubble types, and the cluster galaxies whose star formation ceased 1–2Gyr before the observation are normal disk systems. The redder galaxies are a mixture of elliptical and lenticular types, having harbored a recent star forming episode.

The next candidate population were the "Faint Blue Galaxies", although they were soon discarded because their redshift was not very high, and their luminosities and star formation rates would not be able to account for all the required star formation density.

In recent times, the joint venture between the HST and the 10-m class telescopes have produced the "third wave" of blue star forming, the galaxies known as "Luminous Compact Blue Galaxies" or LCBGs. These systems have luminosities similar to that of the very well known M31 Andromeda galaxy, despite having much smaller NGC-205ish sizes. These galaxies also present very blue colors, indicating a very high star forming rate. It has to be said that, even though the optical appearance of LCBGs is very similar to that of the previously mentioned Faint Blue Galaxies in deep images, their luminosities are much higher. The study of LCBGs requires the use of multi object spectrographs, multiwavelength studies, and a combination of HST+10-m telescopes such as the W.M. Keck or GTC telescopes. The present work deals with the properties of this latter galaxy class.[1]

1.1.2 Evolution of the Luminosity Function.

One of the most obvious issues of galactic evolution is to compare the galaxies we observe in the nearby universe with the more distant galaxies whose light arrives at our telescopes billions of years after it was emitted. It is also clear that it is needed to compare the emitted power at the same frequencies. However, it is not possible to observe the same galaxy at different times, so the evolution of galaxies has to be studied at the population level. For this reason, the concept of *Luminosity Function.* was introduced.

The Luminosity Function $\phi(L)$ is defined as the *co-moving* number density of galaxies per unit luminosity interval. The number of galaxies in a given *comoving* volume dV per luminosity range $\mathrm{d}L$ is then:

$$dN = \phi(L) \times \mathrm{d}V \times \mathrm{d}L$$

Given the definition above, it is easily understood why it is a very important tool to study the evolution of galactic populations. This luminosity function can and has to be derived separately for different galaxy types, emission wavelengths, environments and redshifts.

[1] With HII-like LCBGs, to be precise.

Early Works on the Evolution of the Luminosity Function.

The first attempts to describe the nature of the distant *field* galaxy populations (see e.g., Kron, 1980; Koo, 1986) were based on comparisons of color and magnitude histograms with the corresponding histograms predicted by the models. They produced very qualitative, yet interesting results. In particular, it was noted in Koo (1986) that the fraction of galaxies bluer than $B - V = 0.7$ and brighter than $M_V = -20$ might be significantly higher at $z \sim 0.4$. It was also pointed out that distant faint galaxies showed a very large ultraviolet excess, making their colors similar to very late-type spiral galaxies or Im/Irr galaxies, and indicating a very important star formation activity.

Among the earliest works that tried to determine the evolution of the *cluster* luminosity function, we will only note the very well-known Butcher & Oemler (1984). The main result of this work is that the fraction of blue galaxies in clusters rises with redshift. This effect being universal by $z \sim 0.4$. Other work on the evolution of galaxies in clusters can be found in Lavery & Henry (1986), which confirmed that the excess of blue galaxies in three clusters was due to intense bursts of star formation that had happened at around $z \sim 0.5$. However, since the galaxies this Thesis focuses on are mostly isolated, faint field galaxies, no further discussion on the evolution of *cluster* luminosity functions will be made.

More recently, the Canada France Redshift Survey (CFRS) was used in Lilly et al. (1995) to explore the evolution of the *field* luminosity function up to $z \sim 1.0$. This work used a sample of 730 I-band selected galaxies of which 591 had secure redshifts determinations. Their results clearly showed that the luminosity function does evolve with time. This is shown in the sample plot presented in figure 1.1, taken from Lilly et al. (1995). The evolution of the luminosity function depends most strongly on color, and, to a lesser extent, on luminosity. This effect was also observed by Ellis et al. (1996). The luminosity function of blue galaxies changes much more rapidly than that of red galaxies in both number density and luminosity. This luminosity function has also brightened by 1 mag by $0.5 \leq z \leq 0.75$, but at higher redshifts it saturates at the brightest magnitudes. They also found an overabundance of faint ($M_{AB,B} \sim -18.0$), blue galaxies with respect to the local luminosity function at redshifts $z \leq 0.2$. They could not conclude whether this effect was caused by a different overall normalization factor or by a change in the slope of the luminosity function, though. These results indicate that the population of blue galaxies is responsible for the evolution of the *global* luminosity function. It would be needed to establish if this evolution is caused by

sudden brightening of individual objects or by a density evolution. In particular, it would be very intesting to know if the apparent excess of faint blue galaxies commented before is made of the descendents of the bright blue galaxies with high number density observed at $z \geq 0.5$. On the other hand, the lack of evolution of the red luminosity function might indicate that the population ellipticals and early-type spirals almost entirely formed at some point in the remote past, and has remained largely unevolved ever since, although it might be possible that some combination of evolutionary processes could make this luminosity function constant with time.

In a later work, Cowie et al. (1996) utilized a very large ($26.2\ ^{\prime 2}$) and deep K$\leq$ 20.0 survey of 254 objects observed using the LRIS spectrograph (Oke et al., 1995) on the KECK 10-m telescope. This sample is nearly complete to K= 19.5. Their K-selected sample was enlarged with the inclusion of other I-band selected sources I$\leq$ 23, I$\leq$ 22.5 and a fainter B-band selected sample with a limiting magnitude of 24.5. They studied a total of 393 objects out to a redshift of 1.5. The main result of this work is that galaxies flow rapidly in the Mass–Star Formation Rate–Redshift plane in a way such that more massive galaxies form earlier, at higher redshifts, implying a monotonic decline in the luminosity of very active star-forming galaxies and, consequently, that a large fraction of all galaxy formation took place at $1.0 \leq z \leq 1.6$. This scenario was christened as "downsizing." In this model, then, the luminous L^* galaxies are already formed by $z = 1$, but lower luminosity systems are still forming, as was already pointed out in Broadhurst, Ellis, & Shanks (1988). This galaxy formation model can successfully describe the sinchronization in the color evolution of bright, distant galaxies and the normalization of the luminosity function, although it only leaves room for a mild evolution of the luminosity function from $z = 1$ till the present day. It is striking that the evolution of the maximum luminosity of star forming systems cancels the distance module, naturally explaining the excess of B-band faint blue galaxies and the blueing of faint systems.

Finally, the relevant work presented in Mallén-Ornelas et al. (1999) identifies the properties of the galaxies responsible for most of the evolution seen in the luminosity function. Their work presents the internal kinematics of very luminous star forming galaxies up to $z = 0.8$. The sample includes 24 blue ($U-V_{AB} \leq 1.14$) galaxies from the CFRS. These galaxies were selected regardless of size or morphology. The majority of these galaxies have sizes and velocity widths typical of local irregular galaxies, which is compatible with the observed morphologies and rest-frame colors. However, their luminosities are vastly larger.

The increase in the number density of luminous blue galaxies is caused by this population of small, bright objects at $z \sim 0.5$. These strongly evolving luminous compact blue galaxies are then the major contributors to the luminosity evolution of blue L^* galaxies. These galaxies have Irregular Magellanic or dIrr morphologies, but are as luminous as early type nearby full-fledged spirals.

1.1.3 Cosmic Star Formation History.

It is clear that, if we are to determine when were the galaxies forming the majority of their stars, we need to be able to estimate the star formation density (numbers of newly formed stars per unit time per unit volume in the Universe) as a function of look-back time. In order to accomplish this task, several deep surveys have been carried out. The most famous of these deep surveys is the Hubble Deep Field. This survey, simply known as the HDF, is a multi color survey with a limiting magnitude of around 28.0 in the F300W, F450W, F606W and F814 filters. This survey has allowed (Madau et al., 1996) to determine the star formation density up to $z \sim 3$, using the ultraviolet continuum emission of the observed galaxies (see figure 1.2). Such measurements were compared to the determination of the star formation rate of the local universe, calculated using the Universidad Complutense de Madrid (UCM) Survey (Zamorano et al., 1994, 1996). The HDF measurements of the cosmic star formation history were also compared to the star formation history derived from the Lilly et al. (1995) and Steidel et al. (1996a,b) $0.0 \leq z \leq 1.0$ data. The main result is that there is indeed a star formation density peak between $z = 1$ and $z = 3$, and the metal production density reaches its peak at about $z = 1.5 \pm 0.5$. It has to be kept in mind, however, that much caution should be exercised, because the star formation rate derived from the ultraviolet light can be grossly underestimated due to internal galactic extinction. In more recent times, another very deep survey was produced, this time known as the "Hubble Ultra Deep Field" or UDF for short. This new survey was carried out using the Advanced Camera for Surveys (ACS) instrument, on board the Hubble Space Telescope. The UDF utilizes the F435W, F606W, F775W, and F850LP filters and is around 2.0 magnitudes deeper than the HDF. Among the works that have helped to constrain the star formation history of the universe using the UDF, we note those of Bunker et al. (2004) and Bouwens et al. (2004). Both works were based on the number of F755W drop-outs, which are considered to be $z \sim 6.0$ galaxies, since their flux decrement between the F755W filter and the F850LP filter is likely caused by Lyman-alpha absorption. Alhough such works deal with the reionization epoch of the universe, they can provide important constraints to the star formation history of the Universe in more recent times. In particular, the star formation rate in the Universe was six times lower at $z = 6.0$ than it was at $z \simeq 3.0$. Another conclusion is that the star formation rates involved are not high enough to be responsible for the reionization. In the future, the Spitzer satellite will shed more light on this issue since the star formation rate can also be derived from

infrared light. The Spitzer space telescope, using spacecraft borne infrared instruments, has the ability to detect the infrared light coming from distant galaxies. It can see the unobscured star formation rate, and therefore will present us more accurate star formation histories of the objects observed.

The importance of LCBGs in the global star formation rate was put forward by Guzmán et al. (1997), who argued that LCBGs play a key role in the enhancement of the star formation density of the Universe up to $z \simeq 1.0$. In particular, they represent only 20% of the general galaxy population with I_{AB} brighter than 22.5 but contribute with 45% of the SFR at $0.4 \leq z \leq 1.0$. This further highlights the importance of studying this galaxy class.

1.1.4 Galactic Evolution.

The evolution of galaxies has always been a very important issue in cosmology, although the motivations of these studies have gradually changed since the construction of the first large telescopes. The issue of galaxy evolution was first considered as a mere correction to apply to the studies that tried to determine which one among the different cosmological models was correct. Nowadays, it is considered a much more important issue, having implications on many aspects of astronomy, not only fundamental cosmology.

Among the first formation scenarios for "normal" (meaning spiral or elliptical) galaxies it is mandatory to mention the monolithic collapse model. This picture was put forward by Eggen, Lynden-Bell, & Sandage (1962) and others (Larson, 1974). This model was inspired by the observed ages of the oldest stellar populations found in our galaxy and was also supported by the homogeneity and age of the stellar populations of the older elliptical galaxies. This scenario also succeeded at predicting the surface brightness distribution, the metal content distribution, and the photometric properties of spherical systems. It also gave a very precise epoch for the collapse, namely 1.0 Gyr – 2.5 Gyr after the Big-Bang, and predicted the collapse would last for at least 1.0 Gyr – 2.0 Gyr. It also allowed to imagine quasars as being collapsing spherical galaxies (Larson, 1974). Furthermore, the available data on the age of the oldest stars in spiral galaxies (which are similar to the age of the Universe itself), indicated a sudden collapse taking place during the earliest stages of the Universe. These results lead to think of an epoch in which the Universe was forming a great percentage of its stars several Gyr ago.

There is another galaxy formation and evolution model, known as the hierarchical merging scenario. In this scenario, galaxies are gradually assembled through multiple mergers of

smaller subgalactic units, a process that continues from the early universe to the current epoch (White & Rees, 1978; Cole et al., 1994). The work presented in White & Rees (1978) was successful in predicting that most of the matter in the Universe is not in gas or luminous stars. It could also establish that the inner part of galaxies could not possibly form by purely non-collisional phenomena, highlighting the importance of gas in the dynamics of galaxies. Finally, these models also gave a prediction for the $z = 0$ luminosity function and the mass spectrum of the aforementioned dark lumps. On the other hand, the models shown in Cole et al. (1994) were able to predict galaxy number counts, luminosities, colors, and circular velocities. In addition, the hierarchical models also yield reasonable predictions on the K-band luminosity function, $B-K$ colors as a function of absolute magnitude, Hα luminosities, the cosmic star formation history, and the redshift distribution of faint B and K galaxy counts. However, these models were unable to produce bright, red galaxies or the zero-point of the Tully-Fisher relation. The Universe model used was the now superseded CDM model.

These different scenarios for galaxy formation have an obvious impact on galaxy evolution models. In the monolithic collapse scenario, galaxies of the major morphological types (spirals and ellipticals) are born intrinsically different, since the time scale for the evolution of the basic structural properties of galaxies such as the degree of flattening or the degree of central concentration is so large that these properties have had to remain unchanged since each galaxy's inception. However, in the hierarchical merging scenario, galaxies end up as spirals or ellipticals depending on the particular details of their merger history. As a result, the monolithic collapse model predicts that the number of galaxies of a given type should be approximately constant at all redshifts, whereas the hierarchical model predicts that the number of large galaxies (spirals or ellipticals) should decrease with redshift.

The task of deciding which one of these two models is closer to reality is still underway. The studies aimed at this issue usually take advantage of the very red colors shown by elliptical galaxies; by searching for the reddest galaxies in samples of distant galaxies, it is possible to accurately estimate the fraction of elliptical galaxies at different epochs. High numbers of very red objects in the distant Universe should favor the existence of a large number of elliptical galaxies, although the presence of dust in actively star forming systems makes this picture blurrier (Scodeggio & Silva, 2000; Cimatti et al., 1998). Other problems with this scenario are presented in Totani et al. (2001) and Maihara et al. (2001).

These problems make it impossible for the time being to definitely discard one of the two modes of galaxy formation. Should the monolithic collapse mode be more important, it

would mean that galaxies have existed for the largest part of the history of the Universe. On the other hand, galaxies are relatively new systems in the hierarchical merging model.

The galaxy family this work deals with, LCBGs, can also be used to test the different galaxy formation mechanisms. In the frame work of the hierarchical model, they might be one of the main ingredients of galaxy formation recipes. It's been said that LCBGs are the most rapidly evolving galaxy population at intermediate redshift, and that they were around 10 times more common in the past than they are today. Also, in spite of their small sizes, LCBGs were responsible of a sizeable percentage of the star formation rates at $z \sim 1.0$ since they were host to very powerful starbursts. It is thanks to this starburst that LCBGs are visible over a wide redshift range. The evolution of LCBGs as a class is therefore a key issue in galaxy formation and evolution models.

Nowadays, there are two very different views on the nature and evolution of LCBGs. One view is that the Starburst Nuclei-like LCBGs are the proto-bulges of spiral galaxies (Hammer et al., 2001; Barton & van Zee, 2001). The other view supports the idea that some (the HII-like subtype) LCBGs are the progenitors of today's spheroidal systems (Koo et al., 1995; Guzmán et al., 1996, 1998, 1997; Phillips et al., 1997). These two opposing views can be approximately mapped into either the monolithic collapse model or the hierarchical collapse scenario.

The work presented in Hammer et al. (2001) used Very Large Telescope (VLT) spectra of 14 Luminous Compact Galaxies. These spectra revealed strong metallic absorption lines, including those of α elements and iron, as well as compact narrow emission lines. The star formation rates of the objects observed was very high, typically $40 M_{\odot}$ per year. The spectra also allowed to determine the gas metal abundances, which turned out to be half-solar. The observed spectra could be reproduced by mixing one old and metal rich population with a young stellar generation. According to these models, the creation of the observed systems might have happened during the few billions of years before the photons that are now observed departed the galaxy. The sources presented in this study show many similarities to the bulges of modern spiral galaxies. Among these similarities, the most noteworthy are the masses, the light concentration and the observed range in metallicity in the stellar content. In this scenario, the gas needed to feed the starburst falls from the outer regions of the galaxy, and the metallicity of this gaseous component should be *lower* than that of the older stellar generation already found in the system. Furthermore, some galaxies show nearby companion galaxies and small disks in the process of formation. Should this scenario hold, it would mean

that an important fraction of modern spiral galaxies would have formed the majority of their stars in relatively recent times, 9 billion years ago at most.

The opposing hypothesis, championed by Koo et al. (1995), Koo et al. (1997, in a cluster, not in the field), and Guzmán et al. (1998), argues that HII-like LCBGs are the progenitors of present day spheroidal systems. Koo et al. (1995) presents high S/N spectra of a sample of 17 LCBGs, taken with the HIgh REsolution Spectrograph (HIRES) echelle spectrograph of the Keck 10-m class telescope. The studied objects are very luminous $M_B \sim -21.0$, and the measured velocity widths are in the range σ=28–157 km s^{-1}. The observed LCBGs with lower velocity widths were found to satisfy the same relations between their gas-phase velocity dispersions (σ) and both the $H\beta$ luminosities and B-band luminosities as local HII galaxies. This presents an important link between LCBGs and local HII galaxies. This link was later presented more precisely in Guzmán et al. (1997). LCBGs are also experiencing a very important episode of star formation, as exposed by their blue colors and high equivalent widths. In the hypothesis that the observed starburst is a major event in the history of these galaxies, these systems could fade enough to match the luminosities and surface brightnesses of local spheroidal systems, although the amount of fading depends critically on the actual importance of the underlying stellar population. The work presented in Guzmán et al. (1998) and later on in this thesis explore the possibility of a non-negligible underlying stellar population. The models presented in Guzmán et al. (1998) were constructed with two-bursts evolutionary population models like those of Schmidt, Alloin, & Bica (1995). In these models, LCBGs are assumed to be undergoing their last burst of star formation (which is probably not a bad assumption, since the ensuing supernova-driven galactic superwinds are likely to blow away the remaining gas), superimposed on a much older and massive underlying generation of stars. The predicted fading for the studied sample was about four magnitudes, 2–3 magnitudes less than the Koo et al. (1995) estimate. The resulting colors, absolute magnitudes and mass-to-light ratios match fairly well those of Sph systems. Further support to this evolutionary picture is lent by the observed shapes of these galaxies. In particular, the light profiles of both systems have very similar shapes (Jerjen & Binggeli, 1997).A similar conclusion has been drawn from the comparison of the intrinsic shapes of nearby blue compact dwarfs and Sph galaxies (Sung et al., 1998).

It has to be said that this scenario has received some criticism because local spheroidal systems appear in rich environments, and they are often found to be satellites of larger galaxies, such as the M31–NGC205 case. However, the existence of field, isolated dSphs such

as Tucana, Cetus, or Apples 1 implies that at least dwarf spheroidal systems can indeed exist outside rich galaxy clusters. Furthermore, the space density of the LCBGs studied is too low to find even one descendant, even assuming a factor of 20 higher density of LCBG corpses in a complete all-sky local survey reaching out to 10 Mpc. This is a survey that has yet to be done. Furthermore, as was pointed out above, Koo et al. (1997) show examples of distant LCBGs in clusters. These cluster LCBGs have properties akin to those observed in field LCBGs, and thus, it can be expected that these systems will transform into dwarf ellipticals if the field ones do so, too. In addition, 21-cm HI observations of local HII galaxies, which are very similar to LCBGs, show considerable rotational support (van Zee, Skillman, & Salzer (1998) which is difficult to reconcile with the observed stellar kinematics of spheroidal systems. Dwarf spheroidals also contain very little gas, requiring that HII galaxies or LCBGs lose all of their remaining gas if they are to become spheroidals.

However, the evolutionary scenarios presented up to now are based on the *assumption* that the evolution of LCBGs is very simple, described by the recurrent burst model. According to this model LCBGs form their stars during some, well defined, star forming episodes separated by long periods of inactivity, the duty cycle being around 10^9 yr. In these *passive* models, then, LCBGs experience their last star forming event $\sim 4.5 \times 10^9$ years ago and have been fading ever since. It is clear that this simple picture can not hold for all LCBGs in the Universe, since large fractions of them are bound to experience other phenomena that will alter their evolution. These phenomena include dissipation, merging, tidal stripping, supernova-driven galactic superwinds, and ram pressure striping. All these events will displace any galaxy from its original position in a R_e–$\log\sigma$ diagram. This diagram is particularly useful to learn how remote galaxies relate to local systems, since the position on this diagram is almost independant on the amount of fading a galaxy has experienced. This happens because the luminosity of a galaxy can change many orders of mangitude during its lifetime, while, the mass of a galaxy is expected to remain much more stable. If a galaxy happens to move in this plane, it is bound to have experienced some catastrophic event. In addition, the relative positions of the different major galaxy classes (spirals, ellipticals, etc) are expected to remain the same (Guzmán et al., 1996, 1998).

Among the processes that might change the position of LCBGs in the R_e–σ plane, the most important of them is the presence of galactic winds (Guzmán et al., 1996, 1998). Gas removal caused by collective supernova winds is recognized (Larson, 1974; Yoshii & Arimoto, 1987) as one of the most important individual events that shapes the evolution of a low-mass

systems. The mass loss induced by galactic winds is such that the product $R_e \times \sigma$ remains constant (Vader, 1986). The expected change in the case of low-mass galaxy is about a factor of 2 in velocity sigma. This process makes LCBGs to move closer to local dwarf irregular systems, away from NGC205-like objects. The situation depicted here is somewhat worrying, since the high star formation rates found in LCBGs will give rise to a very large number of massive stars, which will end their lives as type Ib or II supernovae. However, even if these winds can inflate a bubble, it may be the case that the LCBGs do not experience any mass loss, although it will certainly affect the chemical evolution of the galaxy, since it will put off the next important starburst. These collective winds have been found in many local blue compact galaxies (Roy et al., 1991; Martin, 1996), so it can be expected that they will be present in the more luminous and distant LCBGs. The evolution of LCBGs depends then critically on their ability to retain their interstellar medium in the event of a superwind, although it can be foreseen that, given their very low Mass-to-Light ratios, most of the gas within LCBGs will be blown away. Whether or not some LCBGs will develop into dwarf irregulars is still unknown, although the difference in metallicity and velocity widths of both galaxy classes make it somewhat difficult.

The next most important mechanism that will affect the evolution of LCBGs is the production of mergers. Merger episodes come in two flavors, major and minor mergers. Major mergers involve two similarly sized galaxies while for minor mergers, one of the two galaxies is much smaller than the other one and the dynamics of the larger object is not largely disrupted. Minor mergers are known to be much more common that major mergers, as was shown by Hernquist & Mihos (1995). It is obvious that this should be the case since galaxies have very large range of masses. It would therefore be highly unlikely that collisioning objects have the same mass. However, it has to be kept in mind that collision partners are not randomly chosen from the global population of galaxies, but are members of bound clusters or of clusters interacting with other systems. Hierarchical clustering biases the statistics of collision partners. This can be used to test galaxy evolution models, since the reshaping of the luminosity function caused by mergers has to obey these constraints. In the case of mergers involving LCBG-sized systems, two options arise. Either it is a minor merger or a major merger. In the first case, the prey galaxy is merely dissolved in the larger system, never to be seen again. In the second case, the resulting system becomes a little bit larger and more massive than its progenitor. The simulations presented in Hernquist, Spergel, & Heyl (1993) indicate that, in these cases, the absorbing system increases its radius, leaving

its velocity dispersion unchanged, to zero-th order (see, among others, Hernquist, 1992; Heyl, Hernquist, & Spergel, 1996, for a review on the structure of merger remanents). These events would therefore shift the LCBG-sized system towards low-mass spirals or irregular galaxies. However, the most important effect of these merging episodes is that they can start the dormant star forming engine of the LCBG-sized system, maybe transforming it into a real LCBG. This can be accomplished by funneling gas into the core of the newly formed system. In simulations of minor mergers involving spiral galaxies, for instance, it's been found that up to 50% of the gass mass of the primary system will be concentrated in a dense core (Hernquist & Mihos, 1995). Collisions involving LCBG-sized galaxies could be similar to the collisions presented in Hernquist & Mihos (1995) in that a large fraction of the gas mass of the resulting system could end up being concentrated in a dense core, not necessarily in the optical center of the galaxy.

To sum up, LCBGs play a key role in galaxy formation and evolution models, since they can help us discriminate between the two possible formation scenarios. In spite of this importance, the evolution of LCBGs themselves is still poorly understood, and the research on the fate of LCBGs is still underway.

1.1.5 The Luminosity-Metallicity Relationship.

The metal content of galaxies is an important diagnostic of galactic evolution. A useful relationship between evolutionary state and metallicity is the luminosity–metallicity relationship. One reason for the existence of this relationship, assumimg that more luminous galaxies are also more massive, is that more massive objects can lock up the metals created in their stars more easily than less massive galaxies because of their deeper gravitational wells.

This relationship is expected to evolve with cosmic epoch, due in part to "feedback" from supernova driven winds, AGN activity or infall of new, unprocessed gas. It is then very easy to understand that the chemical composition of star-forming galaxies in the distant universe is an important constraint on the evolution of the galaxy populations. Knowledge of the chemical composition can be used to constrain the age of any given galaxy provided that the heavy element abundance of galaxies increases forever with age, and that the gas-phase metallicity can be assumed to be equal to the metal abundance of the stellar population. The first assumption assumes that galaxies evolve in a "closed box" manner. In this model, the metal content of a galaxy should be a function of its gas mass fraction only. The predicting power of this model would therefore be enormous, should this hypothesis be true for at least

some fraction of galaxies. However, galaxies (and star-forming ones in particular) are known to exchange large amounts of gas with the intergalactic medium. It's been mentioned above that star-forming galaxies will likely produce superwinds that will export metal-enriched gas to the intergalactic medium. Merger events will also disrupt this "closed-box" model. Within the framework of this picture, any evolutionary scenario linking LCBGs with dSphs entails the explicit boundary condition that the heavy element abundance of the final evolved spheroidal be equal to or greater than the metallicity of the LCBG that originated it. The second requirement is more complex to verify. First of all, it is clear that it cannot hold for systems like present-day spiral galaxies, in which several generations of stars, each with a different age and metallicity, coexist. In these cases, the gas-phase metallicity does not directly relate to the heavy-element abundance of the galaxy. All that can be said is that the galaxy is evolved enough so as to produce gas of the observed chemical composition. Second, it is very important to keep in mind that the metals ejected from dying stars do not mix instantly into the general interstellar medium of galaxies (Tenorio-Tagle, 1996; Roy & Kunth, 1995). This delay can be as large as one billion years (Tenorio-Tagle, 1996).

The location of distant galaxies in the M_B–$12 + \log(\mathrm{O/H})$ plane is therefore of crucial importance to understand all these topics and the details of the inner workings of LCBGs. This would surely have an impact on the evolution of these sources. It has to be said that the metallicities of distant systems have been historically studied via the absorption lines seen in quasar spectra. However, this method provides metallicity estimates that can't be readily translated into the metal content of high-redshift galaxies (Fall & Pei, 1993). At large redshifts ($z \geq 2.0$), and using emission-line ratios, Kobulnicky & Koo (2000) and Pettini et al. (2001) already find evidence that Lyman Break Galaxies (LBGs) of under-solar abundance are 5–40 times more luminous than local systems of similar metal content, confirming that the luminosity-to-metal ratio varies with time. The luminosity-metallicity relation for intermediate redshift ($z \leq 1.0$) objects is a vital link between the local populations of galaxies and the high-redshift populations, such as Damped Lyman-Alpha (DLA) systems or LBGs. The metal abundance of intermediate redshift star-forming galaxies similar to LCBGs was first studied by Kobulnicky & Zaritsky (1999), and then further extended in Lilly, Carollo, & Stockton (2003), Kobulnicky et al. (2003) and Kobulnicky & Kewley (2004). These three latter studies dealt with field galaxies at $z \sim 0.5$ to 1.0. These intermediate-redshift studies seem to suggest that, at a given metallicity, galaxies were typically more luminous in the past, while the high-redshift samples show metallicities that are sub-solar

with luminosities 5–40 times brighter than local galaxies of comparable metallicity. However, this result must be accepted with caution, since the metallicities presented there were all based on empirical calibrations (Pagel et al., 1979; McGaugh, 1991; Pilyugin, 2000, 2001; Pilyugin & Thuan, 2005, among many others,). No galaxies were found to be less than 1/3 solar in $12 + \log(\mathrm{O/H})$, but this was caused by the fact that these galaxies were *initially assumed* to be metal rich. These works indicate that there has been an evolution of the M_B–$12 + \log(\mathrm{O/H})$ relationship during the last 8.0–9.0 Gyrs, in the sense that local sources are more metal-rich than distant galaxies of similar oxygen content. It has also been found that the evolution is faster for brighter objects. The initial study of Kobulnicky & Zaritsky (1999) included some objects with measurements of the [OIII]λ 4363 Å auroral line. This line is sensitive to electron-temperature (Osterbrock, 1989) and can, together with H_β and other oxygen lines, provide reliable gas metallicities without assumptions about the ionization and metallicity. The luminosity-metallicity relationship of the galaxies presented in this work turned out to be indistinguishable from the relationship followed by local systems, indicating that no evolution of this relationship during the last few billions of years could be detected. The observed chemical properties of the star-forming objects presented in Kobulnicky & Zaritsky (1999) are not compatible with those of young objects undergoing their first burst of star formation, indicating that these sources harbor an important underlying population. The four galaxies included in the Kobulnicky & Zaritsky (1999) work that fulfilled the LCBG requirements fell in the same region as the rest of the other line-emitting sources in the luminosity-metallicity diagram.

It is therefore very important to find a place in the M_B–$12 + \log(\mathrm{O/H})$ plane for distant LCBGs. In the event that LCBGs turned out to be metal–poor, it would be interesting to know how is it possible that these objects happen to attain such large luminosities, given that the number of different stellar generations would then be small. If, on the other hand, it is the case that LCBGs are metal-rich objects, the question would then be: How did such small systems retain the metals they have created?

1.2 Present Day Knowledge on LCBGs.

The nature of the faint blue galaxies seen in deep images of the sky has been the subject of one of the major controversies in observational cosmology over the last 20+ years. There are all-covering reviews on this subject (see Koo & Kron, 1992; Ellis, 1997, and references

therein). The combination of HST and 10-m class telescopes has given a unique insight into the nature of this faint galaxy population. There is now firm observational evidence to conclude that a significant fraction of these faint galaxies are very luminous but low-mass stellar systems that are undergoing a major star-forming episode.

The Guzmán et al. (1997) and Phillips et al. (1997) spectroscopic studies present a very large sample of compact distant galaxies. These two studies still provide much of the knowledge we nowadays have on these sources known as LCBGs. Their sample comprised no less than 61 compact, high surface brightness sources at redshifts lower than 1.4, and apparent brightnesses $I_{814} \leq 23.74$ found in the flanking fields of the Hubble Deep Field. The spectra, taken with the HIRES spectrograph on the W.M. Keck telescope allowed to study emission-line ratios, star formation rates, velocity dispersions, and line equivalent widths. The conclusions of these works are now summarized.

It is found that $\sim 25\%$ of all compact sources studied are early-type galaxies at $0.4 \leq z \leq 0.9$, although the real fraction could be a little bit higher. It is also the case that the majority are emission-line galaxies, two-thirds of them being similar to HII galaxies. The remaining 30% were mapped into small, high surface brightness spirals. These compact emission-line sources can be considered as LCBGs and they were studied in detail in Guzmán et al. (1997). Furthermore, a large fraction of the compact objects presented look like bursting dwarves, however, their luminosities are 10 times larger. Finally, it is also the case that the comoving volume densities of the compact sources observed in the HDF similar to local HII galaxies are very high compared to local values and indicate that this population is a strongly evolving one. Their space densities are somewhat large for them to be the precursor of spheroidal systems. However, uncertainties remain too large to draw firm conclusions about compact spheroidal connections on the basis of volume densities.

Guzmán et al. (1997) used the same sample as Phillips et al. (1997). However, they focused on the evolution of the star formation rate in compact objects during the last 7–8 Gyr. The discoveries of this work are summarized below. It is found that 88% of the objects studied show narrow emission lines, while the remaining 12% have only absorption lines. The larger fraction can be considered as LCBGs. The emission-line profiles of these LCBGs are roughly Gaussian with velocity profiles that range from $\sigma \sim 35$km s^{-1} to 150 km s^{-1}. Rest frame [OII]λ3727 equivalent widths range from 5 to 94 Å. The estimated star formation rates fell in the 0.1 to 14.0 solar masses per year range. Emission-line compact galaxies can be taxonomically divided into two broad classes. About 60% have velocity

widths, excitations, line luminosities, and star formation rates similar to those of local HII galaxies. The remaining objects are very heterogeneous class of more evolved starburst disk galaxies. The star formation rate per unit galaxy mass (specific SFR) of these sources is very similar to the specific SFR found in local HII galaxies. The mass evolution at a given specific SFR supports an evolutionary scenario in which the SFR density of the universe declines by a factor of 10 from $z \sim 1.0$ to the present day. Furthermore, emission-line compact galaxies represent only one fifth of the general field galaxy population with $I_{AB} \leq 22.5$ but are an important contributor to the total SFR density at $0.4 < z < 1$. This fact was used to conclude that compact galaxies are main actors in the evolution of the star formation history of the Universe.

Another vey important parameter to unveil the final destiny of LCBGs is their mass. Mass has proven to be a key tool in galaxy evolution since it can be considered to be independent of the luminosity evolution. It is then possible to make more meaningful comparisons between different galaxy populations. However, the reliability of the various methods used to measure it has been questioned. In particular, virial mass estimates of star-forming galaxies using half-light radii and emission-line velocity widths present several uncertainties. For instance, if the star-forming event is not widespread throughout the whole galaxy, then the half-light radius will fail to measure the real galaxy size. Furthermore, the velocity widths may be influenced by supersonic motions of the ionized gas due to stellar winds or supernova explosions and might not be sensitive to the gravitational field of the galaxy.

The precise determination of mass is also important because, even though LBCGs are undergoing a major burst, they are known to possess previous stellar generations. An accurate measurement of the mass of an LCBG would therefore serve to constrain the underlying stellar population. If LCBGs are thought to be dynamically similar to local HII galaxies, the classical work from Terlevich & Melnick (1981) would then imply that the velocity dispersion measured in LCBGs is caused by gravity, and not by supernovae or their associated phenomena. This interpretation is supported by some models of star-forming regions showing that, just after formation, stellar winds of low-mass stars moving with a velocity dispersion σ_* will stir the remaining gas cloud, imprinting it with an average turbulent motion $\sigma \sim \sigma_*$ (Tenorio-Tagle, Munoz-Tunon, & Cox, 1993). In addition, a comparison between the 21 cm and [OIII] line widths further strengthens this conclusion. For a sample of 18 HII galaxies and starbursts listed in Marlowe et al. (1995) and Telles & Terlevich (1997), one finds (σ[OIII])/σ(21cm) =0.7$\pm$0.1. This result indicates that the ionized gas in HII galaxies is in dynamical

equilibrium within the galaxy gravitational potential. Since most LCBGs are very similar to nearby HII galaxies and other low-mass starbursts, this result could aply to them too. Finally, there is new evidence supporting the reliability of the virial mass estimates for LCBGs. It has been presented using actual measurements of their stellar masses from near infrared images and stellar population models (Brinchmann & Ellis, 2000; Guzmán et al., 2003).

In summary, there is enough observational evidence to admit that LBCGs are low-mass stellar systems (i.e., $M \sim 10^{10} M_{\odot}$, or one order of magnitude smaller than a typical galaxy with similar luminosity today).

There have been some recent studies on the nature of local-Universe LCBGs, in particular, I will mention Werk, Jangren, & Salzer (2004) on the emission-line properties of nearby LCBGs and Garland et al. (2004), which deals with neutral hydrogen observations of local LCBGs.

The Garland et al. (2004) paper presents HI spectra and optical photometric measurements from the Sloan Digital Sky Survey of 20 nearby LCBGs. The LCBGs observed turned out to be very gas-rich, with M(HI) ranging from 5×10^8 to 8×10^9 $M_{\odot}$, the neutral hydrogen mass-to-light ratio going from 0.2 to 2.0, in the range of that shown by many other galaxy classes. The measured galaxy masses within ${R_{25}}^2$ were found to span a wide range. The observed LCBGs also show a variety of morphologies. Interestingly, and similar to what was found for LCBGs at intermediate redshifts, about half of the local LCBGs have dynamical mass-to-light ratios smaller than those found in the local Hubble sequence. The observed LCBGs present dynamical properties consistent with those of Magellanic spiral galaxies and the more massive spheroidal galaxies. This work was enlarged in a later paper (Garland et al., 2005).

Werk, Jangren, & Salzer (2004) focused on the emission-line properties of the 16 local LCBGs found in the Kitt Peak National Observatory International Spectroscopic Survey (KISS). This sample was chosen using the same criteria as those required for distant LCBGs. Furthermore, all LCBGs were selected to be active star-forming systems (as apposed to AGN activity). This sample of local LCBGs turns out to lie on the extreme end of the sequence defined by star-forming galaxies in the Surface brightness–$B-V$ color, unlike the outliers distant LCBGs. The volume sensity of local LCBGs was estimated in 5.4×10^{-4} h Mpc^{-3}. This value is ~ 4 times lower than the volume density of the LCBGs at $0.4 < z < 0.7$ and ~ 10

[2]It is customary to measure a radius R_{25} to where a spiral galaxy's surface brightness falls to a level of 25 mag $''^{-2}$, in the B band.

times lower than the volume density of the population at $0.7 < z < 1.0$. This indicates that this population has evolved quite a lot. Local LCBGs have a higher probability of emitting a detectable radio continuum flux. They also have higher line luminosities, and their metal content is estimated to be somewhat low for their luminosity.

1.3 This Work Contributions.

The present thesis can help to address some of the issues put forward in the preceeding sections of this introduction. This work is structured into two main parts. The first part deals with HII galaxies in the local universe, and the second part deals with the more distant LCBG class.

The first part is presented in chapter 2. This chapter deals with the general properties of HII galaxies in the local Universe, with the aim of constructing a control sample to compare with distant LCBGs. HII galaxies were chosen as the parent population for constructing such control sample since the majority of LCBGs have properties similar to local HII galaxies, as was pointed out by Guzmán et al. (1997). The need for a local sample of LCBGs is indeed recognized. A good control sample would help to settle the debates over the size, mass, morphology, metallicity etc. of LCBGs. If it turned out that local HII galaxies were very similar to LCBGs, it would provide a very good base for tackling higher redshift studies.

Part two spans chapters 3 through 6. The nature of the intermediate redshift population of LCBGs is presented from several points of view. These include the spatially resolved properties of LCBGs, the stellar populations found in these systems, the kinematic properties of LCBGs, and the metal content of LCBGs. Each of these issues can be mapped into chapters 3, 4, 5 and 6 respectively. In these studies the properties of LCBGs are also compared to relevant samples of local systems.

Bibliography

Barton E. J., van Zee L., 2001, ApJ, 550, L35

Brinchmann J., Ellis R. S., 2000, ApJ, 536, L77

Bouwens R. J., et al., 2004, ApJ, 606, L25

Broadhurst T. J., Ellis R. S., Shanks T., 1988, MNRAS, 235, 827

Butcher H., Oemler A., 1984, ApJ, 285, 426

Bunker A. J., Stanway E. R., Ellis R. S., McMahon R. G., 2004, MNRAS, 355, 374

Cimatti A., Andreani P., Rottgering H., Tilanus R., 1998, Natur, 392, 895

Cole S., Aragon-Salamanca A., Frenk C. S., Navarro J. F., Zepf S. E., 1994, MNRAS, 271, 781

Cowie L. L., Lilly S. J., Gardner J., McLean I. S., 1988, ApJ, 332, L29

Cowie L. L., Songaila A., Hu E. M., Cohen J. G., 1996, AJ, 112, 839

Dressler A., Oemler A. J., Butcher H. R., Gunn J. E., 1994, ApJ, 430, 107

Eggen O. J., Lynden-Bell D., Sandage A. R., 1962, ApJ, 136, 748

Ellis R. S., Colless M., Broadhurst T., Heyl J., Glazebrook K., 1996, MNRAS, 280, 235

Ellis R. S., 1997, ARA&A, 35, 389

Fall S. M., Pei Y. C., 1993, ApJ, 402, 479

Garland C. A., Pisano D. J., Williams J. P., Guzmán R., Castander F. J., 2004, ApJ, 615, 689

Garland C. A., Williams J. P., Pisano D. J., Guzmán R., Castander F. J., Brinkmann J., 2005, ApJ, 624, 714

Guzmán R., Koo D. C., Faber S. M., Illingworth G. D., Takamiya M., Kron R. G., Bershady M. A., 1996, ApJ, 460, L5

Guzmán R., Gallego J., Koo D. C., Phillips A. C., Lowenthal J. D., Faber S. M., Illingworth G. D., Vogt N. P., 1997, ApJ, 489, 559

Guzmán R., Jangren A., Koo D. C., Bershady M. A., Simard L., 1998, ApJ, 495, L13

Guzmán R., Östlin G., Kunth D., Bershady M. A., Koo D. C., Pahre M. A., 2003, ApJ, 586, L45

Hammer F., Gruel N., Thuan T. X., Flores H., Infante L., 2001, ApJ, 550, 570

Hernquist L., 1992, ApJ, 400, 460

Hernquist L., Spergel D. N., Heyl J. S., 1993, ApJ, 416, 415

Hernquist L., Mihos J. C., 1995, ApJ, 448, 41

Heyl J. S., Hernquist L., Spergel D. N., 1996, ApJ, 463, 69

Jerjen H., Binggeli B., 1997, ASPC, 116, 239

Kobulnicky H. A., Kewley L. J., 2004, ApJ, 617, 240

Kobulnicky H. A., Koo D. C., 2000, ApJ, 545, 712

Kobulnicky H. A., et al., 2003, ApJ, 599, 1006

Kobulnicky H. A., Zaritsky D., 1999, ApJ, 511, 118

Kron R. G., 1980, ApJS, 43, 305

Koo D. C., 1986, ApJ, 311, 651

Koo D. C., Kron R. G., 1992, ARA&A, 30, 613

Koo D. C., Guzmán R., Faber S. M., Illingworth G. D., Bershady M. A., Kron R. G., Takamiya M., 1995, ApJ, 440, L49

Koo D. C., Guzmán R., Gallego J., Wirth G. D., 1997, ApJ, 478, L49

Lavery R. J., Henry J. P., 1986, ApJ, 304, L5

Lilly S. J., Tresse L., Hammer F., Crampton D., Le Fevre O., 1995, ApJ, 455, 108

Madau P., Ferguson H. C., Dickinson M. E., Giavalisco M., Steidel C. C., Fruchter A., 1996, MNRAS, 283, 1388

McGaugh S. S., 1991, ApJ, 380, 140

Mallén-Ornelas G., Lilly S. J., Crampton D., Schade D., 1999, ApJ, 518, L83

Maihara T., et al., 2001, PASJ, 53, 25

Osterbrock D. E., 1989, *Astrophysics of Gaseous Nebulae and Active Galactic Nuclei,* (Mill Valley:University Science Books)

Pagel B. E. J., Edmunds M. G., Blackwell D. E., Chun M. S., Smith G., 1979, MNRAS, 189, 95

Phillips A. C., Guzmán R., Gallego J., Koo D. C., Lowenthal J. D., Vogt N. P., Faber S. M., Illingworth G. D., 1997, ApJ, 489, 543

Pilyugin L. S., 2000, A&A, 362, 325

Pilyugin L. S., 2001, A&A, 369, 594

Pilyugin L. S., Thuan T. X., 2005, ApJ, 631, 231

Schmidt A. A., Alloin D., Bica E., 1995, MNRAS, 273, 945

Sung E.-C., Han C., Ryden B. S., Patterson R. J., Chun M.-S., Kim H.-I., Lee W.-B., Kim D.-J., 1998, ApJ, 505, 199

Binggeli B., Jerjen H., 1998, A&A, 333, 17

Larson R. B., 1974, MNRAS, 169, 229

Larson R. B., 1974, MNRAS, 166, 585

Lilly S. J., Carollo C. M., Stockton A. N., 2003, ApJ, 597, 730

Marlowe A. T., Heckman T. M., Wyse R. F. G., Schommer R., 1995, ApJ, 438, 563

Martin C. L., 1996, ApJ, 465, 680

Oke J. B., et al., 1995, PASP, 107, 375

Pettini M., Shapley A. E., Steidel C. C., Cuby J.-G., Dickinson M., Moorwood A. F. M., Adelberger K. L., Giavalisco M., 2001, ApJ, 554, 981

Roy J.-R., Boulesteix J., Joncas G., Grundseth B., 1991, ApJ, 367, 141

Roy J.-R., Kunth D., 1995, A&A, 294, 432

Scodeggio M., Silva D. R., 2000, A&A, 359, 953

Steidel C. C., Giavalisco M., Dickinson M., Adelberger K. L., 1996, AJ, 112, 352

Steidel C. C., Giavalisco M., Pettini M., Dickinson M., Adelberger K. L., 1996, ApJ, 462, L17

Telles E., Terlevich R., 1997, MNRAS, 286, 183

Tenorio-Tagle G., Munoz-Tunon C., Cox D. P., 1993, ApJ, 418, 767

Tenorio-Tagle G., 1996, AJ, 111, 1641

Terlevich R., Melnick J., 1981, MNRAS, 195, 839

Thompson L. A., 1986, ApJ, 306, 384

Tinsley B. M., 1972, ApJ, 178, 319

Tinsley B. M., 1972, A&A, 20, 383

Tinsley B. M., 1972, ApJ, 178, L39

Totani T., Yoshii Y., Iwamuro F., Maihara T., Motohara K., 2001, ApJ, 558, L87

Tyson J. A., 1988, AJ, 96, 1

Vader J. P., 1986, ApJ, 305, 669

Werk J. K., Jangren A., Salzer J. J., 2004, ApJ, 617, 1004

White S. D. M., Rees M. J., 1978, MNRAS, 183, 341

Yoshii Y., Arimoto N., 1987, A&A, 188, 13

Zamorano J., Rego M., Gallego J. G., Vitores A. G., Gonzalez-Riestra R., Rodriguez-Caderot G., 1994, ApJS, 95, 387

Zamorano J., Gallego J., Rego M., Vitores A. G., Alonso O., 1996, ApJS, 105, 343

van Zee L., Skillman E. D., Salzer J. J., 1998, AJ, 116, 1186

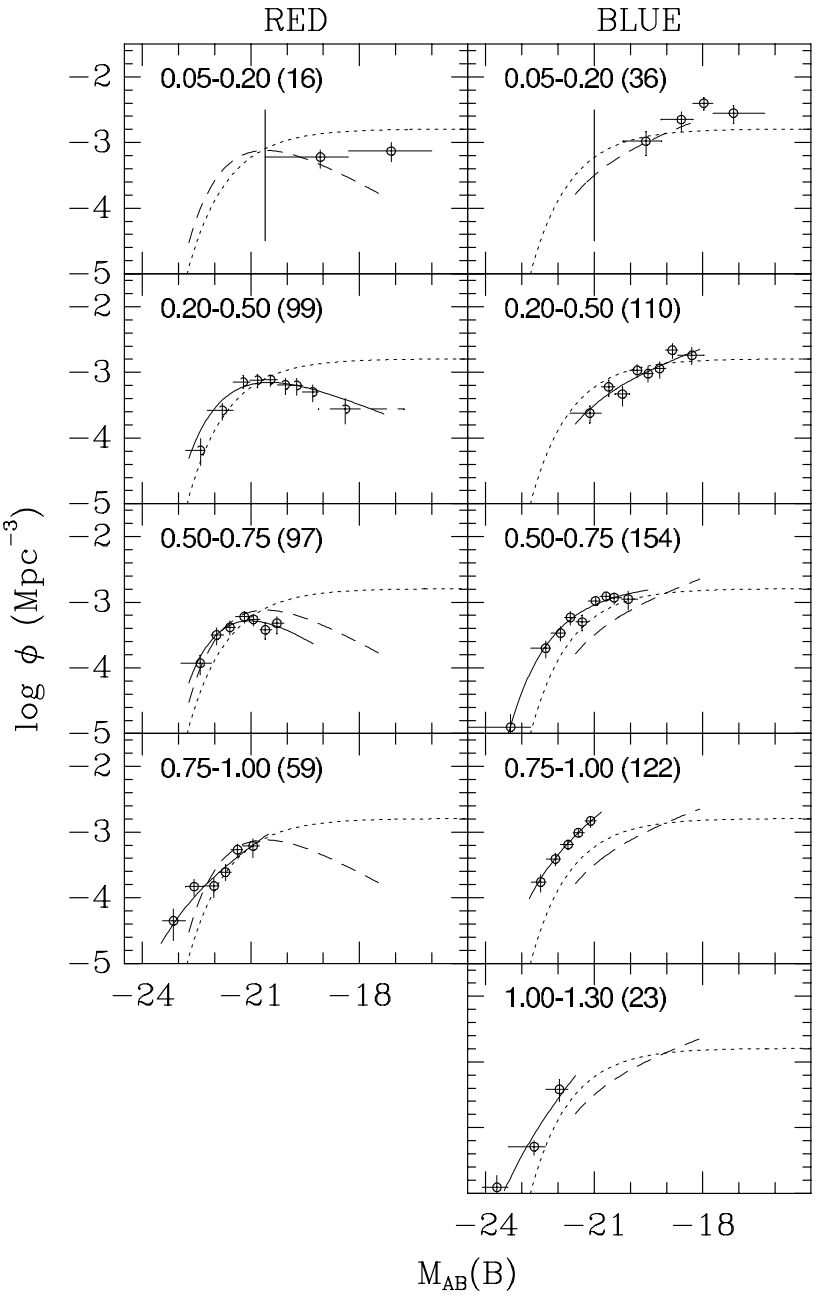

Figure 1.1: "Best estimate" luminosity functions for the CFRS sample split by redshift (vertically as shown by each label) and intrinsic color (redder than Sbc on the left, bluer on the right). Calculated assuming $q_0 = 0.0$. Redshift range and number of objects in that range are indicated by the label in the upper left of each panel. Taken from Lilly et al. (1995). See this reference for details.

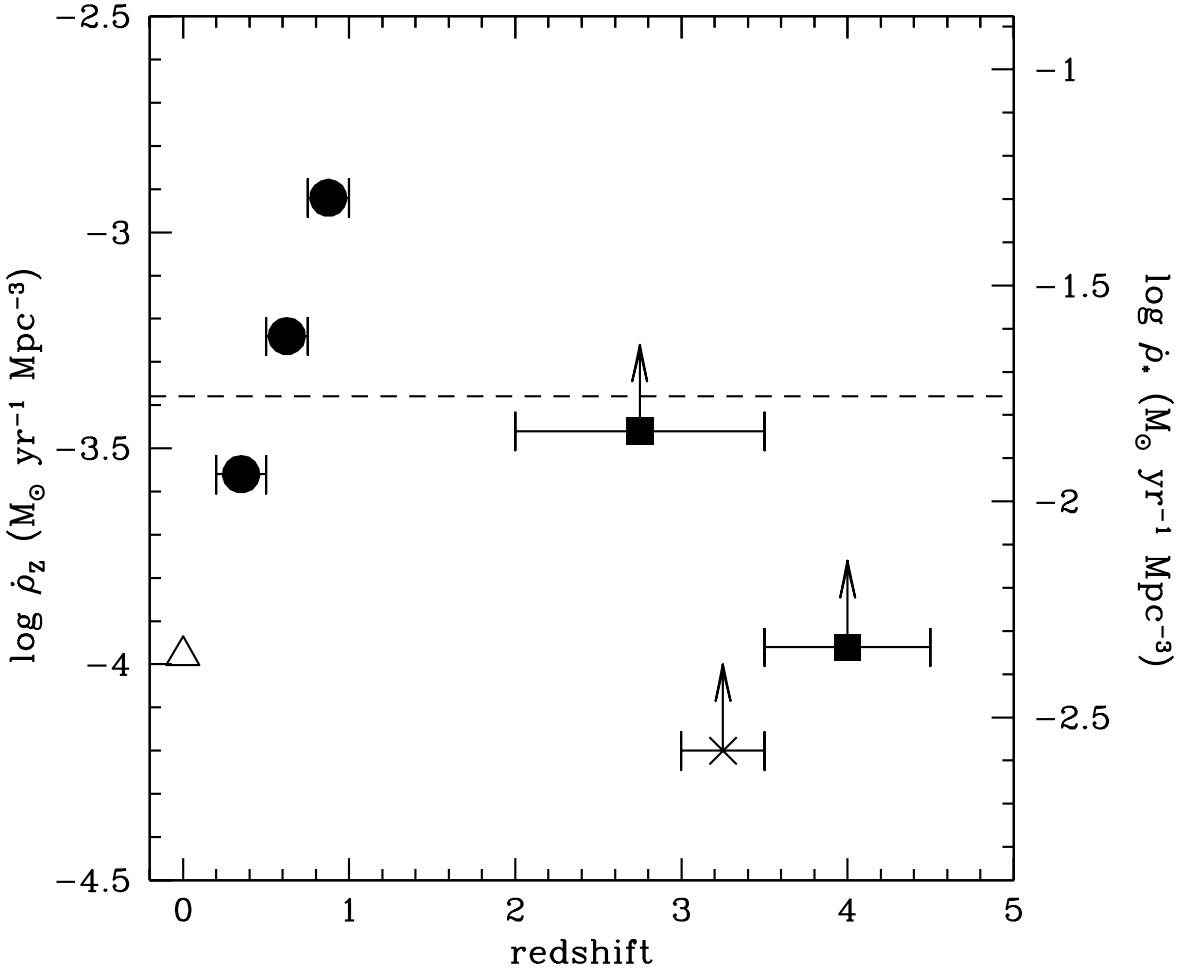

Figure 1.2: Element and star formation history of the universe, taken from Madau et al. (1996). The universal metal ejection density $\dot{\rho}_Z$ is shown as a function of redshift. The total star formation density, $\dot{\rho}_*$ is also shown. Both quantities are linearly related. See Madau et al. (1996) for further details.

Chapter 2

The impact on the general properties of HII galaxies in the local universe of the visibility of the [OIII]λ4363 line.

Abstract.

We present a statistical study of a very large sample of HII galaxies taken from the literature. We focus on the differences in several properties between galaxies that show the auroral line [OIII]λ4363 and those that do not present this feature in their spectra. It turns out that objects without this auroral line are more luminous, more metal-rich and present a lower ionization degree. The underlying population is found to be much more important for objects without the [OIII]λ4363 line, and the effective temperature of the ionizing star clusters of galaxies not showing the auroral line is probably lower. We also study the subsample of HII galaxies whose properties most closely resemble the properties of the intermediate-redshift population of Luminous Compact Blue Galaxies (LCBGs). The objects from this subsample are more similar to the objects not showing the [OIII]λ4363 line. It might therefore be

expected that the intermediate-redshift population of LCBGs is powered by very massive, yet somewhat aged star clusters. The oxygen abundance of LCBGs would then be greater than the average oxygen abundance of local HII galaxies.

2.1 Introduction.

The term "HII GALAXY" currently denotes dwarf emission line galaxies undergoing violent star formation (VSF)(Melnick, Terlevich, & Moles, 1985), a process by which thousands of massive stars (m$\geq$20 $M_\odot$) have recently been formed in a very small volume (a few parsec in diameter) and on the timescale of only a few million years. HII galaxies comprise a subset of the larger class of objects referred to as "blue compact galaxies" (BCG). At optical wavelengths, the observable properties of HII galaxies are dominated by the young component of their stellar population and their spectra are essentially identical to those of Giant Extragalactic HII Regions (GEHR) in nearby spiral and irregular galaxies. The analysis of these spectra shows that many HII galaxies are metal poor objects, some of them – IZw18, UGC4483 – being among the most metal poor systems known.

Although it was initially thought that HII galaxies are compact, essentially spheroidal, in fact they show a variety of morphologies with an appreciable number of them having two or more components and showing clear signs of interactions (Telles et al., 1997). Actually, IIZw40, one of the first HII galaxies identified, when imaged at sufficiently high resolution looks like the result of a merger of two separate subsystems (Melnick et al. (1992)).

The study of blue, compact star forming systems in the distant universe is an important ingredient in galaxy formation and evolution theories. Although such systems probably were not much more powerful than many local HII galaxies, it is believed that they were much more common in the past than they are today and therefore they harboured a great amount of the star formation density in the universe. This fact makes of high redshift blue compact galaxies very interesting targets for observation. Unfortunately, since they are located at large distances, their study can only be carried out with a combination of Hubble Space Telescope providing high spatial resolution and 10-m class telescopes providing high collecting power. Nevertheless, data on this kind of objects are accumulating fast.

Luminous Compact Blue Galaxies (LCBG) are defined as very luminous ($M_B \leq$ -17.5), compact ($\mu_B \leq$ 21.5mag arcsec^{-2}) and blue (B-V) $\leq$ 0.6) galaxies undergoing a major burst of star formation (see e.g., Hoyos et al., 2004). According to this definition LCBGs, as a

family, include the most luminous local HII galaxies. In principle, since they belong to the general category of emission line objects, the techniques used for their analysis are those already developed for the same class of objects in the local universe. However, in order to interpret these analyses properly in terms of evolution, a good comparison sample needs to be available.

There have been many studies of HII galaxies in the local universe, and the errors and uncertainities in the determination of their properties are supposed to be well understood. However, due to the importance of the metallicity effects in controlling the gaseous emission line spectra, most of these studies have been restricted to a subsample that allows a good direct determination of their chemical abundances, through the detection and measure of the weak [OIII] λ 4363 Å line. This implies the selection of the highest excitation objects which, in principle, can't be considered to be an unbiased comparison sample.

The purpose of the present work is to analyse a large sample of local universe HII galaxies. In particular two issues are addressed. The first one is the comparison of several observational parameter distributions for objects with and without measurements of the [OIII]λ4363 Å emission line and the statistical analysis of the whole HII galaxy sample to define their average properties. The second one is the statistical study of a subsample consisting of the most luminous objects, local representatives of LCBG, and its comparison to the whole HII galaxy sample.

The cosmology assumed throughout this chapter is a flat universe with H_0=70km s^{-1} Mpc^{-1}.

2.2 The Sample Selection.

We have compiled published emission line measurements of local HII galaxies from different sources. The data gathered, together with the works we have used to compile the galaxy sample are given in table 2.1. The vast majority of the objects selected for this study were discovered using Schmidt telescopes, searching for strong emission lines or blue colors. Sources with strong emission lines are easiliy detected through objective prism surveys. This technique is best suited to detect objects with high equivalent widths and line strengths. Objects with strong continua are lost in these surveys, since the emission lines are swallowed by the continuum. On the other hand, galaxies with weak lines which have evolved past their peaks of star formation but are still quite blue are found through colour selection techniques.

The objects from references 6 and 10 come from the Tololo (Smith, Aguirre, & Zemelman, 1976) and University of Michigan (UM) (MacAlpine, Lewis, & Smith, 1977) objective prism surveys. The limiting magnitude is about 19.0. The spectroscopic observations for these samples were taken using several telescopes and detectors, and the observing conditions were not always good. Some of the observations were carried out at Las Campanas 2.5m telescope, using narrow apertures. These observations therefore can't provide absolute fluxes. They were also affected by second order contamination. The rest of the spectra were obtained using the 3.6m at ESO. The slit aperture was $8''$, and the spectrophotometry is accurate to 10%.

The objects from reference 7 are the brightest galaxies from the Calán-Tololo objective prism survey (Maza et al., 1989). Its limitinig magnitude is 17.5. The spectra were obtained using a variety of detectors (Vidicon, 2DF, CCDs), and the apertures used range from $2''$to $4''$. The spectra were flux calibrated.

The HII galaxies from reference 19 are located in the voids of the digitized Hamburg Quasar Survey (Hagen et al., 1995). The limiting magnitude of the objective prism survey is 18.5. The data presented in this work were gathered using the 2.2m telescope at the German-Spanish observatory at Calar Alto, Spain, under good photometric conditions using a $4''$slit. This is enough to encompass most of the line-emitting region.

The objects from reference 15 were selected from the Case survey (Pesch & Sanduleak, 1983). This survey searches simultaneously for both a UV excess and strong emission lines. The limiting magnitude is 16.0. The data for the spectroscopic follow-up study were obtained on 9 observing runs, using different telescopes and detectors. The majority of the objects in this sample were observed using CCD detectors, and the spectra were flux calibrated. The slit widths used were $2.4''$and $3.0''$. The spatial region extracted spanned all of the line emission, but did not cover all of the continuum emission.

The objects from the references 13, 14, 16, 17 and 18 were taken from the first Byurakan Survey (FBS, also known as the Markarian survey (Markarian, 1967)) and the second Byurakan Survey (SBS)(Markarian, Lipovetskii, & Stepanian, 1983). The FBS is another objective prism survey that searches for galaxies with a UV excess, and its limiting photographic magnitude is 15.5. Selection of the SBS objects was done according to the presence of strong UV continuum and emission lines. The SBS was carried out using the same Schmidt telescope as the FBS, and its limiting photographic magnitude is 19.5. The observations presented in 13, 14, 16 and 17 are high S/N spectra, taken with the Ritchey-Chrètien spectrograph at the

Kitt Peak National Observatory (KPNO) 4m telescope, with the T2KB CCD. The slit width used was $2''$, and the nights were transparent. The spectroscopic observations from reference 18 were done using the Ritchey-Chrètien spectrograph at the KPNO 4m telescope, and with the GoldCam spectrograph at the 2.1 m KPNO telescope. In the majority of cases, a $2''$slit was used.

Initially, we compiled objects with data on, at least, the intensities of the following emission lines: [OII] $\lambda\lambda$ 3727,29 Å , [OIII] λ 4363 Å , [OIII] $\lambda\lambda$ 4959, 5007 Å , and [SII] $\lambda\lambda$ 6717, 6731 Å . The hydrogen Balmer recombination lines were also required in order to allow a proper reddening correction. The emission lines of [SII] allow the determination of the electron density (see e.g. Osterbrock 1989) and can also be used, as well as the lines of [OII], to estimate the ionization parameter of the emitting gas. The intensities of the auroral and nebular [OIII] emission lines are needed in order to derive accurate values of the electron temperature, and hence of the oxygen abundance. Objects meeting these requirements belong mostly to references 6, 10, 13, 14 and 16. For all the objects in these samples, data on the intensity and equivalent width of Hβ are provided. We have also included data from references 7 and 2, although they lack data on the Hβ equivalent width and line intensity respectively.

Our initial sample was later enlarged to include objects with the same information as above but with no data on the [SII] lines, for which a low density regime was assumed. This is probably not a bad assumption since the average electron density derived for the galaxies with [SII] data is around 200 cm^{-3}.

Finally, a third enlargement was made to include objects with no reported measurements of the [OIII] λ 4363 Å line. These may correspond to objects with low surface brightness and/or low excitation and are generally excluded from emission-line analyses of samples of HII galaxies since the derivation of their oxygen abundances requires the use of empirical calibrations which are rather uncertain (see e.g. Skillman 1989). These objects represent, however, a large fraction of the observed HII galaxies. Most of them have been taken from references 6, 19 and 15. The latter reference does not provide absolute intensities for the hydrogen recombination lines.

The final sample comprises 450 objects: 236 with data on the [OIII] λ 4363 Å line and 214 with no observations of this line. These data have been obtained according to different selection criteria and using different instruments and techniques, and the parent populations of the different samples used are different. The presented sample can't be considered as

complete in any sense. In particular, line selected samples of galaxies are complete to a given line+continuum flux, whereas color selected samples will be complete to a given apparent magnitude. The galaxy sample presented here constitutes, however, the largest sample of local HII galaxies with good quality spectroscopic data, to our knowledge. However, the sample is very inhomogenous, due to different instrumental setups, observing conditions and reduction procedures. An accuracy analysis is therefore needed. This was done by comparing the observations for a few very well studied objects – *e.g.* IZw18, IIZw40, Mk36 – for which several independent observations exist. We have treated them as individual data in order to examine the external observational errors. The average error in redshift determinations is 5%. The average error in Hβ fluxes is 45%, and the average error in the equivalent width of Hβ, W$_\beta$ is 16%. Bin widths in the forthcoming histograms were chosen to be wide enough to engulf these errors. It is also important to note that, however large these numbers seem to be, they were derived from the nearest, brightest and best studied objects. These sources are sensitive to the full range of the aforementioned uncertainties, and are particularly affected by aperture issues (several components, different position angles for the slit, etc). More distant objects will be less affected by such effects, and their measurements will probably be more accurate. The errors previously presented are likely to be upper limits to the real uncertainities.

Table 2.1 lists the emission line properties of the sample objects. Column 1 gives the name of the object as it appears in the reference indicated in column 2. Column 3 gives the galaxy redshift (cz). Columns 4 to 10 give the reddening corrected emission line intensities, relative to that of Hβ, of: [OII] $\lambda\lambda$ 3727,29 Å, [OIII] λ 4363 Å, [OIII] λ 4959 Å, [OIII] λ 5007 Å, [SII] λ 6717 Å and [SII] λ 6731 Å. Column 11 gives the value of the logarithmic extinction at Hβ, c(Hβ). Column 12 gives the reddening corrected Hβ flux, in ergs cm^{-2} s^{-1}. Finally, columns 13 and 14 give the equivalent width of the Hβ and [OIII] λ 5007 Å lines (W_β and $W_{\lambda 5007}$) in Å.

Table 2.1: Complete list of galaxies included in this study.
References to the table: 1,Lequeux et al. (1979); 2,Kunth & Sargent (1983); 3,French (1980); 4,Dinerstein & Shields (1986); 5,Moles et al. (1990); 6,Terlevich et al. (1991); 7,Peña et al. (1991); 8,Pagel et al. (1992); 9,Skillman & Kennicutt (1993); 10,Masegosa et al. (1994); 11,Skillman et al. (1994); 12,Searle & Sargent (1972); 13,Izotov et al. (1994); 14,Thuan et al. (1995); 15,Salzer et al. (1995); 16,Izotov et al. (1997); 17,Izotov & Thuan (1998); 18,Guseva et al. (2000) and 19, Popescu & Hopp (2000).
The first 236 entries of the table contain the objects for which there exist measurements of the auroral line. The last 214 entries of the table contain the objects for which no measurements of the auroral line were found. Both subsamples are separated by a horizontal line in the table. The given line intensities are relative to Hβ. In the case of objects from reference 19, the value given under λ6716 is the sum of the λ6716 and λ6731 lines. The data from references 2 and 15 do not include flux measurements. Reference 7 does not give any data on equivalent widths. The objects from reference 17 whose name ends in "#" were also found in references 13 and 14.

Object.	Reference.	cz	λ3727	λ4363	λ4959	λ5007	λ6584	λ6716	λ6731	c(Hβ)	log F(Hβ).	W_β	$W_{\lambda 5007}$
IIZw70	1	1330	3.090	0.060	1.320	4.170	0.132	0.190	0.150	0.5	-13.37	...	...
IIZw70	2	1330	1.820	0.053	1.430	4.370	0.157	0.185	0.145	0.25	-13.44	49	...
IIZw40	1	679	1.120	0.120	2.450	7.590	0.072	0.060	0.050	1.1	-13.39	...	...
IIZw40	2	679	0.462	0.104	2.550	8.020	0.037	0.050	0.042	1.17	-13.10	300	...
IIZw40	6	899	0.440	0.095	2.547	7.756	0.054	0.063	0.052	0.62	-13.00	268	2122
IIZw40	8	750	0.539	0.111	2.710	7.690	0.042	0.036	0.042	1.25	-13.49	268	...
IIZw40	18	746	0.839	0.109	2.462	7.409	0.063	0.067	0.054	1.16	-13.04	278	...
Mrk5	2	792	2.160	0.039	1.430	4.380	0.123	0.216	0.164	0.23	-13.79	150	...
Mrk5	17	788	2.129	0.044	1.298	3.815	0.138	0.233	0.166	0.42	-13.38	132	...
IZw18	2	751	0.244	0.054	0.643	2.020	$\leq$1.4	$\leq$0.023	$\leq$0.010	0.04	-13.62	69	...
IZw18	8	760	0.278	0.067	0.720	2.020	$\sim$ 0.50	0.023	0.016	0.15	-13.68	83	...
IZw18	9	755	0.308	0.058	0.638	1.899	0.009	0.029	0.021	0.15	-13.87	100	...
IZw18	16	762	0.408	0.060	0.636	1.906	0.012	0.029	0.022	0.06	-13.11	104	...
Mrk36	2	646	1.260	0.109	1.680	5.320	0.060	0.093	0.049	0.1	-13.51	84	...
Mrk36	6	899	0.988	0.107	1.820	5.506	...	0.106	0.109	0.44	-13.36	70	432
Mrk36	17	654	1.293	0.096	1.622	4.834	0.053	0.117	0.084	0.02	-13.26	69	...
CG1116+51	2	1326	0.784	0.064	1.090	3.070	0.086	0.100	0.092	0.07	-14.01	35	...
CG1116+51	4	1326	0.940	0.068	0.920	2.740	Blended.	0.079	0.074	0.43	-14.13	...	...
NGC4861	4	847	1.300	0.102	2.783	8.350	Blended.	0.084	0.065	0.35	-12.35	150	...
NGC4861	16	812	1.102	0.089	1.982	5.802	0.046	0.095	0.071	0.09	-12.81	157	...
Mrk178	2	249	2.290	0.071	2.220	6.760	0.198	0.203	0.076	0.16	-14.32	83	...
Mrk178	18	222	1.264	0.119	0.843	5.466	0.057	0.158	0.122	0.2	-13.89	24	...
Mrk67	2	23084	1.510	0.070	2.100	6.410	0.057	0.128	0.080	0.25	-13.48	105	...
IZw122	2	665	1.270	0.125	2.210	7.010	0.066	0.102	0.075	0.32	-13.25	145	...
PHL293B	2	1550	0.708	0.153	2.070	6.130	0.020	0.068	0.035	0.25	-14.01	110	...
Pox4	3	3555	0.827	0.126	2.320	6.840	0.043	0.057	0.043	0.74	...	223	...
Pox4NW	3	3555	2.520	0.063	1.390	4.170	0.061	0.156	0.097	0.76	...	84	...

Table 2.1: Complete list of galaxies included (cont.)

Object.	Reference.	cz	λ3727	λ4363	λ4959	λ5007	λ6584	λ6716	λ6731	c(Hβ)	log F(Hβ).	W_β	$W_{\lambda 5007}$
Pox36	3	1120	2.670	0.047	1.535	4.390	0.012	0.158	0.102	0.81	...	96	...
Pox105	3	3405	1.250	0.113	1.900	5.540	0.064	0.084	0.056	1.15	...	131	...
Pox108	3	2555	0.877	0.116	2.380	6.940	0.061	0.075	0.054	0.72	...	326	...
Pox120	3	6220	0.790	0.135	2.120	6.290	0.048	0.074	0.047	0.43	...	208	...
Pox139	3	2100	1.470	0.096	2.040	5.710	0.062	0.117	0.077	0.72	...	358	...
Pox186	3	1170	0.408	0.155	2.080	6.070	0.018	0.031	0.018	0.39	...	370	...
Tol2	3	1200	1.950	0.059	1.480	4.420	0.089	0.131	0.087	0.83	...	62	...
Tol3	3	870	1.380	0.048	1.930	5.690	0.095	0.100	0.081	1.25	...	101	...
Tol65	3	2823	0.970	0.094	1.160	3.520	0.017	0.073	0.050	0.98	...	170	...
A21.29	7	40540	2.570	0.060	1.070	3.020	0.575	0.150	0.150	0.48	-13.92	...	...
C30.09	7	6250	2.040	0.070	1.780	5.500	0.157	0.150	0.070	0.01	-13.34	...	...
J01.02	7	9700	2.240	0.030	0.580	1.740	1.073	0.290	0.290	0.7	-13.31	...	...
M01.06	7	3640	0.950	0.070	2.340	6.760	0.100	0.290	0.160	0.6	-13.78	...	...
J03.15	7	3300	2.570	0.030	1.450	4.470	0.134	0.320	0.180	0.01	-13.67	...	...
J04.07	7	3700	2.340	0.040	1.700	5.130	0.200	0.130	0.120	0.3	-13.40	...	...
J04.05	7	4070	2.140	0.080	1.580	4.790	0.106	0.250	0.200	0.1	-14.03	...	...
J07.01	7	3590	1.020	0.120	2.340	6.760	0.080	0.190	0.110	0.11	-12.83	...	...
M08.08	7	1770	1.820	0.020	0.760	2.290	0.240	0.180	0.130	0.33	-12.78	...	...
M18.13a	7	5180	3.240	0.060	1.700	4.900	0.169	0.190	0.170	0.48	-12.77	...	...
J18.02	7	6230	1.580	0.060	2.090	6.170	0.106	0.160	0.060	0.29	-13.15	...	...
UM311	6	1799	1.407	0.023	1.374	4.113	0.158	0.135	0.091	0	-13.04	267	1184
UM311	17	1709	1.800	0.023	1.320	3.975	0.180	0.167	0.124	0.15	-12.98	279	...
Tol0341-407E	6	4497	1.657	0.106	2.102	6.630	0.054	0.117	0.089	0.26	-13.66	197	1458
Tol0633-415	6	5096	1.978	0.065	1.956	5.875	0.129	0.140	0.122	0.34	-13.51	109	694
Tol0645-376	6	7795	2.876	0.055	1.422	4.320	0.263	0.137	0.122	0.5	-13.74	50	292
Mrk709	6	15589	2.016	0.092	1.206	3.654	0.280	0.282	0.321	0.33	-13.76	35	141
Tol0440-381a	10	12292	2.725	0.040	1.647	4.871	0.000	0.067	0.082	0.25	-13.47	35	177
Tol0957-278	6	1499	3.073	0.044	1.386	4.065	0.112	0.255	0.194	0.46	-13.26	29	130
Tol1004-296NW	6	899	2.020	0.048	1.787	5.104	0.112	0.108	0.085	0.75	-12.80	87	488
Tol1004-296SE	6	1199	2.782	0.031	1.421	4.116	0.154	0.164	0.120	0.67	-13.10	51	248
Tol1004-296S	10	1199	2.324	0.035	1.412	4.166	0.140	0.175	0.124	0.2	-13.10	46	...
Tol1004-296N	10	1199	1.604	0.041	1.825	5.268	0.114	0.109	0.081	0.29	-12.80	93	...
Tol1008-286	6	4197	1.182	0.122	2.599	7.814	0.080	0.109	0.067	0.34	-13.68	125	1085
F2	6	16489	1.781	0.060	1.562	5.009	0.215	0.197	0.137	0.2	-13.59	116	629
F30	6	1199	1.258	0.091	2.131	6.429	0.074	0.117	0.088	0.21	-12.77	104	704
Tol1116-325	6	600	1.888	0.037	1.607	5.079	0.092	0.065	0.048	0.49	-13.39	264	1327
UM439G	6	1499	3.870	0.089	1.424	4.225	0.094	0.264	0.155	0.37	-13.90	19	93
UM439	6	1199	0.846	0.125	2.611	7.732	0.037	0.093	0.061	0	-13.44	160	1325
UM448	6	5396	2.736	0.034	0.961	2.826	0.392	0.277	0.197	0.27	-12.98	43	127
UM448	17	5498	2.776	0.030	0.867	2.599	0.409	0.366	0.285	0.33	-12.60	49	...
Tol1147-283	6	2099	3.625	0.055	1.138	3.234	0.143	0.258	0.163	0.3	-13.75	45	155
UM461	6	899	0.455	0.157	2.136	6.434	0.020	0.040	0.032	0	-13.20	342	2254
UM461	17	1007	0.527	0.136	2.039	6.022	0.021	0.052	0.042	0.12	-13.47	223	...

Table 2.1: Complete list of galaxies included (cont.)

Object.	Reference.	cz	λ3727	λ4363	λ4959	λ5007	λ6584	λ6716	λ6731	c(Hβ)	log F(Hβ).	W_β	$W_{\lambda 5007}$
UM463	10	1199	1.255	0.153	1.942	5.687	0.078	0.088	0.091	0.05	-13.77	127	716
UM462SW	6	899	1.599	0.101	1.896	5.660	0.060	0.097	0.081	0.09	-13.24	124	781
UM462SW	17	1028	1.742	0.078	1.663	4.929	0.073	0.168	0.112	0.29	-13.02	100	...
UM462knotA	10	899	1.488	0.102	2.023	6.044	0.071	0.114	0.086	0.03	-13.38	149	...
Tol1156-346	6	2398	0.913	0.123	2.717	7.924	0.054	0.068	0.057	0.58	-13.64	111	978
UM483	10	2398	2.442	0.053	1.982	5.925	0.080	0.121	0.049	0.5	-13.85	27	181
Tol1304-353	10	4197	0.416	0.195	2.240	6.837	0.000	0.034	0.014	0	-13.41	253	1929
Tol1304-386	6	4197	1.251	0.100	2.218	6.750	0.075	0.115	0.080	0.3	-13.27	286	2129
Tol1324-276	6	1799	1.456	0.050	1.915	5.568	0.100	0.123	0.105	0.23	-13.11	113	652
Tol1327-380	6	7794	3.233	0.037	2.067	5.889	0.103	0.128	0.085	1.14	-13.85	53	362
NGC5253a	6	300	1.296	0.066	1.597	4.800	0.223	0.127	0.105	0	-12.15	216	...
Tol1345-420	6	2398	1.765	0.073	1.853	5.476	0.051	0.145	0.137	0.17	-13.85	67	391
Tol1400-411	6	600	0.957	0.121	2.296	6.856	0.043	0.072	0.055	0.05	-12.85	259	1899
Tol1457-262a	6	5096	2.737	0.070	1.894	5.483	...	0.154	0.104	0.68	-13.07	78	480
Tol1457-262b	6	5096	2.181	0.055	1.721	5.514	0.100	0.169	0.106	0.33	-13.12	84	475
Tol1924-416	6	2698	1.287	0.101	1.832	4.918	0.069	0.092	0.078	0	-12.58	87	480
Mrk600	8	1125	0.860	0.116	2.250	6.780	$\sim$0.004	0.065	0.042	0.28	-13.64	58	...
Mrk600	17	1031	1.302	0.118	1.846	5.483	0.035	0.097	0.072	0.24	-13.41	54	...
Tol1214-277	8	7660	0.225	0.154	1.730	5.090	$\sim$0.009	0.017	0.014	0	-13.55	320	...
UGC4483	11	178	0.837	0.071	1.044	3.070	0.029	0.069	0.049	0.06	-13.74	144	...
F301	10	899	3.097	0.040	1.308	3.902	0.143	0.211	0.141	0.38	-13.44	38	...
C0840+1201	10	8994	1.614	0.084	1.610	4.812	0.091	0.138	0.070	0.21	-13.60	136	...
C1148-2020	10	3598	0.929	0.102	2.206	6.430	0.043	0.074	0.054	0.04	-12.85	202	...
C1543+091	10	11692	0.637	0.123	1.925	5.701	0.020	0.049	0.028	0	-13.27	212	...
CS0341-4045	10	4497	1.512	0.100	2.140	6.333	0.055	0.116	0.088	0.07	-13.54	214	...
UM469	10	17388	2.106	0.051	1.336	4.092	0.207	0.142	0.047	0.59	-13.62	68	...
UM160W	10	2398	1.474	0.086	1.815	5.498	0.071	0.157	0.057	0	-13.68	258	...
GR8	5	70	1.230	0.070	1.100	3.640	0.058	0.110	0.090	0.35	-14.58	...	...
SextansB	5	301	2.450	0.021	0.840	2.420	0.067	0.230	0.170	0.1	-14.58	...	...
SBS0946+558	13	1589	1.487	0.082	1.824	5.455	0.064	0.114	0.085	0.18	-13.59	125	...
Mrk1236	18	1877	1.513	0.043	1.395	4.134	0.138	0.189	0.132	0.04	-12.97	118	...
SBS0948+532	13	13880	1.367	0.083	1.810	5.632	0.068	0.138	0.103	0.04	-13.68	164	...
SBS1135+581	13	1019	1.346	0.069	1.791	4.765	0.067	0.117	0.083	0.14	-12.85	128	...
SBS1152+579	13	5156	0.887	0.140	2.112	6.043	0.040	0.068	0.054	0.26	-13.22	204	...
SBS1159+545	13	3567	0.677	0.109	1.124	3.460	0.022	0.054	0.042	0	-13.89	254	...
SBS1159+545#	17	3567	0.678	0.109	1.240	3.724	0.021	0.055	0.041	0.06	-13.72	249	...
SBS1211+540	13	929	0.646	0.116	1.537	4.648	0.020	0.053	0.042	0.1	-13.70	138	...
SBS1331+493	13	600	0.886	0.121	1.788	5.458	0.032	0.067	0.053	0.16	-13.77	192	...
SBS1437+370	13	420	1.401	0.088	1.761	5.268	0.059	0.134	0.094	0.14	-13.49	133	...
SBS1249+493	14	7345	1.070	0.106	1.479	4.364	0.033	0.080	0.044	0.2	-14.70	120	...
SBS1249+493#	17	7345	1.249	0.108	1.557	4.604	0.039	0.076	0.047	0.12	-13.80	124	...
SBS1331+493S	14	600	2.355	0.045	0.996	2.979	0.102	0.273	0.192	0	-14.30	28	...
SBS1415+437	14	480	1.060	0.086	1.014	2.977	0.033	0.086	0.064	0.08	-13.16	150	...

Table 2.1: Complete list of galaxies included (cont.)

Object.	Reference.	cz	λ3727	λ4363	λ4959	λ5007	λ6584	λ6716	λ6731	c(Hβ)	log F(Hβ).	W_β	$W_{\lambda 5007}$
SBS1415+437#	17	480	1.125	0.086	1.157	3.430	0.035	0.068	0.024	0.14	-13.02	163	...
SBS1420+544	14	6176	0.558	0.172	2.133	6.272	0.018	0.049	0.025	0.06	-13.77	231	...
SBS1420+544#	17	6176	0.577	0.184	2.263	6.862	0.019	0.057	0.028	0.16	-13.55	217	...
SBS1533+469	14	5666	2.249	0.077	1.561	4.854	0.154	0.300	0.220	0.04	-13.85	30	...
UM420	17	17514	2.450	0.065	1.352	4.042	0.277	0.270	0.189	0.31	-13.54	101	...
SBS0335-052	17	4077	0.285	0.106	1.019	3.058	0.009	0.018	0.015	0.13	-13.07	217	...
Mrk1089	17	4026	2.377	0.021	0.798	2.394	0.346	0.280	0.211	0.28	-12.95	84	...
Mrk1329	18	1598	1.152	0.046	1.823	5.485	0.074	0.088	0.068	0.05	-12.91	276	...
Mrk1199	17	4059	1.369	0.001	0.115	0.319	1.364	0.349	0.306	0.44	-12.83	20	...
SBS0741+535	16	5576	2.910	0.068	1.467	4.404	0.122	0.217	0.211	0.16	-13.80	44	...
SBS0749+568	16	5471	1.668	0.098	1.672	4.880	0.076	0.178	0.114	0.12	-13.72	117	...
SBS0749+582	16	9548	1.261	0.115	2.602	7.887	0.078	0.095	0.073	0.14	-14.15	143	...
SBS0907+543	16	8124	0.940	0.121	2.288	6.838	0.033	0.065	0.050	0.02	-13.82	187	...
SBS0917+527	16	2305	1.888	0.092	1.583	4.680	0.058	0.164	0.114	0.09	-13.70	85	...
SBS0926+606	16	4122	1.785	0.083	1.628	4.772	0.083	0.182	0.146	0.02	-13.34	119	...
SBS0940+544N	16	1638	0.570	0.135	1.333	3.981	0.016	0.040	0.032	0.05	-13.82	234	...
SBS0943+561A	16	8850	1.244	0.156	1.908	5.863	0.000	0.151	0.126	0	-14.70	48	...
SBS1030+583	16	2269	0.968	0.104	1.704	5.028	0.031	0.096	0.067	0	-13.43	92	...
Mrk1271	17	1013	1.606	0.102	2.061	6.084	0.123	0.152	0.112	0.14	-12.93	91	...
SBS1054+365	16	603	1.066	0.095	2.007	5.948	0.048	0.094	0.065	0.07	-13.59	117	...
Mrk162	17	6458	3.294	0.040	1.231	3.628	0.202	0.344	0.173	0.33	-13.32	55	...
SBS1116+583B	16	9905	0.589	0.117	1.650	4.842	0.027	0.068	0.065	0.1	-14.22	107	...
SBS1124+792	16	3	1.333	0.071	1.143	3.455	0.050	0.103	0.075	0	-13.33	153	...
SBS1128+573	16	1787	0.872	0.143	1.956	5.801	0.033	0.074	0.060	0.01	-14.05	80	...
Mrk750	17	728	1.701	0.056	1.693	5.016	0.091	0.170	0.113	0.14	-12.76	131	...
SBS1205+557	16	1751	2.138	0.083	1.263	3.714	0.083	0.183	0.130	0	-13.92	63	...
SBS1222+614	16	734	1.169	0.102	2.013	5.955	0.038	0.090	0.065	0	-13.04	87	...
SBS1223+487	16	288	0.719	0.127	1.960	5.543	0.029	0.061	0.045	0	-12.84	224	...
SBS1319+579A	16	2060	1.022	0.093	2.333	6.700	0.050	0.101	0.079	0.08	-13.31	214	...
SBS1319+579B	16	1997	2.442	0.050	1.133	3.282	0.161	0.374	0.273	0.01	-14.05	16	...
SBS1319+579C	16	1958	2.383	0.033	1.181	3.520	0.150	0.269	0.192	0.01	-13.80	64	...
SBS1358+576	16	10136	1.672	0.089	1.592	4.874	0.108	0.153	0.111	0.1	-13.39	72	...
SBS1441+294	16	13605	1.503	0.069	1.627	4.927	0.083	0.204	0.138	0.06	-14.05	56	...
SBS1533+574A	16	3355	2.459	0.067	1.297	3.804	0.122	0.234	0.170	0.1	-13.82	24	...
SBS1533+574B	16	3427	2.035	0.065	1.794	5.329	0.087	0.167	0.117	0.33	-13.70	78	...
SBS1535+554	16	624	2.191	0.060	1.577	4.689	0.101	0.208	0.154	0	-13.74	45	...
Mrk930	17	5537	2.371	0.050	1.388	4.170	0.143	0.269	0.198	0.25	-13.16	93	...
HS1222+3741	19	12262	1.680	0.150	1.850	5.560	0.000	0.160	0.000	0.15	-13.78	114	681
HS1236+3937	19	5516	1.160	0.140	1.520	4.450	0.000	0.260	0.000	0.08	-14.24	112	506
HS1258+3438	19	7435	2.220	0.020	1.930	5.340	0.000	0.220	0.000	0.38	-14.36	36	209
HS1304+3529	19	4947	1.850	0.100	1.520	4.510	0.100	0.330	0.000	0.01	-13.32	118	570
HS1312+3847	19	15439	2.420	0.050	1.530	4.450	0.100	0.470	0.000	0.04	-13.82	74	337
HS1312+3508	19	1049	2.610	0.070	1.700	4.920	0.110	0.300	0.000	0.16	-12.99	254	1466

Table 2.1: Complete list of galaxies included (cont.)

Object.	Reference.	cz	λ3727	λ4363	λ4959	λ5007	λ6584	λ6716	λ6731	c(Hβ)	log F(Hβ).	W_β	$W_{\lambda 5007}$
HS1315+3132	19	9443	4.100	0.050	1.230	3.560	0.000	0.420	0.000	0.48	-14.38	36	136
HS1318+3239	19	13041	1.560	0.120	1.980	5.770	0.000	0.230	0.000	0.19	-14.24	79	464
HS1319+3224	19	5456	1.240	0.130	1.630	5.030	0.000	0.140	0.000	0.21	...	49	251
HS1325+3255	19	7885	1.260	0.080	1.870	5.480	0.000	0.120	0.000	0.15	-14.36	74	412
HS1327+3126	19	17028	1.990	0.070	1.820	5.360	0.000	0.250	0.000	0.19	-13.97	91	514
HS1330+3651	19	5007	1.860	0.090	1.640	4.900	0.090	0.350	0.000	0.15	-13.58	72	387
HS1347+3811	19	3088	2.290	0.070	1.890	5.460	0.000	0.330	0.000	0.24	-14.06	64	363
HS1424+3836	19	6535	1.150	0.070	1.810	5.520	0.000	0.120	0.000	0.19	-14.00	104	579
HS1440+4302	19	2548	5.300	0.140	1.910	5.580	0.110	0.360	0.000	0.34	-13.95	44	269
HS1440+3120	19	15739	1.560	0.110	2.110	6.130	0.000	0.200	0.000	0.22	-14.02	152	925
HS1442+4250	19	749	0.970	0.110	1.650	4.750	0.000	0.080	0.000	0.08	-13.53	113	550
HS1507+3743	19	9653	0.870	0.120	2.170	6.580	0.000	0.130	0.000	0.11	-13.46	232	1374
HS1610+4539	19	5876	1.360	0.090	1.360	3.740	0.000	0.420	0.000	0.48	-13.85	26	106
HS1614+4709	19	779	0.790	0.060	2.000	5.900	0.000	0.180	0.000	0.1	-13.12	140	880
HS1645+5155	19	8574	3.490	0.090	1.290	3.870	0.120	0.460	0.000	0.33	-13.81	47	191
HS1728+5655	19	4797	2.110	0.030	1.720	5.000	0.250	0.230	0.000	0.09	-13.62	106	514
IZw18	12	764	0.320	0.070	0.710	2.190	$\leq$0.100	0.129	0.000	0.13	...	83	...
IZw18	1	840	0.380	0.074	0.692	2.138	$\leq$0.050	$\leq$0.107	0.000	0.1	-13.78	83	...
IIZw40	12	750	0.950	0.140	2.340	7.240	$\leq$0.100	0.170	0.000	1	...	268	...
B16.16a	7	6680	2.950	0.090	1.450	3.890	...	0.000	0.000	0.3	-13.64	...	...
B21.03	7	5190	1.230	0.130	2.190	6.610	...	0.000	0.000	0.24	-14.35	...	...
B22.06	7	14390	1.910	0.060	2.040	6.030	0.200	0.000	0.000	0.33	-13.64	...	...
B25.07	7	22530	1.120	0.110	2.090	6.610	...	0.000	0.000	0.29	-13.69	...	...
F27.25	7	12460	0.620	0.160	2.190	6.920	...	0.000	0.000	0.01	-13.83	...	...
F27.22	7	18390	1.700	0.100	1.950	6.310	...	0.000	0.000	0.45	-13.62	...	...
J03.03	7	4030	2.700	0.040	1.480	4.900	...	0.000	0.000	0.71	-13.53	...	...
M02.14	7	17540	1.620	0.070	1.660	4.790	...	0.000	0.000	0.01	-14.12	...	...
M02.13	7	3560	0.870	0.120	2.090	6.030	...	0.000	0.000	0.12	-14.31	...	...
M02.12	7	10540	1.120	0.040	2.140	6.170	...	0.000	0.000	0.22	-14.11	...	...
M02.03	7	11590	1.910	0.080	1.620	4.680	0.112	0.000	0.000	0.01	-13.75	...	...
J04.06	7	4070	2.750	0.070	1.200	3.800	...	0.000	0.000	0.1	-13.83	...	...
K15.01	7	3910	3.800	0.050	0.760	2.240	...	0.000	0.000	0.46	-14.07	...	...
L02.01	7	5190	0.830	0.130	2.240	6.460	0.035	0.000	0.000	0.22	-13.74	...	...
M12.07	7	10630	3.470	0.040	0.980	2.820	...	0.000	0.000	0.78	-14.12	...	...
M13.14	7	4330	1.740	0.040	1.550	4.370	...	0.000	0.000	0.01	-13.62	...	...
M13.16	7	13370	2.240	0.050	1.350	3.890	...	0.000	0.000	0.22	-14.15	...	...
K09.09	7	4350	3.720	0.050	0.850	2.630	...	0.000	0.000	0.48	-14.07	...	...
M18.02	7	8540	1.580	0.040	1.580	4.570	...	0.000	0.000	0.01	-14.25	...	...
M18.13b	7	5250	5.250	0.120	1.660	5.010	$\leq$0.100	0.000	0.000	0.35	-13.12	...	...
A03.03	7	15010	0.830	0.150	2.140	6.610	...	0.000	0.000	0.53	-13.72	...	...
C04.01	7	13560	0.590	0.170	1.950	6.170	...	0.000	0.000	0.01	-13.48	...	...
UM228	6	29380	2.128	0.043	1.419	4.411	...	...	0.296	0.24	-13.69	100	495
UM238	6	4197	1.195	0.119	2.460	7.727	...	...	...	0	-14.12	149	1225

Table 2.1: Complete list of galaxies included (cont.)

Object.	Reference.	cz	λ3727	λ4363	λ4959	λ5007	λ6584	λ6716	λ6731	c(Hβ)	log F(Hβ).	W_β	$W_{\lambda 5007}$
UM382	6	3598	0.748	0.237	1.881	5.495	...	...	...	0.74	-14.15	140	827
UM396	6	6296	0.974	0.059	2.072	6.321	0.075	...	0.064	1.08	-13.74	142	1029
Tol0306-405	6	14090	2.392	0.089	1.975	5.447	0.134	...	0.457	0	-13.74	80	487
Tol0440-381	6	12292	3.112	0.065	1.555	4.607	...	...	0.321	0.31	-13.43	35	177
Tol0513-393	6	14990	0.627	0.159	2.569	7.730	...	...	...	0.27	-13.76	187	1524
Tol0618-402	6	10493	2.072	0.147	1.621	4.964	...	...	0.351	0	-14.26	51	275
Tol0620-386	6	20086	2.887	0.109	1.697	5.059	...	...	0.336	0.74	-13.83	50	284
UM455	6	3598	1.656	0.195	2.072	6.353	...	...	...	0.78	-14.02	52	384
UM463	6	1199	1.139	0.149	1.877	5.654	0.077	...	...	0	-13.85	119	716
UM462ne	6	1199	1.832	0.100	1.561	4.832	...	...	0.255	0.36	-13.43	69	360
UM469	6	17388	2.072	0.053	1.352	4.060	0.210	...	.200	0.68	-13.62	496	313
UM483	6	2099	3.824	0.101	1.980	5.631	0.083	...	...	1.47	-13.87	26	181
Tol1209-285	6	8994	0.912	0.107	2.265	6.680	...	...	...	0	-13.82	191	1353
Mrk1315	6	600	0.905	0.073	2.004	5.733	...	...	...	0	-13.01	391	2381
Tol1214-277	6	7795	0.309	0.144	1.663	5.154	...	...	...	0.28	-13.65	294	1564
UM495	6	8394	6.198	0.158	1.918	5.832	...	...	...	0.51	-14.03	42	312
Tol1223-359	6	2698	0.922	0.119	1.254	3.660	...	...	...	0.48	-13.77	171	696
Tol1247-232	6	14390	1.314	0.057	1.807	5.300	0.174	...	...	0.33	-12.87	97	557
Tol1304-353	6	4197	0.416	0.195	2.298	6.908	...	...	...	0.19	-13.44	272	1929
UM568	6	14390	1.427	0.102	2.146	6.120	...	...	...	0.3	-13.92	184	1091
Tol1334-326	6	3598	0.875	0.115	2.434	7.266	...	...	...	0.03	-13.59	263	1754
Tol2138-405	6	16788	1.144	0.122	1.793	4.722	...	...	...	0.24	-13.55	149	736
UM160A	6	2398	1.474	0.086	1.815	5.498	...	...	...	0	-13.68	258	1431
UM160B	6	2398	1.595	0.073	1.400	4.179	...	...	...	0.3	-14.00	110	500
Mrk930	6	5396	1.865	0.078	1.450	3.350	...	...	...	0.55	-13.05	71	261
UM254	10	13191	3.131	0.061	1.091	3.015	0.000	0.000	0.000	0.64	-13.74	70	...
UM133	10	1499	1.318	0.104	1.346	4.140	0.000	0.000	0.000	0	-13.96	93	...
UM408	10	3598	0.855	0.168	1.871	5.494	0.112	0.000	0.000	0.47	-14.18	52	...
C0357-3914	10	22484	0.974	0.111	1.949	5.811	0.000	0.000	0.000	0.38	-13.74	154	...
Tol0614-375	10	20086	3.071	0.112	1.594	4.847	0.000	0.000	0.000	0.4	-13.74	53	...
C0942-1928	10	9593	3.619	0.038	0.593	1.875	0.000	0.000	0.000	1	-13.48	71	...
CS0953-174	10	3598	1.002	0.128	1.494	4.312	0.000	0.000	0.000	0.16	-14.15	209	...
1210F-38	10	23684	1.426	0.179	2.662	7.557	0.000	0.000	0.000	0.09	-14.37	135	...
14-0016	10	8094	1.533	0.092	2.425	7.920	0.000	0.000	0.125	0.12	-13.24	135	...
C1409+1200a	10	16788	1.697	0.087	2.381	6.811	0.123	0.000	0.000	0.13	-13.72	127	...
Mrk507	10	5996	4.304	0.090	1.911	4.941	0.000	0.000	0.000	0.87	-14.03	54	...
Tol2326-405	10	15289	1.436	0.102	2.069	6.376	0.000	0.000	0.000	0.43	-13.92	92	...
UM203	6	11992	4.156	...	0.839	2.121	0.509	...	...	0.76	-14.00	20	48
UM38	6	1199	3.607	...	1.336	4.028	...	...	...	0.47	-14.04	25	110
UM254	6	13191	3.062	...	1.086	2.994	...	...	...	0.74	-13.74	70	238
UM48	6	4797	2.487	...	0.563	1.801	0.622	...	...	0.31	-13.68	28	53
UM55	6	5396	2.523	...	0.568	1.656	...	...	...	0.25	-14.28	27	47
UM61	6	11092	3.854	...	0.606	1.814	...	...	...	0.08	-14.23	17	33

Table 2.1: Complete list of galaxies included (cont.)

Object.	Reference.	cz	λ3727	λ4363	λ4959	λ5007	λ6584	λ6716	λ6731	c(Hβ)	log F(Hβ).	W_β	$W_{\lambda 5007}$
UM65	6	6296	4.446	...	1.278	3.773	...	...	...	0.92	-14.00	22	95
UM69W	6	1799	4.397	...	1.006	2.918	...	...	...	0.51	-14.04	54	173
UM282	6	11092	1.016	...	1.717	5.766	...	...	...	0	-14.42	66	408
Tol0104-388	6	6296	3.995	...	1.432	4.291	...	...	...	0.37	-13.64	49	226
UM308	6	4797	3.474	...	0.269	0.704	0.787	...	...	1.09	-13.70	34	26
UM309	6	1199	2.588	...	1.452	4.201	...	...	...	1.23	-13.72	359	1959
Tol0121-376	6	10493	5.684	...	1.048	2.890	...	...	...	0.88	-14.13	30	98
Tol0127-397	6	4797	3.278	...	1.142	2.164	...	...	...	0.5	-13.34	38	130
UM133	6	2099	1.859	...	1.336	4.984	...	...	...	0.41	-13.85	77	336
UM369	6	5696	2.259	...	1.499	4.974	...	...	...	0.33	-14.04	86	454
UM372	6	1499	2.146	...	1.308	3.831	...	...	...	0.85	-13.96	138	564
UM143	6	9893	1.448	...	1.796	6.341	...	...	...	0.26	-13.55	126	867
UM374	6	5696	3.774	...	1.169	3.112	...	...	...	1.19	-13.89	43	156
UM376	6	11692	1.755	...	1.564	4.937	...	...	...	0.69	-14.32	64	362
UM380	6	16788	2.053	...	1.607	5.367	...	...	...	0.39	-14.18	59	349
UM389	6	14090	2.772	...	1.704	4.883	...	...	...	0	-14.33	32	169
UM406	6	11392	1.812	...	1.366	3.846	0.249	...	...	0.95	-14.06	109	475
UM417	6	2698	0.330	...	1.875	5.566	...	...	...	0.84	-14.23	144	903
UM418	6	7795	2.055	...	0.106	0.317	1.144	0.132	0.103	1.2	-13.64	13	4
UM420	6	17388	3.190	...	1.413	4.371	...	...	...	0.47	-13.85	151	802
Tol0226-390	6	14090	2.931	...	1.844	5.084	...	...	...	0.45	-13.24	106	568
Tol0242-387	6	37774	3.527	...	1.202	3.068	...	...	...	0.76	-13.66	62	213
Tol0302-407	6	15289	2.682	...	1.674	5.112	...	...	...	0.64	-14.19	54	307
Tol0302-415	6	16788	5.493	...	1.394	4.277	...	...	...	1.25	-13.89	36	181
Tol0319-375	6	16189	2.609	...	1.172	3.646	...	...	...	0.39	-14.09	53	217
Tol0341-376	6	6296	3.312	...	1.609	4.778	...	...	...	0.34	-14.05	27	149
Tol0341-407W	6	4497	3.696	...	1.466	4.473	...	...	...	0.31	-13.98	40	193
Tol0510-400	6	11992	2.718	...	1.437	4.248	0.234	...	0.263	0.56	-13.93	63	294
Tol0538-416	6	13491	3.156	...	1.585	4.597	...	...	0.422	0.38	-13.85	55	275
Tol0559-393	6	24883	5.471	...	0.635	1.857	0.483	0.397	0.434	1.15	-13.92	24	52
Mrk710NE	6	1499	0.958	...	0.171	0.506	0.692	...	0.400	0.71	-14.07	19	4
Mrk710	6	1499	1.513	...	0.112	0.356	1.084	0.251	0.240	0.46	-13.21	41	16
Mrk711	6	5696	2.682	...	0.857	2.563	0.941	0.175	0.146	1	-13.36	36	101
Tol1025-284	6	9593	1.875	...	1.547	4.708	0.240	0.087	0.068	0.46	-13.80	73	385
Fairall5	6	8694	2.023	...	1.573	4.762	0.202	...	0.232	0.51	-13.72	58	285
UM422	6	2099	0.954	...	2.673	8.356	...	...	0.331	0.44	-14.14	344	3370
UM444	6	7195	3.859	...	0.999	3.061	...	...	...	0.77	-13.49	29	98
UM446	6	1799	3.584	...	1.608	4.411	...	...	...	1.24	-13.77	38	197
UM468	6	11092	4.700	...	0.978	2.983	...	...	...	0.58	-13.56	27	91
UM471	6	10493	2.634	...	0.745	2.283	...	...	...	0.8	-14.14	49	128
UM476	6	899	3.547	...	0.483	1.625	0.330	...	...	0.73	-13.82	75	136
UM477	6	1199	1.295	...	0.109	0.294	1.614	0.374	0.392	1.39	-13.39	22	7
Mrk1318	6	1499	2.721	...	1.230	3.514	...	...	...	0.47	-13.08	121	469

Table 2.1: Complete list of galaxies included (cont.)

Object.	Reference.	cz	λ3727	λ4363	λ4959	λ5007	λ6584	λ6716	λ6731	c(Hβ)	log F(Hβ).	W_β	$W_{\lambda 5007}$
UM494	6	8394	6.684	...	1.036	3.279	...	...	...	1.35	-14.29	33	130
UM499	6	2099	3.439	...	0.276	0.705	...	...	...	1.3	-12.74	32	25
Mrk52	6	2398	3.482	...	0.259	0.762	...	...	...	1.4	-12.77	29	25
Tol1223-388	6	3298	2.999	...	0.218	0.765	1.101	0.300	0.216	1.21	-13.54	35	30
UM505	6	1199	2.764	...	0.727	2.162	0.372	0.303	0.192	0.25	-13.62	86	201
UM507	6	5996	2.595	...	1.508	4.638	...	...	...	0.47	-14.18	57	292
UM530	6	20986	3.535	...	0.694	2.333	...	...	...	1	-13.36	28	74
Tol1258-363	6	4497	4.587	...	1.136	3.526	...	...	...	0.86	-13.52	42	169
UM559	6	1499	1.105	...	1.586	4.880	...	...	...	0.25	-13.54	325	1710
UM597	6	6895	5.043	...	0.801	2.445	...	...	...	0.62	-13.92	18	46
NGC5253b	6	300	4.945	...	1.214	3.635	0.183	0.365	0.271	0.34	-13.62	21	86
NGC5253c	6	300	3.212	...	1.278	3.881	0.196	0.298	0.214	0.2	-13.87	42	179
UM618	6	4197	2.557	...	1.442	4.935	...	...	...	0.21	-14.19	38	203
UM619	6	4497	3.224	...	0.896	2.320	...	...	...	0	-13.92	137	338
UM623	6	10193	4.489	...	0.586	1.418	0.637	0.226	0.217	1.24	-13.82	43	71
UM626	6	3298	2.421	...	0.849	2.656	0.441	...	...	0.13	-13.96	119	330
Tol1358-328	6	899	1.707	...	1.459	4.236	...	...	...	0.1	-12.92	166	749
UM628	6	7195	3.780	...	0.536	1.711	0.392	0.157	0.115	0.36	-14.05	29	54
UM653	6	11392	1.356	...	1.675	4.991	...	...	...	0	-14.07	43	223
Tol1457-262c	6	4797	5.648	...	1.307	3.927	...	...	...	0.74	-13.77	41	182
Tol1457-262e	6	5396	3.175	...	1.132	3.144	0.172	...	...	0.47	-12.80	29	97
Tol2259-398	6	8694	2.953	...	0.439	1.358	...	...	...	1.03	-13.51	25	38
Osmer12	6	55162	4.284	...	1.478	3.985	...	...	...	0.99	-14.82	52	232
Tol2311-411	6	9893	5.626	...	1.341	3.795	...	...	...	0.88	-13.67	35	150
UM157	6	7495	6.700	...	1.370	4.279	...	...	...	1.45	-14.13	22	111
UM159	6	8694	2.304	...	1.120	3.521	...	...	...	0	-14.12	52	203
UM160c	6	2398	3.420	...	1.226	3.717	...	...	...	0.8	-14.33	73	307
UM160d	6	2398	2.603	...	1.575	4.338	...	...	...	0.71	-14.40	32	159
Tol2326-405	6	15289	1.192	...	2.090	6.473	...	...	...	0.21	-13.92	92	645
UM167	6	2698	2.983	...	0.548	1.465	1.012	0.215	0.189	1.28	-12.60	28	47
UM168	6	6895	1.532	...	1.755	5.415	...	...	...	0.01	-14.03	106	606
UM172E	6	17688	5.207	...	0.676	1.438	...	...	...	1.2	-14.00	37	60
UM13N	6	13191	2.580	...	0.677	2.268	...	...	...	0.31	-13.89	51	124
UM219	6	3897	3.298	...	1.190	3.923	...	...	...	0.44	-14.06	17	74
UM227	6	8994	6.516	...	0.700	2.498	...	...	...	0.9	-14.36	9	25
Tol0003-402	6	14390	6.828	...	0.874	3.823	...	...	...	0.32	-14.85	14	58
UM33	6	8694	6.569	...	0.423	1.692	...	...	...	0.67	-14.62	12	23
Tol0026-404	6	12891	6.164	...	0.436	1.756	...	...	0.647	0.89	-14.54	10	21
Tol0030-388	6	13790	5.228	...	0.863	2.651	...	...	0.779	0.56	-14.03	18	53
UM78	6	11992	3.100	...	0.504	1.477	0.597	...	...	0	-14.29	10	11
UM80	6	4797	2.670	...	1.472	5.279	...	...	...	0	-14.70	10	68
UM306	6	4797	3.413	...	1.722	4.879	...	...	...	1.17	-13.96	29	160
UM323	6	1799	1.927	...	1.300	4.800	...	...	...	0.36	-14.02	31	162

Table 2.1: Complete list of galaxies included (cont.)

Object.	Reference.	cz	λ3727	λ4363	λ4959	λ5007	λ6584	λ6716	λ6731	c(Hβ)	log F(Hβ).	W_β	$W_{\lambda 5007}$
Tol0124-413	6	13191	3.735	...	0.497	1.665	...	...	0.916	0.64	-14.03	11	21
UM110	6	8994	8.076	...	0.380	1.760	...	...	...	1.46	-14.68	18	38
UM111	6	1799	2.253	...	1.372	4.568	...	...	...	0.5	-14.46	44	221
UM336	6	6296	0.765	...	1.834	5.596	...	...	...	0.11	-14.33	55	331
UM345	6	5696	2.557	...	1.480	4.758	...	...	...	0.67	-14.24	30	145
UM358	6	16788	4.936	...	0.812	2.655	...	...	...	1.38	-14.35	43	143
Tol0140-420	6	6595	2.776	...	1.650	4.677	...	...	...	0.13	-13.92	39	194
UM137	6	1799	1.596	...	1.404	4.001	...	...	...	0.35	-14.29	172	662
UM377	6	8694	3.051	...	0.897	2.802	...	...	...	0.7	-14.37	41	129
UM150	6	12891	3.886	...	0.376	0.938	0.847	...	...	1.47	-14.00	33	34
UM151	6	4797	4.489	...	0.631	1.725	...	...	...	1.13	-14.14	22	42
UM390	6	10193	2.842	...	1.883	4.592	...	...	...	0.47	-14.54	22	115
UM404	6	3598	1.558	...	1.589	4.830	...	...	...	0.36	-14.28	94	512
UM408	6	3598	0.872	...	1.860	5.443	...	...	...	0.6	-14.18	52	307
UM410N	6	6895	1.021	...	1.241	3.598	...	...	...	0	-14.14	53	199
Tol0351-387	6	19786	4.174	...	0.556	1.280	0.426	...	...	0.51	-14.22	14	21
Osmer14	6	79445	4.658	...	1.227	2.926	...	...	...	0.92	-14.72	58	191
Tol0452-416	6	11092	4.089	...	1.904	5.272	...	...	...	1.23	-14.72	15	86
Tol0506-405	6	12591	4.372	...	0.740	2.205	...	...	...	0.82	-14.02	22	54
Tol0527-394	6	4497	1.672	...	1.744	5.343	...	...	...	0.15	-14.38	24	141
Tol0528-383	6	3298	2.841	...	1.560	4.633	...	...	...	0.2	-14.23	18	91
Tol0614-375	6	9893	5.641	...	0.308	0.795	0.726	...	...	1.23	-14.04	8	6
Tol0619-392	6	15889	5.220	...	0.605	1.753	0.755	...	...	1.26	-13.91	15	31
Tol1021-289	6	17688	3.528	...	1.251	3.616	...	...	...	0.57	-14.01	33	141
Tol1025-285	6	9294	5.293	...	0.426	1.253	0.689	0.267	0.190	0.9	-14.10	8	11
Fairall3	6	10193	3.507	...	0.973	2.797	...	...	...	0.69	-14.17	12	37
Fairall6	6	2099	4.111	...	1.851	5.391	...	0.333	...	0.76	-13.24	15	91
Fairall7	6	1499	2.973	...	1.088	3.150	...	...	0.404	0.6	-13.07	29	98
UM437	6	19486	4.733	...	0.302	1.030	0.964	...	...	1.15	-14.37	13	16
UM459	6	13790	5.295	...	1.305	3.816	...	...	...	0.77	-14.49	28	120
UM467	6	5696	1.835	...	0.081	0.243	1.547	...	...	0.7	-14.09	6	1
UM480	6	14690	4.642	...	1.975	4.809	...	...	...	0.7	-14.19	15	83
UM482	6	10792	4.540	...	0.896	2.921	...	...	...	0.68	-13.64	24	79
UM488	6	15289	2.827	...	0.663	1.981	...	...	...	1.07	-13.85	14	31
UM490	6	5696	0.736	...	2.086	5.688	...	...	...	0	-13.89	121	678
UM496	6	12292	1.666	...	1.751	5.688	...	...	...	0.34	-14.34	58	291
UM501	6	2398	1.484	...	1.868	5.789	...	...	...	0.48	-14.06	123	785
UM500	6	2099	3.641	...	1.587	4.970	...	...	...	0.23	-13.85	133	714
UM506	6	1499	2.386	...	0.324	0.931	0.700	...	...	0.26	-14.03	46	46
Fairall12	6	21585	1.823	...	1.506	4.320	...	...	...	0.33	-13.92	44	209
UM512	6	4497	2.000	...	0.650	1.900	...	...	...	0	-14.60	6	21
UM523	6	899	2.214	...	1.582	4.218	...	...	...	0	-14.24	30	137
Mrk59N	6	1499	4.213	...	0.720	2.133	...	...	...	0.54	-14.26	17	35

Table 2.1: Complete list of galaxies included (cont.)

Object.	Reference.	cz	λ3727	λ4363	λ4959	λ5007	λ6584	λ6716	λ6731	c(Hβ)	log F(Hβ).	W_β	$W_{\lambda 5007}$
Tol1257-399	6	12591	2.562	...	1.439	4.319	...	...	0.532	0.45	-13.68	25	117
UM539	6	6895	2.125	...	1.352	4.600	...	...	...	0.69	-14.51	48	249
UM538	6	600	2.649	...	1.508	3.854	...	...	...	0.31	-14.51	77	322
UM564	6	15289	1.768	...	2.390	7.679	...	...	...	0.71	-14.11	50	427
UM591	6	16489	2.567	...	1.430	4.094	...	...	...	0.97	-14.43	39	167
UM601	6	8394	3.336	...	0.470	1.249	0.947	...	...	0.79	-13.64	22	30
UM603	6	15889	3.729	...	2.299	1.665	...	...	...	0.75	-13.74	23	42
Fairall20	6	9893	3.187	...	1.748	5.603	...	...	...	0.49	-13.29	40	245
UM612	6	4497	3.475	...	1.187	3.420	...	...	...	0.69	-14.21	24	93
Tol1400-397	6	8694	1.544	...	1.687	5.096	...	...	...	0.65	-14.16	65	356
UM635	6	7495	3.947	...	2.006	6.172	...	...	...	0	-14.47	26	176
Mrk507	6	5996	4.261	...	1.896	4.884	...	...	...	1.04	-14.03	54	302
Tol2122-408	6	4197	4.901	...	1.577	3.931	...	...	...	0.82	-13.89	13	56
UM162	6	19786	2.171	...	2.358	7.018	...	...	...	0.06	-14.19	81	600
UM3	6	6296	2.425	...	1.107	3.383	...	...	...	0.44	-14.03	33	120
UM4W	6	6296	2.129	...	1.535	4.551	...	...	...	0.04	-13.92	30	144
UM9	6	5096	2.816	...	1.672	4.442	...	...	...	0	-14.39	15	74
UM191	6	7195	4.790	...	0.337	0.727	0.826	...	...	1.33	-13.85	10	8
Mrk109	2	9100	3.810	...	0.426	1.370	0.763	0.519	0.271	0.36	-13.90	27	...
Mrk168	2	10148	3.700	...	1.440	4.370	0.281	0.301	0.233	0.63	-13.95	39	...
NGC3690	2	3121	2.600	...	0.427	1.270	0.968	0.288	0.216	0.73	-12.26	32	...
M03.13	7	10490	2.570	...	1.259	3.548	0.240	0.269	0.295	0.06	-14.11	...	...
CG22	15	7315	7.213	...	1.083	3.281	...	...	...	1.50	...	21	82
CG34	15	5126	2.094	...	1.610	4.879	...	...	...	0.18	...	52	275
CG43	15	4467	6.327	...	0.976	2.957	0.315	...	...	1.41	...	31	101
CG46	15	6266	5.232	...	1.372	4.159	...	...	...	1.50	...	35	162
CG69	15	8634	2.090	...	1.544	4.680	...	...	...	0	...	35	179
CG74	15	13910	4.065	...	1.332	4.037	...	...	...	0.88	...	21	103
CG85	15	14900	4.722	...	1.141	3.458	...	...	...	0.82	...	20	79
CG99	15	7225	9.986	...	1.327	4.022	...	...	...	1.50	...	29	144
CG103	15	1619	3.800	...	0.967	2.929	...	...	...	0.54	...	31	95
CG136	15	6895	3.529	...	1.358	4.116	...	...	...	0.19	...	30	121
CG141	15	6446	1.910	...	1.544	4.680	0.143	...	...	0	...	56	269
CG147	15	3328	5.026	...	0.981	2.973	0.429	...	...	0.93	...	21	62
CG159	15	6356	1.410	...	1.657	5.020	...	...	...	0	...	25	95
CG165	15	8514	0.460	...	2.584	7.830	...	...	...	0	...	162	1290
CG177	15	7885	8.669	...	0.939	2.844	...	...	...	1.50	...	25	85
CG184	15	929	2.799	...	1.315	3.986	...	...	...	0.48	...	83	333
CG189	15	9234	1.040	...	2.686	8.140	...	...	...	0	...	32	272
CG195	15	9503	0.920	...	1.455	4.410	0.114	...	...	0	...	45	177
Mrk1026	18	4011	1.120	...	0.237	0.424	1.065	0.511	0.437	0.19	-14.10	4.9	...
Mrk589	18	3442	2.001	...	0.232	0.574	0.975	0.291	0.280	0.73	-13.92	18	...
Mrk1063	18	1502	2.082	...	0.851	2.507	0.283	0.289	0.215	0.15	-13.17	20	...

Table 2.1: Complete list of galaxies included (cont.)

Object.	Reference.	cz	λ3727	λ4363	λ4959	λ5007	λ6584	λ6716	λ6731	c(Hβ)	log F(Hβ).	W_β	$W_{\lambda 5007}$
Mrk702	18	15898	2.221	...	0.922	2.772	0.384	0.333	0.252	0.2	-13.58	37	...
Mrk710	18	1481	1.261	...	0.114	0.322	1.074	0.319	0.279	0.45	-13.92	36	...
Mrk1259	18	2153	2.103	...	0.522	1.515	0.875	0.198	0.205	0.58	-12.39	36	...
Mrk182	18	6245	2.659	...	0.356	1.038	0.545	0.258	0.152	0.3	-13.85	54	...
Mrk1305	18	3097	4.022	...	0.925	2.382	0.520	0.417	0.341	0.23	-13.72	9	...
HS1232+3947	19	6296	2.560	...	1.400	4.270	0.050	0.210	0.000	0.29	-14.05	29	139
HS1236+3821	19	2188	8.490	...	1.270	3.800	0.190	0.730	0.000	0.6	-14.11	4	23
HS1256+3505	19	10253	4.670	...	0.870	2.510	0.630	0.730	0.000	0.45	-13.80	20	55
HS1301+3209	19	7135	9.120	...	0.990	2.870	0.100	0.520	0.000	0.58	-14.52	10	36
HS1308+3044	19	6266	5.770	...	0.700	1.980	0.590	0.680	0.000	0.56	-14.30	4	13
HS1311+3628	19	929	2.160	...	1.760	4.920	0.130	0.280	0.000	0.16	...	301	1350
HS1328+3424	19	6805	4.340	...	0.840	1.830	0.340	0.250	0.000	0.5	-14.67	8	18
HS1329+3703	19	16698	3.660	...	0.350	1.020	0.850	1.110	0.000	0.21	...	7	9
HS1334+3957	19	2488	2.880	...	1.780	5.190	0.050	0.240	0.000	0	...	71	351
HS1336+3114	19	4737	2.780	...	0.790	1.720	0.510	1.630	0.000	0	...	5	11
HS1340+3307	19	4737	5.030	...	1.740	4.850	0.070	0.490	0.000	0.54	-14.01	20	108
HS1349+3942	19	1619	5.560	...	1.060	2.860	0.260	0.820	0.000	0.34	-13.98	13	45
HS1354+3634	19	5007	4.670	...	0.910	2.550	0.440	0.710	0.000	0.51	-13.95	19	50
HS1354+3635	19	5126	4.680	...	1.180	3.390	0.280	0.610	0.000	0.51	-13.69	21	76
HS1402+3650	19	10403	4.830	...	0.960	2.940	0.200	0.630	0.000	0.56	-13.87	26	85
HS1410+3627	19	10133	6.010	...	1.090	3.050	0.140	0.810	0.000	0.31	-14.29	15	55
HS1413+4402	19	20926	2.140	...	0.260	0.450	1.500	0.620	0.000	0.61	...	10	5
HS1416+3554	19	3088	5.930	...	0.990	2.840	0.180	0.770	0.000	0.33	-14.11	14	49
HS1420+3437	19	7375	4.840	...	0.790	1.960	0.220	0.340	0.000	0.45	-14.12	27	56
HS1422+3325	19	10223	4.790	...	0.900	2.450	0.590	0.860	0.000	0.34	-14.33	20	50
HS1422+3339	19	3418	4.660	...	1.050	2.890	0.210	0.650	0.000	0.35	-13.95	17	58
HS1425+3835	19	6685	5.860	...	0.590	2.000	0.400	0.510	0.000	0.1	...	12	24
HS1429+4511	19	9623	2.050	...	0.110	0.510	0.820	1.120	0.000	0.31	...	15	2
HS1429+3154	19	3508	3.920	...	1.420	4.190	0.190	0.490	0.000	0.14	-13.69	34	144
HS1438+3147	19	13281	3.350	...	1.740	5.070	0.070	0.420	0.000	0.31	-14.18	35	188
HS1440+3805	19	9653	3.970	...	0.780	1.590	0.500	1.180	0.000	0.26	...	7	14
HS1444+3114	19	8904	4.920	...	0.750	2.200	0.430	0.710	0.000	0.41	-13.56	26	60
HS1529+4512	19	6925	4.650	...	1.730	5.020	0.160	0.340	0.000	0.22	-14.53	16	99
HS1544+4736	19	5846	1.040	...	1.470	4.560	0.140	0.520	0.000	0.02	-14.00	32	154
HS1546+4755	19	11302	3.970	...	1.660	4.940	0.060	0.370	0.000	0.48	-14.11	35	181
HS1633+4703	19	2578	5.960	...	1.160	3.090	0.190	0.670	0.000	0.36	-13.87	15	55

2.3 Statistical Properties of the General Sample.

In the study of the ionized medium of star forming regions, the detection of the weak auroral line [OIII]λ4363 Å constitutes an important source of information. It allows the derivation of accurate electron temperatures and hence oxygen abundances. Therefore, it is not surprising that most works on the ionized nebulae of HII galaxies focus on objects with data on this valuable line. In many sources however, this line is not present. Its proximity to the absorption Balmer Hγ line, which often shows prominent wings, and in nearby objects the sky Hg λ 4359 Å line complicates its measurement. In addition, the line is intrinsically weak in objects with relatively low excitation. Furthermore, in the distant universe very few sources are expected to show the line since the cosmological dimming factor $(1+z)^4$, which at a redshift of only 0.4 is about 4, makes its detection very difficult. The study of the properties of sources not showing the [OIII]λ4363 Å line is therefore of great importance in order to provide an adequate comparison sample to study the distant population of blue compact objects.

For our study we have split the total HII galaxy sample into two subsamples. Subsample Sub1 comprises 236 objects with measurements of the [OIII]λ4363 Å line intensity. Subsample Sub2 comprises objects for which the [OIII]λ4363 Å line is not reported or is too weak to be measured. This latter subsample consists of 214 objects.

2.3.1 Subsample Characterization.

In order to get a picture of the observable properties of both subsamples, the distributions of the following quantities were drawn.

(a) Observed Hβ flux, F(Hβ).

(b) Radial velocity, cz.

(c) Extinction, c(Hβ).

(d) Hβ luminosity, L(Hβ).

(e) Hβ equivalent width, W$_\beta$.

The corresponding histograms are presented in figures 2.1 through 2.5. The Hβ flux and W$_\beta$ distributions were drawn using directly the reported data from the literature. The radial velocities were derived from the reported z values. However, in the cases in which

Quantity.	Error	Bin Width	Sub1. Mean	Sub1. Median	Sub1. Standard deviation	Sub2. Mean	Sub2. Median	Sub2. Standard deviation
$\log L(H\beta)$	0.30	0.50	40.1	40.1	1.1	40.6	40.6	1.0
c(Hβ)	0.30	0.30	0.28	0.20	0.29	0.58	0.50	0.43
$\log(cz)$	0.02	0.25	3.50	3.56	0.51	3.78	3.84	0.39
W_β	16	32	131	110	86	46	31	51.6
$\log F(H\beta)$	0.15	0.15	-13.6	-13.6	0.45	-14.0	-14.0	0.43

Table 2.2: Main statistical properties of the galaxies studied.

this number was not given in the literature, the distance value from the NED database was converted to radial velocities using the cosmology given above. The Hβ luminosities were derived from the luminosity-distances and from the extinction-corrected Hβ fluxes. We have neglected the solar system velocity with respect to the CMB, which is 370 km s^{-1}. This effect can only affect the luminosity calculations of the nearest objects. However, for the vast majority of sources, this does not introduce a big error since their radial velocities are much greater. Furthermore, this additional error is engulfed by the $\log L(H\beta)$ histogram bin width. In all cases, the reddening was re-estimated from the available Balmer decrements. For the objects from reference 6 affected by second order contamination, only the objects for which the Hγ/Hβ decrement was available were selected. In some cases however, the nature of the data did not allow an accurate determination. Therefore, in order to minimize any spurious effects, objects with estimated values of the logarithmic extinction at Hβ, c(Hβ), larger than 1.5 were excluded from our analysis. Also, it is found that the extinction is low for most objects. For this reason, even if the determination of $c(H\beta)$ is affected by several issues such as underlying absorptions or the reddening curve adopted, these factors will not have a great impact on derived quantities such as line luminosities or the [OIII]$\lambda\lambda 4959 + 5007$/[OII]$\lambda 3727$ ratio. Simple statistics on the presented distributions are given in table 2.2. Table 2.2 also gathers the estimated error in each variable, and the bin width of the corresponding histogram. It is seen that the bin width is, in all cases, equal to or larger than the given error. We think that the conclusions drawn from these histograms are robust.

Several points can be made from the histograms. Figure 2.1 shows that the observed Hβ flux from galaxies without measurements of the [OIII]λ 4363 Å is lower than the observed flux for galaxies with data on this line. There is an evident excess of Sub2 members at low observed fluxes. On average, the flux from Sub1 objects is 2.4 times greater than that of Sub2 members. In a number of cases, the undetection of the [OIII]λ4363 line will not be due to its weakness *relative* to other lines, but due to the general faintness of the observed

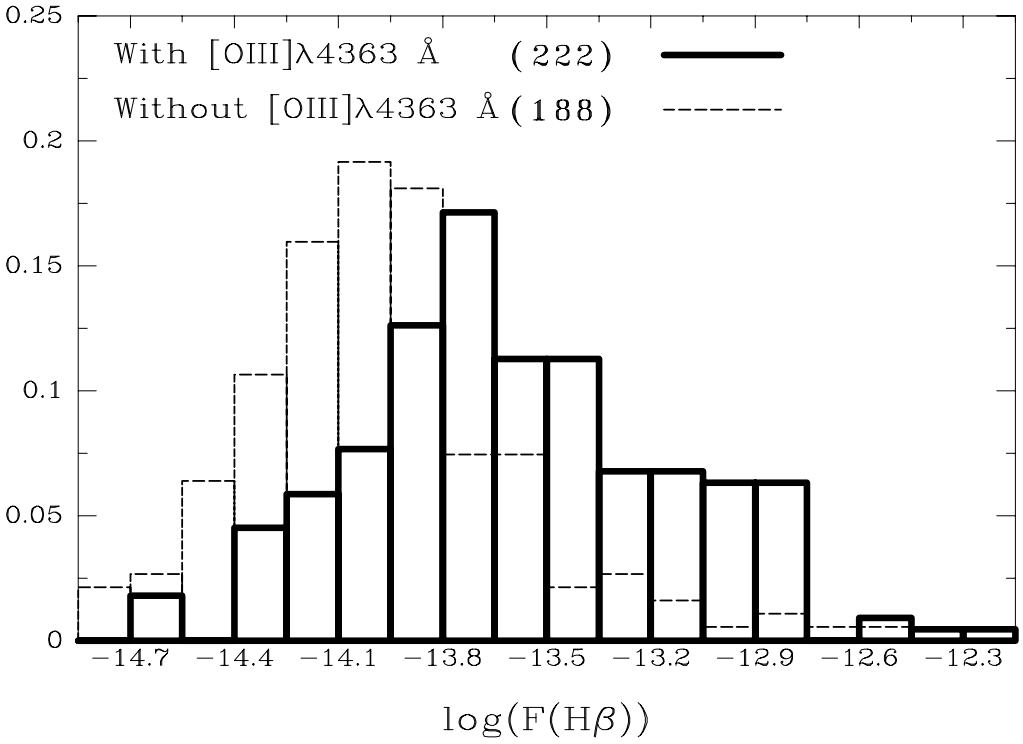

Figure 2.1: *Observed* Hβ flux distributions.

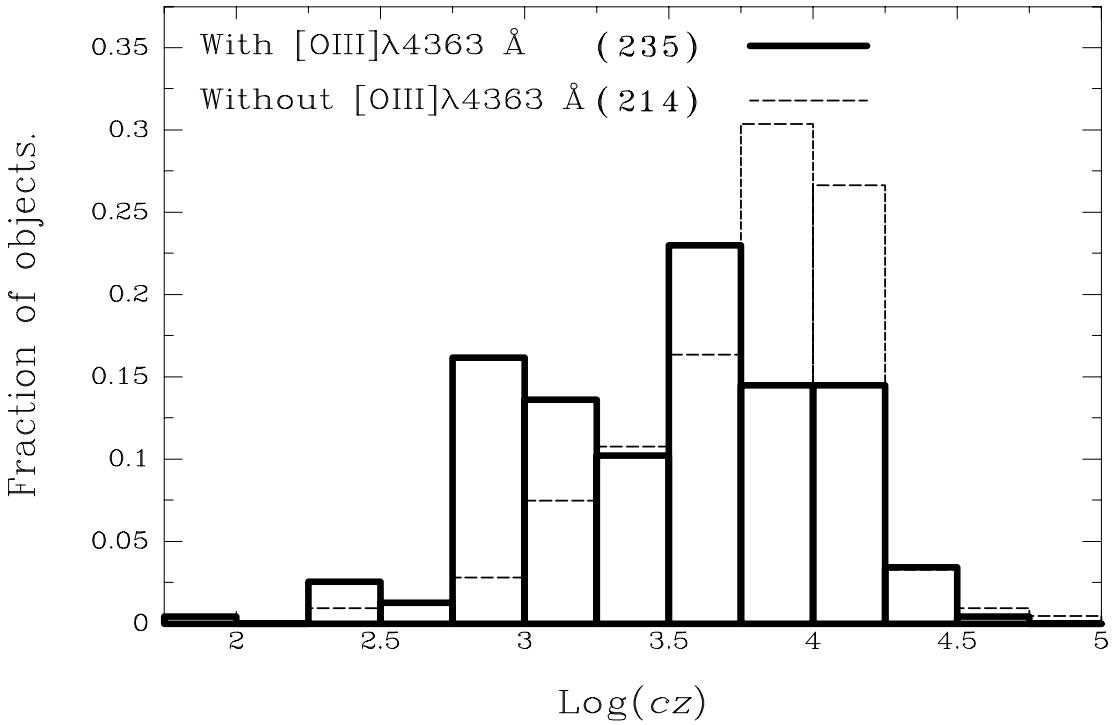

Figure 2.2: Radial velocity distributions.

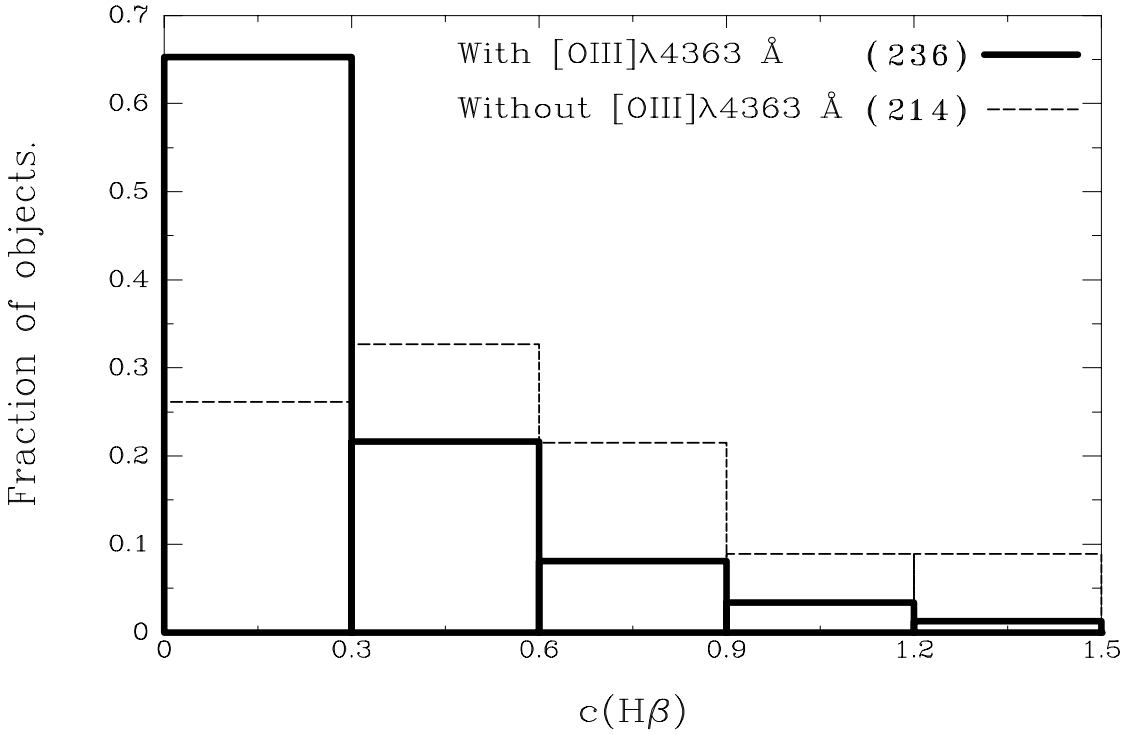

Figure 2.3: c(Hβ) distributions.

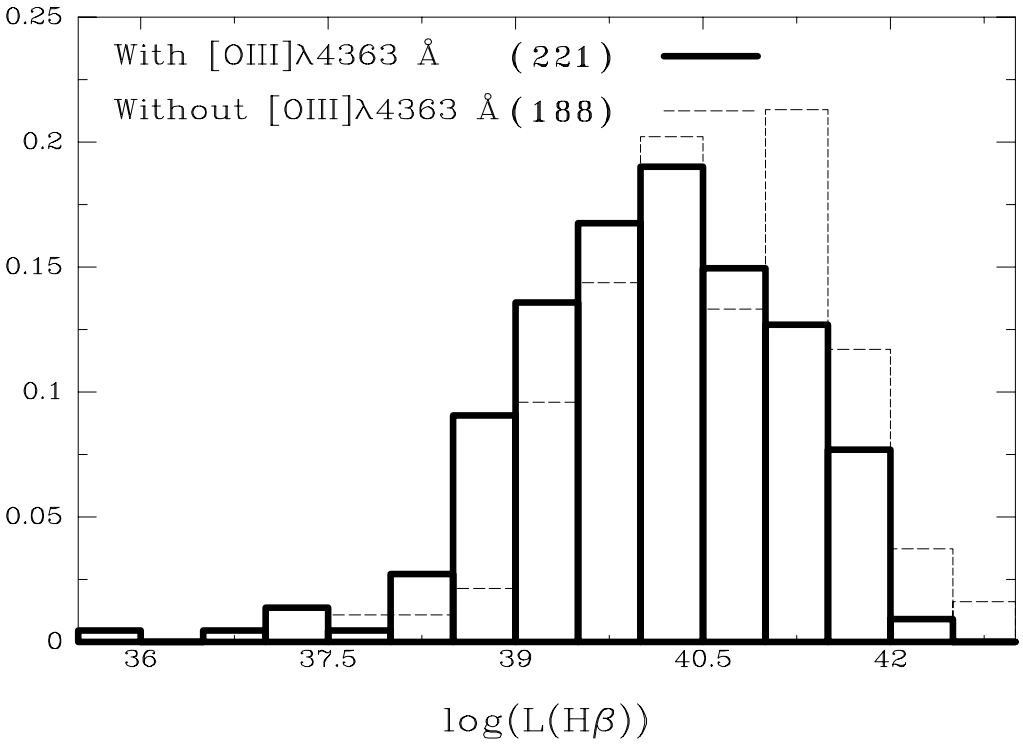

Figure 2.4: Hβ luminosity distributions.

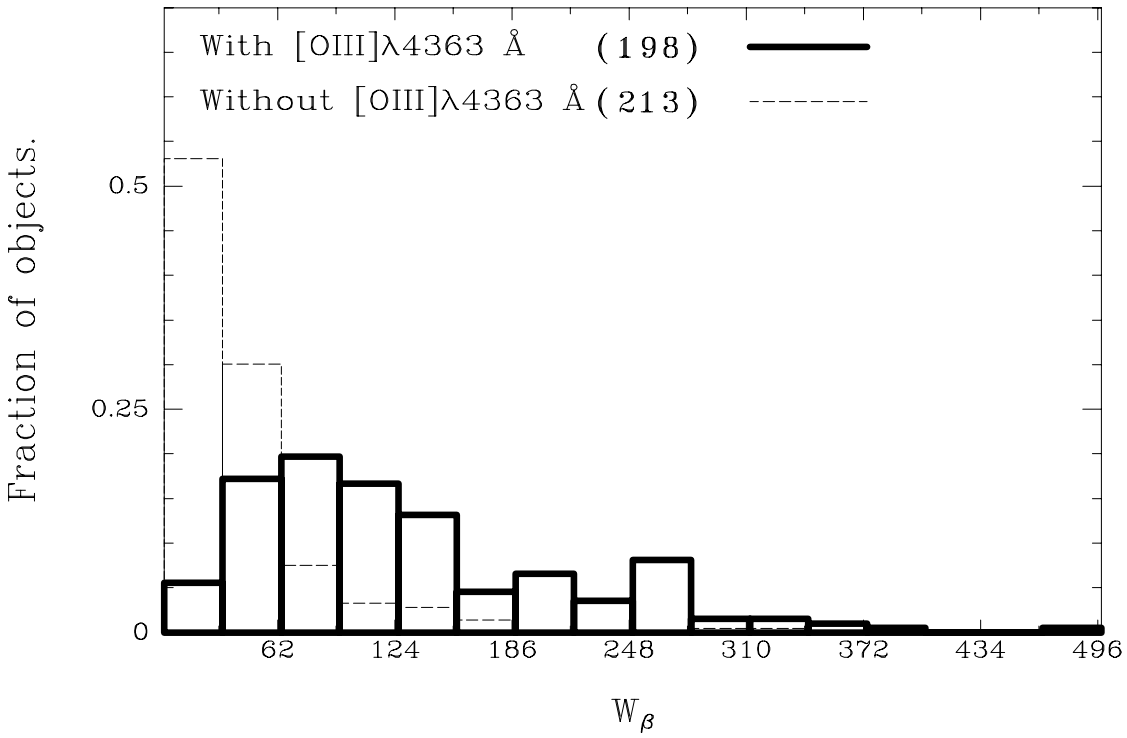

Figure 2.5: W$_\beta$ distributions.

emission line spectrum. Figures 2.2 and 2.3 show the redshift and extinction distributions for both subsamples. It is seen that the objects of subsample Sub1 are located at lower distances than Sub2 members. This will make the [OIII]λ 4363 line easier to detect. Also, sources with the [OIII]λ4363 line seem to be less affected by extinction. The majority of objects presenting the auroral line have logarithmic extinctions lower than 0.5, while that is the average value of the extinction coefficient for subsample 2 sources. In some cases, the auroral line will be absorbed by dust and rendered unobservable. Figure 2.3 also shows that most HII galaxies present low extinctions ($c(H\beta) \leq 0.6$), implying that extinction will not be an important ingredient in the error budget. Finally, figure 2.4 shows that, in spite of all these differences the Hβ luminosity distributions are very similar for both subsamples, Sub2 objects being marginally more luminous. Regarding ionization properties, figure 2.5 shows that Sub1 objects have higher Hβ equivalent widths. The Hβ equivalent width distributions present a different shape too. This points to an evolutionary effect, in the sense that the ionizing clusters of the objects not showing the [OIII]λ4363 line might be more evolved.

2.3.2 The Mass of the Ionizing Cluster.

The mass of the ionizing cluster, M_*, can be calculated from the Hβ luminosities and equivalent widths using the following considerations.

As the star cluster ages, the number of hydrogen ionizing photons per unit mass of the ionizing cluster decreases. Assuming that the age of the ionizing cluster is related to W_β, a relation should exist between the number of hydrogen ionizing photons per unit mass of the star cluster and W_β. Such relation is given for single-burst models in Díaz (1999). The expression used is

$$\log(Q(H)/M_*) = 44.8 + 0.86 \times \log W_{\beta,0} \tag{2.1}$$

In this relation, $W_{\beta,0}$ is the equivalent width, in angstroms, that would be observed in the absence of an underlying population, Q(H) is the number of hydrogen ionizing photons per second and M_* is expressed in solar masses.

No direct information about the presence or absence of an underlying stellar population exists. However, a well defined relation exists between W_β and the degree of ionization of the nebula, albeit showing a scatter larger than observational errors. In figure 2.6, W_β is plotted as a function of the [OIII]$\lambda\lambda$4959 + 5007/[OII]λ3727 ratio[1]. If the degree of ionization is ascribed to the age of the ionizing star cluster, it is reasonable to assume that the vertical scatter shown by the data is due to different contributions of continuum light from underlying populations. A least squares fit is presented as a solid line. The dashed line represents an upper envelope to the data which is located 1.5 times the *rms* above the fit and corresponds to the relation:

$$\log W_{\beta,0} = 2.000 + 0.703 \log \frac{[\mathrm{OIII}]}{[\mathrm{OII}]} \tag{2.2}$$

The objects located on this upper envelope are likely to be the ones in which the underlying population is minimum. We have used this upper envelope to calculate the mass of the ionizing cluster. There is, however, a metallicity effect in figure 2.6. In the absence of any underlying stellar population, HII galaxies with higher metallicity clouds will present a lower [OIII]$\lambda\lambda$4959 + 5007/[OII]λ3727 ratio due to lower effective temperatures of their ionizing stars (Pérez-Montero & Díaz (2005) and Kewley & Dopita (2002)). However, there will be no

[1] This number will be called "ionization ratio" throughout this chapter.

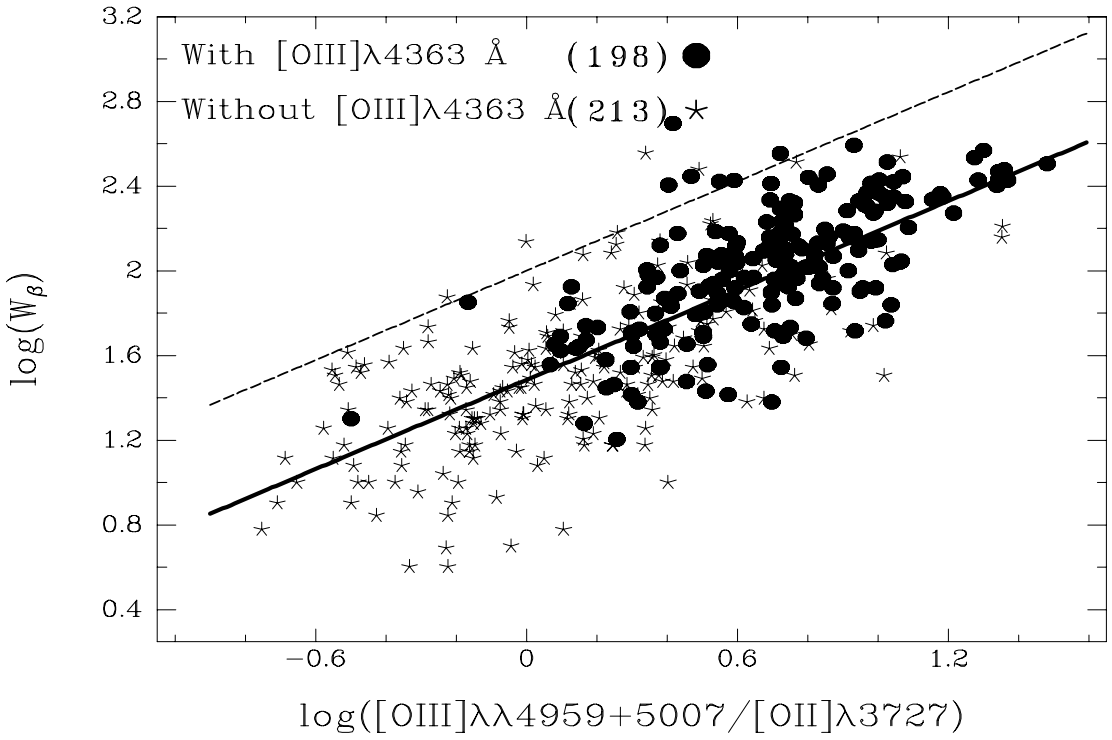

Figure 2.6: W_β *vs.* ionization relation.

change in the equivalent width of Hβ, to zero-th order. Therefore, $W_{\beta,0}$ should be a function of both the ionization ratio and metallicity. However, only the [OIII]$\lambda\lambda$4959 + 5007/[OII]λ3727 will be used here. At any rate, the derived cluster mass constitutes only a lower limit since some photons might be actually escaping from the nebula, or there might be dust globules within the ionized medium. If a significant fraction of the ionizing photons escape from the nebula unprocessed, the ionizing star cluster will appear to be less massive than it really is. On the other hand, if the dust optical depth is large within the nebula, the absorbed energy will be re-emitted at other wavelengths, and the star cluster mass will be underestimated again. Observations at other wavelengths would be required to quantify these issues. Figure 2.7 presents the histograms of the ionizing cluster masses for both subsamples. The estimated error in $\log M_*$ is 0.40, and the bin width is 0.5.

2.3.3 The [OIII]$\lambda\lambda$4959 + 5007/[OII]λ3727 Distributions.

Figure 2.8 shows the [OIII]$\lambda\lambda$4959 + 5007/[OII]λ3727 distributions. The estimated error in the ionization ratio is 0.2dex, and the bin is 0.2dex wide. It is seen that galaxies without the [OIII]λ4363 line show lower ionization ratios. This separation in [OIII]$\lambda\lambda$4959 +

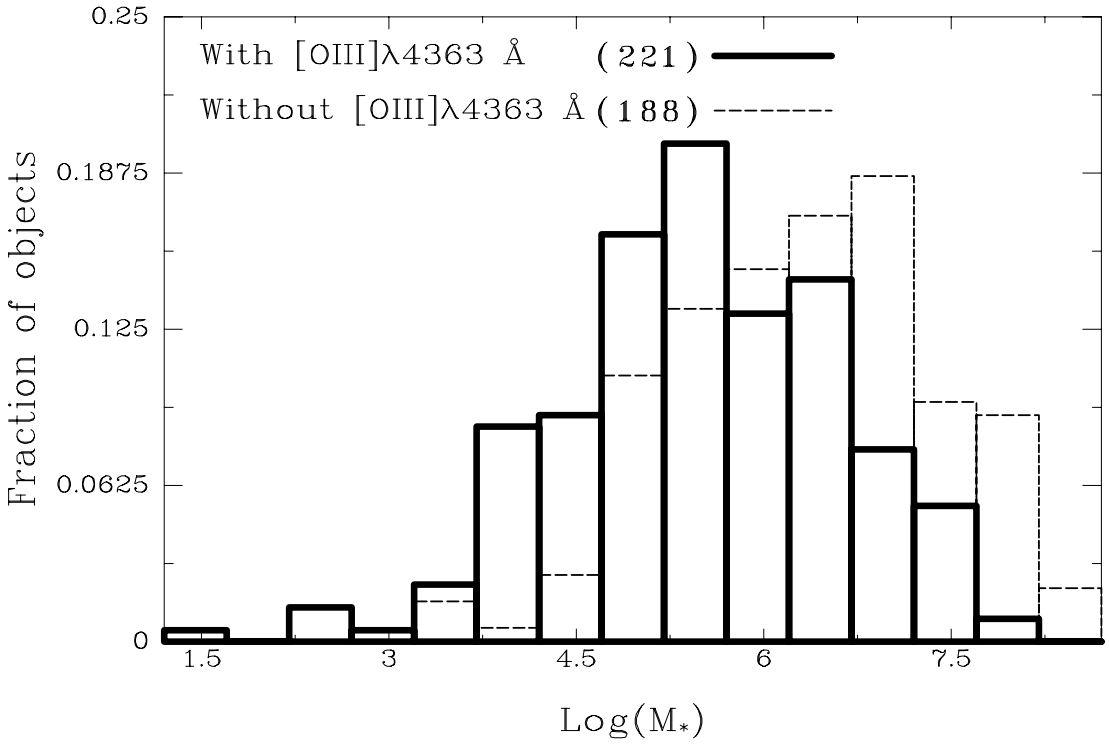

Figure 2.7: Cluster mass distributions.

5007/[OII]λ3727 can't be explained by uncertainties in the reddening determination, since the typical differences in c($H\beta$) observed between both subsamples would only change the ionization ratio by 0.1dex, much less than the observed separation of 0.6dex. Let's come back to figure 2.6 in order to gain insight on what effects could be responsible for the segregation observed in figure 2.8. We begin commenting on two possible evolutionary scenarios:

1. Long-term evolution. In the framework of succesive bursts scenario, as the continuum level and the amount of heavy ions rise, the O^{++} auroral line becomes fainter and might be swallowed under the continuum noise or stellar features. Objects without the auroral line would therefore show lower equivalent widths. This scenario does not require less luminous *starbursts*.

2. Short-term evolution of the *starburst*. The W_β of older clusters is lower than that of younger ones simply because they are less able to produce ionizing photons. This would make the [OIII] line naturally weak and unobservable even in the presence of a not-too-strong underlying population. This is likely to play a major role. Additionally, high-metallicity objects and/or very evolved ones might have a lower effective temperature which would produce a lower [OIII]$\lambda\lambda$4959 + 5007/[OII]λ3727 at comparable ionization

parameter. In figure 2.6, it can be seen that the observed galaxies, with and without [OIII]λ 4363 are separated. The two subsamples lie along the relationship, but on opposite ends of it. This suggests that Sub1 objects are tipically younger than Sub2 subsample objects, according to this picture.

The real picture, of course, will be a combination of the two effects.

Other, non-evolutionary possible reasons as to why the ionization ratio [OIII]$\lambda\lambda$4959 + 5007/[OII]λ3727 may be lowered are:

- The ionization parameter depends on the mass of the ionizing cluster, since more massive clusters will harbour a greater number of massive stars. However, it can be seen in figure 2.7 that the distribution of cluster masses for both subsamples greatly overlap. Furthermore, figure 2.9 shows that objects without [OIII]λ4363 have lower ionization ratios than objects with the auroral line even for the most massive clusters. This indicates that cluster mass is not responsible for this segregation in [OIII]$\lambda\lambda$4959 + 5007/[OII]λ3727.[2]

- If the electron density is higher than the [OII]λ3727 transition critical density, the ionization ratio is reduced. In particular, its value at $N_e = 10^4 \mathrm{cm}^{-3}$ is 3.75 times smaller than its value at $N_e = 200 \mathrm{cm}^{-3}$. Since HII galaxies have an electron density which is well below the critical density, this option is not likely to be responsible for the observed differences in [OIII]$\lambda\lambda$4959 + 5007/[OII]λ3727. However, it is a possibility for some objects.

- Geometry, dust content and photon escape. If an important fraction of the ionizing photons escape the nebula, the ionization parameter is low because of geometrical reasons. If a significant fraction of high-energy photons are absorbed by dust within the nebula, the O^{++} auroral line would be weaker. These phenomena might be partially responsible for the segregation observed in the [OIII]$\lambda\lambda$4959 + 5007/[OII]λ3727 histogram.

2.4 Metallicity Analysis.

The detection or undetection of the [OIII]λ4363 line is affected by several purely observational factors such as distance to the observed galaxy, galactic extinction, quality of the spectrum,

[2] And it also indicates that undersampling of the Initial Mass Function, which lowers the ionization ratio (the so called *richness effect*) may not account for all the separation.

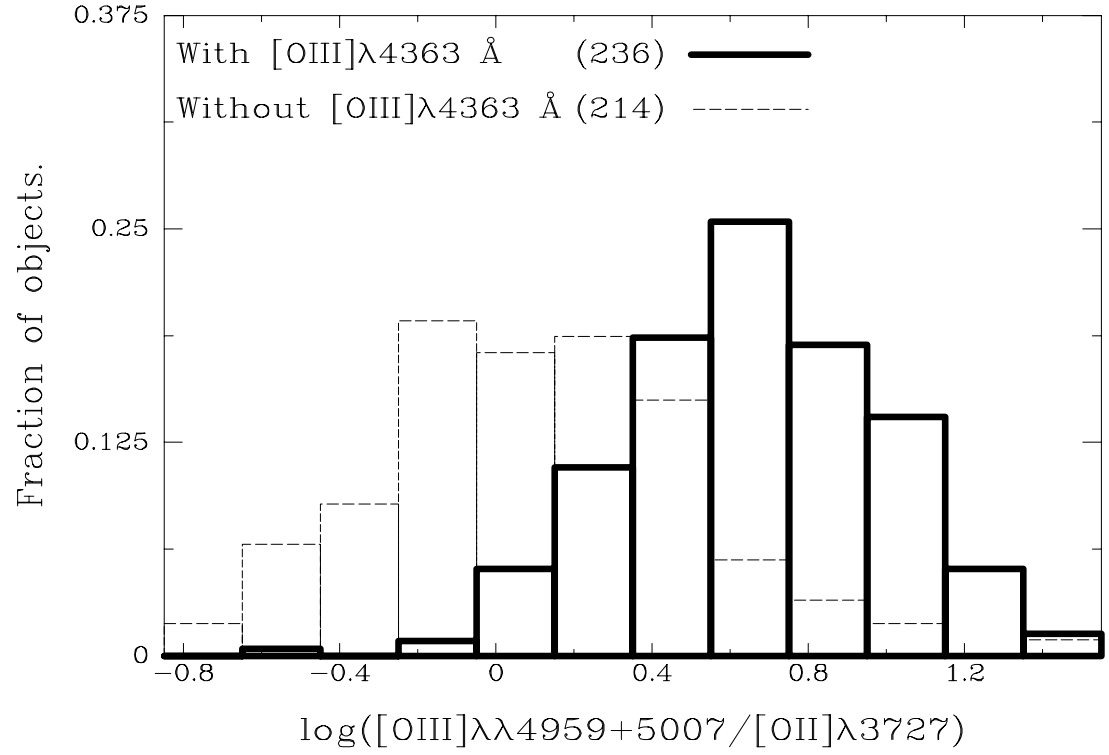

Figure 2.8: [OIII]$\lambda\lambda$4959 + 5007/[OII]λ3727 distributions.

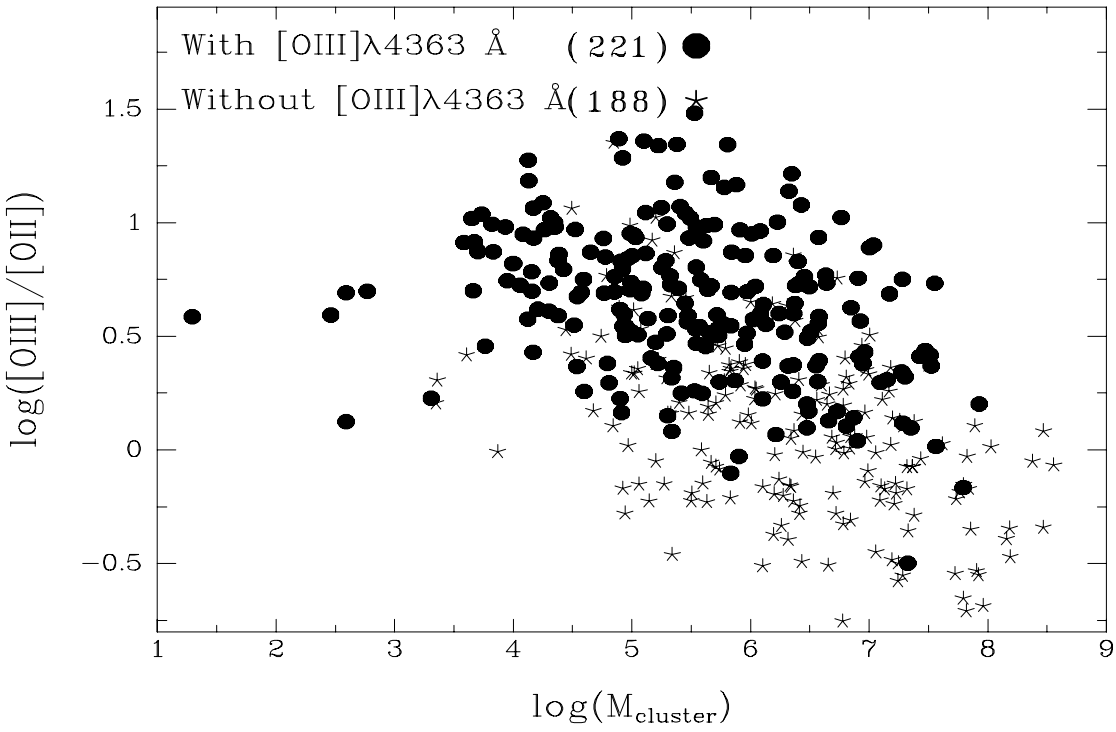

Figure 2.9: Ionization ratio *vs.* Cluster mass relation.

etc. that should not correlate with the oxygen abundance. However, high oxygen abundances, implying low electron temperatures in the gas, could render the line too weak to be detected since the intensity of this auroral line depends on electron temperature. There are then two extreme cases.

1. The objects in subsample Sub2 are, on average, more metal-rich than the Sub1 objects. The [OIII] auroral line would then be naturally weak, and the absence of this line in a particular spectrum would bias the oxygen abundance of the ionized gas of a given galaxy towards higher metallicities. There should be a separation in excitation between subsamples Sub1 and Sub2 in this case. It is seen in figure 2.8 that this is indeed the case.However, it has to be borne in mind that a simple age effect would produce the same effect on the excitation and equivalent width distributions.

2. The objects which do not show the [OIII]λ4363 line have higher extinctions, their continuum is stronger or are affected by other observational problems. This may cause the auroral line to be swallowed in the continuum noise. The non-detection of the auroral line would then be an observational issue only, and the presence or absence of this line in the spectrum of a galaxy should not bias its metallicity in any way.

Since our present knowledge of the metallicity distribution of HII galaxies comes from the analysis of samples for which the [OIII]λ4363 line is observed, it is important to check if the metallicity distributions of subsamples Sub1 and Sub2 really differ.

2.4.1 Metallicity analysis for Sub1 objects.

For subsample Sub1, the oxygen abundance was derived through the determination of the electron temperature using the [OIII]λ4363/[OIII]λ5007 line ratio. The procedure can be reviewed in Pagel et al. (1992). The density was estimated via the [SII]λ6717/[SII]λ6731 ratio, or assumed to be equal to 150 cm $^{-3}$ in the cases in which no [SII] line data exist, and the temperature in the [OII] zone was calculated using the models given in Pérez-Montero & Díaz (2003).

The oxygen abundance distribution derived for subsample Sub1 is presented in the histogram in figure 2.10. It is very similar to the oxygen content histogram presented in Terlevich et al. (1991) both in average value and scatter.

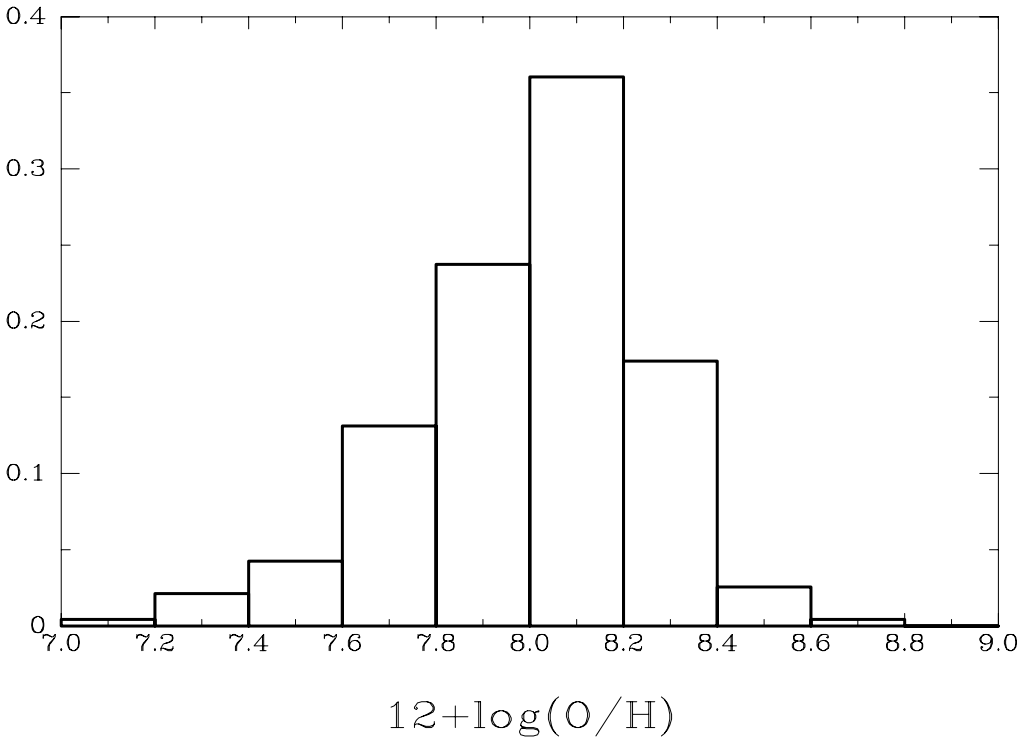

Figure 2.10: Metallicity distribution. Objects *with* [OIII]λ4363. 236 objects included.

2.4.2 Metallicity Analysis for Subsample Sub2 Objects.

For subsample Sub2, the procedure to estimate the metallicity is more complicated.

Objects with Nitrogen Measurements.

It was possible to derive oxygen abundances for 81 out of the 214 sources using the N2 calibration introduced in Denicoló et al (2002).

$$12 + \log(O/H) = 9.12 \pm 0.05 + 0.73 \pm 0.10 \times \log N2 \tag{2.3}$$

where $N2$ is the [NIIλ6584]/$H\alpha$ ratio.

It was shown in Pérez-Montero & Díaz (2005) that, in the case of HII galaxies, this calibration produces good results. The average metallicity of this set of 81 sources is 8.50 dex, and the *rms* is 0.27 dex. The minimum oxygen abundance is 7.8 dex. This group of galaxies is somewhat biased towards higher oxygen abundances with respect to Sub1 sources.

S/N Approach and the use of the Pilyugin (2000) Calibration.

We have also used another independent approach to derive the oxygen content of Sub2 sources. First, we have used the *signal-to-noise* ratio of each spectrum, when available, to find an upper limit to the [OIII]λ4363 line strength. This allows us to impose an upper limit on the electron temperature and hence a lower limit to the oxygen abundance. Only the references 6, 15, 18 and 19 provide the necessary information to carry out this first task. This set of objects consists of 210 objects. Once such lower limits were calculated, those objects for which the lower limit to $12 + \log \mathrm{O/H}$ was greater than 8.15 dex (104 objects) were selected and their oxygen abundance was derived using the calibration for the *upper* branch of the $R_{23} - 12 + \log(\mathrm{O/H})$ by Pilyugin (2000).[3]

The value of $12 + \log \mathrm{O/H}$ derived in this way turns out to be larger than 8.15 only in 59 cases. There are however 33 objects whose metallicities fall in the range from 7.95 to 8.15, within the statistical error of the calibration used. These metallicities are then still compatible with our assumption of $12 + \log(O/H) \geq 8.15$. The remaining 12 objects for which the derived metal content is lower than 7.95 were excluded from the analysis. There are therefore 92 sources for which the calibration from Pilyugin (2000) gives potentially reliable results. This set of 92 sources has 17 objects in common with the 81 sources previously mentioned with metallicities derived from the [NII]λ6584 line. For these 17 objects both determinations of the oxygen abundance agree in the mean (the mean value of the difference is 0.01dex), although the scatter is rather large (rms=0.25).The residuals are found not to depend on the ionization ratio.

The metallicity distribution for this set of 92 objects is compared to that of Sub1 galaxies in figure 2.11. It can be seen that both distributions overlap and show high power at around the same metallicities. The biggest difference arises around $12 + \log(\mathrm{O/H}) = 8.00$, at which there is almost a factor of two difference in the fraction of objects, but otherwise the distributions are similar. It is also interesting to note that there are objects with [OIII]λ4363 at all oxygen abundances traced by objects without the line, even at fairly high oxygen abundances like 8.6 dex. For relatively metal-rich objects ($12 + \log(\mathrm{O/H}) \geq 7.95$), those without the auroral line are only around 0.1 dex more metal rich than objects showing the line, according

[3]For 14 objects the method used to derive the *signal-to-noise* ratio yielded *negative* upper limits to the electron temperature. In these cases, the non-detection of the auroral line might be ascribed to other issues not related to the *signal-to-noise* ratio like the absorption wings of H_γ or spectral resolution effects. These sources were excluded from the analysis.

to the calibration used.

In order to investigate to what extent this method is affected by the differences in ionization degree among our objects, we have examined the dependence of the derived oxygen abundances on the [OIII]$\lambda\lambda$4959, 5007/[OII]λ3727 ratio. This is shown in figure 2.12. It is seen that at low ionization ([OIIλ4959 + 5007]/[OII]λ3727 less than 1.0) the metallicity scatter for Sub2 objects is rather large. Some galaxies have a derived metallicity of around 9.2dex, and the lowest metallicities derived for Sub2 galaxies are also found in this regime. It is also interesting to note that, at high ionizations, it is possible to find Sub1 sources in a quite large range of oxygen abundances.

As a sanity check to test this method, it is applied to Sub1 sources. Figure 2.13 shows the metallicity residuals ($\log(O/H)_{\rm Pilyugin.} - \log(O/H)_{\rm direct.}$) plotted against $\log$[OIII]/[OII]. It can be seen that the S/N+Pilyugin (2000) method slightly underestimates the oxygen abundances at low ionization. At higher values of $\log$[OIII]/[OII] the residuals are closer to zero. We conclude that, for most sources, the use of the upper branch of the Pilyugin (2000) calibration provides reliable results, perhaps underestimating the metallicity for low ionization objects by around 0.2dex, even less for high-ionization objects.

We now turn to examine Pilyugin (2000) algorithm more closely. This method is based in a concept which may be named "metallicity equivalence class". For the upper branch, this means that objects with equal ionization and equal R_2 =[OII]λ3727/Hβ have equal oxygen abundances.

According to Pilyugin (2000) and Pilyugin (2001), the following quantities are defined: R_2 =[OII]λ3727/Hβ, $X_2 = \log R_2$; R_3 =[OIII]$\lambda\lambda$4959+5007/Hβ, $X_3 = \log R_3$; $R_{23} = R_2 + R_3$ $X_{23} = \log R_{23}$; $p_2 = X_2 - X_{23}$ and $p_3 = X_3 - X_{23}$.

Figures 2.14 and 2.15 present the X_2 *vs.* p_2 for both subsamples, and only for subsample Sub2 respectively. Objects belonging to the same "metallicity equivalence class" lie on the same straight line. The metallicity depends on the intersect at $p_2 = 0$ of these lines. It can be seen that very few Sub1 objects lie at values $p_2 \geq -0.3$, while many Sub2 objects occupy that area. This suggests that Pilyugin (2000) method may not be adequate for low-ionization sources, since the Pilyugin (2000) calibration was constructed using objects for which it was possible to derive oxygen abundances by direct methods.

In the low-ionization limit, the upper branch of the Pilyugin (2000) calibration becomes:

$$12 + \log {\rm O/H} = 9.54 - 1.68 \log R_2 - 0.55[{\rm OIII}]/[{\rm OII}] \qquad (2.4)$$

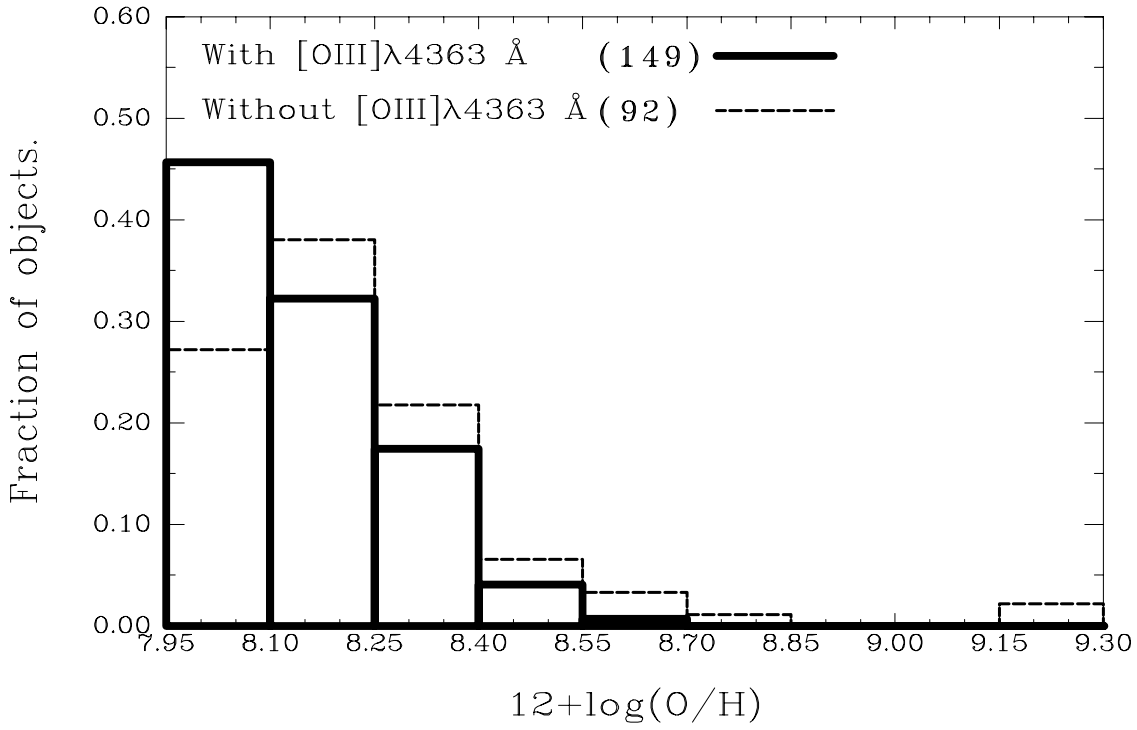

Figure 2.11: Metallicity distribution. The oxygen abundance was derived using Pilyugin (2000) calibration for the objects without [OIII]λ4363. The oxygen abundance was derived using the direct method for the subsample with [OIII]λ4363. The difference in the mean metallicities is 0.1dex.

In this expression, when the [OIII]/[OII] ratio is very low, the calibration becomes sensitive to R_2 only. The large scatter in X_2 observed in figure 2.15 for low ionization ($p_2 \geq -0.3$) Sub2 objects will therefore introduce a large scatter in oxygen content for these sources which is probably unphysical since it is not observed in low-ionization sources from the first subsample in figure 2.12.

It is then neccessary to re-calibrate the $12 + \log(\mathrm{O/H}) - R_{23}$ relation for objects of very low ionization degree. In order to do this, we have used a sample of low-ionization objects for which the oxygen abundance can be determined using direct methods. This sample has been selected from Pérez-Montero & Díaz (2005) and is given in table 2.3. The calibration is shown in figure 2.16.

A simple linear fit $12 + \log(\mathrm{O/H})$-$\log R_{23}$ gives:

$$12 + \log(\mathrm{O/H}) = (8.82 \pm 0.20) - (0.845 \pm 0.31) \times \log R_{23} \tag{2.5}$$

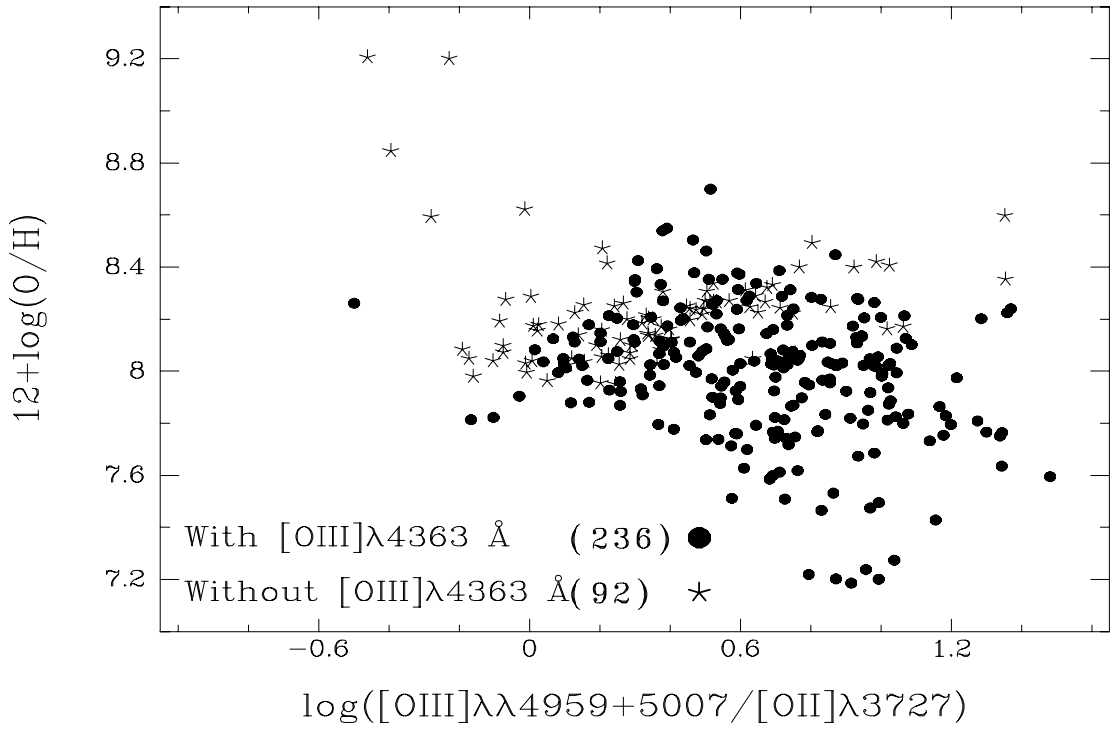

Figure 2.12: Metallicity against [OIII] $\lambda\lambda 4959 + 5007/[\mathrm{OII}]\lambda 3727$ ratio. For Sub1 objects, the direct oxygen abundance is presented. For Sub2 objects the S/N+Pilyugin (2000) method was used.

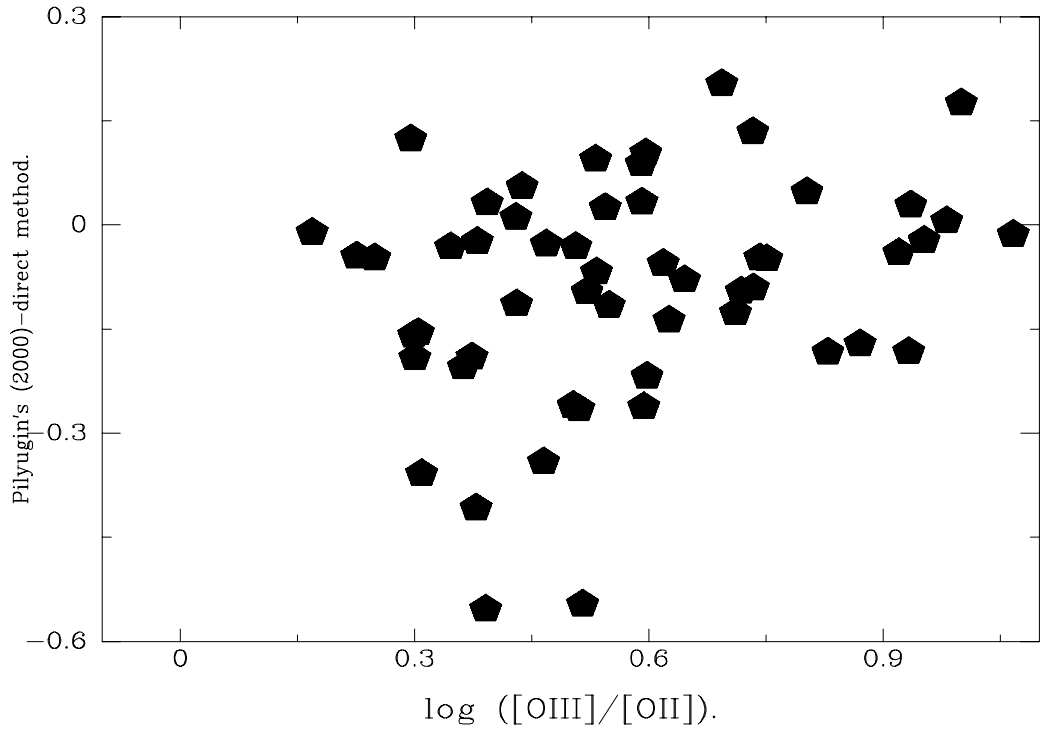

Figure 2.13: Metallicity residuals *vs.* log [OIII]/[OII]. Only sources from the Sub1 subsample are plotted. 58 galaxies presented. It is seen that Pilyugin (2000) calibration has underestimated the oxygen content of these sources, specially at low ionizations. At higher ionizations the residuals are closer to zero.

whose *rms* is 0.3 dex.

This new calibration allows to rederive the oxygen abundance for the Sub2 sources of very low ionization.

This change in the metallicity derivation for low-ionization objects represents an improvement as can be seen in figure 2.17 in which the oxygen content of low-ionization sources were calculated using the empirical calibration given above. The large metallicity scatter of low-ionization sources from subsample 2 has been greatly reduced. The behaviour observed in figure 2.17 is compatible with the evolutionary models and data presented in Stasińska, Schaerer, & Leitherer (2001). The galaxies presented in figure 2.17 overlap with the bulk of the data points presented in that work.

It was also mentioned above that figure 2.12 shows that, in the case of objects from the subsample with [OIII]λ4363, the high ionization objects are observed at all metallicities; on the other hand, at low ionizations only objects with average oxygen abundances are seen.

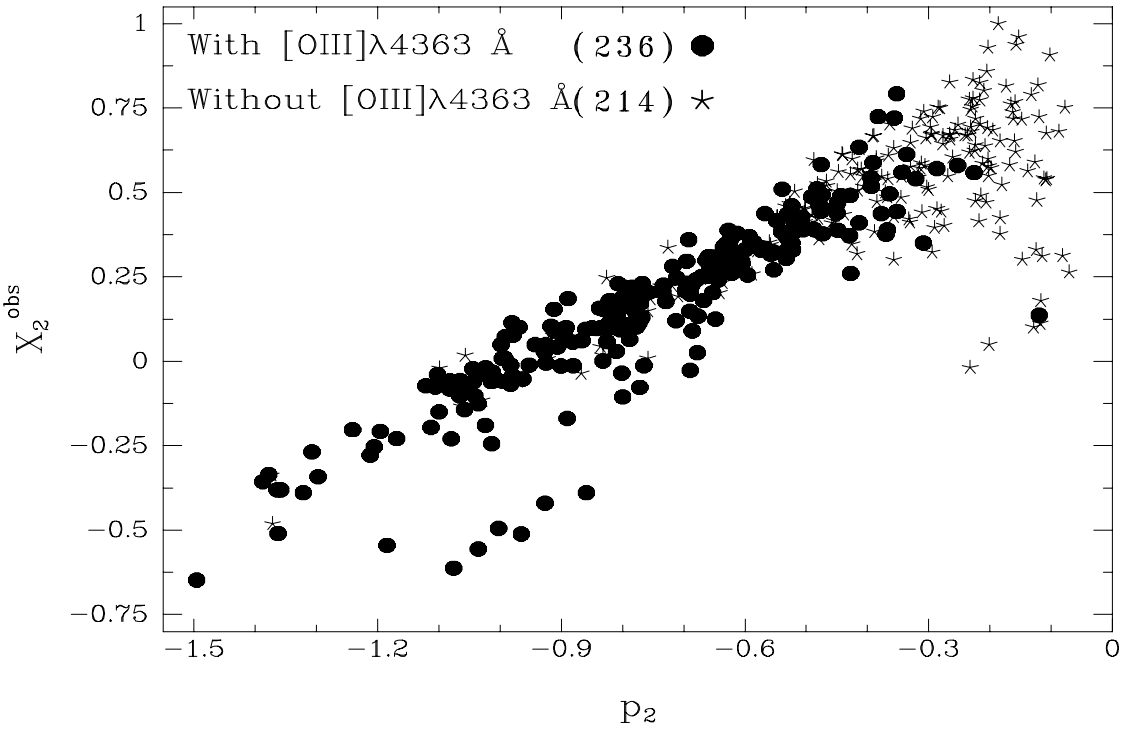

Figure 2.14: X_2 *vs.* p_2. All objects from both subsamples.

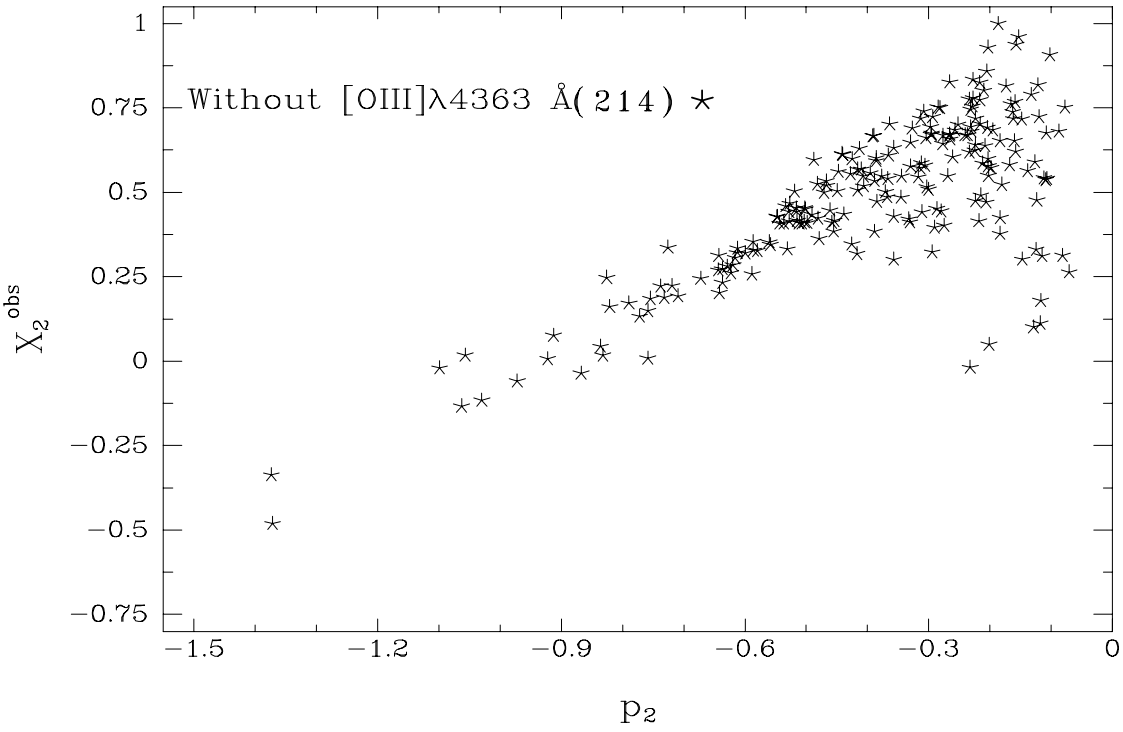

Figure 2.15: X_2 *vs.* p_2. Subsample Sub2 objects only.

Object.	Reference.	X_{23}	log([OIII]/[OII])	(O/H)	N_e (cm^{-3})
N604C	Díaz et al. (1987)	0.58	-0.28	8.33	122
N604E	Díaz et al. (1987)	0.66	-0.10	8.09	50
N3310B	Pastoriza et al. (1993)	0.74	-0.11	7.97	221
N3310E	Pastoriza et al. (1993)	0.77	-0.06	8.16	177
VS38	Garnett et al. (1997)	0.51	-0.16	8.15	129
VS35	Garnett et al. (1997)	0.63	-0.13	8.21	61
VS44	Garnett et al. (1997)	0.68	-0.15	8.02	181
VS41	Garnett et al. (1997)	0.58	-0.04	8.25	50
VS24	Garnett et al. (1997)	0.62	-0.14	8.55	79
VS21	Garnett et al. (1997)	0.63	-0.66	8.34	50
VS3	Garnett et al. (1997)	0.64	-0.02	8.48	67
N79E	Dennefeld & Stasinska (1983)	0.64	-0.19	8.08	50
H40	Rayo et al. (1982)	0.58	-0.39	8.62	115
NGC595	Vílchez et al. (1988)	0.61	-0.05	8.18	50
NGC7714	French (1980)	0.65	-0.015	8.00	752
NGC3690	French (1980)	0.63	-0.19	8.18	137
HS1610+4539	Popescu & Hopp (2000)	1.03	-0.03	7.93	50
Searle5	Kinkel & Rosa (1994)	0.33	-0.84	8.88	50
H13	Castellanos et al. (2002)	0.70	-0.16	8.24	80
H3	Castellanos et al. (2002)	0.88	-0.41	8.23	50
H4	Castellanos et al. (2002)	0.24	-0.23	8.31	50
H5	Castellanos et al. (2002)	0.46	-0.51	8.24	50
CDT1	Castellanos et al. (2002)	0.58	-0.50	8.95	130
CDT3	Castellanos et al. (2002)	0.58	-0.55	8.56	223
CDT4	Castellanos et al. (2002)	0.61	-0.34	8.37	118

Table 2.3: List of galaxies used to derive the low-ionization metallicity calibration.

In the case of the 92 objects from the second subsample, there is also a positive correlation between oxygen content and ionization degree. The existence of this positive correlation was ascertained using Spearman's test on the data presented in figure 2.17. To all practical purposes the test indicated the existence of a fairly strong ($\rho = 0.44$) positive correlation. This correlation is worrying since higher metallicity nebulae should show *lower* ionization degrees unless the ionizing radiation is unusually hard. However, it is seen in figure 2.13 that the upper branch of the Pilyugin (2000) calibration understimates the oxygen content for sources of lower ionization degree. This means that sources with lower ionization ratios ($\log[\mathrm{OIII}]\lambda\lambda 4959 + 5007/[\mathrm{OII}]\lambda 3727 \leq 0.6$) probably have higher metallicities than those derived from the Pilyugin (2000) calibration, suggesting that this unphysical correlation is an artifact introduced by the calibration itself. This also indicates that objects with both high oxygen abundance and high ionization degrees do exist, since Pilyugin (2000) calibration becomes better at high ionization ratios. These sources are likely to be powered by very hot radiation sources.

Summarizing, using the $N2$ calibration for the objects from subsample Sub2 with the

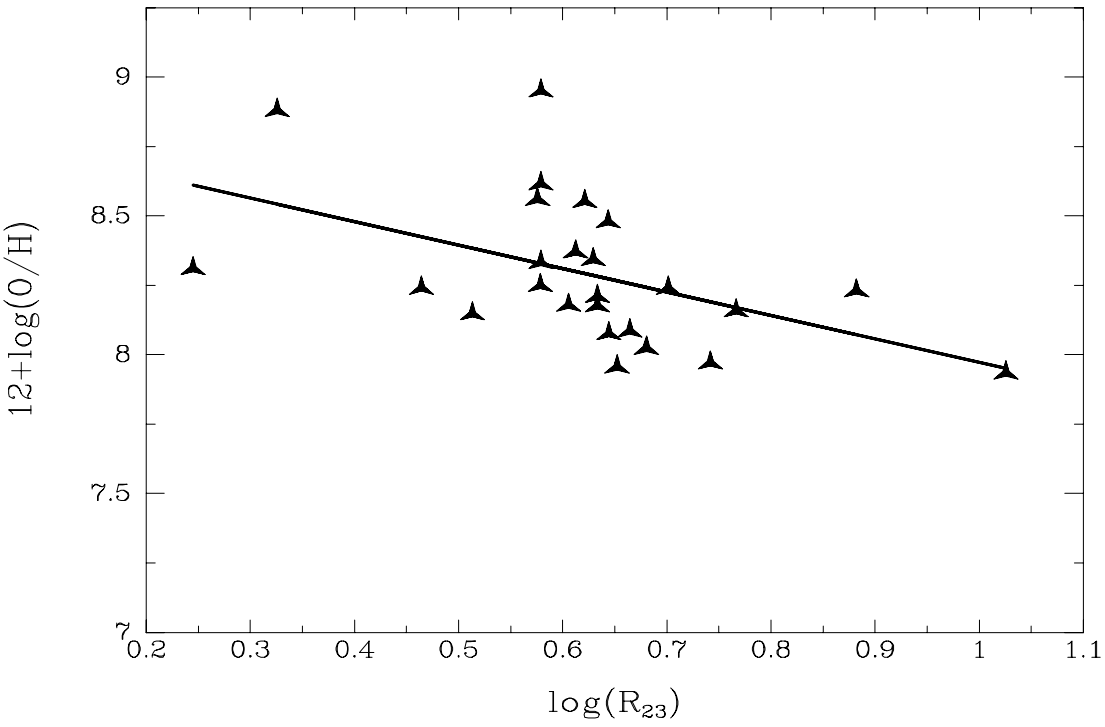

Figure 2.16: $12 + \log(\mathrm{O/H})$-$\log R_{23}$ calibration for low ionization objects. This empirical calibration is used for low ionization sources from the second subsample.

[NII]λ6584 line available (81 objects), the empirical calibration for low-ionization objects presented above (7 galaxies) and the Pilyugin (2000) calibration for the upper branch (68 objects) of the $12+\log(\mathrm{O/H})$-$\log R_{23}$ relation for high-ionization sources, the new metallicity distribution for the subsample without [OIII]λ4363 can be compared to the oxygen abundance distribution for the first subsample. This comparison is presented in figure 2.18.

Figure 2.18 shows that the oxygen abundance distributions for both subsamples do differ. Objects without the auroral line are, on average, *at least* 0.4 dex more metal rich than objects with it. Therefore, it is concluded that objects without the [OIII]λ4363 line are likely to be of higher metalicity than objects with it. In addition, very low ionization objects are only found among objects which do not show [OIII]λ4363. Finally, figure 2.19 shows the relation between metallicity and ionization ratio for all objects for which an oxygen abundance has been derived. As expected, the global correlation is negative, and both subsamples create a well-defined sequence. The objects for which the oxygen abundance was derived either from the calibration presented above or the upper branch of the Pilyugin (2000) calibration lie on the region shared by the first subsample and the objects with [NII]λ6584 measurements from

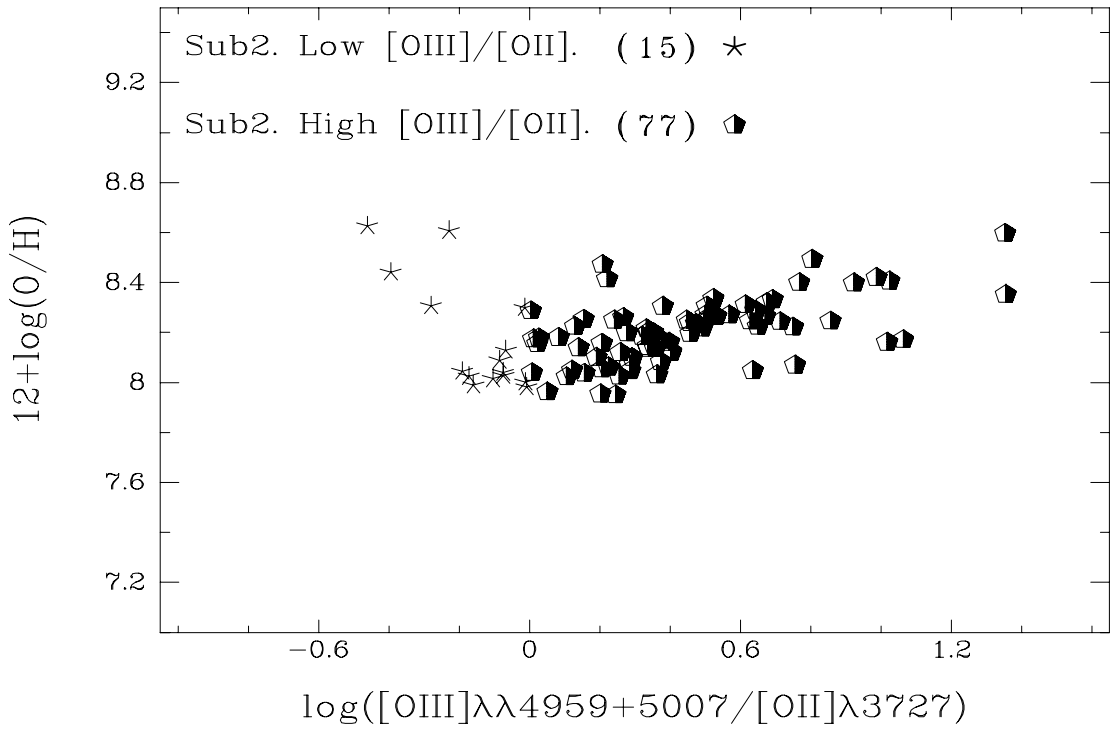

Figure 2.17: Metallicity *vs.* [OIII]$\lambda\lambda$4959 + 5007/[OII]λ3727 ratio. Pilyugin's 2000 and low-ionization empirical calibration used.

the second subsample. The calibration used makes their oxygen abundances to be those of objects with [OIII]λ4363 of similar ionization ratio.

However, figure 2.13 shows that for low ionization sources with [OIII]λ4363, the use of the Pilyugin (2000) calibration underestimates the oxygen abundance by 0.15dex. This opens the possibility that the oxygen content of low-ionization subsample Sub2 sources whose metallicity was derived using Pilyugin (2000) expressions or the low-ionization calibration introduced here might be underestimated. If this turns out to be the case, and some fraction of these low-ionization sources actually lies closer to the other members of the second subsample with nitrogen measurements in figure 2.19, the separation in oxygen abundance between subsamples Sub1 and Sub2 would be somewhat larger.

2.5 Determination of the Ionization Parameter.

The ionization parameter, denoted by U, is defined as the ratio of the density of ionizing photons to the particle density.

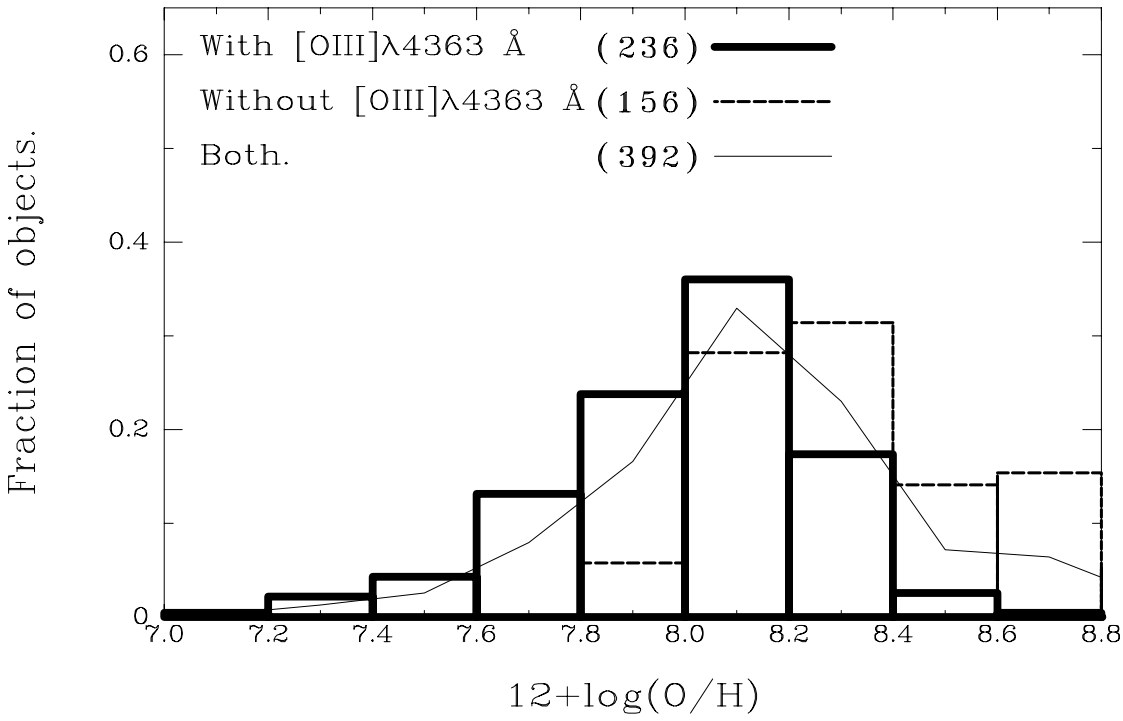

Figure 2.18: Metallicity distributions for both subsamples. Full metallicity range shown. For Sub1 objects, the oxygen abundance was derived using the direct method. For Sub2 objects, oxygen abundances were derived from the empirical calibrations of Denicoló et al. (2002)(81 objects), Pilyugin (2000)(68 objects) or the low-ionization calibration given in figure 2.16(7 objects).

$$U = \frac{Q(H)}{4\pi c n_H r^2} \tag{2.6}$$

where $Q(H)$ is the number of ionizing photons, r is the distance from the star to the inner side of the cloud, and n_H is the density of ionized hydrogen.

It is directly proportional to the ionization degree of the nebula. For its determination, it is common to use ratios of two lines of a given element in different ionization states. This method should be pretty independent of metallicity, although it does depend on the effective temperature of the ionizing radiation.

Figure 2.20 depicts the models used here to calculate the ionization degree. These models are based in the following assumptions:

- The ionizing radiation is provided by a single main sequence star placed at the center of a sphere. The range of effective temperatures used is 35000K-55000K. (Mihalas, 1972)

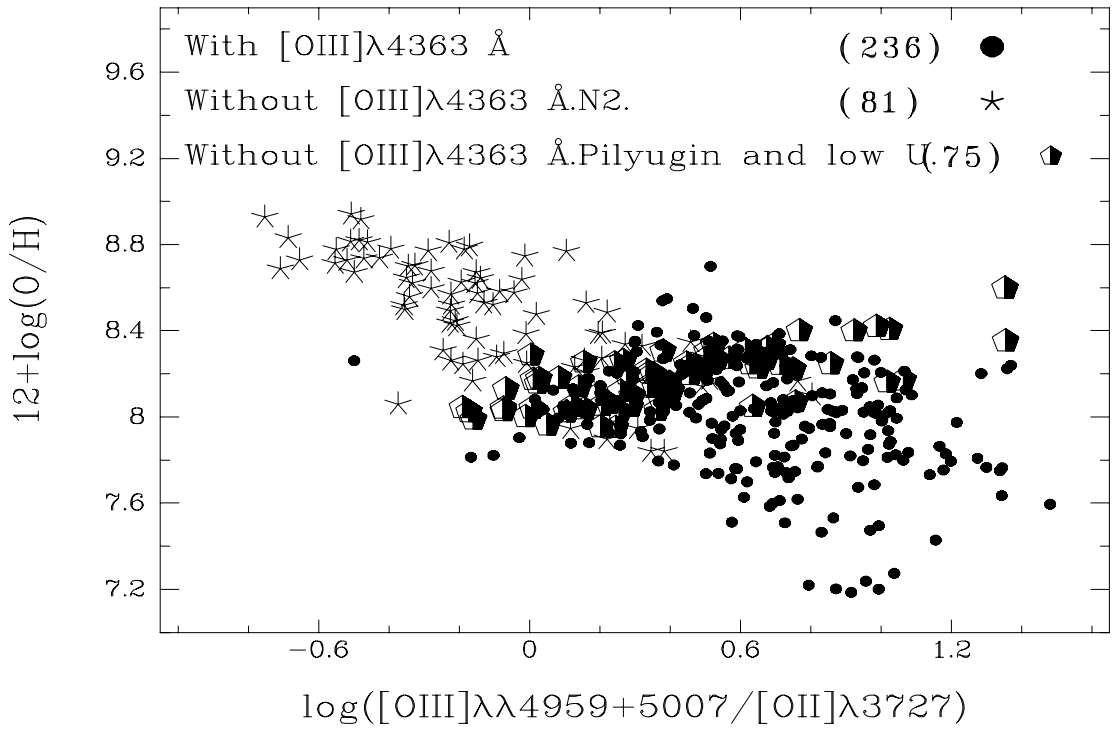

Figure 2.19: Metallicity *vs.* ionization ratio. All sources.

- The gas surrounding the star is located at a given inner radius that is large enough as to provide a plane-parallel geometry. The ionization parameter goes from 0.1 to 0.0004.
- The gas density is assumed to be constant. The gas densities used vary from 10 to 500 cm^{-3}.
- The chemical composition is uniform through the nebula. The gas abundances used range from 1/50 to 1/2 of the solar value.

Under these assumptions, the shape of the ionizing continuum is given by the effective temperature of the ionizing source, and the degree of ionization is parametrized by the ionization parameter U.

Figure 2.20 presents the models with a metallicity 0.1 solar. It shows that the correlation between the different line ratios and ionization degree depends on effective temperature. Models with an effective temperature of 35000K are clearly separated from the rest. In particular, the first panel shows that, at a given U, the [OIII]/[OII] value is always higher for the highest effective temperatures as a result of the increase of the ionization of O^{+} to O^{++}. This behaviour is also observed in Kewley & Dopita (2002). In those models, the

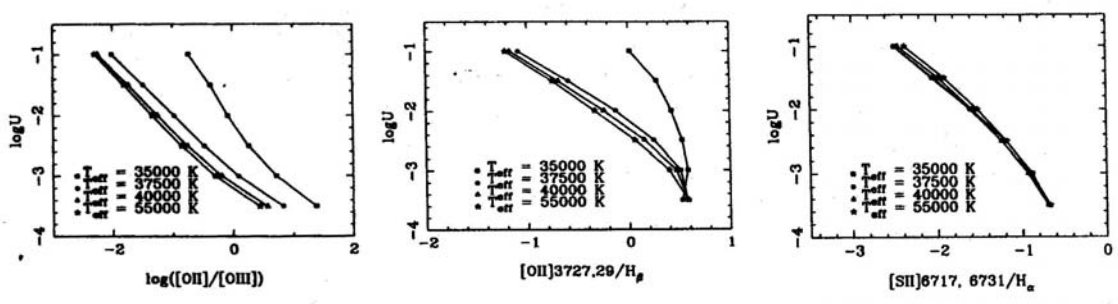

Figure 2.20: Models used to derive the different prescriptions to calculate the ionization parameter.

ionization is provided by zero-age star clusters with a Salpeter IMF. The metallicities were varied from 0.05 to 3 times solar. The relationship there found between ionization degree and metallicity is compatible with ours, since at any fixed age, higher metallicity clusters have a lower effective temperature, and will, in turn, present a lower [OIII]/[OII] for any given U.

The ratio [OIII]$\lambda\lambda$4959 + 5007/[OII]λ3727 can be used to estimate the ionization degree for the cases in which the ionizing field has an equivalent effective temperature greater than 37500 K (see fig 2.20, left panel). This roughly corresponds to a main sequence O7 star. The expression used is:

$$\log U_{\frac{[OIII]}{[OII]}} = 0.80 \times \log \frac{[OIII]}{[OII]} - 3.0 \tag{2.7}$$

However, if this diagnostic is applied to objects of lower effective temperature, the ionization parameter will be underestimated.

The ratio of collisionally excited lines to recombination lines can also be used as an ionization parameter indicator, although this method depends explicitly on the metallicity (Díaz, 1994). Therefore this method should not be used as an independent indicator of the ionization degree. Two different line ratios of this kind have been suggested:

$$\log U_{[OII]} = 0.87 \log \frac{Z}{Z_\odot} - 1.39 \log \frac{[OII]}{H\beta} - 1.68 \tag{2.8}$$

$$\log U_{[SII]} = 1.10 \log \frac{Z}{Z_\odot} - 1.40 \log \frac{[SII]}{H\alpha} - 3.26 \tag{2.9}$$

The first diagnostic is only suitable for effective temperatures greater than 37500 K. The sulphur diagnostic is almost independent of both effective temperature and reddening, thanks to its short baseline, as it is seen in figure 2.20.

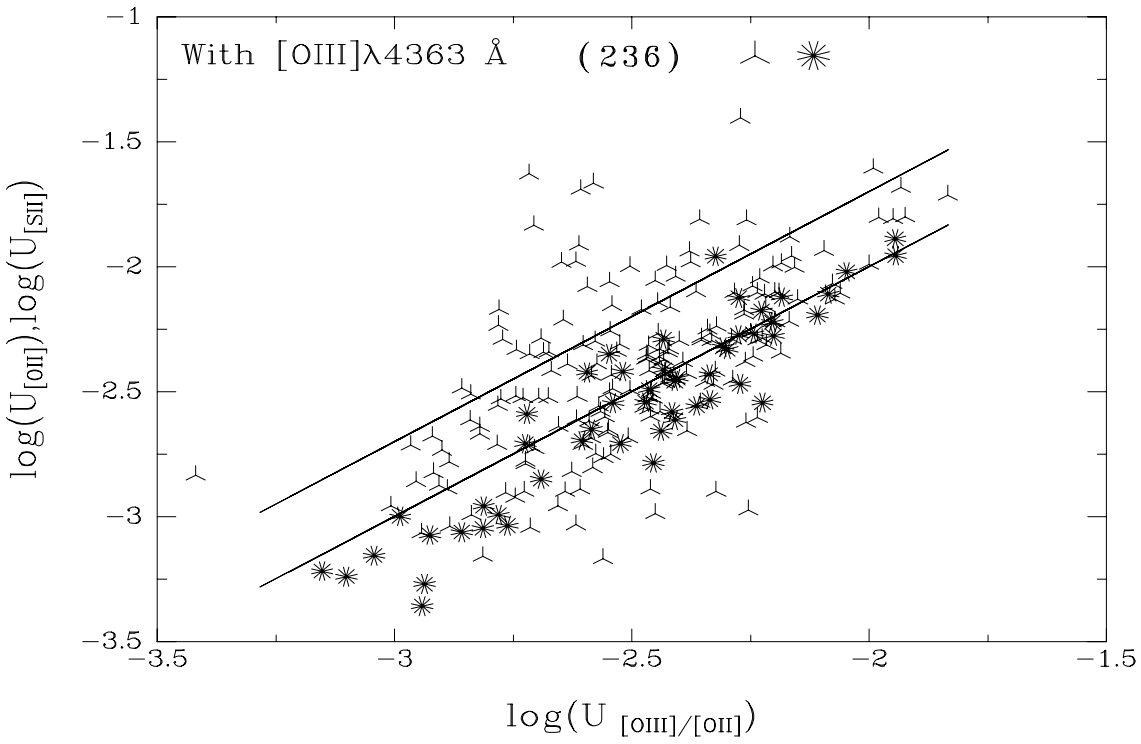

Figure 2.21: Relation between ionization parameters for subsample Sub1. Three vertices stars correspond to $U_{[SII]}$, asterisks correspond to $U_{[OII]}$. The straight lines shown are y=x and y=x+0.3.

For the sources with [SII]$\lambda\lambda$6717, 6731 measurements, $U_{[SII]}$ is plotted against $U_{[OIII]/[OII]}$ in figures 2.21 and 2.22. In the cases for which the [SII] lines are not reported, $U_{[OII]}$ is represented versus $U_{[OIII]/[OII]}$.

Figures 2.21 and 2.22 show that, even though for the vast majority of sources the different ionization dignostics agree very well, there is a significant fraction of sources for which the aforesaid diagnostics do not agree. The effective temperature of the ionizing radiation is for these objects likely to be lower than 37500 K. It is also seen that the fraction of sources showing this effect is greater among subsample Sub2, highlighting another difference between the two subsamples.

2.6 The LCBG-like Subsample.

Luminous Compact Blue Galaxies, hereafter LCBGs, are the high luminosity end of BCGs. They are operationally defined as luminous (M_B more luminous than -17.5), blue ($B-V$ bluer than 0.6) and compact ($\mu_B \leq 21.5$mag arcsec^{-2}) systems. Their spectra indicate that

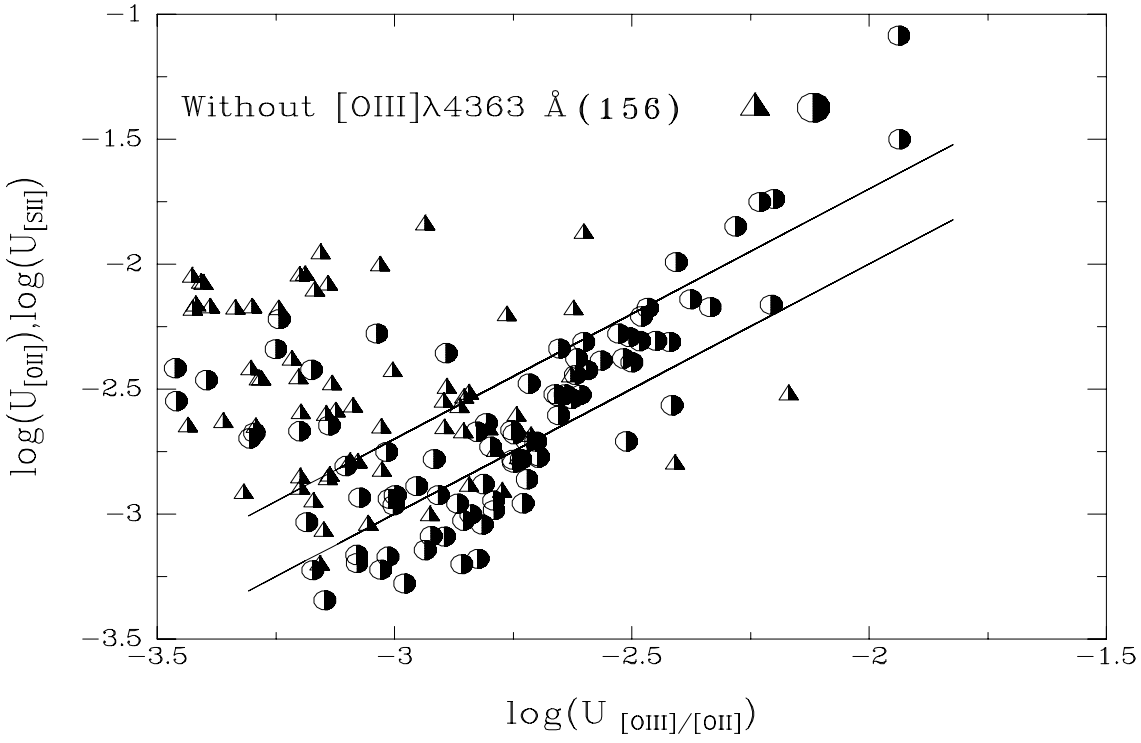

Figure 2.22: Relation between ionization parameters for subsample Sub2. Most outliers come from this subsample, indicating that their effective temperature is probably lower than the 37500 K threshold. Half-filled triangles correspond to $U_{[SII]}$, half-filled circles correspond to $U_{[OII]}$. The straight lines shown are y=x and y=x+0.3.

they are undergoing a major starburst, which produces a significant fraction of their light output. This starburst enhances their surface brightnesses, making it possible to see them at large distances. Hubble Space Telescope images of LCBGs show the presence of an important underlying stellar population too. Spectroscopic studies of LCBGs can be found in Guzmán et al. (1997), Phillips et al. (1997) and Hoyos et al. (2004). HST imaging is presented and discussed in Koo et al. (1994) and Guzmán et al. (1998). In Guzmán et al. (1997), LCBGs are divided into HII-like and Nuclear Starburst-like types. The work presented in Hoyos et al. (2004) further highlights the similarities between LCBGs and the most luminous HII galaxies.

2.6.1 Definition of LCBG-like HII galaxies.

At least some fraction of the population of intermediate-redshift LCBGs can be considered to be very similar to bright, local HII galaxies (Guzmán et al. 1997, Phillips et al. 1997 and Hoyos et al. 2004). We here define LCBG-like HII galaxies as the subsample of local HII galaxies whose preperties resemble those of higher-redshift LCBGs.

In order to extract such subsample of local HII galaxies with properties similar to higher-redshift LCBGs, the first step is to find galaxies more luminous than $M_B = -17.5$ in the sample studied here. The approach we adopt is to represent the observed blue absolute magnitude (M_B) versus the estimator of the blue absolute magnitude presented in Terlevich & Melnick (1981) (B_c).

$$B_c = 79.4 - 2.5 \log \frac{L(H\beta)\mathrm{ergs}^{-1}}{W_\beta(\text{Å})} \tag{2.10}$$

This calibration is introduced to take into account possible aperture/distance or line contamination effects. The number B_c only probes the continuum strength of the fraction of the galaxy that fell inside the slit, but the blue absolute magnitude is sensitive to all light within the passband. This calibration tries to correct for these effects with the aim of deriving an estimate of the blue absolute magnitude for the galaxies we are studying.

The calibration is shown in figure 2.23. This plot presents M_B *vs.* B_c for the galaxies from references 13, 16, 17, 18 and 19 in table 2.1 for which M_B was available. In the case of galaxies from the Hamburg Quasar Survey, M_B was reported in Popescu & Hopp (2000). In the case of galaxies from the First and Second Byurakan Surveys, M_B was found in the NED[4]

[4]NASA/IPAC Extragalactic Database (NED) which is operated by the Jet Propulsion Laboratory, Cali-

Object	$B-V$	Reference.	[OII] λ3727(b)	[OIII] λ5007(b)	W_{3727} Å	W_β Å	$W_{4959+5007}$(a) Å
Tol0127-397	0.56	Terlevich et al. (1991)	3.278	2.164	73	38	130
UM417	0.36	Terlevich et al. (1991)	0.330	5.566	20	144	903
Mrk370(1)	0.48	Cairós et al. (2002)	2.803	1.678	60.7	17.0	37.5
IIZw40	0.52	Terlevich et al. (1991)	0.440	7.76	79	268	2122
Mrk36	0.39	Terlevich et al. (1991)	0.988	5.506	42	70	432
UM462(1)	0.47	Terlevich et al. (1991)	1.777	5.320	96.1	102	615.8
IIZw71(2)	0.55	Jansen et al. (2000)	4.397	2.49	33.2	7.5	22.53

Table 2.4: Galaxies used to re-define the color-criterium. Notes: (a) For Mrk370 and IIZw71 this number is defined as $1.3 \times W_{5007}$; (b) These are the reddening-corrected I_λ/I_β ratios; (1) Given values are $H\beta$ weighted averages of the different zones defined in the respective papers; (2) Integrated spectrophotometry.

or HyperLeda[5] databases. The straight line shown is a least-squares fit to the calibration. The fit expression is:

$$M_B = 0.64 \pm 0.06 B_c - 6.3 \pm 1.0 \tag{2.11}$$

Its scatter is around 1.0 magnitudes, and the residuals are found not to depend on $\log(\text{SlitWidth} \times cz)$. In figure 2.23, B_c was calculated using spectra with slit widths of $4''$(Popescu & Hopp, 2000) and $2''$(objects from the Byurakan surveys). Most spectra used in this chapter were taken with apertures between these two sizes, so the above calibration can be applied to them. Aperture effects for spectra taken with larger apertures or of more distant objects will likely be less important. According to this calibration, objects belonging to the LCBG-like subsample are required to have B_c lower than -17.5, which is the limit adopted.

The color requirement was not straightforward to apply, because not many $B-V$ colors for the HII galaxies included in the sample are available in the literature. For this reason, a simple alternative method, based on spectroscopic criteria had to be developed.

The galaxy sample presented in Cairós et al. (2001a) and Cairós et al. (2001b) provides $B-V$ colors for a sample of 28 blue compact galaxies, six of them appear in the Terlevich et al. (1991) catalogue. This smaller sample is shown in table 2.4.

The adopted approach is to derive a least-squares fit to the observed colors as a function

fornia Institute of Technology, under contract with the National Aeronautics and Space Administration.

[5]HyperLeda is an information system for astronomy: It consists in a database and tools to process that data according to the user's requirements. The scientific goal which motivates the development of HyperLeda is the study of the physics and evolution of galaxies. It can be reached at `http://leda.univ-lyon1.fr/intro.html`

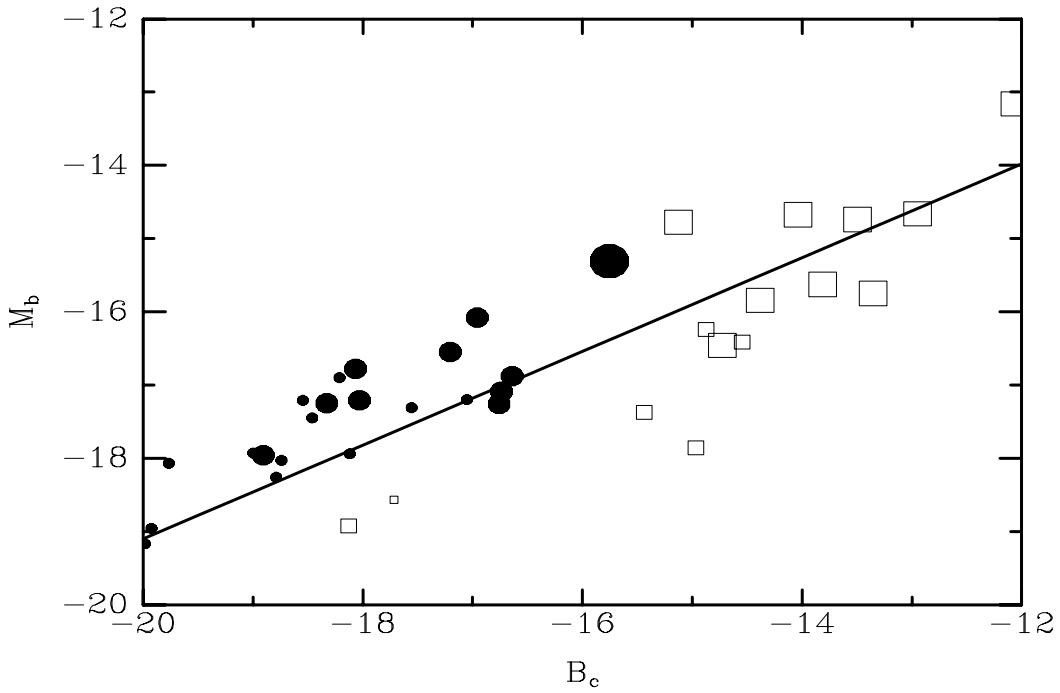

Figure 2.23: M_B vs B_c calibration. Black, solid dots represent objects from reference 19. Open squares are objects from references 13, 16, 17 and 18. Small symbols: galaxies further than $cz = 3600$km s^{-1}; medium symbols: galaxies in the range 1800km s^{-1} $\leq cz \leq$ 3600 km s^{-1}; big symbols: galaxies nearer than 1800 km s^{-1}.

of the continuum strength ratio $x = \frac{[\mathrm{OIII}]\lambda 5007 \times W_{3727}}{[\mathrm{OII}]\lambda 3727 \times W_{4959+5007}}$. The fit is:

$$B - V = (0.54 \pm 0.04) + (0.35 \pm 0.16) \log x \tag{2.12}$$

Using this expression, the color condition translates into $1.57 \leq x$, which is the condition applied.

Unfortunately, not all references report the observed equivalent widths of the two oxygen lines required. Only the Terlevich et al. (1991) catalogue provides all the information. All the objects from Terlevich et al. (1991) which show [OIII]λ4363 included in the presented sample meet this requirement, and 96% of the objects without the auroral line from the Terlevich et al. (1991) sample also match the condition. Therefore, it is assumed that *all* the HII galaxies studied satisfy this condition.

This is not surprising, since the objects presented here were selected from objective prism surveys searching for either strong emission lines or UV excesses. The Tololo and UM surveys, looking for strong lined objects will pick up very blue objects, or compact starbursts with a weak continuum due to the presence of massive, young blue stars. The Markarian or Byurakan surveys, searching for galaxies presenting a UV excess naturally select blue objects. In addition, in these surveys, the photographic plates were more blue sensitive.

Unfortunately, no constraint on the surface brightness or half-light radius can be used with the data at hand. Galaxies satisfying the first two criteria are said to belong to the LCBG-like sample.

In total, 50 objects from subsample Sub1 and 117 sources from the subsample Sub2 were selected. These 167 objects are considered to be LCBG-like HII galaxies.

2.6.2 Properties of LCBG-like Objects.

The aim of this work is to see where LCBG-like sources properties fit within the frame of HII galaxies in general. In order to do this, the distributions of several quantities were drawn. They are shown in figures 2.24 to 2.31.

Figure 2.24 indicates that LCBG-like HII galaxies are mainly found at large distances. Only a tiny fraction of them is located at redshifts lower than ~ 0.01, while this is the median value of the redshift distribution for less luminous systems. Figure 2.25 shows that the observed Hβ flux distribution from LCBG-like objects is remarkably similar to that of the whole sample. In figure 2.26 it is seen that the majority of LCBG-like galaxies have Hβ

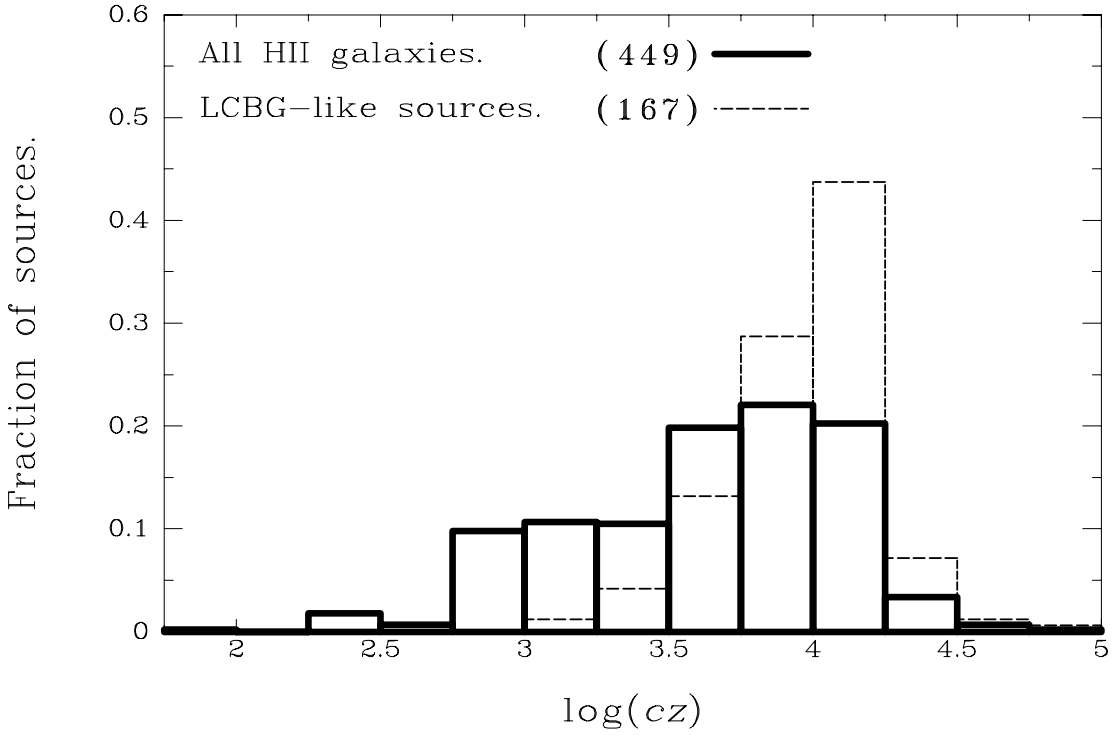

Figure 2.24: Radial velocity distribution of the LCBG-like sources compared to that of all the HII galaxies.

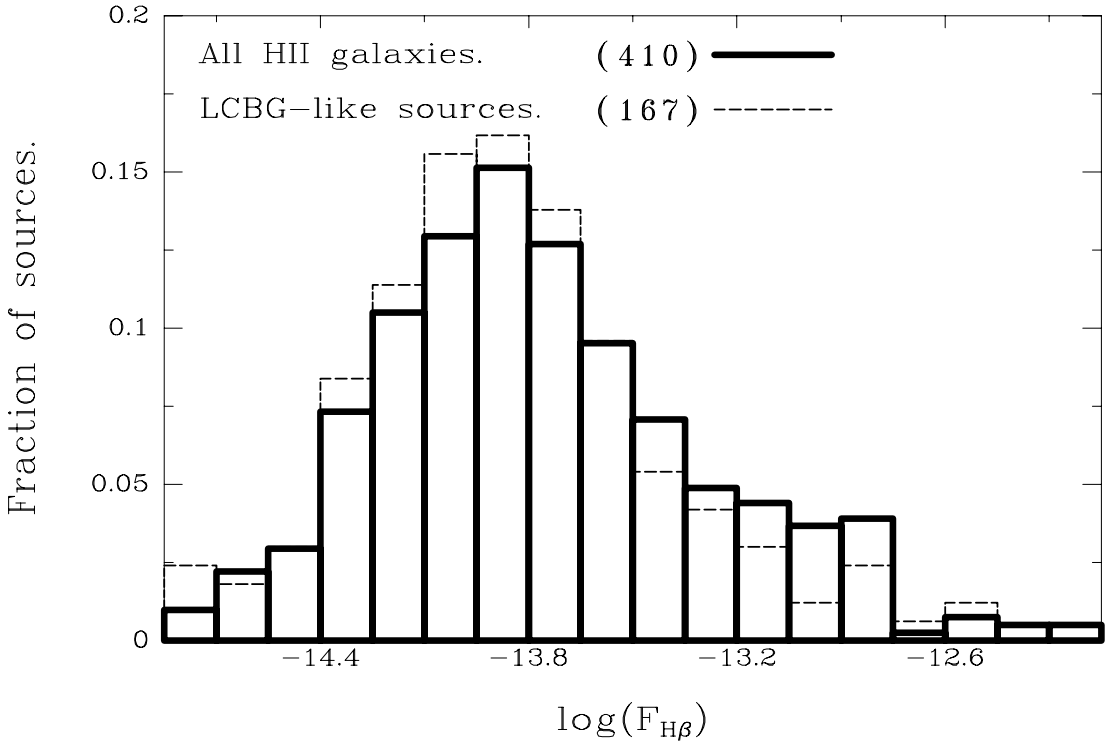

Figure 2.25: As figure 2.24, for the observed Hβ flux distribution.

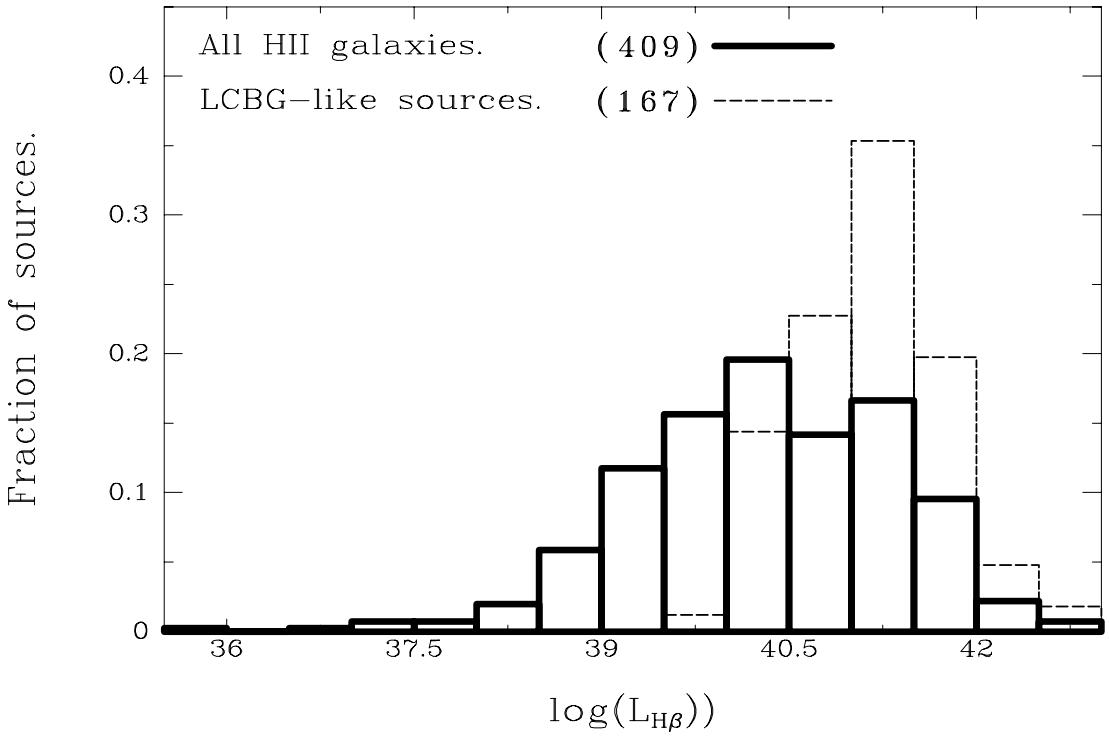

Figure 2.26: As figure 2.24, for the Hβ luminosity distribution.

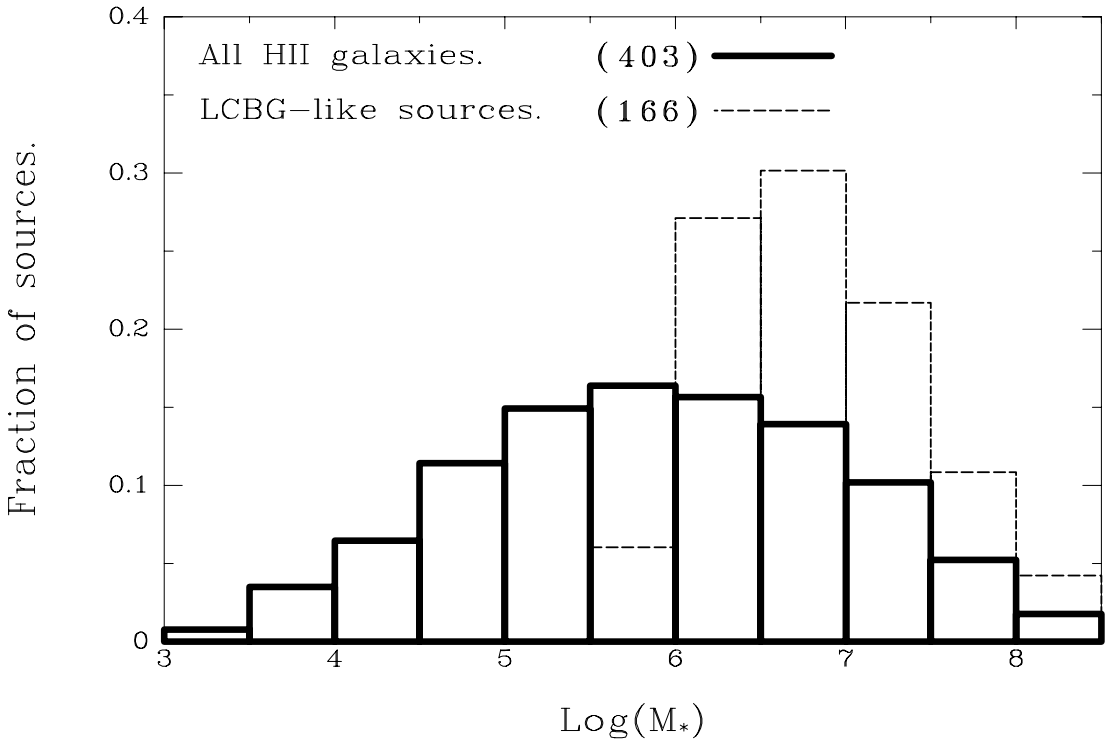

Figure 2.27: As figure 2.24, for the Mass of the ionizing cluster distribution.

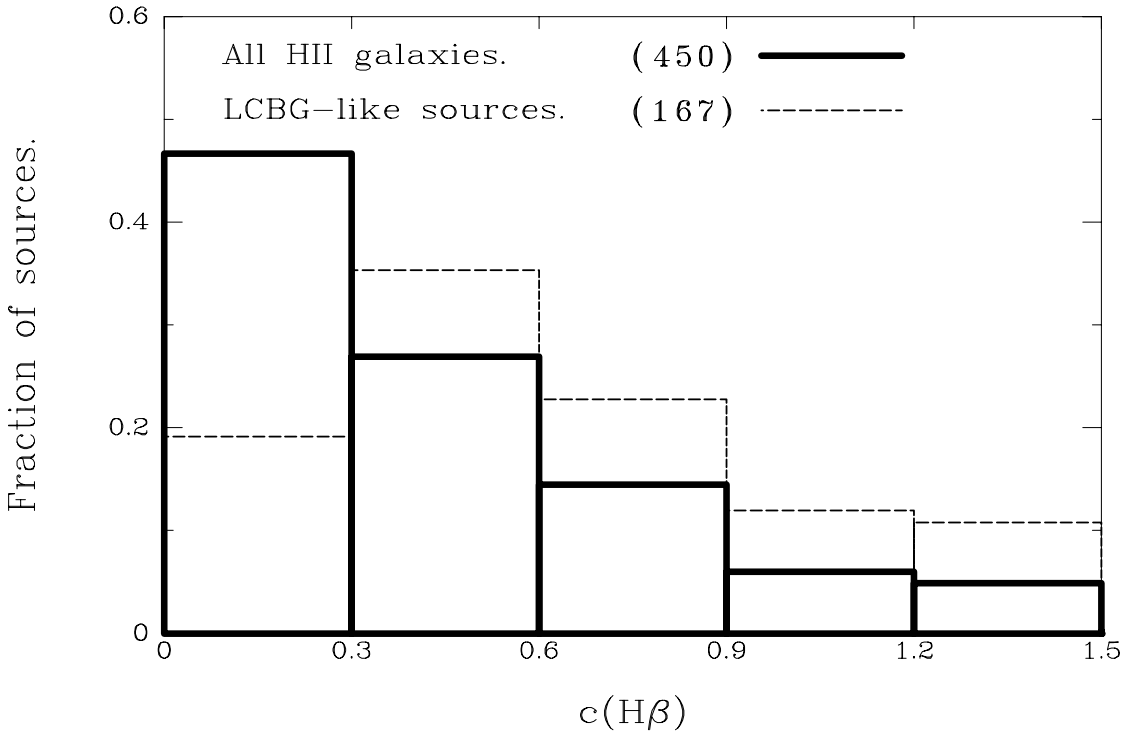

Figure 2.28: As figure 2.24, for the c(Hβ) distribution.

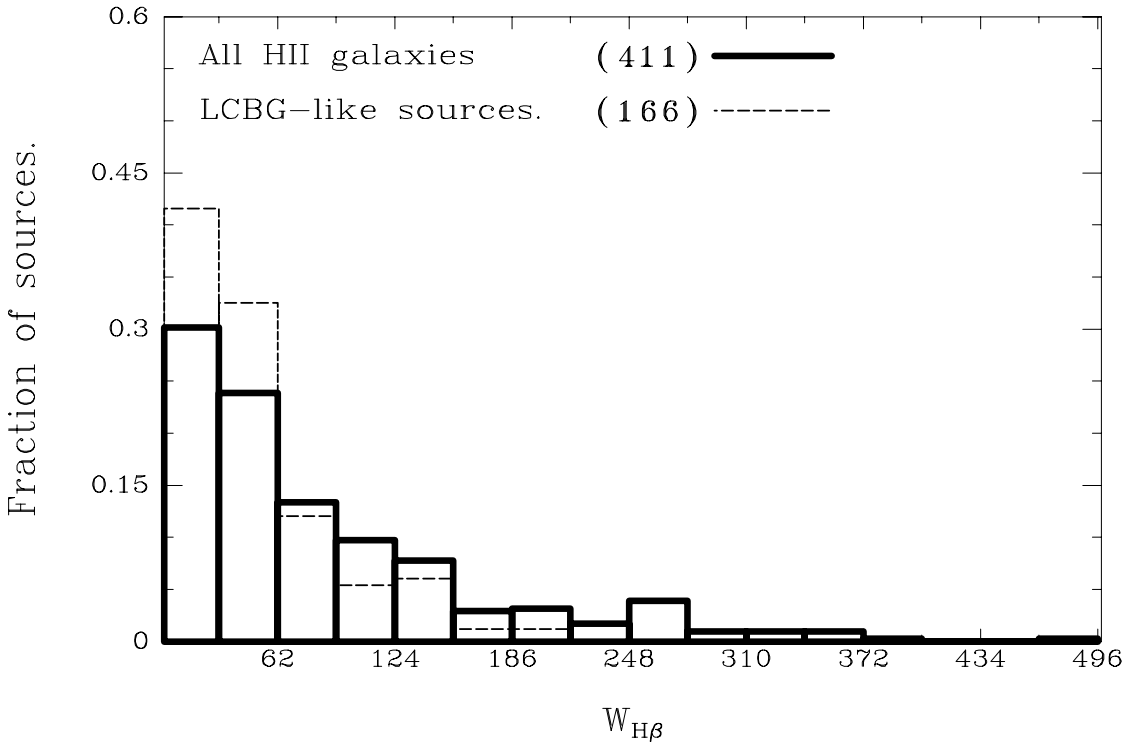

Figure 2.29: As figure 2.24, for the W$_\beta$ distribution.

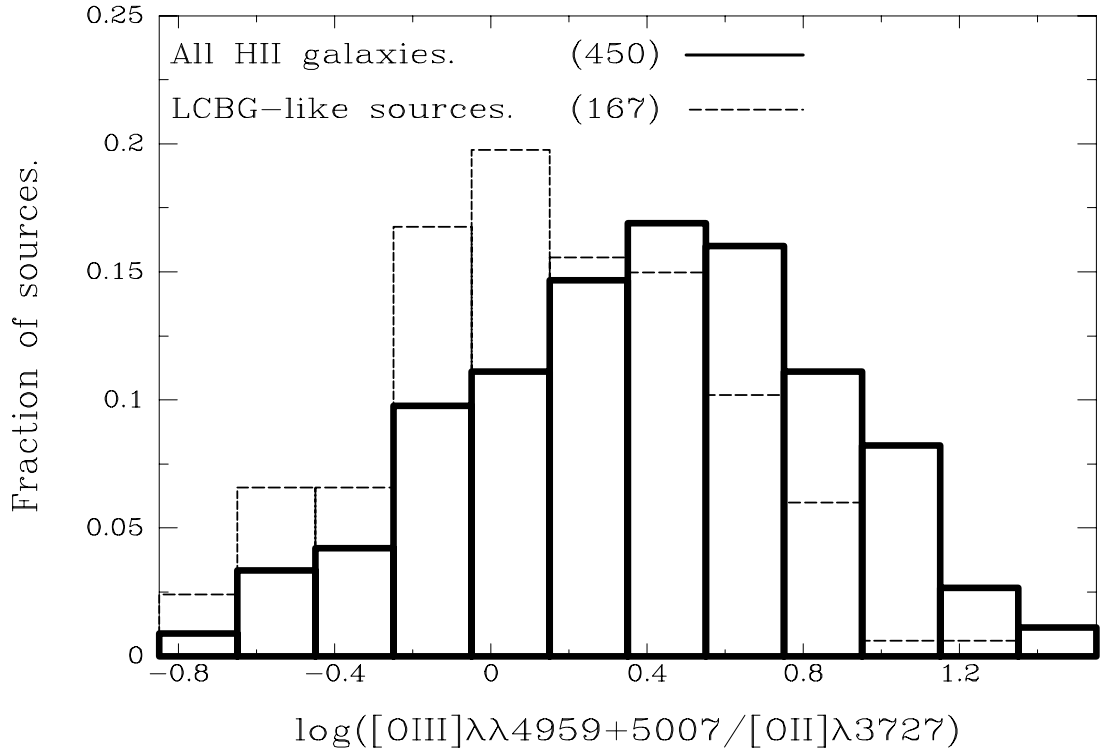

Figure 2.30: As figure 2.24, for the ionization ratio distribution.

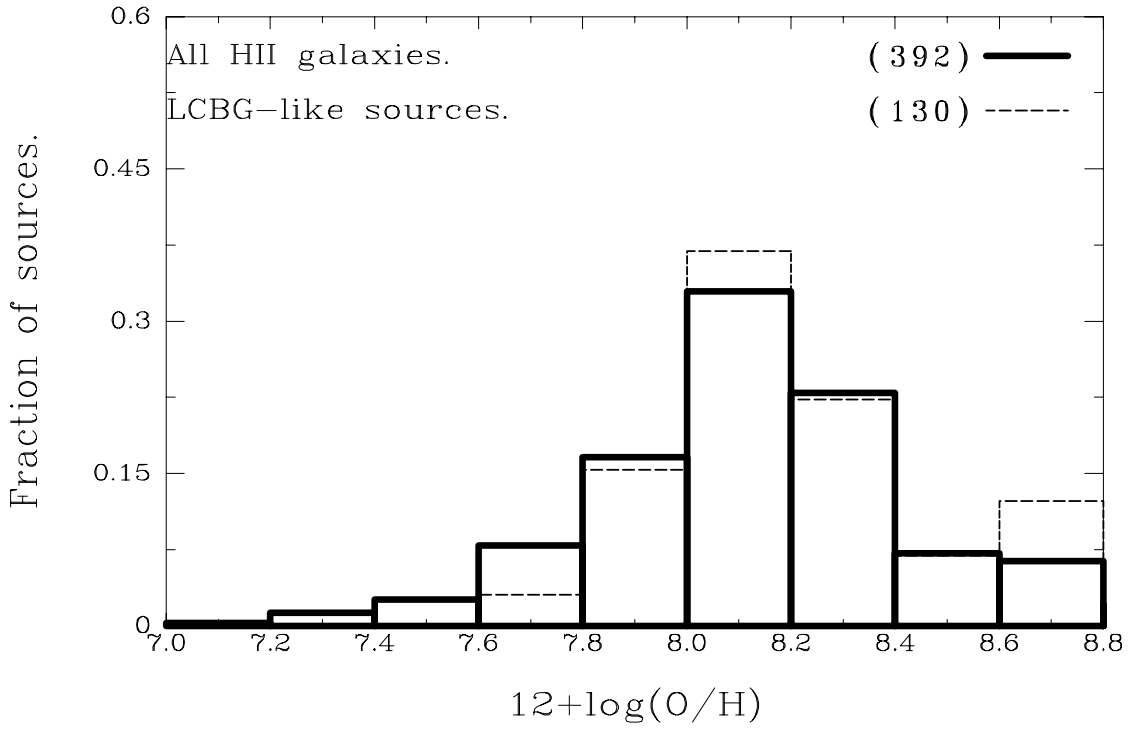

Figure 2.31: As figure 2.24, for the metallicity distribution.

luminosities greater than 10^{41}erg s^{-1}. Only around 16 normal HII galaxies out of 242 are found with line luminosities greater than 10^{41}erg s^{-1}. This suggests that a line luminosity around 3×10^{40}erg s^{-1} might be considered as the cut-off for HII galaxies similar to LCBG. This is a very important difference, since it means that this bright subsample of HII galaxies is powered by a greater number of stars. This is confirmed in figure 2.27, which presents the distribution of the mass of the ionizing cluster for both samples. It is seen that LCBG-like HII galaxies have ionizing cluster masses greater than $10^6 M_\odot$. Only 20 lower-luminosity HII galaxies have clusters that massive. However, since the calculated masses are only lower limits to the actual values due to photon-escape, presence of dust and the systematic error in the *starburst* equivalent width introduced by the underlying, non-ionizing population. Although this was partially corrected for by the use of the upper envelope of the W_β *vs.* log([OIII]/[OII] presented in figure 2.6), LCBG-like HII galaxies are bound to harbor ionizing cluster much more massive than this limit. This is the single, most important difference between LCBG-like HII galaxies and lower luminosity systems. The extinction distribution, shown in figure 2.28, indicates that there is a lack of LCBG-like sources with very low extinctions. At higher dust contents, c(Hβ)$\geq$ 0.30, both distributions follow each other rather closely, though. This distribution also shows that bright HII galaxies are less affected by uncertainties in the extinction than the rest of the galaxies studied.

Figure 2.29 shows the existence of an upper limit to the equivalent width of Hβ of the more luminous systems of around 200Å. The median values are 46.5Å for the LCBG-like subsample and 77.5Å for the less luminous systems. These numbers show that large equivalent widths are mainly found among low luminosity HII galaxies. High equivalent widths are also preferentially found in the case of young starbursts. Therefore, LCBG-like HII galaxies have probably built larger underlying stellar populations. This is further supported by the fact that the LCBG-like histogram shows a higher occupation number at very low equivalent widths. Figure 2.30 shows that the excitation is lower in LCBG-like HII galaxies. This suggests that the ionizing star clusters of LCBG-like HII galaxies are probably more evolved than those of less luminous HII galaxies. The oxygen abundance of LCBG-like systems compared to the whole sample can be seen in figure 2.31. This plot shows that there is a slight bias in the metal content. LCBG-like galaxies never show oxygen abundances lower than 7.6. At the same time, a very metal-rich object is more likely to be a LCBG-like galaxy. However, there seems to be no relationship between metallicity and luminosity since LCBG-like galaxies span pretty much the same metallicity range as the bulk of the whole sample of HII galaxies. We

Property.	With	Without
B_c	0.622	1.228
L(Hβ)	0.911	1.085
log[OIII]/[OII]	0.560	0.955
c(Hβ)	0.446	0.965
W_β	0.889	0.880
$\log M_*$	0.735	1.123
$12 + \log(O/H)$	0.905	0.935

Table 2.5: Normalised dot products between LCBG-like subsample histograms and subsamples Sub1 and Sub2 probability densities.

can say as a consequence that the observed differences in the distributions of the ionization ratio shown in figure 2.30 can't arise from a metallicity effect.

It is also enlightening to see whether LCBG-like galaxies are similar to HII galaxies with [OIII]λ4363, or if they resemble HII galaxies without the auroral line. In order to do this, the dot product between the LCBG-like subsample and both Sub1 and Sub2 subsamples probability densities presented above (i.e. the histograms) were derived. Even though the probability densities for subsamples Sub1 and Sub2 are not orthogonal for any property studied, this should indicate which subsample is more similar to LCBG-like galaxies.

Table 2.5 clearly shows that LCBG-like sources are more similar to objects not showing the auroral line [OIII]λ4363. This table indicates that if a distant LCBG does not show the [OIII]λ4363 line, it is likely that this object will present a massive underlying stellar population, high metallicity and low ionization.

2.7 Summary and Conclusions.

We have conducted a statistical study of a very large spectroscopic sample of HII galaxies from the literature. We have compared galaxies with and without the [OIII]λ4363 auroral line, and we have defined a control sample which can be used to investigate the nature of LCBGs at intermediate z.

It has been found that Hβ fluxes are larger for objects showing the [OIII]λ4363 line, even though the Hβ luminosity distributions for galaxies with and without the auroral line are very similar. This is in part because objects not showing the auroral line are more distant and their extinction is higher. However, it has been shown that the non detection of the [OIII]λ4363

line is a real metallicity effect for at least some cases. Objects without the auroral line are about 0.4dex more metal rich than objects from subsample Sub1. The analysis of the [OIII]/[OII] to $12+\log(O/H)$ relationship reveals the existence of high-ionization, metal rich objects without the auroral line. Objects from the second subsample are found to harbour more massive star clusters, although the differences in excitation between the two subsamples indicate that subsample Sub2 sources are probably powered by somewhat older star clusters.

LCBG-like sources are clearly further away than the average local HII galaxy. The Hβ luminosities of LCBG-like systems are much greater. This is a very important difference between the two subsamples. We have also found that their ionizing star clusters are more massive that those of lower luminosity HII galaxies. LCBG-like HII galaxies have been found to possess larger and probably older underlying populations, and their ionizing star clusters are also more evolved and massive. LCBG-like sources are marginally more metal-rich than the average HII galaxy, but not enough to explain the observed differences in the ionization ratio [OIII]/[OII].

We have also shown that LCBG-like sources are more similar to objects without the auroral line [OIII]λ4363, implying that any local control sample designed to study high-redshift LCBGs is to be made of galaxies not showing the [OIII]λ4363 line. If one observes a distant LCBG and is unable to detect the [OIII]λ4363 line, it is likely that this object will present a massive underlying stellar population, high metallicity and low ionization.

Bibliography

Cairós L. M., Vílchez J. M., González Pérez J. N., Iglesias-Páramo J., Caon N., 2001, ApJS, 133, 321

Cairós L. M., Caon N., Vílchez J. M., González-Pérez J. N., Muñoz-Tuñón C., 2001, ApJS, 136, 393

Cairós L. M., Caon N., García-Lorenzo B., Vílchez J. M., Muñoz-Tuñón C., 2002, ApJ, 577, 164

Castellanos M., Díaz A. I., Terlevich E., 2002, MNRAS, 329, 315

Denicoló G., Terlevich R., Terlevich E., 2002, MNRAS, 330, 69

Dennefeld M., Stasinska G.,1983, A&A, 118, 234

Díaz A. I., Terlevich E., Pagel B. E. J., Vílchez J. M., Edmunds M. G., 1987, MNRAS, 226, 19

Díaz A. I., 1994, in Tenorio-Tagle G., eds Violent Star Formation, from 30 Doradus to QSOs. University Press, Cambridge, p. 105

Díaz A. I., 1999, Ap&SS, 263, 143

Dinerstein H. L., Shields G. A., 1986, ApJ, 311, 45

French H. B., 1980, ApJ, 240, 41

Garcia-Vargas M. L., Bressan A., Díaz A. I., 1995, A&AS, 112, 13

Garnett D. R., Shields G. A., Skillman E. D., Sagan S. P., Dufour R. J., 1997, ApJ, 489, 63

Guseva N. G., Izotov Y. I., Thuan T. X., 2000, ApJ, 531, 776

Guzmán R., Gallego J., Koo D. C., Phillips A. C., Lowenthal J. D., Faber S. M., Illingworth G. D., Vogt N. P., 1997, ApJ, 489, 559

Guzmán R., Jangren A., Koo D. C., Bershady M. A., Simard L., 1998, ApJ, 495, L13

Hagen H.-J., Groote D., Engels D., Reimers D., 1995, A&AS, 111, 195

Hoyos C., Guzmán R., Bershady M. A., Koo D. C., Díaz A. I., 2004, AJ, 128, 1541

Izotov Y. I., Thuan T. X., Lipovetsky V. A., 1994, ApJ, 435, 647

Izotov Y. I., Thuan T. X.,Lipovetsky V. A., 1997, ApJS, 108, 1

Izotov Y. I., Thuan T. X., 1998, ApJ, 500, 188

Jansen R. A., Fabricant D., Franx M., Caldwell N., 2000, ApJS, 126, 331

Kewley L. J., Dopita M. A., 2002, ApJS, 142, 35

Kinkel U., Rosa M. R., 1994, A&A, 282, L37

Koo D. C., Bershady M. A., Wirth G. D., Stanford S. A., Majewski S. R., 1994, ApJ, 427, L9

Kunth D., Sargent W. L. W.,1983, ApJ, 273, 81

Lequeux J., Peimbert M., Rayo J. F., Serrano A., Torres-Peimbert S., 1979,A&A, 80, 155

MacAlpine G. M., Lewis D. W., Smith S. B., 1977, ApJS, 35, 203

Markarian B. E., 1967, Afz, 3, 24

Markarian B. E., Lipovetskii V. A., Stepanian D. A., 1983, Afz, 19, 221

Masegosa J., Moles M., Campos-Aguilar A., 1994, ApJ, 420, 576

Maza J., Ruiz M. T., Gonzalez L. E., Wischnjewsky M., 1989, ApJS, 69, 349

Melnick J., Heydari-Malayeri M., Leisy P., 1992, A&A, 253, 16

Melnick J., Terlevich R., Moles M., 1985, RMxAA, 11, 91

Mihalas D., 1972, Non-LTE Model Atmospheres for B & O Stars, NCAR-TN/STR-76.

Moles M., Aparicio A., Masegosa J., 1990, A&A, 228, 310

Osterbrock D. E., 1989, *Astrophysics of Gaseous Nebulae and Active Galactic Nuclei,* (Mill Valley:University Science Books)

Pagel B. E. J., Simonson E. A., Terlevich R. J., Edmunds M. G., 1992, MNRAS, 255, 325

Pastoriza M. G., Dottori H. A., Terlevich E., Terlevich R., Díaz A. I., 1993, MNRAS, 260, 177

Peña M., Ruiz M. T., Maza J., 1991, A&A, 251, 417

Pérez-Montero E., Díaz A. I., 2003, MNRAS, 346, 105

Pérez-Montero E., Díaz A. I., 2005, MNRAS, 361, 1063

Pesch P., Sanduleak N., 1983, ApJS, 51, 171

Phillips A. C., Guzman R., Gallego J., Koo D. C., Lowenthal J. D., Vogt N. P., Faber S. M., Illingworth G. D., 1997, ApJ, 489, 543

Pilyugin L. S., 2000, A&A, 362, 325

Pilyugin L. S., 2001, A&A, 369, 594

Popescu C. C., Hopp U., 2000, A&AS, 142, 247

Rayo J. F., Peimbert M., Torres-Peimbert S., 1982, ApJ, 255, 1

Salzer J. J., Moody J. W., Rosenberg J. L., Gregory S. A., Newberry M. V., 1995, AJ, 109, 2376

Searle L., Sargent W. L. W., 1972, ApJ, 173, 25

Skillman E. D., 1989, ApJ, 347, 883

Skillman E. D., Kennicutt R. C., 1993, ApJ, 411, 655

Skillman E. D., Televich R. J., Kennicutt R. C., Garnett D. R., Terlevich E., 1994, ApJ, 431, 172

Smith M. G., Aguirre C., Zemelman M., 1976, ApJS, 32, 217

Stasińska G., Schaerer D., Leitherer C., 2001, A&A, 370, 1

Terlevich R., Melnick J., 1981, MNRAS, 195, 839

Telles E., Melnick J., Terlevich R., 1997, MNRAS, 288, 78

Terlevich R., Melnick J., Masegosa J., Moles M., Copetti M. V. F., 1991, A&AS, 91, 285

Thuan T. X., Izotov Y. I., Lipovetsky V. A., 1995, ApJ, 445, 108

Vílchez J. M., Pagel B. E. J., Díaz A. I., Terlevich E., Edmunds M. G., 1988, MNRAS, 235, 633

Chapter 3

HST Spectroscopy of Four Luminous Compact Blue Galaxies at Intermediate *z*.

Abstract.

We present a spectroscopic study of 4 blue ($B-V \leq 0.6$) compact ($\mu_B \leq 21.0$ mag arcsec^{-2}) field galaxies with redshifts $0.095 \leq z \leq 0.438$ and absolute magnitudes M_B between -17.5 and -21.1. The spectra, taken with the STIS spectrograph on board of the HST telescope, show prominent emission lines whose spatial profiles reveal, at least in two cases, the existence of various star-forming regions and an underlying stellar population. The derived Star Formation Rates from Hα luminosities in these star forming regions range between 0.5 and 7 $M_{\odot} yr^{-1}$. These are typically ten times more luminous than and approximately twice as large as the well known giant HII region 30-Doradus in the LMC. When compared to local star bursting galaxies, the objects presented here turn out to be very similar to the brightest HII galaxies in terms of the areal star formation rate and in the ratio between the half-light diamter of the *galaxy* to the half-light diameter of the *line-emitting* region (D_{eff}/D_0).

3.1 Introduction.

Blue Compact Galaxies (BCGs) were first identified by Zwicky (1965) as faint star-like field galaxies on Palomar Sky Survey plates. BCGs often present an emission line spectrum and a UV excess.

The *Hubble Space Telescope* (HST) has provided a great deal of information about the nature of these faint blue compact galaxies. Such galaxies include low luminosity dwarfs at low redshift (Im et al., 1995), starburst galaxies (Cowie, Songaila, & Hu, 1991), and low-luminosity active galactic nuclei at $z \leq 1$(Tresse et al., 1996). Faint blue compact galaxies also include the so-called Compact Narrow Emission Line Galaxies (CNELGs; Koo et al. (1994), Koo et al. (1995) and Guzmán et al. (1996).)

In Jangren et al. (2001, submitted) the name Luminous Compact Blue Galaxies (LCBG) was assigned to those luminous (M_B brighter than -17.5), compact ($\mu_B \leq 21.0$ mag arcsec^{-2}), and blue ($B-V \leq 0.6$) galaxies undergoing a major starburst. This definition is meant to include the most luminous local BCGs as well as various families of starbursts at intermediate z. An important feature of our sample selection is that this population of generally isolated, high surface-brightness objects can be observed over a wide redshift range. For instance, Lyman-Break galaxies (Lowenthal et al. (1997) and Pettini et al. (1998)) at z greater than 2 would be among the brightest LCBGs, according to this definition. LCBGs are thought to contribute up to $\sim$50% of the star formation rate density in the universe at $z \approx 1$, and they are the most rapidly evolving population responsible for the observed evolution of the luminosity function (Lilly et al., 1995). They are therefore of great relevance for the study of the star formation rate in the universe and a key to our understanding of the evolution of galaxies at cosmic scales.

Their relation to local populations, however, is not well understood. A detailed study of 45 such objects can be found in Guzmán et al. (1997) and Phillips et al. (1997). This population of LCBGs is far from being a homogeneous class of objects: around 60% of them are "HII-like" objects, whereas the rest are classified as "Star-burst disk-like." HII galaxies are a subset of BCGs in which the spectrum is completely dominated by a component, present almost everywhere within the galaxy, which resembles the emission of an HII region (Sargent & Searle, 1970). Star-burst Nuclei were introduced in Balzano (1983); they show high extinction values, with very low [NII]λ 6584/Hα ratios and faint [OIII]λ5007 emission. Their Hα luminosities are always greater than 10^8 solar luminosities. In order to investigate

further the nature of LCBGs at intermediate redshift and identify their local counterparts, we have studied the sizes and the areal star formation of the star forming regions in LCBGs. The half-light radius of both the line emitting region and the host galaxy can be used to parametrize the size of the starburst relative to the underlying population, while the star formation rate per unit area and galactic mass are used to rank the intensity of the star forming episode.

In this chapter we present two-dimensional spectra of four LCBG with redshifts between 0.095 and 0.438 which were obtained with STIS, on the HST. These objects were originally classified as CNELGs in Koo et al. (1994). They were selected as stellar-like objects with colors unlike typical stars in UBV two-color diagrams. Two of the galaxies presented here were observed with the WFC/HST camera (Koo et al., 1994) and the other two were observed with the WFPC2/HST camera (Guzmán et al., 1998). Spectroscopic works dealing with these objects can be found in Guzmán et al. (1996) and Koo et al. (1995). The selected sources are in the fields SA68, SA57 and HER1, and were selected to span a wide range in luminosity, ($-21.1 \leq M_B \leq -17.5$).

HST spatially resolved spectroscopy can help us constrain better the nature of these LCBGs by providing:

- The distribution of the stellar component and the nebular component within these galaxies, as it yields a measure of the size of the star forming region relative to the galaxy as a whole. The fraction of the galaxy involved in the star forming event is also of importance since the amount of fading depends on it.

- The star formation rate per unit area, which yields a measurement of the intensity of the star forming episode and of the star forming efficiency as well.

- Well resolved rotation curves. This would give a direct determination of the mass enclosed within the line-emitting region. This kinematic study will be presented in a follow-up paper (Bershady *et al.*, in preparation).

Section 3.2 of this chapter describes the details of the observations, data reduction and involved errors and uncertainties. The analysis of the structure, and the star formation properties of the star forming regions are presented in Section 3.3. The summary is Section 3.4.

The cosmology assumed throughout this chapter is a flat universe with $\Omega_\Lambda = 0.7$ and

	H1-13088.	SA57-10601.	SA68-6134.	H1-13385.
Obj ID.	1	2	3	4
RA	17 20 19.67	13 08 47.8	00 18 11.34	17 21 15.72
DEC	50 01 04.7	29 23 41.1	15 47 52.8	50 01 38.0
Obs Date.	2000 Nov 06	2000 Jul 05	2001 Oct 20	2001 Aug 10
Total Exp Time.	4932	4696	4656	4932
z.	0.436	0.438	0.285	0.095
$t_{look-back}$(Gyr)	3.9	3.9	2.9	1.2
M_B	-21.1	-20.4	-19.8	-17.5
R_e	2.7	2.1	1.0	0.69
m_B	21.0	21.6	21.4	20.9
r_e	0.47	0.36	0.23	0.39

Table 3.1: Log of HST/STIS spectroscopy. RA is given in hours, minutes, and seconds. DEC is given in degrees, arcminutes, and arcseconds. Coordinates given for equinox J2000. Half-light radii are given in kpc (R_e) and arseconds (r_e).

$\Omega_{matter} = 0.3$. The resulting cosmological parameters are: H_0=70 km s^{-1}Mpc^{-1}, q_0=-0.55. Given these values, $1''$ corresponds to 1.8 kpc at $z = 0.1$ and to 5.8 kpc at $z = 0.45$.

3.2 Observations and Data Reduction.

Target names, redshifts, look-back times, B absolute magnitudes and half light-radii, as well as an identifying number for the observed objects are given in table 3.1.

The spectra were obtained using the STIS instrument, on board the Hubble Space Telescope. The detector used was the STIS/CCD, a SITe 1024x1024 chip, with $0.05''$ square pixels operating from ~2000 to 11000 Å.

The instrumental configuration used was a low resolution grating, G750L, providing a dispersion of 4.92 Å per pixel or about 190 km s^{-1} per pixel which, in combination with a slit $0.5''$ wide, gives a spectral resolution of about 29Å(FWHM). The spectral coverage provided by this setup is about 5000 Å. The central wavelength is 7750 Å. For each target, two different observation sets, each one consisting of two different exposures were carried out. The exposure time for each single exposure is around 1200s. Total exposure times for each object are gathered in table 3.1. The spectra allowed to measure emission line fluxes for [OII]λ3727, Hβ, [OIII] $\lambda\lambda$4959, 5007, Hα and, for one object, [SII]$\lambda\lambda$6717, 6731. The spectra were not dithered along the slit.

A higher resolution grating G750M was used too. It provides a dispersion of 0.53 Å per

pixel or about 35 km s^{-1} per pixel. The slit width used was $0.2''$ wide, thus giving a spectral resolution of about 2.1Å(FWHM). The spectral coverage provided by this setup is about 500 Å. The results from this data will be presented in a forthcoming paper (Bershady *et al.*, in preparation).

The data were reduced using the STSDAS [1] package within IRAF [2]. Reduction steps follow standard procedures: bias substraction, cosmic ray-rejection within one data set, dark current removal, flatfielding, wavelength calibration, flux calibration and the combination of the two datasets, to increase the signal-to-noise ratio (*snr*). Fringing of the CCD was found to be important and the standard de-fringing technique available in STSDAS was used. De-fringing raised the signal-to-noise ratio by around 15% in the red end of the spectra.

Additional steps to remove survivor cosmic rays and bad (i.e., both *cold* and *hot*) pixels were performed. These additional steps are inspired by the *lineclean* task in IRAF in order to remove *cold* pixels, and make use of a consistency check to remove cosmic rays and *hot* pixels (Hoyos, 2002). They are explained in more detail below.

Cold pixels are flagged fitting a 6^{th} degree polynomial to every line in the spectral direction of the two-dimensional spectrum. For this fit, both the 20 pixels whose DN[3] is greatest and the 20 ones whose DN is lowest are discarded. The pixels whose signal is lower than the fitted polynomial value at that column by more than three times the *rms* of the fit are flagged as *cold* pixels. Such pixels are set to the value of the fit, and the resulting cleaned image is referred to as the *partially corrected spectrum.*

Hot pixels and survivor cosmic rays not removed by the standard procedures within STSDAS are identified by comparing the different spectra from the two observation datasets. First, a minimum image is created from the two datasets obtained for each source. This image does not contain any *hot* pixel or cosmic-ray hit. *Cold* pixels from this minimum image are removed using the method outlined above. This new frame is called the *minimum corrected* image. The difference between the *partially* corrected spectrum obtained when removing *cold* pixels and the *minimum corrected* spectrum is therefore a spike map. Every pixel in this image brighter than 3.5 times the *rms* of the *minimum corrected* frame calculated in a featureless area is flagged. *Hot* pixels and cosmic rays are removed by substituting them by

[1]Space Telescope Science Data Analysis System, from the Space Telescope Science Institute, operated for NASA by AURA.

[2]Image Reduction and Analysis Facility. Distributed by the National Optical Astronomy Observatories, which is operated by AURA (Association of Universities for Research in Astronomy, Inc) under cooperative agreement with the National Science Foundation.

[3]DN stands for Data Number, or CCD counts.

their value in the *minimum corrected* frame.

This method has one pitfall, if a *hot* pixel is consistent and has the same value in both images it will not be properly flagged.

3.2.1 Description of the Spectra.

The slit placement can be seen in figure 3.1, overlaid on HST images of the observed sources. The frames for objects 1 & 2 are I814W HST/WFPC-2 images (Guzmán et al., 1998). Images for objects 3 and 4 are F555W HST/WF-1 data (Koo et al., 1994). In figure 3.1 the spectra have been scaled and approximately aligned with the images.

Overall, the spectra are rather flat. The continuum decreases only by a factor of two from [OII]λ3727 to Hα. No stellar features in absorption can be observed since the continuum level is very low. The main features in the spectra are emission lines. Integrated spectra for all the sample galaxies can be seen in figure 3.2.

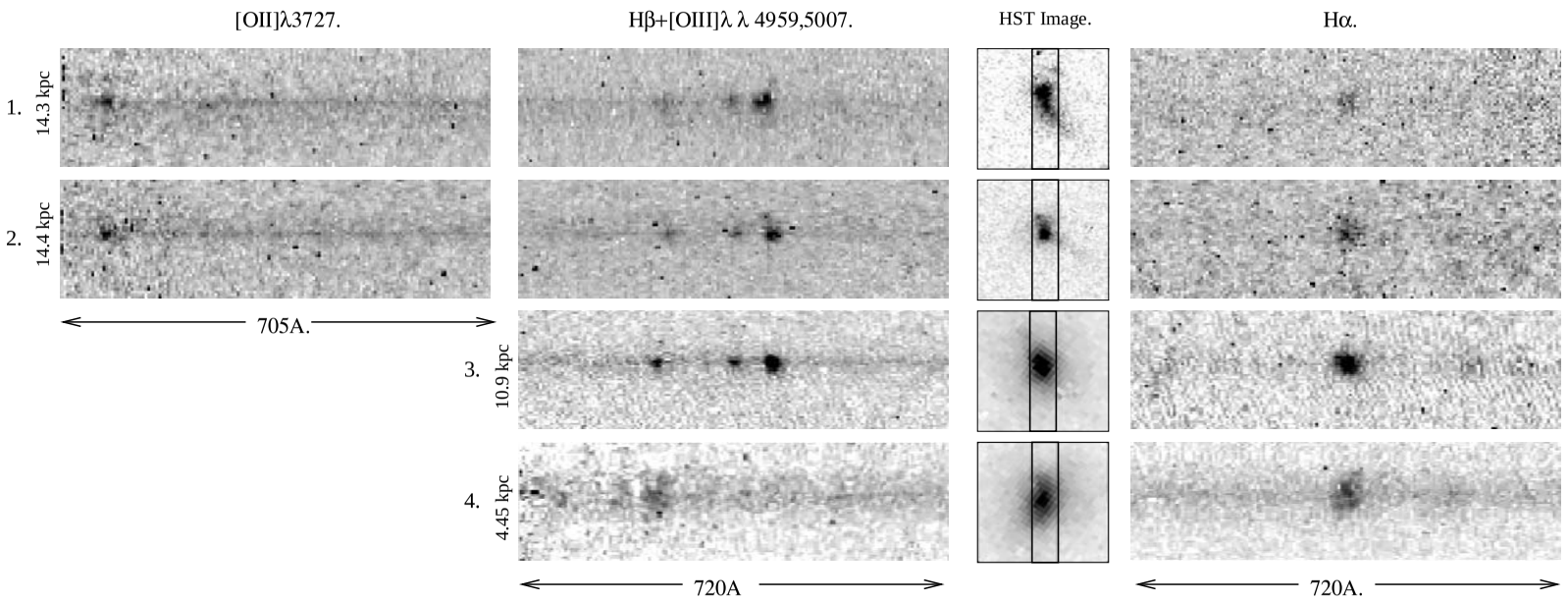

Figure 3.1: Comparison between the STIS 2-D spectra with HST/WFPC-2 I814W (objects 1 & 2) and HST/WF-1 F555W (objects 3 & 4) images (see Koo et al. (1994) and Guzmán et al. (1998), respectively). Object 1 is H1-13088, object 2 is SA57-10601, object 3 is SA68-6134 and object 4 is H1-13385. Each spectral strip spans 2.5″ in the spatial direction. The dispersion is 4.92 Å per pixel and the spatial scale is 0.05″ per pixel. The slit orientation is shown superimposed on the HST images which are 2.5″× 2.5″in size.

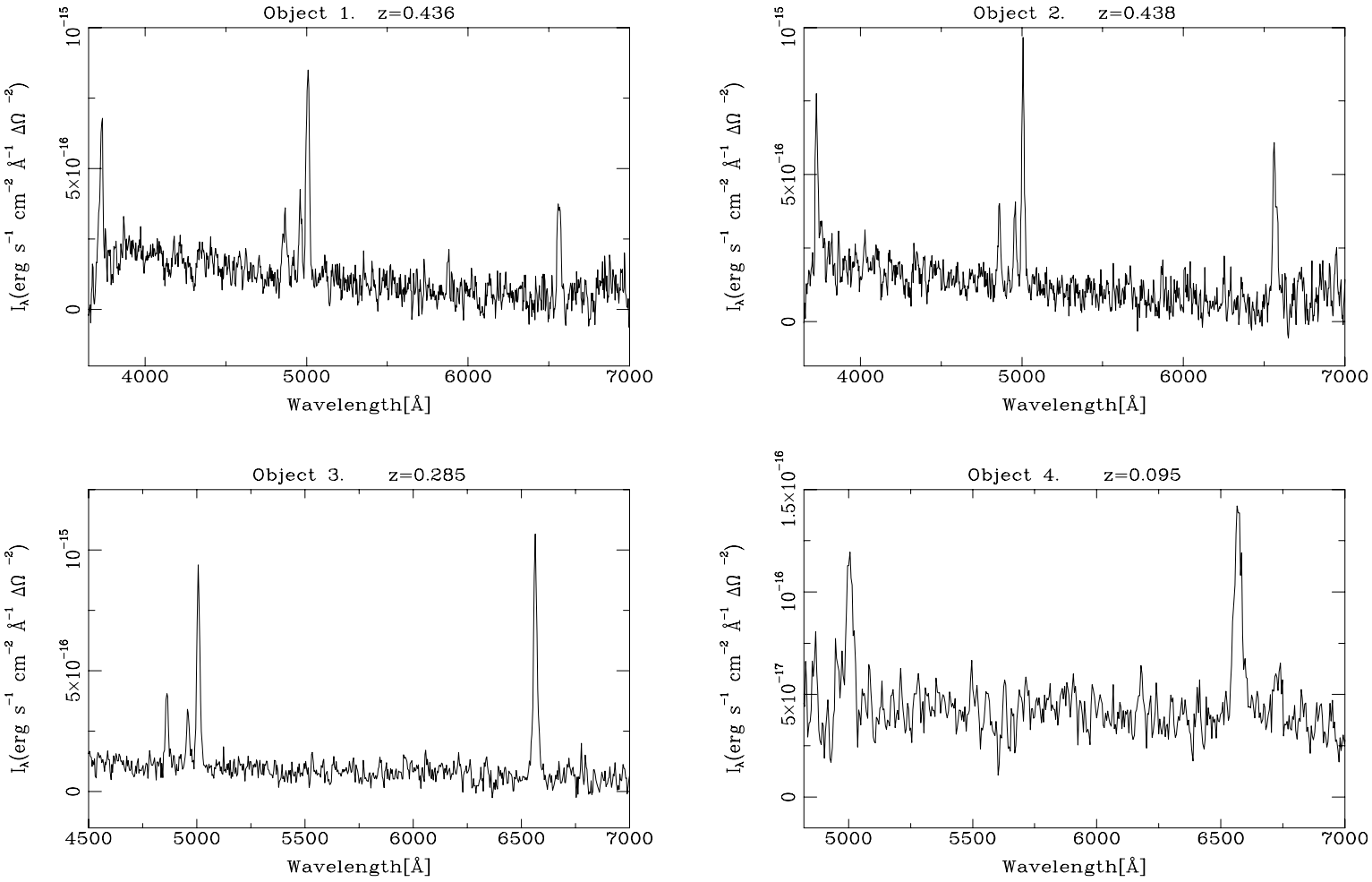

Figure 3.2: One dimensional spectra of the four galaxies in the sample, showing the observed emission lines. Vertical axis units are erg s^{-1} cm^{-2} arcsec^{-2}Å^{-1}.

3.2.2 Errors and Uncertainities.

The three major sources of uncertainties in the emission line measurements are: (1) the read-out noise of the CCD, (2) the variation of charge transfer efficiency and (3) cosmic rays and bad pixels.

- The read-out noise for the STIS-CCD chip for gain=1 is 5.3 DN(rms) per pixel. This contribution is non-negligible since the objects under study are very faint. Typically $\sim$ 100 DN are accumulated per pixel in the brightest lines and some of the measured lines reach only around 20 DN per pixel at their peaks. The continuuum level is $\sim$8 DN. This effect can modify the brighter emission lines by around 5% per pixel and the faintest lines signal can be changed by 25% per pixel.

- The STIS-CCD imperfect charge transfer efficiency causes some signal to be lost when the charge is transferred through the chip at readout time. The amplifier is situated at the top right corner of the STIS CCD, making objects at lower rows appear fainter than they would if they were at high line numbers (parallel losses) and making objects on the left side of the chip appear fainter than on the right side (serial losses). This imperfection on the STIS-CCD has a very negative impact for faint sources in faint backgrounds like the spectra presented here, where less than 150 electrons are accumulated per pixel in even the brightest lines. At these levels, around 15% of the charge is lost during readout time. This imperfect parallel charge transfer efficiency then causes the observed fluxes to be seen as lower limits to the actual ones and the serial losses cause an artificial increase of the derived extinction coefficient from the Balmer decrement from Hα to Hβ too. This later effect is thought to be small. Due to this problem in the STIS-CCD chip the measured fluxes are to be considered as lower limits, as they may be up to 15% higher. Serial losses are believed to be less important than parallel losses.

- The rate of cosmic ray hits for the HST is very high. There are also a good number of bad pixels. Since the exposure times were very long because of the faintness of the observed galaxies, it is not uncommon for pixels to be hit in two different images within the same dataset making them very difficult to recover.

3.3 Results and Analysis.

3.3.1 Emission-Line and Continuum Distribution.

In star forming regions, gas and stars often follow different spatial distributions. It is then interesting to take advantage of STIS spatial resolution to see whether the continuum and the emission lines share a common spatial distribution or not. This can help to model what fraction of the mass of the system is involved in the star forming event.

Using the IRAF task *fit1d*, a "continuum image" was made by fitting 3 cubic spline pieces to every line in the spectra, and then, a "line image" was constructed by subtracting the "continuum image" from the original 2-D spectroscopic frame.

In the spectra presented here, wavelength varies along lines whilst the spatial coordinate varies along columns. The spatial distributions of both continuum and lines were investigated using the STSDAS task *ngaussfit*. This task can fit to a set of x-y values the sum of a straight line, known as the baseline, and one or several gaussian profiles. This task also gives approximate errors for the fitted parameters, calculated by resampling.

To study the continuum spatial distribution, we fit several gaussians to the wavelength-averaged continuum images to allow for subcomponents in the stellar population. In all cases the sum of two gaussians provided a good fit to the continuum data. For the emission lines, we tried a two-gaussians fit similar to that performed for the continuum. However only object 2 had enough substructure with high *snr* in the line emitting region for the best fit to require the sum of two gaussians. Objects 1,3 & 4 had not enough *snr* or evidence for substructure to distinguish several components and thus only one gaussian is fitted. In summary, the procedure to choose how many gaussians should be used to fit any given profile is as follows. First of all, a single gaussian is fit and the residuals are plotted. If these residuals, when compared to the statistical error of the data, still show evidence for a non-zero substructure a new model with two gaussians is tried. This process could be iterated but it was found that two gaussians were always enough. This recipe naturally leads to the continuum being fit by two gaussians, and to the line-emitting region being fit by a single gaussian model in most cases. The continuum profile is the result of averaging around 1000 columns, and the line emitting profile is obtained by collapsing only a few ones, therefore the noise in the former case is proportional to $1/\sqrt{1000}$ and in the latter case, to $1/\sqrt{\text{a few}}$. This makes it neccessary to fit two gaussians for the continuum models and only one gaussian for the line-emitting region in most cases since any remaining substructure of the residuals after the first fit is

much more likely to be larger than the noise when fitting the continuum than when fitting the emission lines. The exception is the emission region of object 2, in which the second iteration is clearly needed becaus its emission-line profile shows a plateau, as can be seen in figure 3.3. This feature can not be properly fitted with a single gaussian.

Table 3.2 lists the central position of the line emitting region with respect to the continuum center and the spread of both continuum emitting region and line emitting region, as defined in what follows.

For single gaussian fits, the centroid is just the gaussian central position, but for double gaussian fits the centroid $\overline{x}$ is calculated as

$$\overline{x} = \frac{A_1 \times x_1 + A_2 \times x_2}{A_1 + A_2} \tag{3.1}$$

where x_i is the central position of the ith gaussian and A_i its amplitude.

The line central positions given in table 3.2 are calculated with respect to the continuum centroid.

The spread of single gaussian fits is defined as simply the FWHM of the gaussian, while for double gaussian fits the spread is defined as:

$$\text{Spread} = |x_2 - x_1| + \frac{A_1 \times \text{FWHM}_1 + A_2 \times \text{FWHM}_2}{A_1 + A_2} \tag{3.2}$$

where x_i is the central position of the ith gaussian, A_i its amplitude and FWHM$_i$ its full width at half maximum. This number equals the FWHM in the case of single gaussian fits, but this is not true for the cases in which the sum of two gaussians was used. All values in this table are given in arcseconds. From its definition, in the case of two equal intensity gaussians of equal width, the spread is the FWHM plus the difference in the centroid values of the two gaussians.

The spatial profiles in figure 3.3 show the fitted data in histogram form. When plotting the continuum distributions the baseline component is substracted in order to show only the gaussian parts of the fits.

From figure 3.3, and table 3.2, it can be seen that:

1. Object 1 shows two interesting features: (1) The nebular component center does not coincide with the continuum centroid. The offset is about one third the size of the emission line themselves; (2) the spread of the continuum is about three times that

of the emission line component. This is interesting because, optically (Guzmán et al., 1998), this galaxy presents both a knot (coincident with the observed line-emitting region in the spectrum) and a tail. This seems to indicate that the starburst does not involve all the optical host galaxy, but is concentrated on one end of it. It also indicates the presence of a very important underlying population. Figure 3.3 also shows that Hβ and [OIII]λ5007 occupy a common region within the source. This object is very similar to the so-called "cometary Blue Compact Dwarfs" in the nearby universe (Noeske et al., 2000).

2. For object 2, the diferences in the centroid positions for the continuum and the emission components are much smaller than the spread of both. The centroid positions are also very similar. Figure 3.3 in fact shows that the line-emitting component and the continuum-emitting component trace each other rather well. Figure 3.3 also suggests that this galaxy consists on two different subsystems, separated by around 1.3 kpc. The star forming region is also weaker relative to the underlying continuum in the fainter subsystem than in the more luminous one. HST/WFPC-2 observations from Guzmán et al. (1998) reveal that optically this galaxy appears to have two knots of star formation. This is consistent with figure 3.3.

3. In object 3, the continuum and the line-emitting component can be said to share a common center, well within their respective distributions. The spatial extent of the oxygen and hydrogen emission are found to be about the same, while the continuum size is clearly larger than that of the line-emitting region, as is seen in figure 3.3. Optically (Koo et al., 1994) this galaxy appears as a single knot, which suggests that the star-forming region is confined to the central part of the galaxy.

4. For object 4, the distributions of the continuum, [OIII]λ5007 and Hα emission are clearly coincident. In HST/WF-1 observations from Koo et al. (1994) a single knot is identified. These two facts suggest that the starburst is in this case widespread.

Of the three error sources discussed in Section 3.2.2 above, none of them can affect the results presented in this section to a large extent. Bad pixels and survivor cosmic rays are rejected from the fit by a rejection algorithm. The read-out noise is taken into account by the constant coefficient of the baseline, and its importance further reduced during the fitting procedure as several columns are to be collapsed (to fit the "continum image" around 1000

columns are co-added, while to fit the emission component, about 6 lines are collapsed). Finally, the parallel charge transfer inefficiency does not affect the conclusions of this section, since the gaussian fits are normalized, and serial charge loss does not affect the measurements performed on the "line image," since this error source is unimportant on scales of a few columns.

In all cases but the last, the spreads of [OIII]λ5007 and Hβ are compared, discarding Hα and [OII]λ3727. This is done this way because [OIII]λ5007 and Hβ are closer to each other in wavelength space and therefore they are affected by a similar extinction. Differences in their spreads can then reveal real differences in their distributions and not just reddening. The observed differences in the spread of Hα and Hβ or [OIII]λ5007 and [OII]λ3727 can be accounted for by a moderate extinction, within the measurement errors. The spread values given in table 3.2 do not take into account the error introduced by the extinction error. This uncertainty makes it impossible to detect unambiguosly any extinction gradient or ionization structure. No differences in the spatial extent of HII and OII or OIII can be established either. In all four cases then, the line-emitting component does not reveal any composition differences. Table 3.2 lists in its last column the ratio of the spread of the corresponding emission line to that of the continuum. The large scatter of values in the relative sizes of nebular emission and the continuum indicates that LCBGs are a very inhomogeneous population.

It should be noted that the "continuum image" is constructed based on the *observed* spectrum (i.e. not dereddened). The real continuum has more power in shorter wavelengths and the actual shape of the normalized continuum will be slightly different. Therefore, although the actual numbers may change, the main results are robust. This is true even if the serial charge loss were important, since it would mimic an increase in the extinction coefficient.

It is also interesting to note that not all starbursts are located in the center of their host galaxies as parametrized by the continuum light distribution (e.g. object 1). Some questions naturally arise, for instance: What mechanisms could trigger such a massive star forming event displaced from the center of the host galaxy?; how does this diversity affect the evolutionary scenarios of these objects?. More data is needed to characterize the frequency of these off-center star forming regions and their effect in the morphological evolution of LCBGs.

ID	Scale. (kpc/″)	Continuum spread. (″)	Line	Line central position. (″)	Line spread (″)	Line/Cont spread ratio.
1	5.68	0.84±0.02	[OII]λ3727	0.15±0.01	0.20±0.02	0.24
		0.84±0.02	Hβ	0.10±0.03	0.37±0.02	0.44
		0.84±0.02	[OIII]λ5007	0.154±0.005	0.298±0.009	0.35
		0.84±0.02	Hα	0.14±0.02	0.46±0.04	0.55
2	5.70	0.56±0.02	[OII]λ3727	-0.03±0.01	0.30±0.02	0.52
		0.56±0.02	Hβ	-0.03±0.02	0.68±0.09	1.20
		0.56±0.02	[OIII]λ5007	-0.016±0.005	0.582±0.009	1.03
		0.56±0.02	Hα	-0.05±0.05	0.6±0.1	1.06
3	4.31	0.59±0.01	Hβ	0.00±0.01	0.211±0.008	0.36
		0.59±0.01	[OIII]λ5007	0.008±0.003	0.241±0.004	0.41
		0.59±0.01	Hα	-0.003±0.005	0.296±0.006	0.50
4	1.76	0.79±0.01	[OIII]λ5007	-0.10±0.03	0.90±0.03	1.14
		0.79±0.01	Hα	0.00±0.01	0.82±0.02	1.04

Table 3.2: Spatial distribution data. "Line central position" means the difference between line and continuum centroids. Positive values indicate that the line emitting component is above the continuum in the spectra shown in figure 3.1. Line/Continuum spread ratio (see text) is given in the last column. All spread and central position values given in arcseconds.

3.3.2 Line Ratios, Reddening and Equivalent Widths.

The observed flux in each emission line has been measured by means of a gaussian fit, using again the STSDAS task *ngaussfit*. This fitting procedure was used instead of summing the flux in the line image directly because of residuals of bad pixels. Observed line surface brightnesses are calculated using the amplitude and Full Width at Half Maximum yielded by *ngaussfit* simply as $1.064 \times \text{Amplitude} \times \text{FWHM}$, which is the expression for the area under a gaussian given its amplitude and Full Width at Half Maximum. Two different positions are considered for each galaxy corresponding to (a) the inner and (b) the outer regions of each object. These two one-dimensional extractions are defined as to encompass approximately the same line luminosity. For position (a), both the central wavelength and FWHM are left as free parameters, but for position (b) the FWHM is fixed to that measured in position (a), in order to increase the goodness of the fit. The physical sizes of the two extractions considered are given in table 3.3. The sum of the two quantities is therefore the total physical size of the observed line emitting region.

[OII]λ3727 can be observed in objects 1 and 2, Hβ and [OIII]λλ 4959, 5007 can be observed in all cases (although see comments to table 3.3), and Hα is observed in objects 2,3 & 4. Hα is detected in object 1 too, but it is affected by several bad pixels that make it unrecoverable. It can be seen in figure 3.2, that the amplitude of Hα is only about twice that

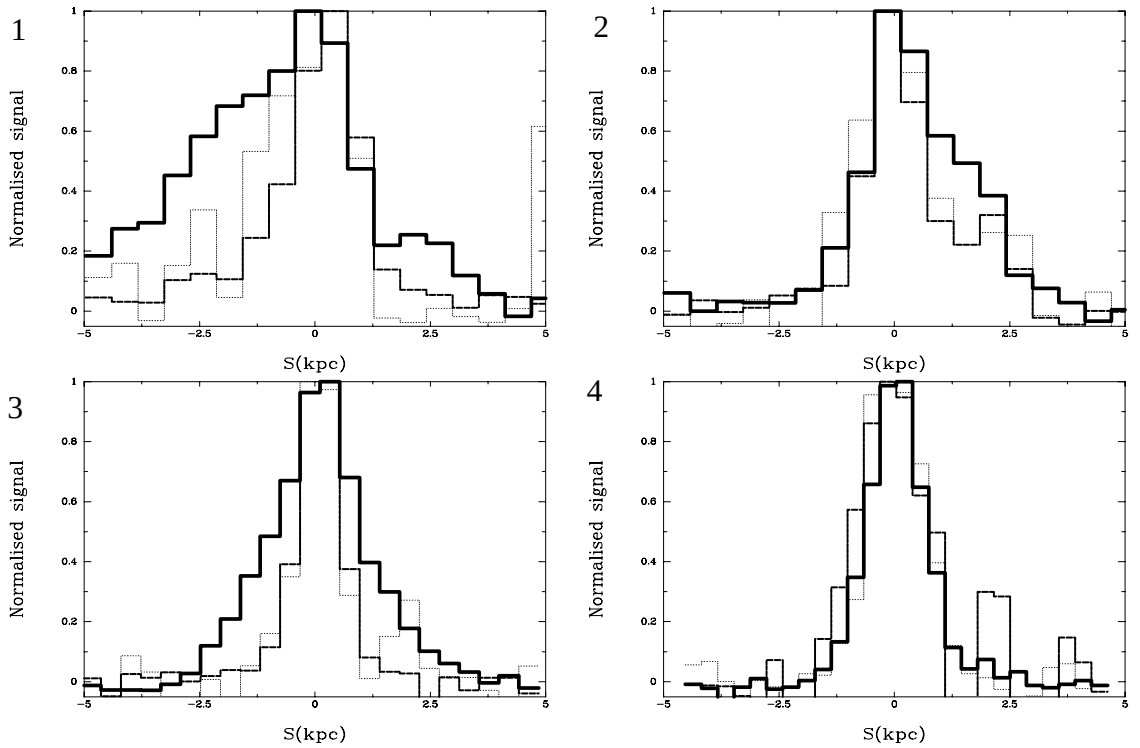

Figure 3.3: Continuum and emission line profiles of the selected objects. In all cases, the S axis is placed with respect to the slits depicted in figure 3.1. Increasing S's correspond to upper positions in that figure for each object. The continuum is the solid, thickest line; [OIII]λ5007 is the thick dashed line and Hβ is the dotted, thin line.

of Hβ, although it should be at least 2.85 times larger. [SII]$\lambda\lambda$6717, 6731 is observed only in the nearest object.

The amount of extinction can be parametrized using the logarithmic extinction coefficient c(Hβ). It is derived using standard nebular analysis techniques (Osterbrock, 1989) using Balmer line ratios. The observed targets are at high Galactic latitude, suffering galactic extinctions $A_B < 0.11$ mag, which corresponds to a c(Hβ)< 0.05 (Burstein & Heiles (1984); Sandage & Tammann (1974)). Therefore, it is assumed that all the extinction occurs within the target objects. Consequently the spectra have been dereddened in the rest frame of the target according to a standard reddening curve (Whitford, 1958), assuming case B recombination theoretical line ratios. The use of different extinction curves would not significantly change the results, since they do not differ from the one used here in the wavelengths of interest.

The logarithmic extinction coefficient is determined independently for the inner and outer regions for objects 2 and 3, but for object 4 due to poor *snr* a global value is adopted. In the case of object 1, for which Hα is unfortunately not well measured a global value of

c(Hβ) = 0.1 $\pm$ 0.05, typical of local HII galaxies is adopted. No underlying stellar hydrogen absortion is detected, as the continuum is very low. The observed extinction coefficients are given in table 3.3. Assuming A_B=4.3×E($B-V$) (see Burstein & Heiles (1984)), the $B-V$color excess ranges from 0 to 0.35.

Line fluxes are then de-reddened using the standard expression.

$$I(\lambda)_{corrected} = I(\lambda)_{obs} \times 10^{c(H\beta)\times(1+f(\lambda))} \tag{3.3}$$

Table 3.3 lists the de-reddened line strengths, along with the measured Hβ equivalent width and the derived extinction coefficient c(Hβ).

ID	1	1	2	2	3	3	4	4
Position.	inner	outer	inner	outer	inner	outer	inner	outer
Size.	1.42	3.41	1.43	2.28	0.86	2.16	0.79	1.23
c(Hβ)	0.10±0.05	0.10±0.05	0±0.1	0.10±0.2	0.4±0.1	0.7±0.2	0.6±0.2	0.6±0.2
$\log W^0_{\mathrm{H}\beta}$	1.68±0.09	1.57±0.07	1.59±0.03	1.51±0.05	1.71±0.04	1.48±0.07	1.55±0.09	1.55±0.09
[OII] λ3727	5±1	4.3±0.8	2±1	2±1	...	...	...	...
H β	2.1±0.5	2.3±0.4	1.4±0.5	1.6±0.7	5±1	6±3	5±3	5±3
[OIII] λ4959	2.6±0.6	2.0±0.5	1.7±0.6	1.0±0.5	4±1	5±3	5±3	5±3
[OIII] λ5007	8±2	6±1	5±1	3±1	13±3	16±7	15±9	15±9
Hα	...	...	4±1	4±1	13±2	17±5	15±6	14±5
[SII] $\lambda\lambda 6717, 6731$	...	...	...	...	...	...	3±1	2±1
log(([OIII]$\lambda\lambda$4959, 5007)/Hβ)	0.7±0.1	0.54±0.08	0.67±0.03	0.44±0.06	0.56±0.03	0.55±0.07	0.6±0.1	0.61±0.09
log([OIII]/[OII])	0.28±0.09	0.26±0.07	0.43±0.06	0.33±0.09	0.3±0.1	0.1±0.1	0.2±0.1	0.2±0.1
$\log R_{23}$	0.89±0.08	0.73±0.06	0.80±0.03	0.61±0.05	0.72±0.04	0.79±0.07	0.8±0.1	0.8±0.1
$(12+\log(\mathrm{O/H}))_{\mathrm{low}}$	8.1±0.2	7.8±0.2	7.8±0.2	7.6±0.2	8.4±0.2	8.4±0.2	8.3±0.2	8.3±0.2
$(12+\log(\mathrm{O/H}))_{\mathrm{high}}$	8.2±0.2	8.5±0.2	8.4±0.2	8.7±0.2	8.5±0.2	8.5±0.2	8.6±0.2	8.6±0.2
STIS [NII]λ6584/Hα upper limit.	...	...	0.38	0.38	0. 18	0.18	0.21	0.21
HIRES [NII]λ6584/Hα actual value.	...	...	...	...	0. 15	0.15	0.18	0.18

Table 3.3: Absorption coefficients, $\mathrm{W}_{H\beta}$ and de-reddened Line Strengths/Ratios. Hβ equivalent width is given in Å . Flux units are 10^{-16}erg s^{-1} cm^{-2}. Fluxes are apparent fluxes. R_{23} is defined as the reddening-corrected ratio ([OII]λ3727+[OIII]$\lambda, \lambda 4959, 5007$)/H$\beta$. In the second row the physical sizes of each aperture in linear kpc are given. For object 1, Hα is not observed and the listed value for the logarithmic extinction coefficient is an *assumed* value, typical for local HII galaxies. For object 4, Hβ and [OIII]λ4959 are only measured for the integrated spectra, because of several bad pixels that make unfeasible to measure them on a per position basis. For this object, the given values for c(Hβ) and $\log W^0(\mathrm{H}\beta)$ correspond to the integrated spectra and the listed de-reddened fluxes for the measured emission lines are just one half of the values measured in the integrated spectrum. This table also includes the upper and lower limits to the metallicity, as defined in the text, as well as the HIRES nitrogen measurements and the upper limits to the [NII]λ6584/Hα ratio than can be set from the STIS spectra.

Line ratios are then calculated according to:

$$\left(\frac{I_1}{I_2}\right)_{corr} = \frac{I_{1,obs} \times (1 + (\Delta I_{2,obs}/I_{2,obs})^2)}{I_{2,obs}} \times 10^{c(H\beta)\times[f(\lambda_1)-f(\lambda_2)]} \tag{3.4}$$

The rationale behind the factor $(1+(\Delta I_{2,obs}/I_{2,obs})^2)$ is explained in the appendix, whereas the factor $10^{c(H\beta)\times(f(\lambda_1)-f(\lambda_2))}$ is used to de-redden the line ratio. For SA68-6134 and H1-13385, [OII]λ 3727 is not observed. Based on the fact that a relation seems to exist between ionization parameter and equivalent width of Hβ for local HII galaxies (Díaz, 1999) the following expression, which represents a linear fit for a sample of HII galaxies was used to estimate [OII]λ3727.

$$\log \frac{[\mathrm{OIII}]}{[\mathrm{OII}]} = (0.877 \pm 0.042) \times \log W_{H\beta} - 1.155 \pm 0.078 \tag{3.5}$$

The *rms* in the fit is indicated by the given errors.

Table 3.3 lists the de-reddened line ratios. Line ratios are less affected by uncertainities in the determination of c(Hβ) than line strengths are.

In principle, oxygen abundances can be estimated from the intensities of the optical emission lines using the R_{23} number, defined as the reddening-corrected ratio ([OII]λ3727+[OIII]λ, λ4959, 5007)/Hβ. (Pagel et al., 1979). The main problem with this empirical method is that the calibration is double-valued, and some *a priori* knowledge of the metallicity range is needed in order to solve this degeneracy. Unfortunately, due to the poor *signal-to-noise* ratio, no reliable metallicity determinations can be derived for the LCBGs presented here. However, the ionization ratio log([OIII]/[OII]) and R_{23} values given in table 3.3 allow to draw some very general conclusions. First of all, both extremely low (below $12 + \log(\mathrm{O/H}) = 7.6$) and oversolar ($12 + \log(\mathrm{O/H}) \geq 8.7$) abundances can be ruled out. Also, since it would be very unlikely that the inner and outer parts of the line emitting region fell in different branches of the $R_{23} - 12 + \log(\mathrm{O/H})$ calibration, strong spatial variations of the metal content can be ruled out too.

Equivalent widths are calculated from *ngaussfit* results as:

$$W = \frac{I(1 + (\Delta C/C)^2)}{(1+z) \times C} \tag{3.6}$$

where C is the baseline value at the central wavelength of the corresponding emission line, and the factor $1 + z$ transforms the equivalent width to rest-frame. The $(1 + (\Delta C/C)^2)$ is

used for the same reason as in the line ratios case, and is explained in the appendix.

The most important source of error in the derived line strengths for these data is the uncertainty in the determination of c(Hβ). The main systematic error that may affect the extinction coefficient is the serial charge transfer inefficiency, that may increase its value. However the measurement of a zero extinction coefficient in zone (a) of object 2, together with the comparison of the c(Hβ) value with that reported by Kobulnicky & Zaritsky (1999) for the same object using LRIS on the W.M. Keck telescope, suggests that this serial loss is not very important, and would, in any case, introduce an increase in the extinction coefficient less than 0.1. Line ratios and equivalent widths are much less affected than line strengths by this uncertainity.

On the other hand, parallel losses may introduce a systematic decrease of around 15% in the observed line strengths, as previously noted. The values quoted in table 3.3 are not corrected for this systematic error, and should therefore be regarded as lower limits to the true values.

The statistical error budget is again dominated by the read-out noise, which is the most important per pixel statistical uncertainity source for the data. The poisson photon noise is only important for the brightest lines such as [OIII]λ5007 and Hα. Outliers such as bad pixels and cosmic rays are excluded from the fit by *ngaussfit* rejection algorithm. The error estimates provided by this task are considered as 1σ error bars.

3.3.3 Empirical Oxygen Abundances.

The spectrum from a star forming region depends strongly on the electron temperature and metallicity of the nebula. The ratio of the auroral line [OIII]λ4363 to the lower excitation lines [OIII]$\lambda\lambda 4959, 5007$ gives a direct determination of the electron temperature where O^+ and O^{++} are the dominant species, but beyond certain metallicities, the increasing cooling leaves no energy to collisionally excite the upper levels. When this is the case, one must resort to determine the oxygen abundance empirically.

In principle, oxygen abundances can be determined from the intensities of the optical emission lines using the R_{23} number, defined as the reddening-corrected ratio ([OII]λ3727+[OIII]$\lambda, \lambda 4959, 5007$)/H$\beta$. This method developed originally by Pagel et al. 1979 (see also Pagel, Edmunds, & Smith (1980), Edmunds & Pagel (1984), McGaugh (1991), Kewley & Dopita (2002) and references therein). The main problem with this empirical method is that the calibration is two-folded, and some *a priori* knowledge of the metallicity range is needed in order to solve this degen-

eracy. One initial estimate can be provided by the ratio [NII]λ6584/Hα.

Since [NII]λ6584 can not be observed, as it is completely blended with Hα due to low dispersion, the only available information is the 3σ upper limit. These upper limits, together with actual values derived from observations with the W.M. Keck Telescope (HIRES) for objects 3 and 4 (Guzmán et al., 1996) are listed in table 3.3.

For objects 3 and 4, the HIRES values are compatible with the STIS non-detection, yet they are large when compared with typical values found in local HII galaxies ($\log($[NII]λ6584 / H$\alpha) \simeq 0.03$), (Denicoló, Terlevich, & Terlevich, 2002)) and by themselves constrain the oxygen abundance to the high metallicity branch of the R_{23}-12+log(O/H) calibration ($12+\log(O/H) \geq 8.00$). Using the calibration given by Denicoló, Terlevich, & Terlevich (2002), oxygen abundances (12+log(O/H)) of 8.5 and 8.6 are found for objects 3 and 4, with an uncertainty of about 0.2 dex. [OII] is not observed in these objects, but the calibration of [OIII]/Hβ (Pagel, Edmunds, & Smith, 1980) can provide a lower limit to the oxygen abundance as: $12 + \log(O/H) > 8.4 \pm 0.2$. The metallicity values obtained using the Denicoló, Terlevich, & Terlevich (2002) calibration are called $((12+\log(O/H))_{high})$, and the lower limits derived following Pagel, Edmunds, & Smith (1980) are referred to as $((12+\log(O/H))_{low})$. Table 3.3 gathers these values.

For objects 1[4] and 2 the 3σ upper limits for [NII]λ6584 are rather high and by themselves do not provide useful constraints to the oxygen abundance. In these cases, however, there are observations of [OII] and we can constrain the value of 12+log(O/H) from R_{23} taking into account the degree of ionization. Using the method developed by Pyliugin for HII regions in the lower and upper branch (Pilyugin, 2000, 2001) we get $8.07 \pm 0.20 \leq 12+\log(O/H) \leq 8.22 \pm 0.20$ for the core (extraction (a)) of object 1 and $7.85 \pm 0.20 \leq 12+\log(O/H) \leq 8.42 \pm 0.20$ for the core of object 2. The metallicity values derived using the upper branch of the R_{23}-12+log(O/H) are called $(12+\log(O/H))_{high}$ and those derived using the lower branch $(12+\log(O/H))_{low}$. They are shown in table 3.3, together with the metallicities of objects 3 and 4[5].

To summarize, different determinations of the metallicity have been presented which yield lower and upper limits to the oxygen abundance. In broad terms, the metallicity is bounded between 7.6 and 8.7. This implies that these objects do not rank among the most metal poor objects known such as IZw18. In fact, although undersolar metallicities can not be

[4] If we assume that its Hα luminosity is roughly equal to that of object 2, similar limits on [NII]λ6584 can be set.

[5] It should be recalled that the extinction coefficient used for object 1 is only an *assumed* estimate. An increase of the extinction by an order of magnitude would translate into a decrease of the oxygen abundance by 0.2 dex.

entirely ruled-out, two of the observed objects show [NII]λ6584/Hα ratios that point to oxygen abundances comparable to solar (12+log(O/H)= 8.69; Allende Prieto, Lambert, & Asplund (2001)). Upper limits for the detection of [NII] line in the other two objects leave room for even larger [NII]λ6584/Hα. Obviously, larger samples are clearly needed to find out whether LCBGs are at the high metallicity end of the distribution for HII galaxies or not. Most interestingly, the metallicity estimates for the four LCBGs presented here derived from either branch of the R_{23} calibration are in very good agreement with the observed distribution of metallicities characteristic of the Lyman-break galaxy population at $z > 2$ (Pettini et al., 2001). Like many local HII galaxies, both Lyman-break galaxies at high-redshift and LCBGs at intermediate redshifts are overluminous for their metallicity, as it is seen in Hoyos et al. (2005).

It is somewhat unfortunate that the metallicities of these objects cannot be determined to a higher degree of accuracy due to low *snr*. With the results above the *past* star formation history of these objects remains open, and it can not be firmly established the existence of a oxygen abundance variation between the inner and outer regions of the galaxies under study.

3.3.4 Star Formation Rate and Structural Parameters of Star Forming Regions.

Table 3.4 contains the star formation rate, the star formation rate per unit area and the half-light radii of both the galaxy and the line-emitting region for our four objects.

The main aim of this study is to investigate the nature of LCBGs. In this section, the intermediate-z sample this chapter deals with is compared to two samples of local vigorously star forming systems. The first sample is made of 39 local HII galaxies from the Telles, Melnick, & Terlevich (1997) sample. These galaxies are among the brightest ones in the SCHG (Spectrophotometric Catalogue of HII galaxies) (Terlevich et al., 1991), with equivalent widths between 30Å and 280 Å . This sample is made of HII galaxies of different morphologies. The velocity dispersions range from 20 km s^{-1} to 130 km s^{-1} although with a preference for the lower values. The other sample consists on 25 starburst galaxies from the Lehnert & Heckman (1996) sample. The galaxies from this latter sample are edge-on (with axial ratios[6] a/b greater than 2), IR warm ($S_{60\mu m}/S_{100\mu m} > 0.4$) and infrared bright ($S_{60\mu m} > 5.4$ Jy). The infrared luminosity of this sample ranges from 10^{10} to $10^{12} L_{\odot}$. This

[6] a is the length of the major axis and b is the length of the minor axis

sample consists on a mixture of various disk galaxy types, spirals (Sa to Sd), lenticulars and irregulars. The rotation speeds range from around 120 km s^{-1} to approximately 300 km s^{-1}. The first local sample was chosen for comparison purposes since HII galaxies are known to show conspicuous and galaxy-wide emission line spectra. They are quite similar to the LCBGs presented here in this regards, as suggested by Koo et al. (1994) and Guzmán et al. (1997). Furthermore, their velocity dispersions and small radii imply that they should be about as massive as the galaxies analyzed here. They are also known to harbor violent star forming systems, like intermediate-z LCBGs. The second local sample was selected because these starburst galaxies also host powerful and galaxy-wide star forming complexes, although they are much larger systems. These starburst galaxies are not only bigger, but their rotation speeds are greater than typical velocity dispersions of HII galaxies or LCBGs at intermediate z. These systems are likely to be more massive and their global star formation rate should be higher, accordingly.

Calculated Hβ luminosities lie in the range 0.2×10^{41}ergs s^{-1} to 2.7×10^{41}ergs s^{-1}. These luminosities are in the high luminosity tail of the distribution for normal spiral galaxies (Kennicutt, 1983) and HII galaxies (Hoyos & Díaz, 2006).

The star formation rates were calculated from the Hα luminosity as in Kennicutt, Tamblyn, & Congdon (1994), valid for $T_e = 10^4 K$ and case B recombination (all the ionizing photons are processed by the nebular gas). We used their equation:

$$SFR(M_\odot yr^{-1}) = 7.9 \times 10^{-42} L_{H\alpha}(erg\ s^{-1}) \tag{3.7}$$

The calculated star formation rates are in the range from 0.7 to 8 $M_\odot \mathrm{yr}^{-1}$, indicating that the star forming regions are very strong. For comparison, 30 Dor SFR is 0.1 $M_\odot \mathrm{yr}^{-1}$, as derived from its Hα luminosity (Schaerer, 2002). The measured rest-frame Hβ equivalent widths are between 30 Å and 50 Å, within the observed range for local HII galaxies, indicating either that the observed burst cannot be very young or that a substantial underlying stellar population is present.

A most interesting quantity is the star formation rate per kpc^2, the areal star formation rate. This is directly proportional to the Hα surface brightness, after correcting for cosmological dimming.

For the galaxies studied in this chapter and for the Lehnert & Heckman (1996) sample,

ID	Pos	SFR ($M_\odot yr^{-1}$)	SFR_A ($M_\odot yr^{-1} kpc^{-2}$)	D_{eff} (kpc)	D_0 (kpc)	$\log M/M_\odot$.
1	inner	3.2±0.7	2.1±0.3	5.4	1.42	9.8
	outer	3.6±0.7	...	...	...	...
2	inner	2.2±0.7	1.5±0.4	4.2	1.43	9.7
	outer	2.5±1.0	...	...	...	...
3	inner	2.6±0.6	5.0±2.0	2.0	0.86	9.3
	outer	3.3±1.7	...	...	...	...
4	inner	0.25±0.10	0.5±0.1	1.4	.79	9.6
	outer	0.24±0.09	...	...	...	...

Table 3.4: Star formation parameters, effective diameters *of the line-emitting regions*, effective diameters and virial mass estimates for the observed galaxies. The effective diameter of the line-emitting region given here is the size of the (a) aperture defined previously. It is equivalent to the half-light radius of a bidimensional gaussian luminosity distribution of the same Full Width at Half Maximum. Since the areal star formation, half-light radii and mass are properties of the galaxy as a whole, they are listed only once for each galaxy. The results presented here are mainly affected by the parallel losses of the STIS/CCD, and may be underestimating the real values by around 15%. Statistical errors are again dominated by the CCD's read-out noise.

the expression used is:

$$\mathrm{SFR_A}\left(\frac{M_\odot \mathrm{yr}^{-1}}{\mathrm{kpc}^2}\right) = \frac{2 \times 7.9 \times 10^{-42} L_{H\alpha}}{\pi D_0^2} \tag{3.8}$$

where $L_{H\alpha}$ is the reddening corrected Hα luminosity (in ergs s^{-1}), and D_0^2 is the half-light diameter of the line-emitting region (in kpc). For the LCBGs presented here, D_0 is defined as the size of the central extraction (a), defined previously. Since it contains 50% of the line luminosity from the starburst it can be considered as the half light radius of the line emitting region. In the case of the starburst galaxies from the Lehnert & Heckman (1996) sample, D_0 is the line-emitting region effective diameter, as measured in narrow band Hα+[NII] images, which trace the size and luminosity of the starburst. In order to derive the Hα luminosity for this sample from the values listed in Lehnert & Heckman (1996) it is needed to correct for internal extinction and for [NII]λ6584 contamination. A simple statistical approach was adopted such that $L_{H\alpha\,\mathrm{corr}} = 1.56 \times L_{H\alpha\,listed}$.[7]

The areal star formation rate for the Telles, Melnick, & Terlevich (1997) sample is calculated as:

[7] This is just the average value of the number $10^{0.63 \times c(H\beta)}/(1+[\mathrm{NII}]\lambda6584/\mathrm{H}\alpha)$ when the extinction varies from 0.2 to 0.6 and the nitrogen to hydrogen ratio varies from 0.01 to 0.32.

$$\mathrm{SFR_A}\left(\frac{M_\odot \mathrm{yr}^{-1}}{\mathrm{kpc}^2}\right) = \frac{7.271 \times 10^{c(H\beta)} \times F_{H\beta} \times (1+z)^4}{D_0^2} \tag{3.9}$$

where D_0 is the line-emitting region effective diameter (in arcseconds), as observed in the V band. $F_{H\beta}$ is the *observed* Hβ flux, while the other factors take care of the cosmological dimming and internal reddening. The burst half-light radius given in Telles, Melnick, & Terlevich (1997) are FWHM of the circular brightness profiles centered on the peak intensity of the burst region of the galaxy, after correcting for seeing effects.

In order to compare the properties of the star forming regions in LCBGs with those of the local samples of star forming systems, two plots are presented. Figure 3.4 shows the Hα luminosity plotted versus the *burst* half light diameter.

Figure 3.5 shows the ratio between the *galaxy* half light diameter and the *line-emitting* region half light diameter (D_{eff}/D_0) for the galaxies from Telles, Melnick, & Terlevich (1997), Lehnert & Heckman (1996) and for the intermediate-z galaxies against the areal star formation rate SFR_A.

From figures 3.4 and 3.5 it is seen that the intermediate-z galaxies presented here are very similar to the galaxies from the sample of bright local HII galaxies. The star forming region size scales with the host galaxy size in a similar fashion in LCBGs and in their local counterparts of similar areal star formation rate. This indicates similar morphological properties between HII galaxies and LCBGs. The Hα luminosity of intermediate-z LCBGs is similar to the Hα luminosity of bright local HII galaxies with similar line-emitting region sizes. The starburst galaxies from the Lehnert & Heckman (1996) sample have a much lower areal star formation rate. Despite having star forming regions around 6 times larger on average, their star formation rates do not exceed the observed rates in the intermediate-z objects or bright local HII galaxies. This happens even though the fraction of the host galaxy occupied by the burst is three times larger in starburst galaxies than in LCBGs or HII galaxies.

Figure 3.4 also shows two well known examples of violent star formation in the nearby universe. NGC7714, (González-Delgado et al., 1995), is a starburst galaxy classified as SBb peculiar by de Vaucouleurs et al. (1991). It is in interaction with NGC7715. Most of the galaxy is undergoing a major starburst, which is unusually active in the nucleus, where the star formation rate per unit area is very high. 30 Doradus is a large star forming region in the Large Magellanic Cloud. It is the nearest example in which violent star formation can be studied in detail (Schaerer, 2002). Figure 3.4 shows the star forming regions of LCBGs

are all larger than both the circunnuclear star forming region in NGC7714 and 30Doradus. The Hα luminosity of the line emitting region of LCBGs varies from 3 to 50 times that of 30 Doradus. Three out of four have Hα luminosities similar to the central region of NGC7714. We conclude that the star forming regions found in LCBGs, although extreme, are not rare in the local universe, since they are found not only in the brightest HII galaxies, but in other vigorously star forming systems as well.

Another very useful parameter to study the nature of distant, young galaxies is mass, since mass is much less dependent on evolution than luminosity or colors. Galaxies of the same mass can be compared independently of the evolutionary stage of their stellar populations.

Mass estimates are obtained via the virial theorem, using the half-light radius and velocity width as measures of galaxy size and gravitational potential respectively[8].

$$\log M/M_{\odot} = 6.08 + \log R_e(\mathrm{kpc}) + 2 \times \log \sigma(\mathrm{km\,s^{-1}}) \tag{3.10}$$

For the LCBGs analyzed here, the half light radii are given in Koo et al. (1994) and Guzmán et al. (1998). The velocity dispersions are taken from Guzmán et al. (1996) and Koo et al. (1995). For the HII galaxies sample, both the effective radius and the velocity dispersion are given in Telles, Melnick, & Terlevich (1997). For starburst galaxies from the Lehnert & Heckman (1996) sample, the velocity dispersion is set to 0.7 times the rotation speed, following Phillips et al. (1997), and inclination effects are partially corrected for by multiplying the rotation speed by $\sqrt{1-(a/b)^{-2}}$[9]. This correction assumes all these galaxies are circular and flat in shape.

Figure 3.6 shows the virial mass estimates plotted against the areal star formation rate. In this diagram LCBGs also fall among the brightest, more massive HII galaxies. It is also seen that intermediate-z LCBGs present a much higher areal star formation rate than local starburst galaxies of similar mass. On the other hand, LCBGs tend to have masses consistent with the low-mass end distribution of the Lehnert & Heckman (1996) sample. Even if local starburst galaxies have larger star forming regions (as is shown in figure 3.4) and are much more massive, their areal star formation rate does not rival that of LCBGs and bright HII galaxies. We conclude that the properties of star forming regions in LCBGs at intermediate

[8]The expression used originates from $M = 3kG^{-1}R_e\sigma^2$, where the structural constant k varies with different galaxy surface density profiles. Since the surface brightness profile of LCBGs is consistent with an exponential law (Koo et al., 1994), we adopt $k = 1.7$, following Bender, Burstein, & Faber (1992)

[9]In this expression, (a/b) is the axial ratio.

redshift are very similar to those found in the local universe in very bright and massive HII galaxies like Tol0440-381 or starburst galaxies like NGC1808 with similar star formation properties.

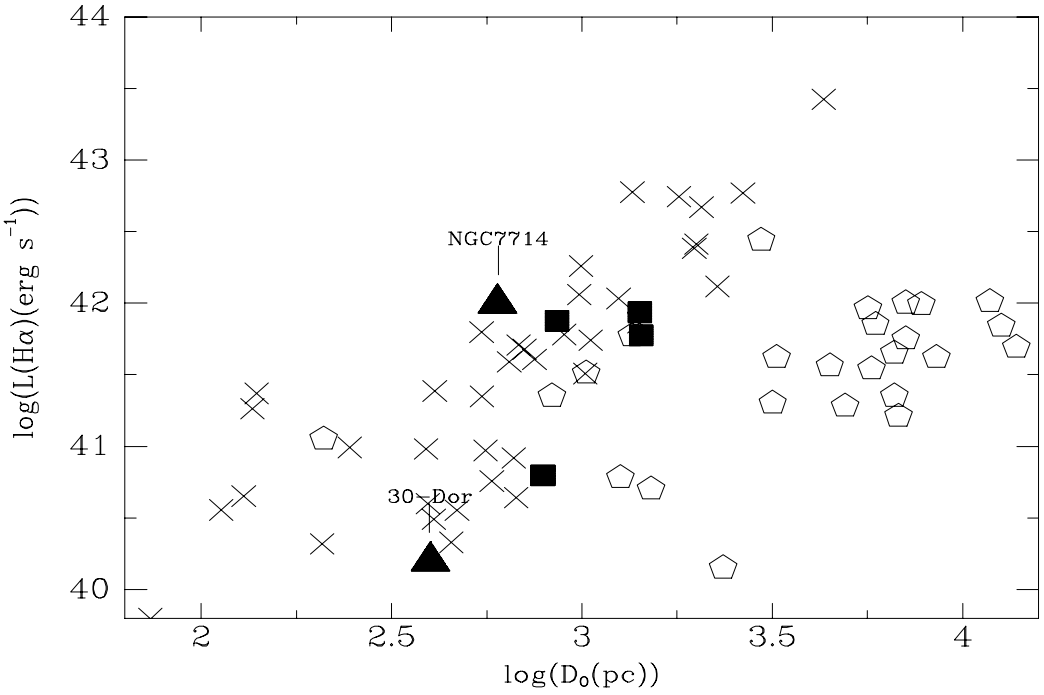

Figure 3.4: Star forming region size-H_αLuminosity relationship. (Crosses):Local HII sample. (Black squares):Intermediate z LCBGs. (Black Triangles):30 Dor nebula and circunnuclear HII region in NGC7714 (from the data of González-Delgado et al. (1995) and Schaerer (2002)). (White Pentagons): Local starburst galaxies sample (Lehnert & Heckman, 1996). D_0 is the *burst* half light diameter for the Telles, Melnick, & Terlevich (1997) and Lehnert & Heckman (1996) samples and the diameter of the inner aperture for the LCBG sample.

3.3.5 Galactic Superwinds.

As explained by Chevalier & Clegg (1985), a superwind is originated by the kinetic and thermal energy provided by supernovae and winds from massive stars, mainly Wolf-Rayet stars. When flows from masive stars and supernovae intersect within the gaseous component of the galaxy, the kinetic energy is converted very efficiently into thermal energy because of the high resulting temperature and low density. The combined effect creates a region of very hot, ($\sim 10^8 K$), X-ray emitting gas, with a pressure greater than that of the ambient ISM. This gas then expands, sweeping ambient gas and entering a radiative phase, which occurs when the cooling time scale of the ambient material being pushed and shocked becomes

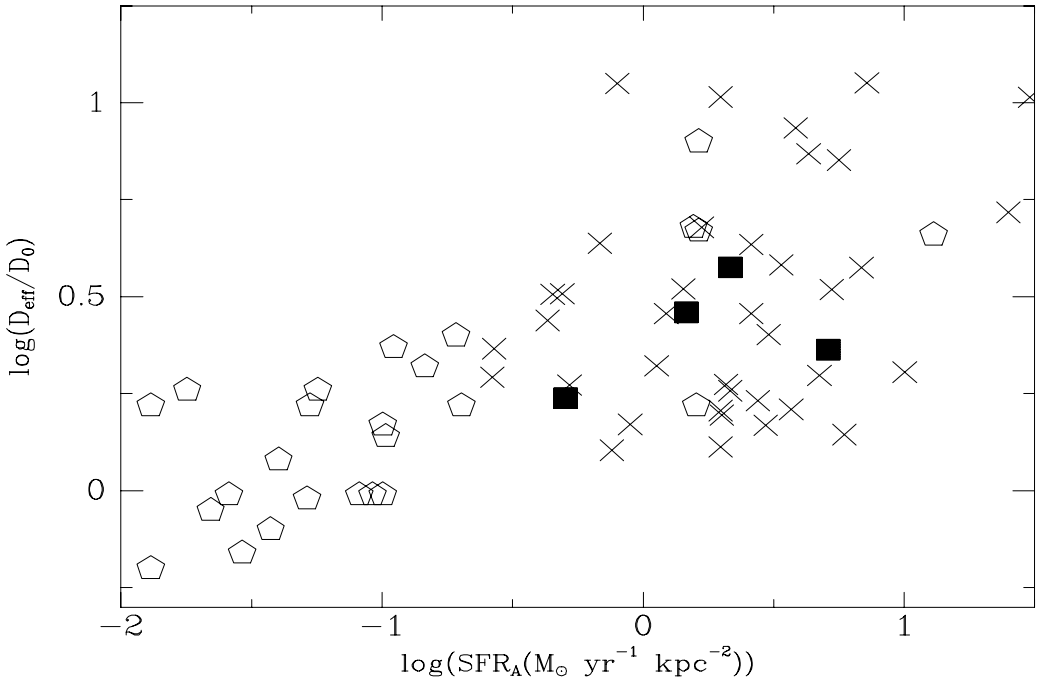

Figure 3.5: Galaxy size-to-burst size ratio *vs* SFR_A. Symbols as in 3.4.

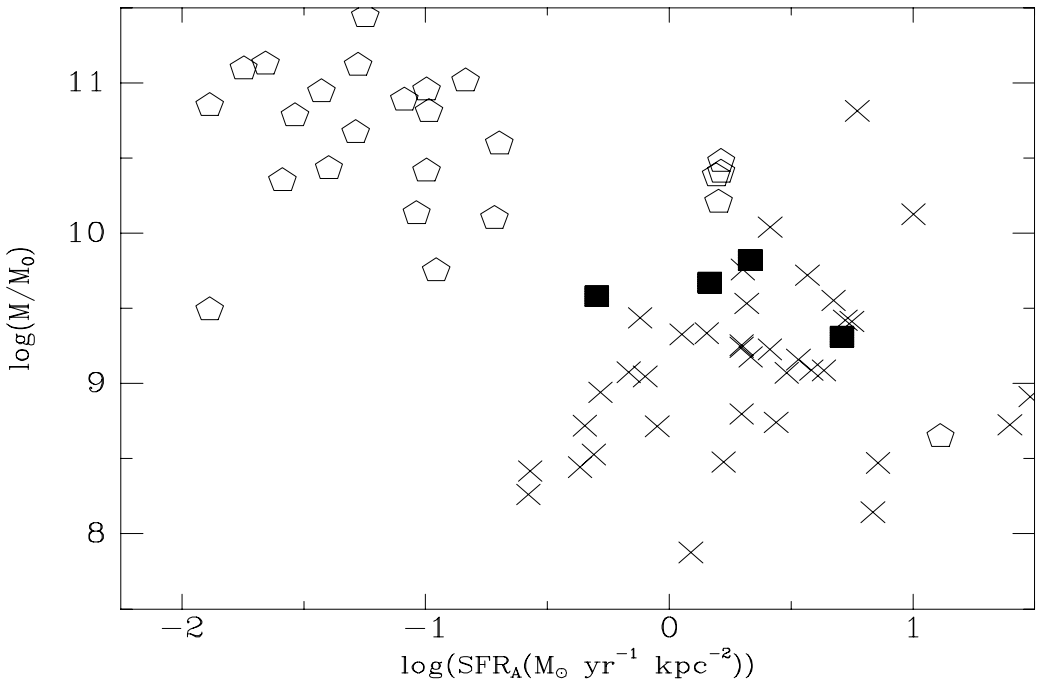

Figure 3.6: Mass-Areal Star Formation Rate relationship. Symbols as in 3.4.

shorter than the time scale for the wind expansion.

Galactic superwinds are a very interesting phenomenon in star forming galaxies (see Schaerer (2002)). The case of M82 is the best known example of a starburst galaxy with superwinds (Clegg & Chevalier, 1985). The gas removal caused by this mechanism is likely to be a very important factor that will affect the final state of low mass galaxies. The effect could in fact reduce the galactic mass by a factor of 0.5 (Vader, 1986), although the final answer depends critically on the geometry and multiphase nature of the ISM.

If the gravitational well of the host galaxy is not very steep and there are superwinds, this gas will expand and might escape from the galaxy. This superwind will carry with it metals to enrich the intergalactic medium. Because of their origin, superwinds can only take place where the rate of supernova events per unit volume is high enough, so that supernovae ejecta and stellar winds from evolved massive stars can collide. The key parameter is then the areal star formation rate. According to Heckman (2002) and Kennicutt (1998), if this quantity is greater than 0.1 $M_{\odot}yr^{-1}kpc^{-2}$ then superwinds will take place, whereas if the SFR_A does not reach this value the superwinds will not make its way out of the galaxy. However, this is not the only relevant parameter to decide whether or not the supernova ejecta will be able to escape from the galaxy. If there exists a very large or dense ambient HI or H_2 cloud surrounding the galaxy, or the geometry is not the appropriate, the material expelled from the supernoave and massive stars may not be able to escape from the galaxy. For these reasons, very few clear-cut cases for superwinds have been detected until now.

From figure 3.5, it can be seen that all four galaxies in the intermediate-z sample match the areal star formation rate criterion implying that superwinds might indeed be present in these systems.

The hot, X-ray emitting region made of the thermalized ejecta from the starburst pushes and shocks *ambient* interstellar gas around the star cluster. Such *ambient* gas will then emit a line spectrum with a distinct spectroscopic signature. The [OII]λ3727 line is stronger that [OIII]λ5007 (Baldwin, Phillips, & Terlevich, 1981). This can be used as another tool to probe the existence of superwinds.

In (Baldwin, Phillips, & Terlevich, 1981), the average excitation excess is defined as:

$$< \Delta E >= \frac{0.191 + \log(I_{5007}/I_{H\beta}) + \log(0.32 + x) + \frac{5\times(\log(I_{6584}/I_{H\alpha}) - \log(x/(1.93+x))) + 2\times\log(I_{6300}/I_{H\alpha})}{10}}{3} \tag{3.11}$$

where x is the reddening corrected I_{3727}/I_{5007} line ratio. The excitatation excess, together with the reddening corrected I_{3727}/I_{5007} ratio allows to discriminate, to first order, between the different excitation mechanisms in line-emitting regions.

Since no data for [NII]λ6584 or [OI]λ6300 is measurable from the spectra analysed in this chapter, it is only possible to set upper limits to the excitation excesses of each of the two zones in which the presented galaxies have been divided. Figure 3.7 shows such limits to the position of the sample presented here in the excitation diagram of (Baldwin, Phillips, & Terlevich, 1981). The real values of $< \Delta E >$ is lower than the values shown, then. It can be seen that all the objects lie on the HII region zone of the diagram. Therefore, for the objects studied in this chapter, a large fraction of the emission spectra is bound to come from a photoionized region rather than from a shock-heated region. Although this supports the idea that shock heating is not the prime excitation mechanism for the ionized gas phase of these objects, it does not imply that no gas is leaving the galaxy. It may well be the case that a small fraction of gas, not enough to be regarded as a proper superwind or change the observed line ratios to a great extent, is indeed shock-heated and is escaping the galaxy.

To sum up, although superwinds should probably be present in these galaxies according to their high areal star formation rates (see figure 3.5), since no *direct* evidence for SN-driven winds has been found by examining the calculated excitation excesses (figure 3.7), there may be something preventing the winds from happening. This might indicate that the *ambient* gaseous medium surrounding these objects is very dense. This surrounding component may be effectively locking the nebular material within the gravitational well of the galaxy, allowing the ignition of several bursts, separated by quiescent periods making the metallicity of the galaxy increase with time. It might be the case too, that the mass of these systems is high enough to keep the ejected material within the gravitational well of the galaxy.

3.4 Summary.

We have used spatially resolved STIS long-slit spectroscopy to investigate the nature of four LCBGs at intermediate z. In particular we have shown that the distributions of the continuum and emission lines along the spatial direction indicate that the starburst usually occupies more than 50 % of the continuum emitting region. The star forming regions in LCBGs have very

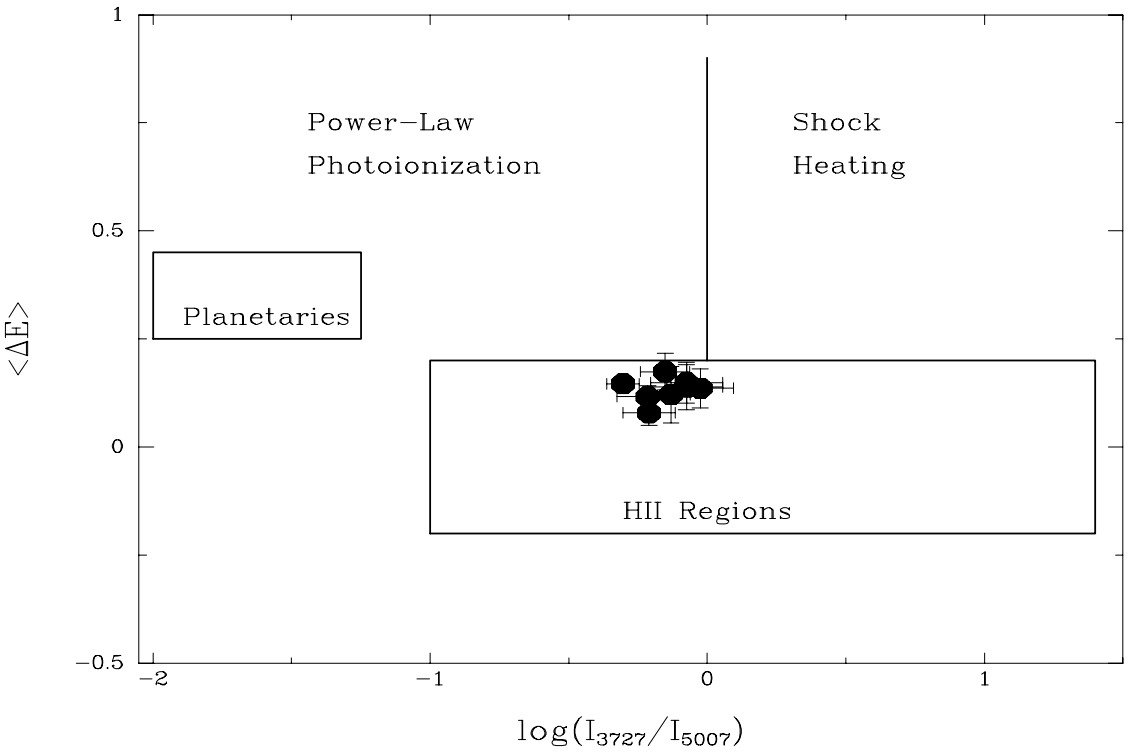

Figure 3.7: Baldwin, Phillips, & Terlevich (1981) excitation diagram for the observed LCBGs. The upper limit to the average excitation excess is plotted as a function of the reddening-corrected $\log I_{3727}/I_{5007}$ number. The eight points presented correspond to the two zones in which the four LCBGs presented in this chapter were divided. The plot clearly shows that the majority of the ionized gas within the observed LCBGs is photoionized.

similar properties to the star forming regions of high luminosity HII galaxies. It has also been found that the LCBGs at intermediate z presented do not show unusually high star formation rates per unit area, although they are more massive than the average HII galaxy of similar star formation rate per unit area. Finally, even though superwinds should exist these galaxies according to their high areal star formation rates, no conclusive evidence for superwinds has been found.

Appendix 1.

Quotients between low-*snr* random variables.

It is possible to derive an approximate expresion useful to calculate ratios between two quantities when the snr of the denominator is very low.

Let a,b be two random variables, and let c be their quotient.

The mean value of c is.

$$\bar{c} = \int \frac{a}{b} \times f(a,b) da db \tag{3.12}$$

where $f(a,b)$ is the joint probability density.

If the random variables a and b are independent, this can be expressed as:

$$\bar{c} = \bar{a} \times \int \frac{1}{b} \times f_b(b) db \tag{3.13}$$

in which $f_b(b)$ is the probability density of b.

If a Taylor polynomial is fit to $1/b$ around $\bar{b}$, the following expression can be written.

$$\bar{c} = \frac{\bar{a}}{\bar{b}} \times \int (1 - \frac{\delta b}{\bar{b}} + \frac{\delta b^2}{\bar{b}^2} - \frac{\delta b^3}{\bar{b}^3} + \frac{\delta b^4}{\bar{b}^4} - ...) \times f_b(\delta b) d\delta b \tag{3.14}$$

In the previous integral, the cofficient linear in $1/\bar{b}$ vanishes by definition of $\bar{b}$, and it will converge or not depending upon the analytical properties of f_b, but even if the series turns out to be asymptotic and eventually diverges it can be used to approximate the integral provided that only a few series terms are added. With this in mind, and from the fact that there is no easy way to estimate the skewness of the error distributions in the data only the first non zero term is used, yielding

$$\bar{c} = \frac{\bar{a}}{\bar{b}} \times (1 + \frac{\sigma_b^2}{\bar{b}^2}) \tag{3.15}$$

Which is the expression used.

Bibliography

Allende Prieto C., Lambert D. L., Asplund M., 2001, ApJ, 556, L63

Baldwin J. A., Phillips M. M., Terlevich R., 1981, PASP, 93, 5

Balzano V. A., 1983, ApJ, 268, 602

Bender R., Burstein D., Faber S. M., 1992, ApJ, 399, 462

Bershady M.A., et al. (in prep)

Burstein D., Heiles C., 1984, ApJS, 54, 33

Chevalier R. A., Clegg A. W., 1985, Natur, 317, 44

Clegg A. W., Chevalier R. A., 1985, BAAS, 17, 587

Cowie L. L., Songaila A., Hu E. M., 1991, Natur, 354, 460

Denicoló G., Terlevich R., Terlevich E., 2002, MNRAS, 330, 69

Díaz A.I., 1999, APSS , 263, 143

Edmunds M. G., Pagel B. E. J., 1984, MNRAS, 211, 507

González-Delgado R. M., Perez E., Diaz A. I., Garcia-Vargas M. L., Terlevich E., Vilchez J. M., 1995, ApJ, 439, 604

Guzmán R., Jangren A., Koo D. C., Bershady M. A., Simard L., 1998, ApJ, 495, L13

Guzmán R., Gallego J., Koo D. C., Phillips A. C., Lowenthal J. D., Faber S. M., Illingworth G. D., Vogt N. P., 1997, ApJ, 489, 559

Guzmán R., Koo D. C., Faber S. M., Illingworth G. D., Takamiya M., Kron R. G., Bershady M. A., 1996, ApJ, 460, L5

Heckman T. M., 2002, ASPC, 254, 292

Hoyos C., Master Thesis., 2002, Universidad Autónoma de Madrid, Spain.

Hoyos C., Díaz A. I., 2006, MNRAS, 365, 454

Hoyos C., Koo D. C., Phillips A. C., Willmer C. N. A., Guhathakurta P., 2005, ApJ, 635, L21

Im M., Ratnatunga K. U., Griffiths R. E., Casertano S., 1995, ApJ, 445, L15

Jangren A., Bershady M.A., Conselice C., Koo D.C., Guzmán R., 2003, AJ submitted

Kennicutt R. C., 1983, ApJ, 272, 54

Kennicutt R. C., Tamblyn P., Congdon C. E., 1994, ApJ, 435, 22

Kennicutt R. C., 1998, ApJ, 498, 541

Kewley L. J., Dopita M. A., 2002, ApJS, 142, 35

Kobulnicky H. A., Zaritsky D., 1999, ApJ, 511, 118

Koo D. C., Bershady M. A., Wirth G. D., Stanford S. A., Majewski S. R., 1994, ApJ, 427, L9

Koo D. C., Guzman R., Faber S. M., Illingworth G. D., Bershady M. A., Kron R. G., Takamiya M., 1995, ApJ, 440, L49

Lehnert M. D., Heckman T. M., 1996, ApJ, 472, 546

Lilly S. J., Tresse L., Hammer F., Crampton D., Le Fevre O., 1995, ApJ, 455, 108

Lowenthal J. D., et al., 1997, ApJ, 481, 673

McGaugh S. S., 1991, ApJ, 380, 140

Noeske K. G., Guseva N. G., Fricke K. J., Izotov Y. I., Papaderos P., Thuan T. X., 2000, A&A, 361, 33

Osterbrock D.E., 1989, Astrophysics of Gaseous Nebulae and Active Galactc Nuclei (Mill Valley:University Science Books)

Pagel B. E. J., Edmunds M. G., Blackwell D. E., Chun M. S., Smith G., 1979, MNRAS, 189, 95

Pagel B. E. J., Edmunds M. G., Smith G., 1980, MNRAS, 193, 219

Pettini M., Kellogg M., Steidel C. C., Dickinson M., Adelberger K. L., Giavalisco M., 1998, ApJ, 508, 539

Pettini M., Shapley A. E., Steidel C. C., Cuby J.-G., Dickinson M., Moorwood A. F. M., Adelberger K. L., Giavalisco M., 2001, ApJ, 554, 981

Phillips A. C., Guzman R., Gallego J., Koo D. C., Lowenthal J. D., Vogt N. P., Faber S. M., Illingworth G. D., 1997, ApJ, 489, 543

Pilyugin L. S., 2000, A&A, 362, 325

Pilyugin L. S., 2001, A&A, 369, 594

Schaerer D., 2002, in Summer School on Stellar Physics X, Star Formation and the Physics of Young Stars, ed. J. Bouvier and J.P. Zahn. (Les Ulis;EAS Publications Series)

Sandage A., Tammann G. A., 1974, ApJ, 190, 525

Sargent W. L. W., Searle L., 1970, ApJ, 162, L155

Telles E., Melnick J., Terlevich R., 1997, MNRAS, 288, 78

Terlevich R., Melnick J., Masegosa J., Moles M., Copetti M. V. F., 1991, A&AS, 91, 285

Tresse L., Rola C., Hammer F., Stasinska G., Le Fevre O., Lilly S. J., Crampton D., 1996, MNRAS, 281, 847

Vader J. P., 1986, ApJ, 305, 669

de Vaucouleurs G., de Vaucouleurs A., Corwin H.G., Buta R.J., Paturel G., & Fouqué P., 1991, Third Reference Catalogue of Bright Galaxies (New York: Springer)

Whitford A. E., 1958, AJ, 63, 201

Zwicky F., 1965, ApJ, 142, 1293

Chapter 4

The Stellar Populations Found in the Central Regions of Distant Luminous Compact Blue Galaxies at Intermediate *z*.

Abstract.

We investigate the star formation history of four Luminous Compact Blue Galaxies (LCBGs) at intermediate redshift using evolutionary population synthesis techniques. LCBGs are blue ($B-V \leq 0.6$), compact ($\mu_B \leq 21.0$ mag arcsec^{-2}) galaxies with absolute magnitudes M_B brighter than -17.5. The observational data used were obtained using the STIS spectrograph and the WF/PC-2 camera, both instruments are on board of the Hubble Space Telescope (HST). The redshifts of the objects presented is $0.436 \leq z \leq 0.525$. We find evidence for various stellar populations. One of them is identified as the ionizing population, and the other one is the underlying, older stellar generation. We compare the stellar populations found in the line-emitting region of LCBGs with the stellar populations present in bright, local HII

galaxies, and nearby spheroidal systems. Our models indicate that the first episodes of star formation the presented LCBGs underwent happened ~ 7 Gyr ago ($z \sim 0.7$), and that their underlying stellar populations are very similar to those of local HII galaxies. It is also the case that the passive color evolution of the LCBGs could convert them into the most luminous and redder local spheroidal galaxies without any further assumption. Our results help to impose constraints on evolutionary scenarios for the ubiquitous population of Luminous Compact Blue Galaxies. The estimated masses of the inferred populations are compatible with the dynamical masses to within the order of magnitude. We have also calculated Star Formation Rates from Hα luminosities. These range between 0.5 and 7 $M_{\odot} yr^{-1}$. The star forming regions of these objects are thus typically ten times more luminous than and approximately twice as large as the well known giant HII region 30-Doradus in the LMC.

4.1 Introduction.

Luminous Blue Compact Galaxies (LCBGs) are luminous (M_B brighter than -17.5), blue ($B-V \leq 0.6$), and compact ($\mu_B \leq 21.0$ mag arcsec^{-2}) systems experiencing a very important starburst. The huge number of massive stars formed in a very small volume allow these objects to be seen from cosmological distances. LCBGs are believed to contribute up to $\sim$50% of the star formation rate density in the universe at $z \approx 1$. Their rapid evolution from those times till the present day makes them responsible for most of the observed evolution of the luminosity function (Lilly et al., 1995) as well as for the evolution of the star formation rate in the universe.

Despite their importance, their relation to local galaxies is poorly known. The works presented in Guzmán et al. (1997); Phillips et al. (1997); Hoyos et al. (2004) give a glimpse of the similarities between LCBGs and the local HII and Starburst Nuclei populations. HII galaxies are a subset of BCGs[1] in which the spectrum is completely dominated by a spectral component present almost everywhere within the galaxy whose spectrum resembles the emission of a HII region (Sargent & Searle, 1970). Starburst Nuclei were introduced in Balzano (1983), they show high extinction values, with very low [NII]λ 6584/Hα ratios, greater velocity dispersions and fainter [OIII]λ5007 emission. Their Hα luminosities are always greater than 10^8 solar luminosities. One of the main ingredients in any theory attempting to explain

[1] Blue Compact Galaxies (BCGs) were first identified by Zwicky (1965) as faint star-like field galaxies on Palomar Sky Survey plates. BCGs often present an emission line spectrum and a UV excess.

the final destiny of LCBGs is bound to be an accurate knowledge of the stellar generations already existing in these distant sources. The similarities found between LCBGs and many local HII galaxies make it possible to think that the star formation histories of both types of objects are very similar. Even though HII galaxies were originally thought to be truly young objects, experiencing their very first star formation episodes (Searle & Sargent, 1972; Sargent & Searle, 1970), this hypothesis is no longer tenable after very deep CCD imaging of such objects Telles & Terlevich (1997); Telles, Melnick, & Terlevich (1997), or other very similar sources known as Blue Compact Dwarves[2] (Papaderos et al., 1996,b; Loose & Thuan, 1986) which show clear evidence of an older extended population of stars. The properties of this host galaxy has been further studied photometrically (see, e.g. Caon et al., 2005; Telles, Melnick, & Terlevich, 1997, and elsewhere). The current view on local HII galaxies is that they are a mixture of three populations. The first of them is the youngest population, responsible for the observed emission lines. The second population is an intermediate age generation, older than 50Myr but younger than a few hundred Myr. This population is unable to ionize the HI gas, and contains many Asymptotic Giant Branch Stars. The third population is the oldest one, older than 1Gyr. This population generally dominates the stellar mass by a large factor, and it also occupies a larger volume. The luminosity of this population is dominated by red giant stars. The contribution to the total luminosity of this population is small, though.

In this chapter we present two-dimensional spectra and deep images of four LCBGs with redshifts between 0.436 and 0.525 which were obtained using the STIS instrument and the WF/PC-2 camera, both instruments belong to the instrumental array of the *Hubble Space Telescope* (HST). The goal of this study is to characterize the stellar populations present in the line-emitting regions of intermediate redshift LCBGs by combining the spectral and color information available from these data with evolutionary population synthesis techniques. The modelled stellar populations are then compared to the stellar populations found in HII galaxies. It is also interesting to study the future evolution of the predicted stellar populations, to see whether or not they can become dwarf elliptical systems (dE, or Sph), as suggested by Koo et al. (1995); Guzmán et al. (1998), or the bulges of modern-day spiral galaxies (Hammer et al., 2001).

The observations are described in section 4.2. Section 4.3 presents the analysis of the

[2]BCDs. The qualitative properties of BCDs are similar to those of BCGs or HII galaxies, but are an order of magnitude less luminous.

	SA57-7042.	SA57-5482	SA57-10601.	H1-13088.
RA	13 07 26.3	13 09:08.8	13 08 47.8	17 20 19.67
DEC	29 18 25.7	29 15:57.7	29 23 41.1	50 01 04.7
Obs Date.	2002-05-05	2002-04-09	2000-07-05	2000-11-06
G750L Exp. Time.	9898	...	4696	4932
G750M Exp. Time.	2760	18106	5571	5947
G430L Exp. Time.	...	2790	...	...
G430M Exp. Time.	...	7709	...	...
WF/PC-2 F606W Exp. Time.	700	700	700	700
WF/PC-2 F814W Exp. Time.	900	900	900	1000
Obj ID.	1	2	3	4
z.	0.525	0.453	0.438	0.436
$t_{look-back}$(Gyr)	5.2	4.7	4.6	4.5
M_B	-20.6	-20.8	-20.4	-21.1
R_e	1.4	1.5	1.9	2.4
m_B	22.3	21.6	21.6	21.0
r_e	0.25	0.29	0.36	0.47

Table 4.1: Log of HST/STIS and HST/WF/PC-2 observations. RA and DEC coordinates are given for equinox J2000. Half-light radii are given in kpc (R_e) and arcseconds (r_e). All quantities given were calculated assuming $q_0 = -.55$ and $H_0 = 70$km s^{-1}Mpc^{-1}.

observational data. The evolutionary models that have been constructed to explain the observations are explained in section 4.4. Section 4.5 puts the resulting models in the context of two relevant populations of local systems. The summary is section 4.6.

The cosmology assumed here is a flat universe with $\Omega_\Lambda = 0.7$ and $\Omega_M = 0.3$. The resulting cosmological parameters are: H_0=70 km s^{-1}Mpc^{-1}, q_0=-0.55. Given these values, $1''$ corresponds to 1.8kpc at $z = 0.1$ and to 5.8kpc at $z = 0.45$.

4.2 Observations and Data Reduction.

Target names, redshifts, look-back times, B absolute magnitudes, exposure times, and half light-radii, as well as an identifying numeral for the observed objects can be seen in table 4.1.

The data used to study these objects includes long slit spectra and deep V (F606W) and I (F814W) images.

The long slit spectra were obtained using the spacecraft borne STIS instrument. The detector used was the STIS/CCD, a SITe 1024x1024 chip, with $0.05''$ square pixels operating from ~2000 to 11000 Å. Several instrumental configurations were used. The instrumental setup used to observed objects 1, 3 & 4 used the low resolution grating G750L. This instrumental setup provides a dispersion of 4.92 Å per pixel or about 190 km s^{-1} per pixel which,

in combination with a slit $0.5''$ wide, gives a spectral resolution of about 29Å(FWHM). The spectral coverage provided by this setup is about 5000 Å. The central wavelength is 7750 Å. The higher resolution grating G750M was also used for objects 3 & 4. It provides a dispersion of 0.53 Å per pixel or about 35 km s^{-1} per pixel. The slit used was $0.2''$ wide, thus giving a spectral resolution of about 2.2Å(FWHM). The spectral coverage provided by this setup is about 500 Å. These spectra are used to study the gas-phase velocity field, and the results from this work are presented in Bershady *et al.* (in preparation). Object 2 was observed using the lower-resolution grating G430M and the high-resolution grating G750M. The G430M grating has a dispersion of 2.7 Å per pixel and the slit width used is $0.2''$. The central wavelength is 4300 Å, and the spectral coverage is 2800 Å. The data were reduced using the STSDAS[3] package within IRAF[4]. For a complete account of the reduction procedures, uncertainties and detailed descriptions of the spectra, see Hoyos et al. (2004)

The images used were taken with the WFPC2 instrument, which is also included in the instrumental array of the Hubble Space Telescope. The detector used was the Planetary Camera. This is a 800×800 CCD, with $46 \times 10^{-3}''$ square pixels. Two broadband filters were used, the F814W filter and the F606W filter. For each object and filter, two $\sim$ 400s exposures were obtained to allow for cosmic ray rejection. The details of the reduction and analysis procedures can be found in Guzmán et al. (1998).

4.3 Results and Analysis.

4.3.1 Emission-Line and Continuum Distribution.

It is interesting to investigate whether or not the continuum distributions and the emission-line distributions differ. This will help determine where did the starburst take place in the observed objects. This information can be helpful to understand the starburst triggering mechanism and to construct models for these sources. Here, the analysis presented in Hoyos et al. (2004) is followed although it is presented in a much simpler way. Furthermore, only objects 1 & 2 are presented here since the other two sources were dealt with in Hoyos et al. (2004). The spatial profiles in figure 4.1 present the data for the two new objects studied.

[3](Space Telescope Science Data Analysis System) from the Space Telescope Science Institute, operated for NASA by AURA

[4]Image Reduction and Analysis Facility. Distributed by the National Optical Astronomy Observatories, which is operated by AURA (Association of Universities for Research in Astronomy, Inc) under cooperative agreement with the National Science Foundation.

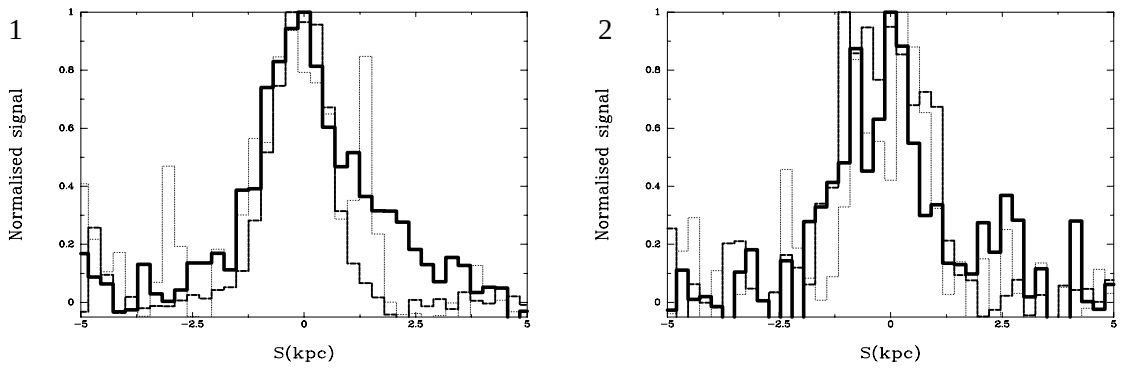

Figure 4.1: Continuum and emission-line spatial profiles. Only objects 1 & 2 are presented since the spatial profiles for objects 3 & 4 were given in Hoyos et al. (2004). The S-axis is placed with respect to the slits depicted in Fig.4.2. Increasing S corresponds to upper positions in that figure. The continuum is the thickest, solid line; [OIII]λ5007 is the thick line and the dotted line represents Hβ.

Figure 4.1 shows that:

1. The spatial distribution of the ionized gas and underlying stellar population in object 1 is very similar to the distributions observed in SA57-10601 or H1-13088 (Hoyos et al., 2004). The nebular component center does not coincide with the continuuum centroid. This object is very similar to the cometary Blue Compact Dwarves. In this particular case, the spread of the continuum is about twice the size of the line-emitting region. In the optical images, this object shows a conspicuous tail, and a very bright knot. It is also seen that the spatial extent of the two emission lines used to trace the ionized gas is very similar.

2. For object 2, the differences in the centroid positions for the continuum and the line-emitting region are very small when compared to the spread of both. In this case, the ionized gas can be said to lie in the center of the optical galaxy. It is also interesting to note that, the distributions of each component are very noisy, even for the continuum, and that the distributions of Hβ and [OIII]λ5007 are very similar to each other.

As in Hoyos et al. (2004), the Hβ and [OIII]λ5007 lines were chosen to probe the ionized gas phase because [OIII]λ5007 and Hβ are very close to each other in wavelength space and therefore they are affected by a similar extinction. For this reason, differences in their spreads can then reveal real differences in their distributions and not just a reddening effect. As it was pointed out in Hoyos et al. (2004), the observed differences in the spread of Hα and Hβ or [OIII]λ5007 and [OII]λ3727 can be accounted for by a moderate extinction, within

the measurement errors, making it impossible to detect extinction or excitation gradients unambiguously. Finally, the inclusion of these two new objects to the sample of LCBGs with high quality spatially resolved spectroscopy allows to give a first estimate of the frequency of off-center starbursts in LCBGs. Since it results that three out of six LCBGs with STIS spectroscopy happen to have their starburst displaced from their centers, all that can be said is that the fraction of LCBGs with shifted starbursts lies between 30% and 99%. More theorethical work is needed to asses the frequency and impact of this in the evolution of an individual LCBG.

4.3.2 Line Ratios, Reddening, Equivalent Widths and Metallicities.

The observed flux of each emission line and the equivalent widths have been measured using gaussian fits according to the method outlined in Hoyos et al. (2004). The emission lines were fitted rather than summed because of residuals of bad pixels. Two different positions are considered for each galaxy corresponding to (a) the inner and (b) the outer regions of each object. These two one-dimensional extractions are defined as to encompass approximately the same line luminosity. The linear sizes of both extractions are given in table 4.2. For position (a), both the FWHM and central wavelength are left as free parameters, but for position (b), the FWHM is fixed to the FWHM derived for position (a) to decrease the number of free parameters and hence increase the goodness of the fit in poor S/N conditions. The [OII]λ3727, Hβ and both [OIII] lines can be observed in all cases. However, athough Hα is detected for H1-13088, it is affected by many bad-pixels that render the line unusable. In the case of object 1, Hγ was detected, too.

The amount of extinction is here parametrized using the logarithmic extinction coefficient c(Hβ). It was always derived using standard nebular analysis techniques (Osterbrock, 1989) using Balmer line ratios. In the case of object 1, the Hγ line was used to obtain another independent calculation of the extinction coefficient. It agreed well with that derived from Hα and Hβ. Since the observed galaxies are at high Galactic latitude, suffering galactic extinctions $A_B < 0.11$ mag, which corresponds to a c(Hβ)< 0.05 (Burstein & Heiles (1984); Sandage & Tammann (1974)), it was assumed that all the extinction occurs within the target objects. Consequently the spectra have been dereddened in the rest frame of the target according to a standard reddening curve (Whitford, 1958), assuming case B recombination theorethical line ratios. The use of different extinction curves would not significantly change the results, since they do not differ from the one used here in the wavelengths of interest.

The value of c(Hβ) is determined independently for the inner and outer regions for all objects but H1-13088, for which Hα is unfortunately not well measured. A global value of c(Hβ) = 0.1 ± 0.05, typical for local HII galaxies (Hoyos & Díaz, 2006) is adopted. No underlying stellar hydrogen absortion is detected, as the continuum is very low.

The measured extinction coefficients and de-reddened line ratios are given in table 4.2, together with *rest-frame* equivalent widths. It is seen that the extinction values are always very small.

The Oxygen Content. Metallicity Estimates. One of the main goals of any nebular analysis is to estimate the metallicity of the emitting nebula. There are many reasons to determine the metallicity of the ionized gas in a galaxy, but chief among them is that it yields an up-to-date determination of the chemical composition of the most recent generation of stars born in the galaxy studied.

The spectrum from a star forming region depends strongly on the electron temperature and metallicity of the nebula. The ratio of the auroral line [OIII]λ4363 to the lower excitation lines [OIII]$\lambda\lambda 4959, 5007$ gives a direct determination of the electron temperature where O^+ and O^{++} are the dominant species, but beyond certain metallicities, the increasing cooling leaves no energy to collisionally excite the upper levels. When this is the case, one is bound to determine the oxygen abundance empirically.

In principle, oxygen abundances can be determined from the intensities of the optical emission lines using the R_{23} number, defined as the reddening-corrected ratio ([OII]λ3727+[OIII]$\lambda, \lambda 4959, 5007$)/H$\beta$. This method was originally developed by Pagel et al. (Pagel et al., 1979) (see also Pagel, Edmunds, & Smith (1980), Edmunds & Pagel (1984), McGaugh (1991), Kewley & Dopita (2002) and references therein). The main problem with this empirical method is that the calibration is two-folded, and some *a priori* knowledge of the metallicity range is needed in order to solve this degeneracy. Since the S/N of the spectra used is not very large, no other lines that could help break this degeneracy are detected and the lack of this initial knowledge about the oxygen content remains. The metal content of the galaxies studied cannot be cleanly determined, then. Instead, the metallicity values that result from the use of the Pilyugin (2000) calibration for both the lower and upper branches are calculated. The Pilyugin (2000) metallicity estimates are given in table 4.2. Unfortunately, the measured values for $\log R_{23}$ squarely place our objects in the turnaround region of the $12 + \log(\mathrm{O/H})$–$\log R_{23}$ plot. In this regime, the only thing that can be safely said is the the metallicity is between 7.7

and 8.4. This analysis can only conclude that these LCBGs have oxygen abundances greater than 7.7, but lower than solar abundances. It can also be concluded that the R_{23} method is not best suited to determine the oxygen abundance of LCBGs.

ID	1	1	2	2	3	3	4	4
Position.	inner	outer	inner	outer	inner	outer	inner	outer
Size.	0.83	1.66	1.04	2.01	1.28	2.03	1.27	3.04
c(Hβ)	0.0±0.1	0.0±0.1	0.0±0.1	0.0±0.2	0±0.1	0.10±0.2	0.10±0.05	0.10±0.05
log(([OIII]$\lambda\lambda$4959, 5007)/Hβ)	0.71±0.04	0.60±0.03	0.60±0.03	0.39±0.04	0.67±0.03	0.44±0.06	0.7±0.1	0.54±0.08
log([OIII]/[OII])	0.48±0.04	0.38±0.02	-0.31±0.04	-0.38±0.05	0.43±0.06	0.33±0.09	0.28±0.09	0.26±0.07
log R_{23}	0.83±0.04	0.75±0.02	1.08±0.02	0.92±0.06	0.80±0.03	0.61±0.05	0.89±0.08	0.73±0.06
log $W_{[OII]\lambda 3727}$	1.88	1.94	2.18	2.11	1.65	1.43	1.93	1.79
log $W_{H\beta}$	1.79	1.87	0.60	0.47	1.59	1.51	1.67	1.57
log $W_{[OIII]\lambda\lambda 4959+5007}$	2.51	2.53	1.10	0.77	2.28	2.00	2.40	2.13
log $W_{H\alpha}$	2.00	1.82	...	...	2.30	2.16	...	...
$12+\log(\mathrm{O/H})_{\mathrm{hi}}$	8.4	8.5	7.8	8.1	8.4	8.7	8.2	8.5
$12+\log(\mathrm{O/H})_{\mathrm{lo}}$	7.8	7.7	8.8	8.6	7.7	7.5	8.0	7.7
$B-V_{\mathrm{Observed.}}$	0.41	0.49	0.28	0.27	0.08	0.25	0.26	0.35
$B-V_{\mathrm{Stellar.}}$	0.13	0.20	0.34	0.33	-0.08	0.16	0.12	0.28

Table 4.2: Absorption Coefficients, De-reddened Line Ratios, Rest-Frame Equivalent Widths, Oxygen Abundances and Stellar Colors. In the second row the physical sizes of each aperture in linear kpc are given. For object 1, the logarithmic extinction coefficient was derived from the $H\gamma/H\beta$ ratio. Its value was consistent with the value derived using $H\alpha$, but the error was smaller. For object 2, the [OII]λ3727 flux is first measured in the integrated G430L spectra and the intensities in each zone (a) or (b) are then derived by imposing that both zones emit 50% of light each. This is true to within 5% for the other three lines seen in the other instrumental setup. The reported values of log $W_{([OII]\lambda 3727)}$ correspond to the integrated spectra too. For object 4, Hα is not observed and the listed value for the logarithmic extinction coefficient is an *assumed* value, typical for local HII galaxies. Row 6 gives the reddening-corrected ratio [OIII]λ, λ4959, 5007/[OII]λ3727. The other line ratios are also reddening-corrected. R_{23} is defined as the reddening-corrected ratio ([OII]λ3727+[OIII]λ, λ4959, 5007)/Hβ. The reported rest-frame equivalent widths are in units of Å. The average error in the rest frame equivalent width is 17%. This corresponds to an error of 0.07 in the log. Most errors fell in the 15%-20% interval. The G750M spectra used for object 2 bear the largest uncertainties since the slit width used was 0.2″wide, compared to the 0.5″slit used for the other three objects. The errors in the equivalent widths for object 2 are therefore 30%, corresponding to 0.13 in the log. The oxygen abundances derived using both the upper and lower branches of the Pilyugin (2000) calibration are given in rows 11 and 12. The uncertainty in the *observed* colors is 0.01 magnitudes in all cases, while the errors in the *stellar* colors are 0.03 magnitudes for objects 1, 3 & 4, and 0.05 magnitudes for object 2 for the reasons outlined above.

4.3.3 Scaling and Registering of the Data. Calculation of the Stellar Colors.

In order to study the stellar populations found in the presented galaxies, it is needed to match the STIS spectroscopic frames with the WFPC-2 images. This is done by forcing that each galaxy's centroid in the F814W imaging frames coincides with the center of the continuum distribution of the STIS spectroscopic frames. Once both centroids are calculated, the slit orientation with respect to the image is used to determine what pixels in the WFPC-2 frames correspond to the *inner* and *outer* zones defined previously for the STIS spectra.

Figure 4.2 shows the slit placement in the F814W and F606W WFPC-2 images. The bidimensional spectra presented for objects 1, 3 & 4 are low-resolution G750L frames, whilst the spectra presented for SA57-5482 are from a high-resolution G750M frame, for the Hβ and [OIII] lines, and a G430L spectrum for the [OII] line. In this figure, the spectra have been scaled and approximately aligned with the images. It is seen that the STIS spectra can only probe the most luminous regions of the observed objects, corresponding to the line-emitting region. The stellar population analysis presented in the following section 4.4 is therefore only appropriate for the volume within the line-emitting regions of the studied galaxies. This region has a typical radius of 1.7kpc for the presented objects.

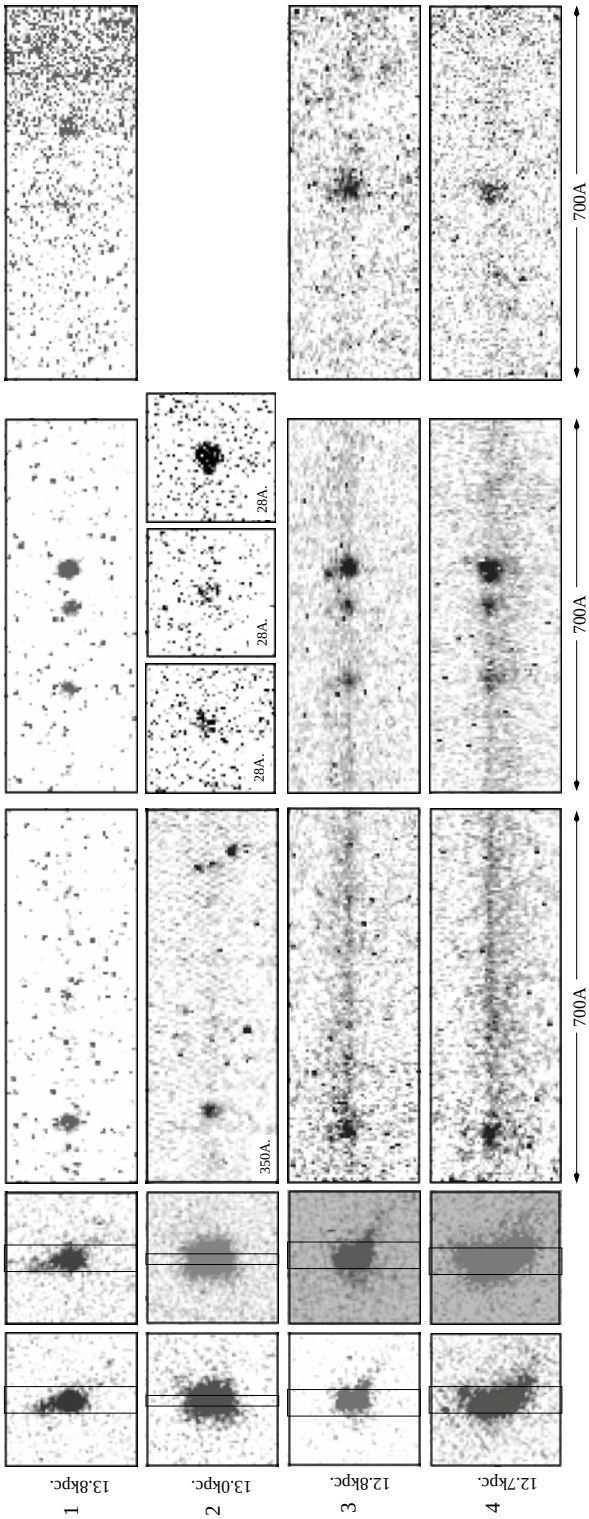

Figure 4.2: Matching between the STIS 2-D spectra and the HST/WFPC-2 images. Each spectral strip spans 2.5″in the spatial direction. The linear scale is given for each object in the figure. Each spectral strip spans 700Å except for object #2, in which the wavelength coverage is given in each image. The slit orientation is shown superimposed on HST F606W and F814W images which are 2.5″×2.5″on a side.

The next step is to determine the $B-V$color of the areas that match the *inner* and *outer* zones of the line-emitting region in the STIS spectra. In order to accurately determine said color, several issues are to be taken into account. The first of them is to correct the integrated DN (counts) in each area for the imperfections of the charge transfer mechanism. The web page found at
`http://www.stsci.edu/instruments/wfpc2/Wfpc2_cte/wfpc2_cte_calc.html` provides different tools to estimate this effect. The second choice available within this web page was used. The second step is to derive the required k-correction. The fits given in Fukugita, Shimasaku, & Ichikawa (1995) for the case of an Irregular Magellanic spectrum, the bluest one found in that work, are used. The third step is to derive the *emission-line free* colors. The recipe presented in Telles & Terlevich (1997) is adopted. It uses line equivalent widths as measures of the impact of the emission lines on the observed colors. Finally, the E($B-V$) color excess is derived from the c(Hβ) values for each zone. These color excesses happened to be very small. When this last correction is applied, it is implicitly assumed that the extinction towards the stars is the same as the extinction towards the gas. This is the "dust screen" model. The resulting colors are therefore *rest-frame*, stellar population only, extinction corrected $B-V$colors. Given the large number of corrections involved in deriving these quantites, the photometric errors are somewhat larger, in the range 0.03–0.05. These colors are also gathered in table 4.2.

4.4 Evolutionary Models.

The main aim of this study is to investigate the nature of the stellar populations found in distant LCBGs, and to shed light on the possible evolution and age of these galaxies. In this section, the star formation history of the four LCBGs is studied using evolutionary population synthesis techniques.

The observational data gathered for the LCBGs presented here can be used to construct galaxy models that represent the objects. Although the models presented are very crude and tailored, they provide at least a feeling of the stellar inventory and possible evolution of these LCBGs. The models have been built using the Bruzual & Charlot (2003) and Leitherer et al. (1999) evolutionary models. For each galaxy and extraction, two simple stellar populations are combined. One population is designed to mimic the observed properties of the ionizing stellar population, and the other population is chosen to match the observed

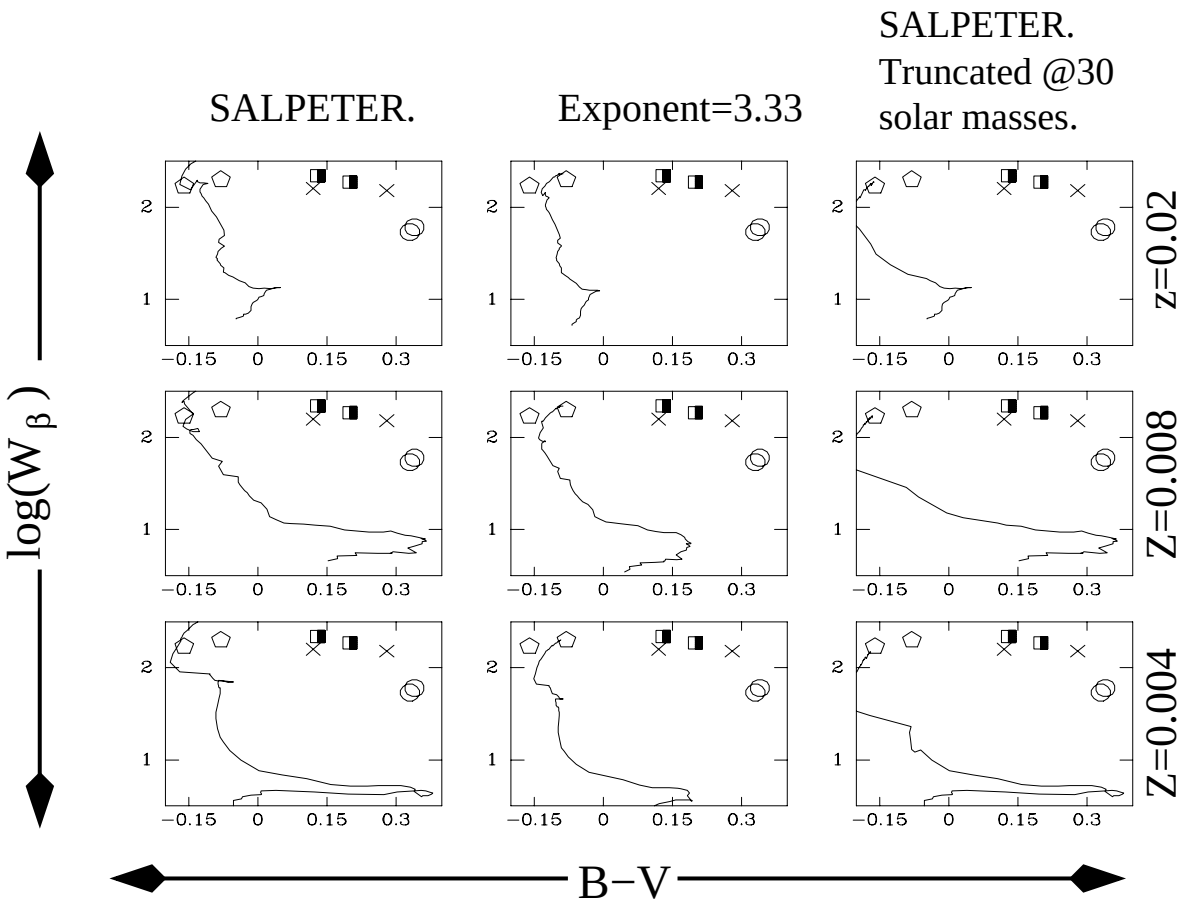

Figure 4.3: Evolution of a single stellar population in the $\log W_{H\beta}$–$(B-V)$ plane from $t = 0$ to $t = 10$Myr. The data were taken from the Leitherer et al. (1999) library. In all cases, an instantaneous burst is assumed. Three different oxygen abundances ($Z = 0.004$, $Z = 0.008$ and $Z = 0.02$) and three different IMFs (Salpeter from $1.0M_{\odot}$ to $100M_{\odot}$, a power law with an exponent $\alpha = 3.3$ with the same mass limits and a Salpeter IMF truncated at 30 $M_{\odot}$) are plotted. The location of the LCBGs modelled are also plotted. Object 1 is represented by half-filled squares, object 2 is represented by ◯, the location of object 3 is given by pentagons and × denotes object 4. In most cases, the (b) extractions have redder colors.

colors and line equivalent widths, when combined with the ionizing population. This latter population therefore represents the underlying population. The metallicity of the ionizing stellar population is assumed to be equal to the metallicity of the ionized gas. Since the only information available on the metallicity of the ionizing population of these sources is that it lies between 7.8 and 8.4, two sets of models are constructed. Models 1 assume the ionizing population has a metallicity of $Z = 0.008$, models 2 adopt $Z = 0.004$ for the oxygen abundance of the ionizing cluster. These metallicities correspond to $12+\log(\mathrm{O/H}) = 8.30$ and $12+\log(\mathrm{O/H}) = 7.95$, assuming solar chemical proportions. The mass of the ionizing cluster is another very important parameter. It can, in principle, be derived from the luminosities

of the observed recombination lines according to the following considerations. As the star cluster ages, the number of hydrogen ionizing photons per unit mass of the ionizing cluster decreases. Assuming that the age of the ionizing cluster is related to the intrinsic $W_{H\beta}$[5] , a relation should exist between the number of hydrogen ionizing photons per unit mass of the star cluster and W_β. Such relation is given for single-burst models in Díaz (1999). The expression used is

$$\log(Q(H)/M_*) = 44.8 + 0.86 \times \log W_{H\beta} \tag{4.1}$$

where Q(H) is the number of hydrogen ionizing photons per second. This number is derived directly from the calculatted line luminosities. The mass of the ionizing cluster M_* is expressed in solar masses, and $W_{H\beta}$ is the "intrinsic" equivalent width, the one that would be observed if no underlying stellar population was present.

However, the presence of the underlying stellar population introduces a degeneracy in the measurements of the equivalent widths. This prevents us from measuring directly the intrinsic equivalent widths. In order to solve this degeneracy in equivalent width introduced by the presence of the underlying population, the upper envelope of the relationship between $\log W_{H\beta}$ and log([OIII]/[OII]) presented in (Figure 6 of, Hoyos & Díaz, 2006, Chapter 2.) was used to estimate the equivalent width that would be observed in the absence of any underlying stellar population. This "effective " equivalent width is called (W_β^0). It tries to be a closer estimate to the intrinsice equivalent width. This "effective" equivalent width allows to estimate, or at least to place significant limits to, the age and intrinsic color of the ionizing population via the Leitherer et al. (1999) models assuming that the "effective" W_β^0 is equal to the real or "intrinsic" equivalent width. Of course, the "effective" estimate is only a lower limit to the "intrinsic" value of the equivalent width. This means that the derived value for the mass of the ionizing cluster obtained using W_β^0 can only be a lower limit to the real value. However, even if this "intrinsic" value could be somehow known, the resulting mass of the ionizing cluster would remain a lower limit, because some photons could actually be escaping from the nebula, dust globules will always be present amidst the gas clouds or other effects.

Figure 4.3 presents nine models from the Starburst99 Leitherer et al. (1999) library, which represent the evolution in the $\log W_\beta$ *vs.*–$(B-V)$ plane of a single stellar population from its

[5]Defined here as the equivalent width that would be observed in the absence of the non-ionizing population.

birth till it is 10Myr old. Three different metallicities and IMFs are presented, as indicated in the figure. The W_β^0 is plotted against the *emission-line free, reddening-corrected* color in the case of the observed LCBGs. It is seen that 3/4 of the objects studied require the presence of an underlying stellar population since they do not lie along the sequence defined by the different single stellar populations presented. Figure 4.3 also indicates that the models whose IMF is the Salpeter one have to be chosen. The models whose IMF has a slope of 3.33 are redder than the inner region of SA57-10601, which makes it impossible to accomodate any older and redder underlying population in the model. In addition, the truncated Salpeter IMF does not reproduce the derived high values of W_β^0 of many extractions, which are in any case only a lower limit to the true "intrinsic" equivalent width. Both observations indicate that the ionizing clusters of the observed LCBGs harbor many massive stars, and that W_β^0 can not be very far from the intrinsic equivalent width. The SFR was calculated from the Hα luminosity as in Kennicutt, Tamblyn, & Congdon (1994), valid for $T_e = 10^4 K$ and case B recombination (all the ionizing photons are processed by the nebular gas).

$$SFR(M_\odot yr^{-1}) = 7.9 \times 10^{-42} L_{H\alpha}(erg\ s^{-1}) \tag{4.2}$$

Finally, the measured Hβ luminosities are then used to estimate the total stellar mass of each model, following the expression given above. The resulting ages, intrinsic colors, star formation rates and stellar masses of the ionizing population are given in tables 4.3 and 4.4 for models 1 and 2 respectively.

The single stellar population used to describe the underlying generation of stars are chosen from the Bruzual & Charlot (2003) library. The evolutionary tracks used are the Padova 1994 ones and the IMF chosen is the Salpeter IMF. The metallicity of this underlying stellar population is $Z = 0.004$ for the case of models 1 and $Z = 0.0004$ for the case of models #2. The metal abundance of the underlying stellar population is therefore lower than the metal abundance of the ionizing populations. This tries to emulate the chemical evolution of the galaxy since its inception till the onset of the observed starburst. Although the choice adopted is not justified by the use of any particular chemical evolution model, it is at least a zero-th order solution to the problem since the Bruzual & Charlot (2003) models only offer a limited array of metallicities for the different single stellar populations. The age and initial mass of this underlying stellar population are chosen so that the predicted equivalent width by the time the current starburst is observed matches the *measured* equivalent width, and

the *total* color equals the calculated *rest-frame*, stellar population only, extinction corrected $B-V$color. In this step, the ionizing cluster is represented by the single stellar population available in the Bruzual & Charlot (2003) library that most closely resembles the Leitherer et al. (1999) model used before in terms of metallicity, IMF and age. See Díaz et al. (2000) for a complete account of how to mix several single stellar populations to match the observed properties of star forming regions.

The results are presented in tables 4.3 and 4.4.

Finally, in order to get a better picture of how is the mass in these galaxies distributed, the mass of neutral hydrogen has been estimated using the density profiles given in van Zee, Skillman, & Salzer (1998) and Garland et al. (2004). These profiles are strongly peaked towards the center of the studied galaxies. It is also the case that the HI peak approximately coincides with the center of the optical galaxy. The HI column density peak is a function of the galaxy's luminosity. For very luminous blue compact dwarves, this column density is 0.57 $M_{\odot}\mathrm{pc}^{-2}$. It is found that the contribution of HI to the total mass of the central regions of the studied galaxies is very small. The HI mass estimate is presented in tables 4.3 and 4.4 too. Although it can be considered to be speculative to assume that the distant LCBGs follow the same HI mass scaling law as the luminous blue compact dwarf galaxies do, these estimates indicate that the HI component is not the dominant one within the line-emitting regions of the observed LCBGs.

ID	1	1	2	2	3	3	4	4
Position.	inner	outer	inner	outer	inner	outer	inner	outer
Age of the ionizing cluster.(Myr)	3.1	3.2	4.8	4.9	3.2	3.2	3.3	3.3
$B-V$color of the ionizing cluster.	-0.16	-0.14	-0.10	-0.08	-0.14	-0.14	-0.15	-0.15
Age of the underlying population.(Myr)	450	1500	925	800	17.5	275	400	1260
Mass ionizing cluster.($\log M/M_{\odot}$)	6.9	7.11	6.5	6.7	6.8	7.0	7.1	7.2
Mass underlying/ionizing.	80	140	260	1340	9.0	100	76	190
Stellar mass/Dynamical mass.	0.20	...	0.60	...	0.20	...	0.60	...
SFR ($M_{\odot}\mathrm{yr}^{-1}$)	6.5±0.3	...	0.8±0.06	...	4.7±1.0	...	6.8±1.2	...
Neutral HI mass.($\log M/M_{\odot}$)	6.6	...	6.2	...	6.7	...	6.9	...

Table 4.3: Best fits for the first set of models. Ages of the two single stellar populations used, relative masses, neutral HI mass estimates and the ratio of the modelled mass to the measured dynamical mass are given. The mass of the ionizing cluster is calculated following Díaz (1999). The uncertainty in the age of the underlying population is estimated in 50×10^6–100×10^6 yr. Dynamical masses were calculated as in Hoyos et al. (2004).

ID	1	1	2	2	3	3	4	4
Position.	inner	outer	inner	outer	inner	outer	inner	outer
Age of the ionizing cluster.(Myr)	2.9	3.2	4.9	5.1	2.9	4.0	4.0	4.1
$B-V$color of the ionizing cluster.	-0.17	-0.14	-0.08	-0.07	-0.17	-0.12	-0.13	-0.13
Age of the underlying population.(Myr)	630	790	1020	980	60	550	410	910
Mass ionizing cluster.($\log M/M_{\odot}$)	6.9	7.11	6.5	6.7	6.8	7.0	7.1	7.2
Mass underlying/ionizing.	70	90	520	750	28	220	90	230
Stellar mass/Dynamical mass.	0.05	...	0.40	...	0.40	...	0.70	...
SFR ($M_{\odot}\mathrm{yr}^{-1}$)	6.5±0.3	...	0.8±0.06	...	4.7±1.0	...	6.8±1.2	...
Neutral HI mass.($\log M/M_{\odot}$)	6.6	...	6.2	...	6.7	...	6.9	...

Table 4.4: Best fits for the second set of models. Ages of the two single stellar populations used, relative masses, neutral HI mass estimates and the ratio of the modelled mass to the measured dynamical mass are given. The mass of the ionizing cluster is calculated following Díaz (1999). The uncertainty in the age of the underlying population is estimated in 50×10^6–100×10^6 yr. Dynamical masses were calculated as in Hoyos et al. (2004).

Tables 4.3 and 4.4 show that the ionizing populations are very young, less than 5Myr in almost all cases, although the average age is slightly over 3Myr. The ionizing clusters are then largely unevolved. The resulting ages in both model sets indicate that these galaxies are being observed at the peak (or a little bit past of) of their line luminosities. The inferred underlying populations are very different amongst the studied galaxies. There are systems with fairly young non-ionizing populations (around 300Myr old), but there are LCBGs whose underlying populations are very old (older than 1.0Gyr). In the case of the inner region of SA57-10601, the estimated stellar population is roughly compatible with a single stellar population. The average age of the underlying stellar populations found are 700Myr for models #1 and 670Myr for the other set of models. The underlying stellar populations found in the presented LCBGs are therefore much younger than the underlying stellar generations found in local HII galaxies, which is older than 1Gyr (Westera et al., 2004). They seem more like a somewhat aged intermediate age population, in the notation given in Westera et al. (2004). The derived stellar masses account for 20% to 60% (the average value being 40%) of the virial masses within the line-emitting region, according to the first set of models. In the case of models 2, the stellar mass account for 4%–70% (the average value is again 40%) of the derived virial masses. The virial masses within the line-emitting region were calculated as in Hoyos et al. (2004) following the considerations presented in Bender, Burstein, & Faber (1992); Guzmán et al. (1996), assuming that the measured gas phase velocity dispersions are equal to the *stellar* velocity dispersions and that the observed objects are virialized. Since the stellar mass estimates the toy-models used here yield are only lower limits for the reasons outlined above, there is not much room left for the presence of dark matter[6] in the central regions of these objects. It might be tempting to think that this might be hinting the existence of a very old stellar population, too red to leave a trace in the $B-V$color used here but as massive as the already detected underlying stellar population. However, this phantom population can not be older than ∼5Gyr simply because of look-back time reasons. Such population would still be vigorously shining in the B and V bands, implying that the existence of this very old population is somewhat unlikely because it would affect the presented color measurements. It is therefore concluded that the resulting stellar inventory found using the simple models devised here can not be very far from reality.

[6]Which would, in any case, be spread out in a vast halo around the objects by its very nature.

4.5 Bright, Local HII Galaxies as Nearby LCBGs. The LCBG-Spheroidal Connection.

It is interesting to compare the evolution of the simple models described here with present-day galaxy samples. In this section, several predicted observables are compared to the properties found in local systems. The goal of the first subsection is to determine whether the stellar populations predicted by our models are similar to the underlying stellar populations of local HII galaxies. The second half of this section will deal with the passive evolution of LCBGs, and their connection with the local population of *local* dwarf spheroidal systems. In the following figures 4.4 through 4.9 the evolution of the simple models that describe the presented LCBGs is shown using a single line for each galaxy. The model results for the inner and outer regions of each galaxy have been mixed together and scaled using the appropriate weights to derive the properties of the whole source. The main assumption is that the underlying stellar population of the central kpcs of these objects is qualitatively similar to the stellar population found in the outskirts[7] of each galaxy. The absolute luminosities were further corrected by multiplying them by a factor of two, to account for the luminosity of the stars found in the outskirts of the studied objects. This way, the observed galaxies can be represented by a single point each in color-color or color-magnitude diagrams.

4.5.1 Stellar Populations in HII galaxies and distant LCBGs.

Here, the stellar populations that have been found to match more closely the properties of LCBGs are compared to the populations found in bright local HII galaxies. The HII galaxy control sample used here was taken from the Telles & Terlevich (1997) sample. This sample comprises 15 galaxies which were selected from the Spectrophotometric Catalogue of HII galaxies (Terlevich et al., 1991, SCHG Catalogue). Their equivalent widths are between 26Å and 170 Å , and are very luminous even for HII galaxies standards. The measured velocity dispersions range from 16 km s^{-1} to 50 km s^{-1}. The galaxies also exhibit a wide morphological variety. This sample was chosen since HII galaxies also show conspicuous and galaxy-wide emission line spectra. They are quite similar to the LCBGs presented here in this respect, as hinted by Koo et al. (1994), Guzmán et al. (1997) and Hoyos et al. (2004). Their small radii and velocity dispersions indicate that they ought to be as massive as distant

[7]Here, the word "outskirts" means "outside the line-emitting region."

LCBGs. In addition, they are also known to posses violent star forming systems, just like intermediate-z LCBGs. It is then natural to wonder if bright, local HII galaxies are nearby copies of distant LCBGs or if they are different from the distant sources in some respect.

Figure 4.4 presents the evolution of the simple models devised here to match the properties of the observed LCBGs in the $(V-R)$–$(R-I)$ plane. The underlying stellar population of the 15 bright HII galaxies from Telles & Terlevich (1997) is represented by half-filled dots. The $V-R$ colors of the local systems lie in a very narrow range around 0.4 but the $R-I$ color has a much greater range of variability, from 0 to 1. This figure shows that the $V-R$ color of the underlying population found in local HII galaxies is indeed attainable by LCBGs at some point during their evolution. In particular, according to the (1) models, the underlying populations of LCBGs presented such $V-R$ colors 4.9 Gyr ago, when the observed starbursts were taking place. In the case of the metal poor models, this happens 4.5Gyr ago, just after the observed starbursts occured. As for the $R-I$ color, the first set of models reaches the average $R-I$ of the local sample $\sim$ 2.3Gyr ago, while the (2) models will attain this $R-I$ color in the future. This suggests that the underlying stellar populations of local HII galaxies emit more power in the I band than intermediate redshift LCBGs of otherwise similar optical properties. This I band excess could be caused by the presence of very luminous red giant stars, existing in the extensions and wings of the local HII galaxies that emit a lot of their power in the I band. Distant LCBGs are bound to harbor lower *relative* numbers of red giant stars than the redder HII galaxies since they have had much less time to evolve since the onset of the red giant phase of the evolution of their dominant stellar populations. More modeling and observational work is clearly needed in order to establish if this hypothesis is true or not.

It can be concluded that the presented star formation histories are similar to some extent to the star formation histories of HII galaxies described in Westera et al. (2004). Both HII galaxies and LCBGs are therefore age-composite systems. They have an old stellar population, together with a young stellar generation. However, since the underlying stellar population of LCBGs is somewhat younger than the underlying stellar populations described in Westera et al. (2004), the relative content of red giant stars might be lower in the intermediate redshift LCBGs.

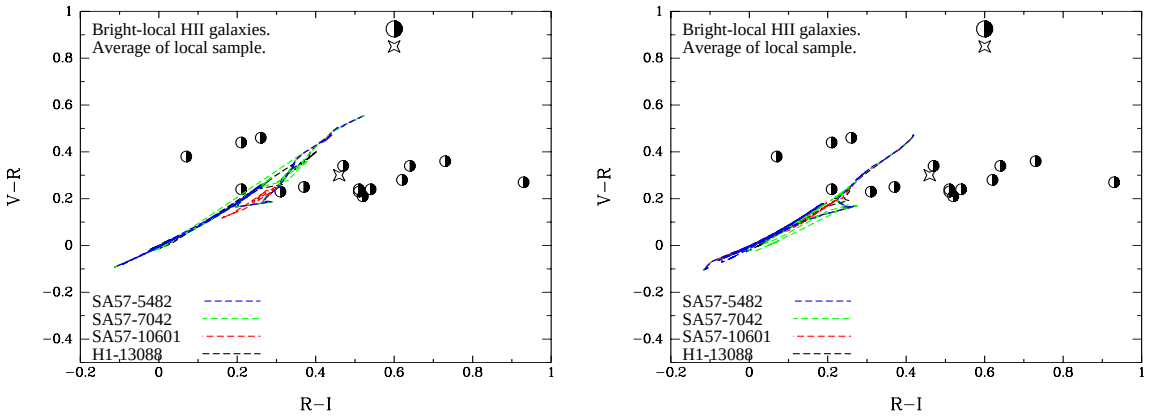

Figure 4.4: Both panels represent the evolution in the $(V-R)$–$(R-I)$ plane of the models used here to describe the evolution of the four observed LCBGs. The first panel represents the first set of models, while the second panel represents the metal-poor models. The local data are taken from the HII Telles & Terlevich (1997) galaxy sample, and have been corrected for extinction.

4.5.2 Passive Evolution of LCBGs. Will They Ever Become Local Sph Galaxies?

Once the stellar populations of the observed LCBGs have been characterized, it is possible to investigate the *passive* evolution of these systems. This scenario of a passive evolution assumes that no further episodes of star formation takes place from their look-back times to the present day. It is also assumed that there is no gas infall from the surrounding ISM. Given the high intensity of the observed starburst, it is not unlikely that the interstellar medium will be cast out of the galaxy, preventing further starbursts from happening. However, it has to be borne in mind that the look-back times of the LCBG sample used here are $\sim 5 \times 10^9$yr. This means there is a huge amount of time for they to undergo other star formation episodes, mergers, gas infall or other phenomena that would, of course, not be represented by the simple passive evolution scenario used. Here, the issue of whether or not the observed LCBGs could transform into today's dwarf elliptical systems[8] is tackled. The Sph sample used for comparison purposes is that of Guzmán (1994). We also use four other well-known dwarf elliptical galaxies. The observed LCBGs galaxies are also briefly compared with The Large Magellanic Cloud.

Figures 4.5 to 4.9 present the evolution of the constructed models. Figure 4.5 shows the evolution of the *stellar* $B-V$color as a function of look-back time. The symbols at $t \sim 0$

[8]Also called Sph systems.

represent four well known spheroidal systems, as indicated in the figure. The metal rich models do end their evolution near the position occuppied by the dE galaxies. It can also be seen that the second set of models does not reach the very red colors of the presented Sph galaxies. Further, these metal poor models can only reach $B-V=0.7$ in the distant future. In figure 4.6, the evolution of the presented models in the $\log(M/L_B)$–$(B-V)$ diagram is shown. The positions of the LMC and individual dwarf elliptical systems is presented too. The $B-V$color of the LMC has been corrected for the contribution of the line-emitting region and extinction by subtracting 0.1 to the color. This is a representative value of the correction, as table 4.2 allows to think. Again, models (1) end their evolution much closer to the Sph galaxies, although neither model falls within the region defined by the Sph galaxies shown. The fact that the mass-to-light ratios of the first set of models is more similar to those of the Sph systems shown than those of models #2 allows to think that the rest of the other colors of dE will be more similar to the color predicted by models #1. It is also the case that the stellar populations of the presented models have a mass-to-light ratio lower to that of the LMC by the time their $B-V$color is similar. This suggests that the star formation has proceeded for a longer period of time in the LMC than in LCBGs, which is again consistent with LCBGs being observed at very high look-back times.

Figure 4.7 shows how the presented models evolve in the M_B–$(U-B)$ plane. The position of the LMC and of a large sample of spheroidal systems taken from Guzmán (1994) is presented too. The contribution to the $(U-B)$ color from the 30-Doradus cluster is assumed to be 0.05. The distance modulus used to derive the blue absolute magnitudes of the Guzmán (1994) sample is 35.0 ± 0.3, which is the average value of the Terlevich, Caldwell, & Bower (2001) sample. It is again seen that the final stage of the first set of models is much more similar to the observed properties of the Sph galaxies. Furthermore, all the models converge towards a point around $U-B=0.3$, $M_B=-17.0$. This suggests that any Sph descendant of the distant LCBGs should be among the redder and more luminous ones. However, since the model used is very simple, it is also possible that this "focusing effect" towards this subset of the Sph galaxies merely reflects a weakness of the models. Indeed, should any major star forming episode happen in these objects, the final position of the evolved LCBGs would be different. It is also interesting to note that the LCBG models run very near the LMC at some point in the past, some time after the observed starbursts took place.

Finally, figures 4.8 and 4.9 show the evolution of the stellar populations predicted by our models in the $(U-B)$–$(B-R)$ plane. Figure 4.8 shows all the Sph galaxies from Guzmán

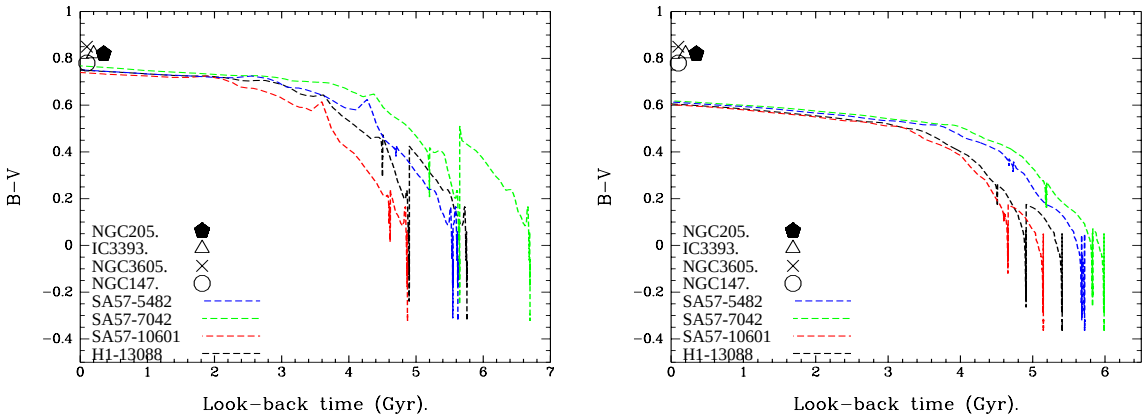

Figure 4.5: Temporal evolution of the stellar $B-V$color with look-back time. Panel (a) represents the first set of models, while panel (b) represents the metal-poor models. Individual symbols represent the $B-V$ color of several well known local spheroidal systems,as indicated in the figure.

(1994), while figure 4.9 only presents galaxies brighter than $M_B = -15.0$. It is again seen that the first set of models ends its evolution much closer to the Sph galaxies than the metal poor ones. In addition, the models converge towards the bulk of the dwarf elliptical galaxies, and this conclusion also holds when only the bright Sph systems are considered, strengthening the idea that the Sph descendents of LCBGs are the more luminous ones.

4.6 Summary and Conclusions.

We have used spatially resolved STIS long-slit spectroscopy together with WFPC2 I and V imaging to investigate the stellar populations found in the innermost (line-emitting) regions of four LCBGs at intermediate z. We have shown evidence for a very important underlying stellar population. This population is somewhat evolved and accounts for most of the mass of the systems, despite the high look-back times probed. The line-emitting region is found to be very concentrated, although it is not always in the center of the observed galaxies. It has also been found that, should LCBGs finally evolve into dwarf elliptical galaxies via the passive evolution scenario presented here, their metal content must be in the higher end of the interval allowed by their observed line ratios. Furthermore, their Sph descendants can only be the more luminous and red of such systems. The comparison of the LCBG models with the underlying population of luminous and local HII galaxies indicates that, with the data at hand, the star formation histories of the observed LCBGs and local HII galaxies are similar in that both galaxy types are age composite systems. The observed differences in the

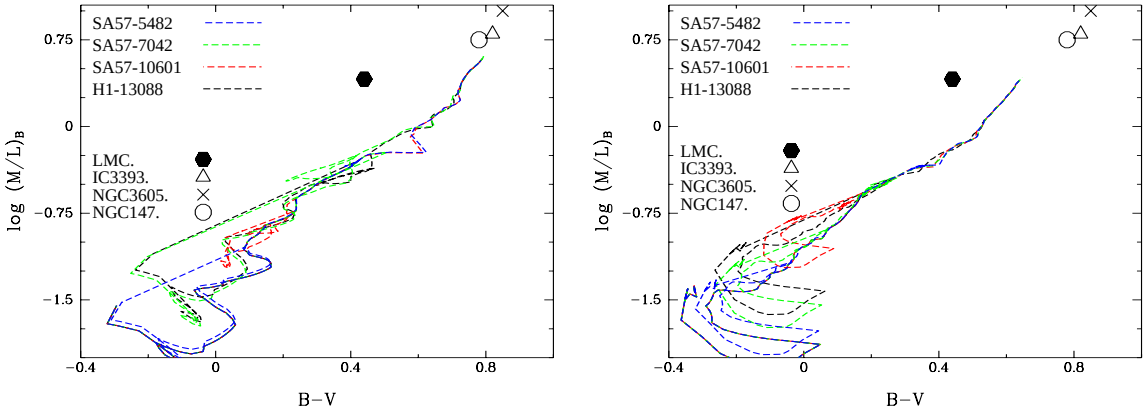

Figure 4.6: Model evolution in the $(B-V)$–(M/L_B) plane. As before, the left panel represents the first set of models, while the right panel represents the metal-poor models. Individual symbols represent the position of several well known local spheroidal systems, as indicated in the figure. The Large Magellanic Cloud is included, too.

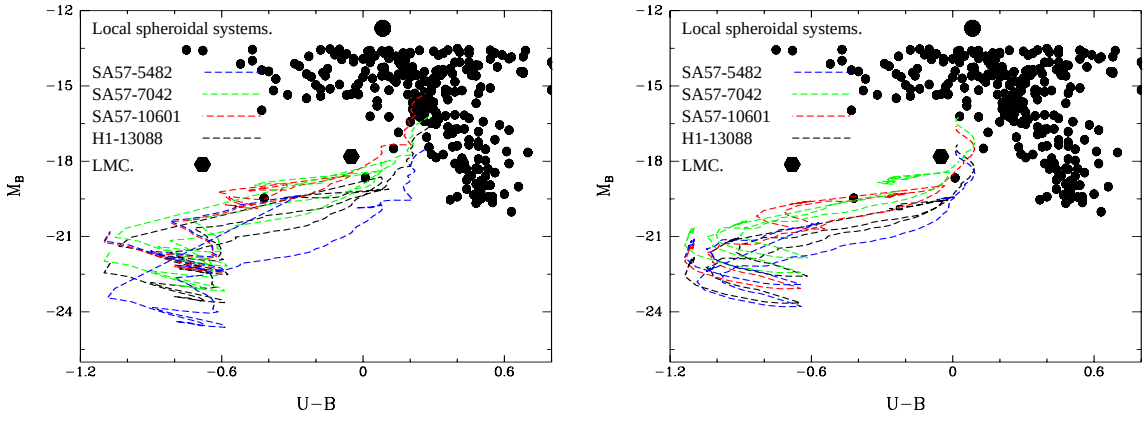

Figure 4.7: Model evolution in the $(U-B)$–M_B plane. The black dots represent the dwarf elliptical systems from Guzmán (1994). The Large Magellanic Cloud is included as an hexagon.

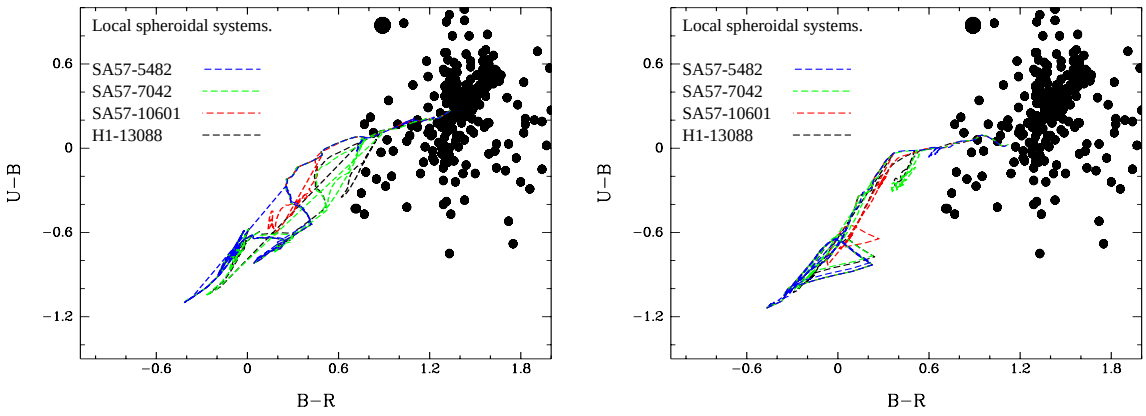

Figure 4.8: Evolution in the $(U-B)$–$(B-R)$ plane of the stellar populations that best represent the observed LCBGs. The left panel represents the first set of models, while the right panel represents the metal-poor models. Symbols as in the previous figures..

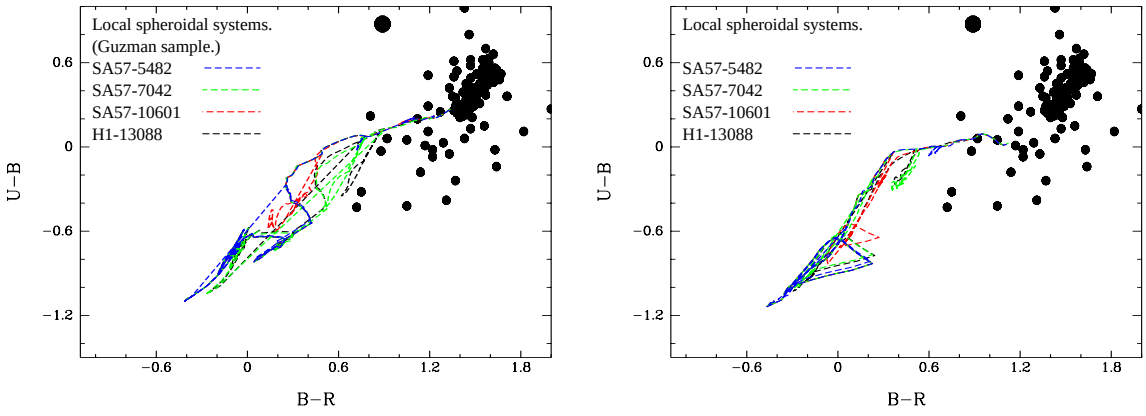

Figure 4.9: Same as figure 4.8. Only Sph galaxies brighter than $M_B = -15.0$ are included.

red colors might arise from differences in the relative numbers of red giant stars caused by age differences.

Bibliography

Balzano V. A., 1983, ApJ, 268, 602

Bender R., Burstein D., Faber S. M., 1992, ApJ, 399, 462

Bershady M.A., et al. (in prep)

Bruzual G., Charlot S., 2003, MNRAS, 344, 1000

Burstein D., Heiles C., 1984, ApJS, 54, 33

Caon N., Cairós L. M., Aguerri J. A. L., Muñoz-Tuñón C., 2005, ApJS, 157, 218

Díaz A.I., 1999, Ap&SS , 263, 143

Díaz A. I., Álvarez M. Á., Terlevich E., Terlevich R., Portal M. S., Aretxaga I., 2000, MNRAS, 311, 120

Edmunds M. G., Pagel B. E. J., 1984, MNRAS, 211, 507

Fukugita M., Shimasaku K., Ichikawa T., 1995, PASP, 107, 945

Garland C. A., Pisano D. J., Williams J. P., Guzmán R., Castander F. J., 2004, ApJ, 615, 689

Guzmán, R. PhD Thesis 1994, University of Durham, UK.

Guzmán R., Koo D. C., Faber S. M., Illingworth G. D., Takamiya M., Kron R. G., Bershady M. A., 1996, ApJ, 460, L5

Guzmán R., Gallego J., Koo D. C., Phillips A. C., Lowenthal J. D., Faber S. M., Illingworth G. D., Vogt N. P., 1997, ApJ, 489, 559

Guzmán R., Jangren A., Koo D. C., Bershady M. A., Simard L., 1998, ApJ, 495, L13

Hammer F., Gruel N., Thuan T. X., Flores H., Infante L., 2001, ApJ, 550, 570

Hoyos C., Guzmán R., Bershady M. A., Koo D. C., Díaz A. I., 2004, AJ, 128, 1541 (Chapter 3)

Hoyos C., Díaz A. I., 2006, MNRAS, 365, 454 (Chapter 2)

Jangren A., Bershady M.A., Conselice C., Koo D.C., Guzmán R., 2003, AJ submitted

Kennicutt R. C., Tamblyn P., Congdon C. E., 1994, ApJ, 435, 22

Kewley L. J., Dopita M. A., 2002, ApJS, 142, 35

Koo D. C., Bershady M. A., Wirth G. D., Stanford S. A., Majewski S. R., 1994, ApJ, 427, L9

Koo D. C., Guzman R., Faber S. M., Illingworth G. D., Bershady M. A., Kron R. G., Takamiya M., 1995, ApJ, 440, L49

Leitherer, C., et al., 1999, ApJS, 123, 3

Lilly S. J., Tresse L., Hammer F., Crampton D., Le Fevre O., 1995, ApJ, 455, 108

Loose H.-H., Thuan T. X., 1986, ApJ, 309, 59

McGaugh S. S., 1991, ApJ, 380, 140

Osterbrock D.E., 1989, Astrophysics of Gaseous Nebulae and Active Galactc Nuclei (Mill Valley:University Science Books)

Pagel B. E. J., Edmunds M. G., Blackwell D. E., Chun M. S., Smith G., 1979, MNRAS, 189, 95

Pagel B. E. J., Edmunds M. G., Smith G., 1980, MNRAS, 193, 219

Papaderos P., Loose H.-H., Thuan T. X., Fricke K. J., 1996, A&AS, 120, 207

Papaderos P., Loose H.-H., Fricke K. J., Thuan T. X., 1996, A&A, 314, 59

Phillips A. C., Guzman R., Gallego J., Koo D. C., Lowenthal J. D., Vogt N. P., Faber S. M., Illingworth G. D., 1997, ApJ, 489, 543

Pilyugin L. S., 2000, A&A, 362, 325

Sandage A., Tammann G. A., 1974, ApJ, 190, 525

Sargent W. L. W., Searle L., 1970, ApJ, 162, L155

Searle L., Sargent W. L. W., 1972, ApJ, 173, 25

Telles E., Melnick J., Terlevich R., 1997, MNRAS, 288, 78

Telles E., Terlevich R., 1997, MNRAS, 286, 183

Terlevich R., Melnick J., Masegosa J., Moles M., Copetti M. V. F., 1991, A&AS, 91, 285

Terlevich A. I., Caldwell N., Bower R. G., 2001, MNRAS, 326, 1547

van Zee L., Skillman E. D., Salzer J. J., 1998, AJ, 116, 1186

Westera P., Cuisinier F., Telles E., Kehrig C., 2004, A&A, 423, 133

Whitford A. E., 1958, AJ, 63, 201

Zwicky F., 1965, ApJ, 142, 1293

Chapter 5

Internal Kinematics of Luminous Compact Blue Galaxies.

Abstract.

We describe the dynamical properties which may be inferred from *Hubble Space Telescope* (HST) spectroscopic observations of Luminous Compact Blue Galaxies (LCBGs) between $0.1 < z < 0.7$. The spectra used were obtained using the STIS instrument on board the HST. While the sample is homogeneous in blue rest-frame color ($B-V \leq 0.6$), small size ($R_e \leq 3.0$kpc.) and line-width (velocity dispersion $\sigma \leq 65$km s^{-1}), and high surface-brightness ($\mu_B \leq 21.0$ mag $''^{-2}$) , their detailed morphology is eclectic. Here we determine the amplitude of rotation versus random, or disturbed motions of the ionized gas. This information affirms the accuracy of dynamical mass and Mass-to-Light ratios estimates from previously obtained integrated line-widths using the Low Resolution Imaging Spectrograph in the W.M. Keck telescopes, and hence also the predictions of the photometric fading of these unusual galaxies. The resolved kinematics indicates that this small subset of LCBGs are dynamically hot, and unlikely to be embedded in disk systems.

We then focus our attention on two galaxies that merit special attention. One of them is the only dynamically cold member of the sample and the other one has a very high areal star formation rate. These two LCBGs lie at $z = 0.095$ and $z = 0.285$, and their blue absolute magnitudes are -17.5 and -19.8 respectively. These galaxies are very compact, their

apparent half-light radii being $0.90''$and $0.79''$. These objects also present exponential light profiles. The imaging data used were obtained with the Wide Field Camera, which was also installed on the HST. Using these data, mass-to-light (M/L) ratios can be derived for these two particular sources, and are used to constrain the stellar populations present in their central regions.

The kinematical properties of these two sources are also compared with the properties observed in both local and intermediate redshift galaxy samples, with the aim of placing these galaxies in the Hubble sequence.

5.1 Introduction.

The temporal evolution and fate of galaxies is a key issue in cosmology. Although this subject is far from being closed, it is known that the earlier universe had a greater fraction of blue galaxies than the present-time universe. This evolutionary trend has been observed both in clusters (Lavery, Pierce, & McClure, 1992; Dressler et al., 1993) and in the field (Lilly et al., 1995; Ellis et al., 1996) The low-mass, starbursting galaxies known as Luminous Blue Compact Galaxies (LCBGs) are certainly responsible for a great part of this color evolution in field galaxies (see, for instance Guzmán et al., 1997; Cowie et al., 1996; Ellis et al., 1996). The evolution of LCBGs is a matter of debate. These galaxies are unusual in their blue colors, small sizes and line-widths, yet large luminosities. It has been proposed that at least a fraction of these very luminous, blue, compact objects are the progenitors of spheroidals (Sph) systems like NGC205 or NGC147 (Koo et al., 1995; Guzmán et al., 1998). It has also been pointed out that these systems might be bulges in the process of formation (Hammer et al., 2001; Barton & van Zee, 2001) However, samples at intermediate redshift often include heterogeneous populations in which the explored objects span a range in size, color, luminosity, surface-brightness, and morphology. The different objects will therefore follow a broad variety of evolutionary paths. This very broad LCBG class contributes to 45% of the comoving star formation rate between $0.4 \leq z \leq 1.0$, although it contributes with a negligible amount to today's global SFR (Guzmán et al., 1997). The galaxies analyzed here belong to an extreme LCBG sub-class. They are among the smallest, bluest and highest surface-brightness objects (Koo et al., 1995). Their properties are $M_B \sim -21$ (H_0=70 km/s/Mpc, Ω=1, Ω_Λ=0.7), rest-frame $B-V\sim$0.25, half-light radii of $R_e \sim$ 2kpc, mean surface-brightness within R_e of $\sim$19 mag/arcsec^2 (rest-frame B band), and integrated line-widths of $\sigma_{gas}\sim$65 km/s. Many of these

are good candidates for Sph progenitors. If so, their internal kinematics should reveal they are dynamically hot, while deep imaging should show they lack outer disks. Another very important issue for galatic evolution models is to detect any change in the Tully-Fisher or Faber-Jackson relationships. At very large distances, peculiar motions can be safely neglected and thus, any deviation from the local relationship larger than the intrinsic scatter is likely to be caused by evolution. In this sense, intermediate redshift galaxies, being bluer, should be more luminous than local systems of similar rotation speeds or velocity dispersions. In this chapter, two very different examples of this LCBG class are selected for further inspection. One of them is a clearly rotating system, with a well defined disk, while the other is a dynamically hot system, dominated by random motions. The observations and analysis are presented in section 5.2. Section 5.3 presents the kinematical analysis of the observed objects and its evolutionary implications for the observed galaxies. The two more interesting systems are compared to both local and distant systems in section 5.4.2. The conclusions follow in section 5.5.

The cosmology assumed through this chapter is a flat universe with H_0=70km s^{-1}Mpc^{-1} and a decceleration parameter $q_0 = -0.55$.

5.2 Details of the Observations.

The data used to study these objects includes high-resolution long-slit spectra and deep V images. The latter are used here to further study the nature of the two selected LCBGs.

The long-slit spectra were obtained in 2001 and 2002 using the STIS instrument, on board the Hubble Space Telescope. The detector used was the STIS/CCD, a SITe 1024x1024 chip, with $0.05''$ square pixels operating from ∼2000 to 11000 Å. For most of the objects, the grating used was the G750M with a slit width of only $0.2''$. It provides a dispersion of 0.53 Å per pixel or about 35 km s^{-1} per pixel. The spectral resolution is therefore about 2.2Å (FWHM). The spectral coverage provided by this setup is about 500 Å. The spectra allowed to measure the gas-phase velocity dispersion via the Hα line. For a complete account of the reduction procedures, see chapter 3. The lower-resolution grating G430M and the high-resolution grating G750M were also used. The G430M grating has a dispersion of 2.7 Å per pixel and the slit width used is $0.2''$. The central wavelength is 4300 Å, and the spectral coverage is 2800 Å. The last instrumental setup used employed the low resolution grating G750L. This instrumental setup provides a dispersion of 4.92 Å per pixel or about 190 km

	SA68-6134	H1-13385
RA	00 18 11.34	17 21 15.72
DEC	15 47 52.8	50 01 38.0
Exp time.	5519(3400)	5947(2400)
z.	0.285	0.095
$t_{look-back}$(Gyr)	2.9	1.2
M_B	-19.8	-17.5
R_e	0.94	0.67
m_B	21.4	20.9
r_e	0.23	0.39
$M_{B,core}$	-19.11	-17.05
B-V	0.32	0.33
$\log R_{25}^V$	1.8	3.4

Table 5.1: Main properties of two galaxies studied in more detail. Coordinates given for equinox J2000. STIS Spectra exposure time(WFC1 Imaging exposure time). Half-light radii are given both in Kpc (R_e) and arcseconds (r_e). $M_{B,core}$ is defined in the text. $R_{0.25}$ is the radius containing 25% of the total light in the *rest frame V band*, in Kpc units, assuming an exponential disk (Koo et al., 1994).

s^{-1} per pixel which, in combination with a slit $0.5''$ wide, gives a spectral resolution of about 29Å(FWHM)

The deep V images used were obtained using the WF/PC-1 instrument, which was also carried by the HST. The detector used was the WFC, which is an array of 2×2 800x800 chips, with $0.102''$ square pixels. Two exposures were taken for each object using the F555W filter to allow cosmic ray-rejection. The two exposures were offset by one half pixel in each direction. The details of these observations, as well as a more detailed analysis including drizzling of the images to improve the spatial sampling by a factor of 1.4 and careful Lucy restoration of the spatial information are given in Koo et al. (1994).

The data reduction and analysis were carried out using the STSDAS[1] package, which is available within the IRAF [2] routines.

Target names, redshifts, look-back times, B absolute magnitudes, exposure times and half light-radii for the two selected objects can be seen in table 5.1.

[1]Space Telescope Science Data Analysis System. This package was programmed by the Space Telescope Science Institute, operated for NASA by AURA

[2]Image Reduction and Analysis Facility. Distributed by the National Optical Astronomy Observatories, which is operated by AURA (Association of Universities for Research in Astronomy, Inc) under cooperative agreement with the National Science Foundation.

5.3 Kinematical Analysis. Are LCBGs Dynamically Hot or Cold?

The position–velocity and position–linewidth diagrams for the ionized component of the observed objects are plotted using STIS long-slit measurements along what appears to be the photometric major axes of 6 LCBGs between $0.2 < z < 0.7$, and one other LCBG at $z \sim 0.1$ which is 2-3 mag lower luminosity than the others. This latter source is studied in more detail below. One example is given in figure 5.1. With 0.2 arcsec slits, STIS delivers instrumental resolutions (σ) of 13-19 km s^{-1}. The line-emission of these galaxies is not always centered on the continuum (see chapter 3). The continuum centroid is adopted as the kinematic center.

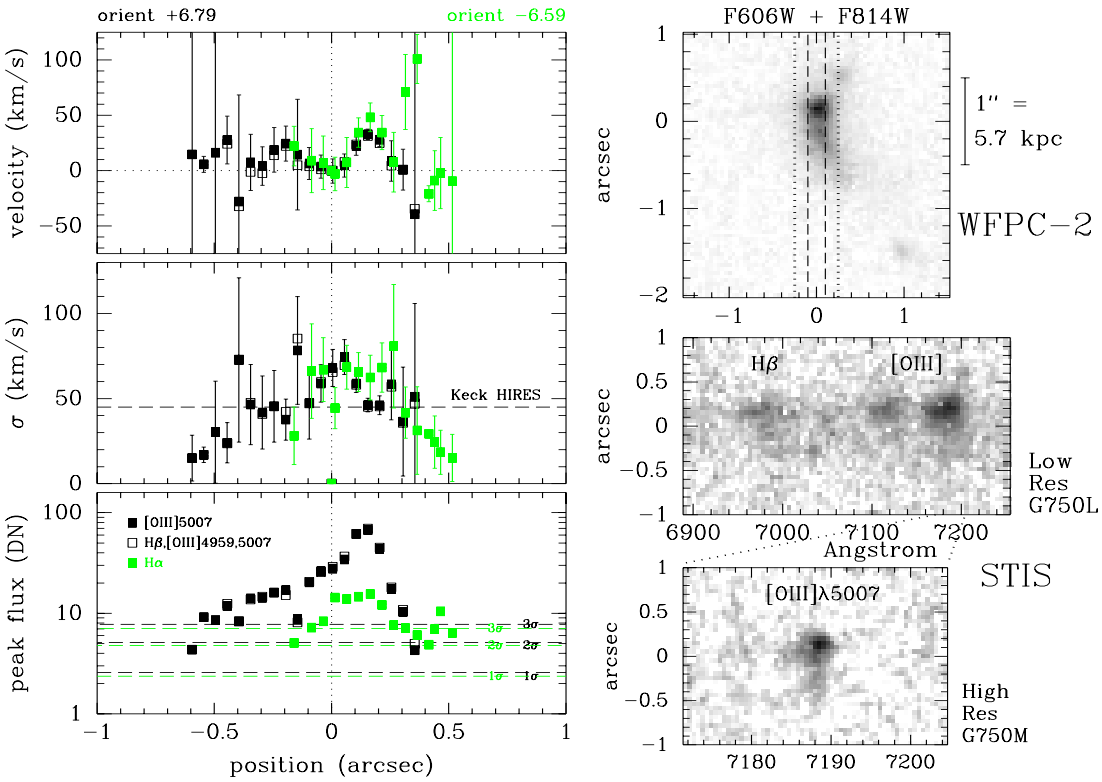

Figure 5.1: Morphology and kinematics of LCBG H-13088 at $z = 0.44$. Left: HST/WFPC-2 image showing distorted, tail-like source morphology and mean STIS slit positions (0.2 and 0.5 arcsec). STIS spectra for low and high-resolution gratings are at bottom. Right: Position vs velocity, line-width, and line-flux for two sets of high-resolution data taken at two position angles varying by $\sim 13°$. Spectral data consistently show extended line-emission with little velocity gradient, no evidence for rotation, and dispersions that agree in the mean with Keck HIRES integrated measurements (dashed line, middle panel).

We find Keck HIRES integrated line-widths (Koo et al., 1995) agree in the mean with the resolved velocity dispersions from STIS spectroscopy. Therefore, integrated dispersions are not due to large-scale bulk motion. This secures our previous dynamical estimates of Mass-to-Light ratios and their use as constraints on photometric fading (Guzmán et al., 1998). Only the low-L, low-z system shows clear rotation and substantially different integrated versus resolved line-widths.

The lack of rotation coupled with their ellipticity squarely places these sources in the "spheroidal" region of the $V_{\rm rot}/\sigma-$ ellipticity plane, illustrated in figure 5.2. For fair comparison to local samples, ellipticities are measured at the half-light radius near rest-frame V-band from HST images, rotation velocities are set to half the difference between minimum and maximum velocities, and σ is the observed central velocity dispersion. While there is a range of observed $V_{\rm rot}/\sigma$, LCBGs lie well below the region where disk systems dwell, with values comparable to local Sph, particularly if recent observations of dEs with larger rotational components are considered (Pedraz et al., 2002; van Zee, Skillman, & Haynes, 2004). LCBGs are therefore dynamically hot systems, similar to dE galaxies in that the inner kinematics of both galaxy types are dominated by random motions.

5.3.1 The Evolution of the Observed LCBGs. Evidence from Kinematical Data.

How do we know that we aren't just sampling a bulge, or a face-on nuclear star-burst? NGC7673 has been suggested by Homeier, Gallagher, & Pasquali (2002) as a nearby example. Indeed this source has the right color, surface-brightness, size, luminosity and integrated line-width, and has a faint, extended outer disk, and the Hα velocity map presented in Homeier & Gallagher (1999) shows clear evidence for rotation in the inner, star-burst region. However, we would see similar structures and rotation curves in the STIS spectra *if they existed*, as the detection of the rotation curve for the nearest galaxy clearly shows. Independently, deep CFHT imaging reveals no strong evidence for extended, normal disks around the sources presented here nor around other similar objects at intermediate redshift. (Barton, van Zee, & Bershady, 2006). These two facts lend further support to the idea of LCBGs being galaxies supported by random motions, rather than being rotationally-supported systems.

It is therefore concluded that the observed LCBGs are kinematically similar to Sph systems.

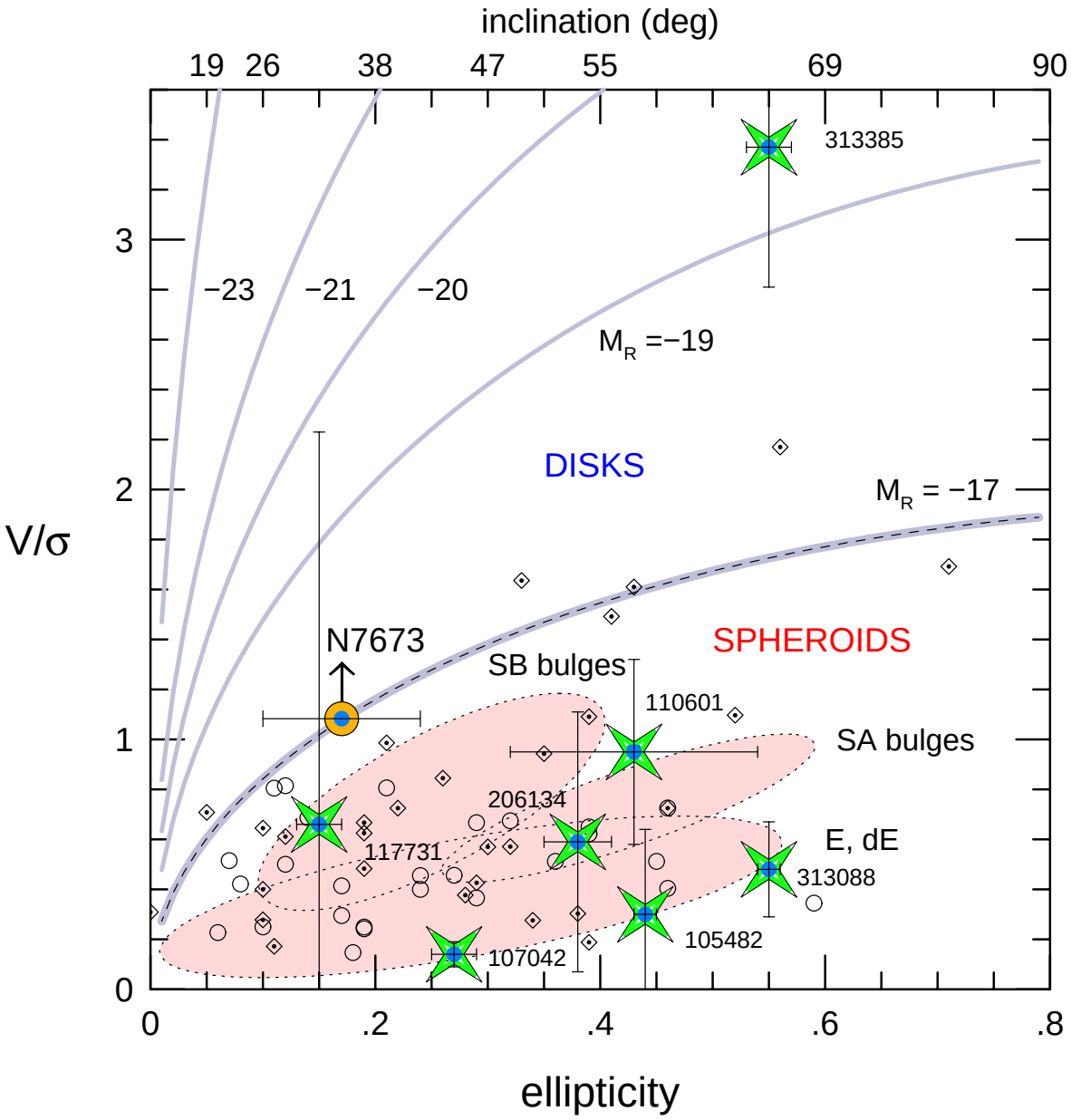

Figure 5.2: V/σ versus ellipticity or inclination for LCBGs (dotted stars), NGC 7673 (circle/lower limit) and early-types galaxies from Simien & Prugniel (2002) (circles, dotted diamonds). Lines represent trajectories as a function of inclination for disk-galaxies of different luminosity assuming they lie on the Tully-Fisher relation and σ_{gas} = 25 km s^{-1} (Andersen et al., 2006). Shaded regions are adopted from Kormendy & Kennicutt (2004).

5.4 The Central Kpc of H1-13385 and SA68-6134.

5.4.1 Data Analysis. Position-Velocity Diagrams and Light Profiles.

The STIS spectra allow to study the kinematics of the hot gas phase present in the target objects in high detail. In particular, we focus on the conspicuous rotation curve observed in the H1-13385 data and the variation of the velocity dispersion along the slit. The rotation curve was built using the Intensity-Weighted Velocity Method (Warner, Wright, & Baldwin, 1973), using the Hα line to probe the circular velocity curve of the ionized gas phase. Figure 5.3 presents the rotation curve along the photometric major axis of H1-13385. The point with highest surface brightness is taken to be the center of the galaxy, and its rotation speed is set at 0 km/s. The formal uncertainty in the velocity points is roughly the size of the points used and reflects the quality of the Gaussian fits to the data. These formal errors are much larger than any systematic error. The velocity dispersion is also measured in each data point along the slit. The vertical difference of the two thin lines of figure 5.3 is twice the velocity dispersion. It is seen in figure 5.3 that H1-13385 presents a clear rotation curve. The measured rotation velocity is 107 ± 8 km s^{-1}. However, the velocity dispersion does not vary a great amount along the slit. Its average value is 55 km s^{-1}, and the *rms* is 13 km s^{-1}. The integrated velocity dispersion is 60 ± 5 km s^{-1}. This system is therefore a dynamically cold system, mainly supported by rotation, although random motions are not negligible in the integrated velocity dispersion budget. In this case, the integrated velocity dispersion arises predominantly from the galaxy's own rotation. The rotation curve plotted in figure 5.3 is obviously not complete, since it does not reach the flat regime observed in disk galaxies. The position-velocity diagram for this galaxy does not reach beyond 1 kpc. This might indicate that there is not much ionized gas at larger distances, or it may merely reflect that the spectra used do not have enough S/N to probe the outer regions of the galaxy. Although both possibilities are bound to have a say in the final answer, it can be anticipated that the first option is the more relevant, since the velocity dispersion for this object reported in Guzmán et al. (1996) is 68 km s^{-1}, measured with the HIRES instrument on the W.M. Keck telescope, only 13% higher than the STIS measurement.

In the case of SA68-6134 no ordered motion was detected. The position-velocity diagram is shown in figure 5.4. In most cases, the measured radial velocity has an error smaller than the size of the points used. However, for the outermost extractions, the wavelength uncertainty is much larger because it was neccessary to sum many lines. It is seen that

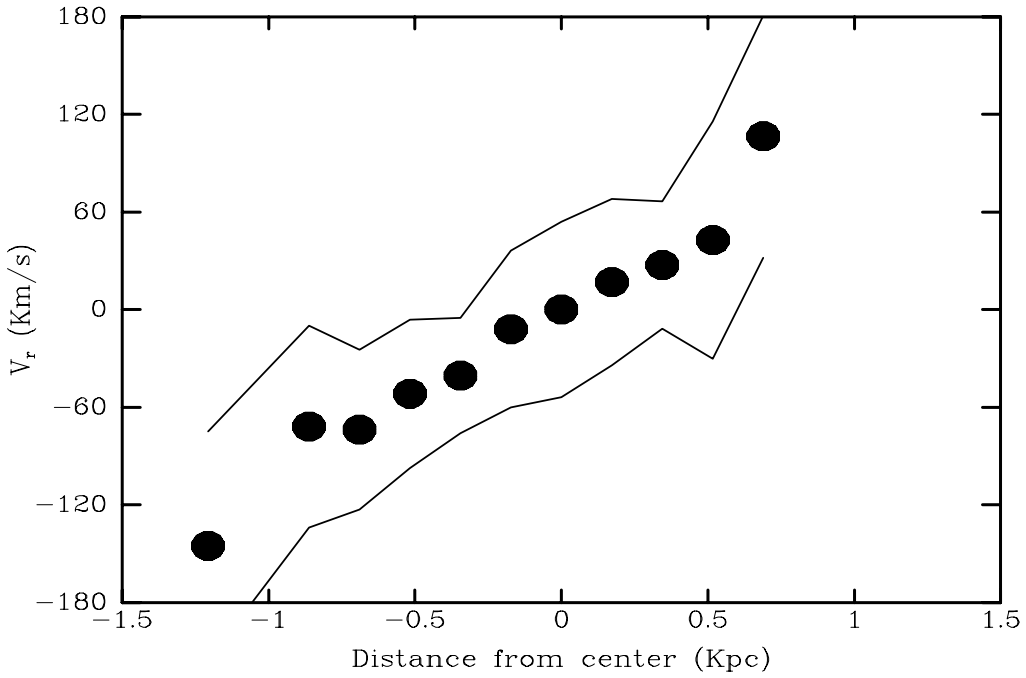

Figure 5.3: Hα rotation curve for H1-13385. The two lines surrounding the data points represent the velocity sigma at each point.

SA68-6134 is indeed a kinematically hot source. No ordered motions are detected along its photometric major axis. The velocity sigma is also pretty much constant along the slit. The average value is 55 km s^{-1}, and the *rms* is again 14 km s^{-1}. These two observations indicate that this is indeed a dynamically hot system. The integrated velocity dispersion does not arise from large-scale, bulk motions. The integrated velocity dispersion measured for this object is 47 ± 5 km s^{-1}. This system has to be supported by random motions. As in the previous case, it is believed that the STIS spectra probe the vast majority of the ionized gas in this object, since the HIRES measurement, again given in Guzmán et al. (1996) is 41 km s^{-1}.

The WFC1 broadband images were used to study the light profiles of the two LCBGs presented. The luminosity profiles were derived by simply fitting circular apertures to the images, keeping the center of each aperture fixed in each object's centroid. Figures 5.5 and 5.6 show both profiles. The vertical axis is proportional to the *observed* V-band surface brightness, although it is not calibrated on any absolute scale. It can be clearly seen that both galaxies have exponential profiles, although it is also true that both systems present a

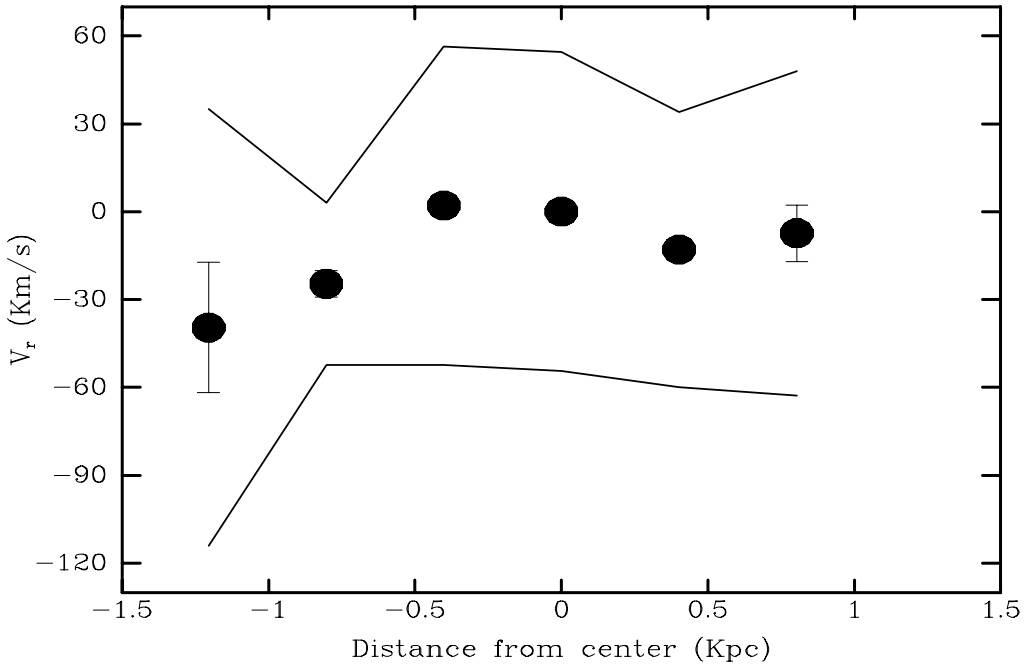

Figure 5.4: Hα position-velocity diagram for SA68-6134. The two lines surrounding the data points represent the velocity sigma at each point.

bump in their profiles. It has to be said, however, that the presented light profiles were built from images that were manufactured by simply registering and co-adding the two available WF/PC-1 images (i.e. no drizzling or Lucy restoration was performed, as in the much more detailed work of Koo et al. (1994)). These figures are shown so as to have a crude idea of the light profiles of these two systems. The disk scale lengths, obtained from the Koo et al. (1994) fits, are 0.40 kpc and 0.56 kpc for H1-13385 and SA68-6134 respectively.

The STIS and WFC1 data also allow to estimate the mass-to-light ratios of the central regions of the two sources presented. The mass within any given radius can be obtained via the virial theorem, according to this expression[3]:

$$\log M/M_{\odot} = 6.08 + \log R(\mathrm{kpc}) + 2 \times \log \sigma(\mathrm{km\ s^{-1}}) \tag{5.1}$$

This expression is used to calculate the mass within the line-emitting region of the studied objects.

[3]The expression used originates from $M = 3kG^{-1}R\sigma^2$, where the structural constant k varies with different galaxy surface density profiles. Since the surface brightness profile of the presented sources is an exponential law, we adopt $k = 1.7$, following Bender, Burstein, & Faber (1992); Guzmán et al. (1996).

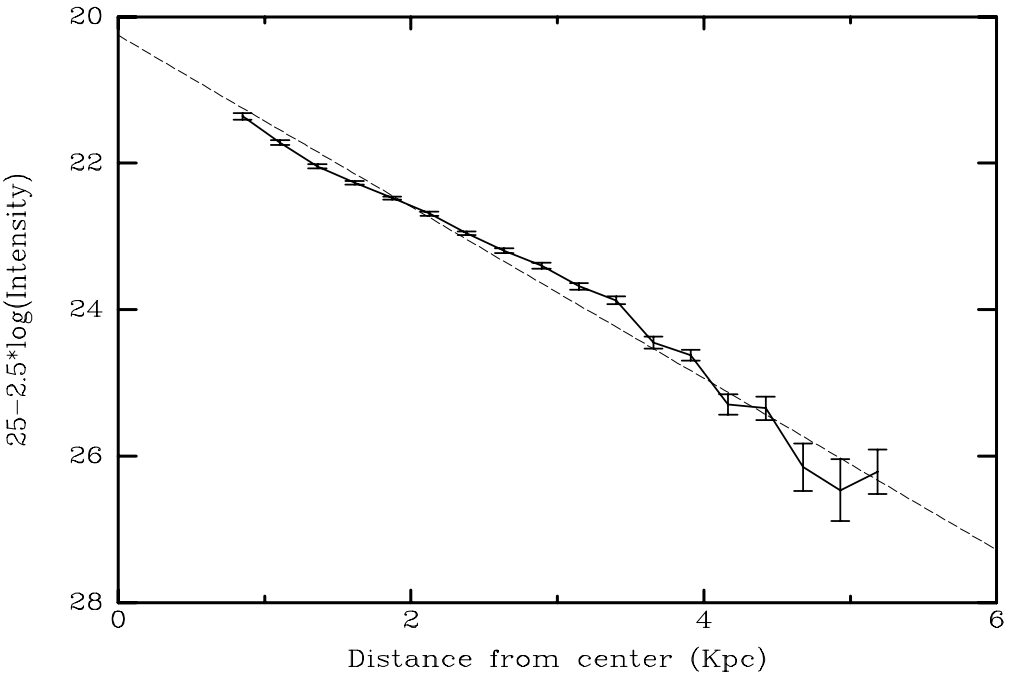

Figure 5.5: Light profile for H1-13385. The straight line shown is a linear fit to the data. The vertical axis is proportional to the *observed* V-band surface brighness, but it is not calibrated on an absolute scale.

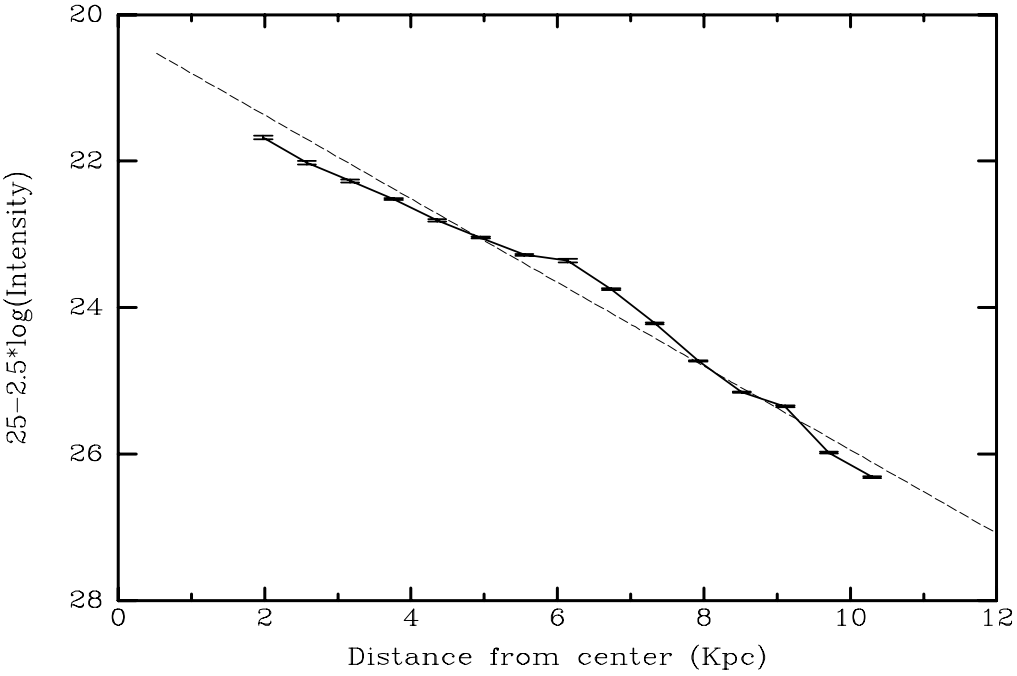

Figure 5.6: Light profile for SA68-6134. The straight line shown is a linear fit to the data. The vertical axis is proportional to the *observed* V-band surface brighness, but it is not calibrated on an absolute scale.

In H1-13385 it extends to 0.95 kpc, whereas the ionized zone of SA68-6134 has a radius of 1.0 kpc. In the case of H1-13385, the velocity sigma used is set to 0.7 times the rotation speed, following Phillips et al. (1997). No correction for inclination is taken into account. Therefore, the mass calculations are only lower limits. The mass within the central kpc of H1-13385 is $10^{9.81\pm0.07} M_{\odot}$ and the mass within the line-emitting region of SA68-6134 is $10^{9.4\pm0.1} M_{\odot}$.

On the other hand, the HST images allow to estimate the luminosity output from the central Kpc of the galaxies studied.

$$L_{core}/L_{\odot} = 10^{\frac{5.48 - M_{B,core}}{2.5}} \tag{5.2}$$

where 5.48 is the sun's B-band absolute magnitude and $M_{B,core}$ is the B-band magnitude of the central Kpc. It is estimated using the following expression.

$$M_{B,core} = M_B + \Delta + 0.73 - 0.6516 \times z \tag{5.3}$$

where M_B is the blue absolute magnitude reported in Koo et al. (1994), the Δ is the fraction of the total luminosity emitted originating from the line emitting region estimated using the exponential fits given in Koo et al. (1994), and the rest of the expression is used to convert the Koo et al. (1994) magnitudes to the cosmology used in this work.

Using these data, it results that the mass-to-light ratio of the central Kpc of H1-13385 and SA68-6134 are 6.3 and 0.4, respectively. Assuming that M/L is constant throughout both galaxies, the total masses would be $10^{10.0\pm0.07} M_\odot$ and $10^{9.70\pm0.1} M_\odot$ for H1-13385 and SA68-6134 respectively.

These Mass-to-Light ratios correspond to very different stellar populations. In the case of SA68-6134, the derived ratio is indicative of a population 4.50×10^8–10^9 years old. The stellar populations found in H1-13385 are much older, probably older than 5.5×10^9 years, according to the Bruzual & Charlot (2003) models. The stellar inventory found in H1-13385 is probably very similar to that found in S0, or early type spiral galaxies. This shows that the stellar populations found in distant LCBGs can be quite different from one another. This is likely to have a critical impact on the evolution of this galaxy class. On the other hand, the stars found in the SA68-6134 system are bound to be more similar to the stars found in post-starburst systems. We are probably witnessing a new starburst on top of yet another starburst not quite extinguished.

The available data allow to speculate further about the nature of the presented objects. This step is carried out by trying to place the intermediate redshift objects in the Hubble sequence. In particular, blue absolute magnitudes, $B-V$colors and B-band bulge effective radii are used. The comparison samples selected are those of Simien & de Vaucouleurs (1986) and Roberts & Haynes (1994).

For the Irregular Magellanic (Im) galaxy type, the average M_B is -17.95 ± 0.2, the average $B-V$is 0.4 ± 0.1, and the average bulge effective radius is 0.25 ± 0.10 kpc. The blue absolute magnitude and $B-V$color of H1-13385 lie well within the given range for the Im family. In addition, the only value of the average bulge effective radius among the different Hubble types found in Simien & de Vaucouleurs (1986) compatible with the observed R_e of H1-13385 is the one reported for Im galaxies, the other galaxies having bulges larger than 0.67kpc in R_e. We therefore conclude that H1-13385 is very similar to an Im galaxy. This view is also supported by the fact that the star forming cluster hosted by this object is very similar in both luminosity and areal star formation rate to the 30 Doradus cluster, in the Large

Magellanic Cloud (Hoyos et al., 2004, Cap 3.). This suggests that H1-13385 is a distant twin of the Large Magellanic Cloud. Furthermore, the LMC also presents a disk structure and a rotation curve (Gondolo., 1993; Alves & Nelson, 2000) very similar to the position-velocity curve presented in 5.3. Both circular speed curves are very steep, although the rotation curve of the LMC is somewhat flatter, maybe because of inclination effects. This strengthens our conclusion and H1-13385 is best classified as an Im galaxy (Guzmán et al., 1998).

The case of SA68-6134 is more complex, and it is not possible to find a neat place for it in the Hubble sequence. The blue absolute magnitude of this galaxy is compatible with virtually every major galaxy type along the sequence. The position–velocity diagram indicates that this galaxy is not likely to have a clearly defined disk structure. It is also the case that the effective radius of this galaxy is large enough so as to make it compatible with a very broad range of galaxy types. In addition, the observed $B-V$color of this galaxy is very similar to that shown by Sd spirals or irregular galaxies. We conclude that SA68-6134 is an irregular system, which can not be unambiguously classfied in the Hubble sequence. It is likely to be similar to local BCGs or HII galaxies.

5.4.2 Comparison with Local Galaxy Samples.

The rotation curve shown in figure 5.3 is, to our knowledge, the most detailed one of an intermediate redshift Blue Compact Galaxy (BCG) presented till now. It is therefore very interesting to compare it to the rotation curves observed in similar local systems. In this section, the galaxy H1-13385 is compared to a sample of 8 BCGs taken from Östlin et al. (1999). Their objects are very similar to the two objects presented in this chapter. The blue absolute magnitudes[4] range from -17.8 to -20.0, and the masses go from $10^{9.3}M_{\odot}$ to $10^{10.7}M_{\odot}$. Mass-to-Light ratios are in the 0.2 to 8.6 interval, although most of the values lie in the much shorter range 1–3. These intervals engulf the values for the two galaxies analysed here.

It is very difficult to properly compare the rotation curve for H1-13385 with the data given in Östlin et al. (1999), since the rotation curve of the intermediate-redshift object is not complete nor it is as detailed as those available for the local sources. However, it is possible to compare the slope of the rotation curve and the circular speed at a distance of 1kpc. The first quantity is directly related to the depth of the gravitational well of the galaxy, while the second one is indicative of the mass concentration. The slope of the position–velocity curve

[4]Assuming $B-V$=0.5.

of H1-13385 is 110 ± 3km s^{-1}kpc^{-1}, and the circular speed at 1 kpc is 106 ± 8 km s^{-1}. The measured slope of the rotation curve of H1-13385 is typical of spiral systems (Sofue & Rubin, 2001). In the case of the local BCGs, their slope has an average value of 58 km s^{-1}kpc^{-1}, and the *rms* is 23 km s^{-1}kpc^{-1}. All of them have a slope flatter than that of the intermediate redshift object. The rotation velocity attained at 1kpc is between 18 km s^{-1} and 55 km s^{-1} for the local BCG sample, while the rotation speed at 1 kpc for H1-13385 is 106 ± 8 km s^{-1}. These numbers indicate that the mass concentration towards the center is much larger in the intermediate-redshift object.

It is also interesting to compare the rotation curve of H1-13385 to other rotation curves of distant spiral galaxies, in an attempt to discover if this galaxy fits within the Tully-Fisher (TF) relation (Tully & Fisher, 1977; Tully et al., 1996; Pierce & Tully, 1988). The spiral galaxies presented in Vogt et al. (1993), Vogt et al. (1996) and Simard & Pritchet (1998) are used. The distant spiral galaxies presented in Vogt et al. (1993) and Vogt et al. (1996) show rotation curves much flatter than the rotation curves found in the intermediate redshift objects or local BCGs, despite attaining much higher *final* rotation speeds. The rotation curves of the distant spiral galaxies show *observed* slopes mostly in the range 30 ± 10km s^{-1}kpc^{-1}, indicating again that the mass density in H1-13385 is larger than the density of the distant spiral galaxies. The distant spiral galaxies presented in Simard & Pritchet (1998) are very similar to the galaxies studied in Vogt et al. (1993) and Vogt et al. (1996). Therefore, the same conclusions are drawn from the comparison of this galaxy sample to H1-13385. There are, however, three galaxies in this sample with properties very similar to the galaxy studied here. On average, the Simard & Pritchet (1998) galaxies are typically 3 magnitudes brighter than H1-13385 and they rotate faster, although their mass concentration is lower.

After comparing the intermediate redshift rotating LCBG with distant spiral galaxies, it is almost mandatory to see whether or not it fits within the Tully-Fisher relation. Here, the B-band calibration for the TF relationship given in Pierce & Tully (1988) is used. It results that H1-13385 is either about 0.8 magnitudes too bright or is rotating 30 km s^{-1} too fast. However, given the *rms* of the parametrization used it is concluded that there is no reason to believe that H1-13385 does not conform to the local Tully-Fisher relation, even though this galaxy is a very active star forming system.

5.5 Conclusions.

The kinematic data presented is against bulge formation in disk systems and in favor of a dE-like descendant scenario *for all of the specific sample presented here* with $M_B \leq -20$ (6 out of 7). However, the disturbed morphology and kinematics makes clean interpretations difficult. What is the gas really telling us about dynamics? Are these systems in dynamical equilibrium? While their morphology and resolved kinematics would argue otherwise, the agreement between integrated velocity dispersions and resolved profiles indicates that the systems cannot be too far out of equilibrium. Stellar velocity and dispersion profiles would provide a much clearer dynamical picture.

We have also studied two very different objects, both belonging to the Luminous Compact Blue Galaxy class. One of them is very similar to the Large Magellanic Cloud. The mass distribution of this objects is very peaked towards its center and mainly supported by rotation, as evidenced by its steep rotation curve. The derived Mass-to-Light ratio shown by this object implies that it is not a young system. The observed starburst is not likely to contribute to a large extent to the stellar mass already built in this system. This system is also interesting because it shows that isolated, LMC-like galaxies, did exist 2Gyr ago, and that they have remained such till today, this is a very interesting result because this is antihierarchical in nature. On the other hand, SA68-6134 is a much younger object, mainly supported by random motions. This is a very luminous irregular system very similar to the most luminous HII galaxies in the local universe.

Bibliography

Alves D. R., Nelson C. A., 2000, ApJ, 542, 789

Andersen E. J., et al., 2006, in preparation.

Barton E. J., van Zee L., 2001, ApJ, 550, L35

Barton E. J., van Zee L., Bershady, M. A., 2006, in preparation.

Bender R., Burstein D., Faber S. M., 1992, ApJ, 399, 462

Bruzual G., Charlot S., 2003, MNRAS, 344, 1000

Cowie L. L., Songaila A., Hu E. M., Cohen J. G., 1996, AJ, 112, 839

Dressler A., Oemler A. J., Gunn J. E., Butcher H., 1993, ApJ, 404, L45

Ellis R. S., Colless M., Broadhurst T., Heyl J., Glazebrook K., 1996, MNRAS, 280, 235

Guzmán R., Koo D. C., Faber S. M., Illingworth G. D., Takamiya M., Kron R. G., Bershady M. A., 1996, ApJ, 460, L5

Guzmán R., Gallego J., Koo D. C., Phillips A. C., Lowenthal J. D., Faber S. M., Illingworth G. D., Vogt N. P., 1997, ApJ, 489, 559

Guzmán R., Jangren A., Koo D. C., Bershady M. A., Simard L., 1998, ApJ, 495, L13

Gondolo P. , 1993, astro, arXiv:astro-ph/9312011

Hammer F., Gruel N., Thuan T. X., Flores H., Infante L., 2001, ApJ, 550, 570

Homeier N. L., Gallagher J. S., 1999, ApJ, 522, 199

Homeier N., Gallagher J. S., Pasquali A., 2002, A&A, 391, 857

Hoyos C., Guzmán R., Bershady M. A., Koo D. C., Díaz A. I., 2004, AJ, 128, 1541

Koo D. C., Bershady M. A., Wirth G. D., Stanford S. A., Majewski S. R., 1994, ApJ, 427, L9

Koo D. C., Guzmán R., Faber S. M., Illingworth G. D., Bershady M. A., Kron R. G., Takamiya M., 1995, ApJ, 440, L49

Kormendy J., Kennicutt R. C., 2004, ARA&A, 42, 603

Lavery R. J., Pierce M. J., McClure R. D., 1992, AJ, 104, 2067

Lilly S. J., Tresse L., Hammer F., Crampton D., Le Fevre O., 1995, ApJ, 455, 108

Östlin G., Amram P., Masegosa J., Bergvall N., Boulesteix J., 1999, A&AS, 137, 419

Pedraz S., Gorgas J., Cardiel N., Sánchez-Blázquez P., Guzmán R., 2002, MNRAS, 332, L59

Phillips A. C., Guzmán R., Gallego J., Koo D. C., Lowenthal J. D.,Vogt N. P., Faber S. M., Illingworth G. D., 1997, ApJ, 489, 543

Pierce M. J., Tully R. B., 1988, ApJ, 330, 579

Roberts M. S., Haynes M. P., 1994, ARA&A, 32, 115

Simard L., Pritchet C. J., 1998, ApJ, 505, 96

Simien F., de Vaucouleurs G., 1986, ApJ, 302, 564

Simien F., Prugniel P., 2002, A&A, 384, 371

Sofue Y., Rubin V., 2001, ARA&A, 39, 137

Tully R. B., Fisher J. R., 1977, A&A, 54, 661

Tully R. B., Verheijen M. A. W., Pierce M. J., Huang J.-S., Wainscoat R. J., 1996, AJ, 112, 2471

Vogt N. P., Herter T., Haynes M. P., Courteau S., 1993, ApJ, 415, L95

Vogt N. P., Forbes D. A., Phillips A. C., Gronwall C., Faber S. M., Illingworth G. D., Koo D. C., 1996, ApJ, 465, L15

Warner P. J., Wright M. C. H., Baldwin J. E., 1973, MNRAS, 163, 163

van Zee L., Skillman E. D., Haynes M. P., 2004, AJ, 128, 121

Chapter 6

The DEEP2 Galaxy Redshift Survey: Discovery of Luminous, Metal-poor, Star-forming Galaxies at Redshifts $z \sim 0.7$

Abstract.

We have discovered a sample of 17 metal-poor, yet luminous, star-forming galaxies at redshifts $z \sim 0.7$. They were selected from the initial phase of the DEEP2 survey of 3900 galaxies and the Team Keck Redshift Survey (TKRS) of 1536 galaxies as those showing the temperature-sensitive [OIII]λ4363 auroral line. These rare galaxies have blue luminosities close to L^*, high star formation rates of 1 to 30 $M_\odot \mathrm{yr}^{-1}$, and oxygen abundances of 1/3 to 1/10 solar. They thus lie significantly off the luminosity-metallicity relation found previously for field galaxies with strong emission lines at redshifts $z \sim 0.7$. The prior surveys relied on indirect, empirical calibrations of the R_{23} diagnostic and the *assumption* that luminous galaxies are *not* metal-poor. Our discovery suggests that this assumption is sometimes invalid.

As a class, these newly-discovered galaxies are: (1) more metal-poor than common classes

of bright emission-line galaxies at $z \sim 0.7$ or at the present epoch; (2) comparable in metallicity to $z \sim 3$ Lyman Break Galaxies but less luminous; and (3) comparable in metallicity to the local population of metal-poor star forming dwarves known as eXtreme Blue Compact Galaxies (XBCGs), but more luminous. Together, the three samples suggest that the most-luminous, metal-poor, compact galaxies become fainter over time.

6.1 Introduction.

The metal content of galaxies is an important diagnostic because it relates directly to the integral history of star formation, galaxy mass, and the inward and outward flows of gas (see reviews by Kunth & Östlin, 2000; Pagel, 1997, or, for a review on chemical evolution models, see Cen & Ostriker, 1999). Local studies reveal the existence of a luminosity-metallicity relation (LZR) (Lequeux et al., 1979; Skillman, Kennicutt, & Hodge, 1989; Kinman & Davidson, 1981; Richer & McCall, 1995; Campos-Aguilar, Moles, & Masegosa, 1993) that presumably arises from the higher retention rate of enriched gas in the gravitational wells of galaxies with larger masses, where the assumption is that more luminous galaxies are also more massive. The luminosity-metallicity relation (LZR) is expected to evolve over the lifetime of galaxies, but any predicted changes in the slope, offset, and dispersion of the LZR are subject to many uncertainties.

The metallicities of distant ($z > 0.5$) systems have been historically studied via the absorption lines seen in quasar spectra. However, this method provides metallicity estimates that can not be readily translated into the metallicities of high-redshift galaxies (Fall & Pei, 1993). At large redshifts ($z \geq 2$), and using emission-line ratios, Kobulnicky & Koo (2000, henceforth KK00) and Pettini et al. (2001) already find evidence that Lyman Break Galaxies (LBGs) of under-solar abundance are 5–40 times more luminous than local systems of similar metal content, confirming that the luminosity-to-metal ratio varies with time. The luminosity-metallicity relation for intermediate redshift ($z \leq 1$) objects is a vital link between the local populations of galaxies with high-redshift populations, such as Damped Lyman-Alpha (DLA) systems or LBGs.

Observations of the metallicity of galaxies at intermediate redshifts $z > 0.5$ have been few and include three studies of field galaxies at $z \sim 0.5$ to 1 by Kobulnicky et al. (2003, henceforth K03), Lilly, Carollo, & Stockton (2003, henceforth L03), and Kobulnicky & Kewley (2004, henceforth KK04). The distant galaxy metallicities in these studies were all based on the

[O/H][1] of the emission lines and estimated from the empirical R_{23} method introduced by Pagel et al. (1979), and further developed by McGaugh (1991) and Pilyugin (2000), among many others. No galaxies had less than 1/3 solar abundances, but this was due to the *assumption* of using the metal-rich (upper) branch of the R_{23}-metallicity relation. In addition, the K03 and KK04 studies used line equivalent widths instead of line fluxes to calculate the R_{23} number and the ionization ratio [OIII]$\lambda\lambda$4959, 5007/[OII]λ3727. Although this is the only thing that can be done with spectra that are not flux calibrated, it introduces additional uncertainities that are to be added to the intrinsic scatter of the particular R_{23}-[O/H] calibration to which it is to be plugged. Unless the derived oxygen abundance is extreme, the metallicities calculated in this way will be affected by very large errors. This alteration of the R_{23} method effectively enlarges the turnaround region of the R_{23}-[O/H] calibration, in which the metallicity is very uncertain. At any rate, the L03, K03 and KK04 studies suggest that, at any given metallicity, galaxies were typically more luminous in the past.

This chapter presents a new sample of distant galaxies selected for the presence of the [OIII]λ 4363 Å auroral line. This line is sensitive to electron-temperatures (Osterbrock, 1989) and can, together with H_β and other oxygen lines, provide reliable gas metallicities without assumptions about the ionization and metallicity. This selection also strongly favors [O/H] abundances less than $\sim$ 1/3 solar and has enabled us to discover a new distant sample of luminous metal-poor field galaxies. We summarize our observations and measurements in section 6.2; we present our data analysis and compare our results to the LZR derived from previous studies of field galaxies in section 6.3. Section 6.4 presents the photometric properties of some of the objects studied. The star formation properties of the sample is investigated in section 6.5 The main conclusions of this study are presented in the last section.

We adopt the concordance cosmology, i.e., a flat Universe with $\Omega_\Lambda = 0.7$ and $h = 0.7$. Magnitudes are all on the Vega system.

6.2 Observations & Measurements.

The studied galaxies were selected by eye inspection of reduced spectra from two redshift surveys of faint field galaxies, DEEP2 (Deep Extragalactic Evolutionary Probe) and TKRS (Team Keck Treasury Redshift Survey), both using the DEIMOS spectrograph (Faber et al., 2003) on the 10-meter Keck II Telescope. The DEEP2 (Davis et al., 2003) spectra had a

[1]We will henceforth refer to 12+log(O/H) as "[O/H]".

total exposure time of one hour. The wavelength range covered is $\sim$ 6400-9000 Å and the grating used was the 1200 mm^{-1} grating, which yielded FWHM resolutions of around 60 km s^{-1}. The initial DEEP2 sample consisted of 3900 galaxies, 1200 of which had redshifts that allowed the [OIII]λ4363 and [OIII]λ4959 lines in principle to be observed. This search yielded 14 galaxies, or about 1%, that display the weak auroral line [OIII]λ4363 along with Hγ, Hβ and [OIII]$\lambda, \lambda 4959, 5007$. In some cases, it was also possible to measure [OII]λ3727. The TKRS survey (Wirth et al., 2004) is a similar one hour survey targeting the GOODS-North field (Giavalisco et al., 2004). It used the 600 mm^{-1} grating, and covered a wider range of wavelengths (4600–9800 Å). It had, however, a lower FWHM resolution of 170 km s^{-1}. This survey yielded 1536 galaxies with reliable redshift determinations. For 1090 galaxies, the redshifts allowed the [OIII]λ4363 and [OIII]λ4959 lines to be observable. Of these, three galaxies, or 0.3%, showed the auroral line and had redshifts above $z \sim 0.5$. Figure 6.1 shows one example along with its HST image. Table 6.1 identifies all 17 targets, henceforth called the O-4363 sample and tabulates our measurements described below.

For the DEEP2 sample, 4 out of the 14 galaxies had all the required lines whereas the other ten objects did not show [OII]λ3727 because of their lower redshift.For TKRS, all three sources had all the required lines. For the 10 objects without [OII]λ3727, this line strength is estimated using the following fit, which is based on a large sample of local HII galaxies, both with and without [OIII]λ4363 (Hoyos & Díaz, 2006).

$$\log \frac{[\mathrm{OIII}]}{[\mathrm{OII}]} = (0.877 \pm 0.042) \times \log EW(H\beta) - 1.155 \pm 0.078 \tag{6.1}$$

We think the preceeding expression can be used to give at least a rough estimate of the [OII] line strength for the O-4363 objects because the selected TKRS sources turn out to be proper LCBGs (see section §6.4), and many LCBGs have been shown to be very similar to local HII galaxies (see Chapters 1 through 3 in this work), although the uncertainities in the final oxygen abundances will be obviously larger for these objects. The intermediate-redshift galaxies found via the [OIII]λ4363 line are probably similar to low-metallicity local HII galaxies. HII galaxies are compact, star forming systems whose spectra are completely dominated by the emission of HII regions (Sargent & Searle, 1970). Even though HII galaxies were originally thought to be truly young objects, experiencing their very first star formation episodes (Searle & Sargent, 1972; Sargent & Searle, 1970), this hypothesis is no longer tenable after very deep CCD imaging of such objects Telles & Terlevich (1997); Telles, Melnick, &

Terlevich (1997), or other very similar sources known as Blue Compact Dwarves[2] (Papaderos et al., 1996,b; Loose & Thuan, 1986) which show clear evidence of an older extended population of stars. The properties of this host galaxy has been further studied photometrically (see, e.g. Caon et al., 2005; Telles, Melnick, & Terlevich, 1997, and elsewhere). However, the quest for genuinely young objects is still underway, and was one of the original drivers of this study.

The [O/H] metallicities are derived from emission lines, including the temperature sensitive [OIII]λ4363 line along with [OII]λ3727, H_γ, H_β and [OIII]$\lambda, \lambda 4959, 5007$, using the formulae given in Pagel et al. (1992). Objects showing [OII]λ 3727 have abundance uncertainties set to 0.1 dex, while the others have uncertainties of 0.2 dex. The electron temperature in the [OII] zone was however derived according to the density-dependent method given in Pérez-Montero & Díaz (2003). The oxygen abundances of giant HII regions found in emission line galaxies derived in this way are almost instantaneous measurements of the oxygen abundance, since distant starburst regions fade beyond detection after 10Myr.

For the DEEP2 sources, the blue absolute magnitudes (M_B) and rest-frame $U-B$ colors were calculated from the *BRI* photometry (Coil et al., 2004). For the TKRS sources, such quantites were derived from the 4-band *HST-ACS* photometry in the GOODS-N field of the TKRS, with K-corrections following those described by Willmer et al. (2005). Redshifts, oxygen abundances, line ratios, Hβ equivalent widths, blue absolute magnitudes, velocity dispersions, half light-radii as well as other quantities can be found in table 6.1.

[2]BCDs. The qualitative properties of BCDs are similar to those of BCGs or HII galaxies, but are an order of magnitude less luminous.

ID	z	RA (J2000)	DEC (J2000)	[O/H]	[OIII]/Hβ	EW(Hβ) $z=0$ Å	M_B	$U-B$ (mag)	SFR ($M_\odot yr^{-1}$)	Vel. σ (km s^{-1})
D^2-1	0.851*	23 29 08.20	+00 20 40.70	8.1±0.1	8.0±0.8	98±5	-19.90	-0.47	4 ±7	40±14
D^2-2	0.730*	02 29 33.65	+00 26 08.00	7.9±0.1	8.1±0.8	90±5	-19.24	-0.47	0.6±0.7	25±6
D^2-3	0.749*	16 53 03.49	+34 58 48.90	7.8±0.1	6.3±0.6	96±5	-19.23	-0.35	2±4	30±14
D^2-4	0.631	23 28 47.84	...	8.0±0.15	6.1±0.6	88±5	-19.27	-0.51	2±1	32±4
D^2-5	0.636	23 28 41.65	+00 18 20.00	8.2±0.15	8.1±0.8	96±5	-19.24	-0.34	0.5±0.4	28±4
D^2-6	0.530	...	...	8.1±0.15	7.8±0.8	160±20	...	...	2±1	34±5
D^2-7	0.706	16 50 05.43	+35 06 30.40	8.1±0.15	7.4±0.7	70±5	-20.10	-0.35	4±3	41±4
D^2-8	0.659	02 31 17.32	+00 37 28.20	8.1±0.15	6.6±0.7	70±10	-19.97	-0.49	12±13	50±10
D^2-9	0.750*	02 30 20.03	+00 42 49.70	8.1±0.1	5.9±0.6	91±5	-20.55	-0.49	4±5	40±10
D^2-10	0.657	02 28 38.46	+00 28 52.30	8.3±0.15	4.9±0.5	60±10	-21.40	-0.52	20±30	60±16
D^2-11	0.551	02 28 40.39	+00 36 07.70	8.0±0.15	8.1±0.8	81±9	-18.48	-0.45	0.2±0.8	20±20
D^2-12	0.680	02 28 45.05	+00 41 32.80	8.2±0.15	9.4±0.9	110±15	-21.00	-0.28	1.0±0.6	32±2
D^2-13	0.702	02 30 02.06	+00 47 34.70	8.3±0.15	4.8±0.5	91±3	-19.94	-0.55	1±2	30±16
D^2-14	0.725	02 30 12.32	+00 36 52.50	7.8±0.15	7.1±0.7	59±5	-19.53	-0.29	5±4	37±5
TK-1	0.855*	12 36 42.83	+62 20 01.58	8.0±0.1	5.3±0.5	150±20	...	...	30±20	57±6
TK-2	0.681*	12 36 33.02	+62 15 37.52	7.8±0.1	8.2±0.8	100±15	-19.35	-0.38	20±10	48±4
TK-3	0.512*	12 36 50.22	+62 17 17.91	7.8±0.1	3.2±0.3	16±3	-19.30	-0.28	0.3±0.6	21±8

Table 6.1: [OIII]λ4363 Selected Galaxies. Redshifts, J2000 coordinates, oxygen abundances, [OIII]/Hβ, Hβ rest-frame equivalent widths (EW$_\beta$), rest-frame absolute magnitudes, rest-frame colors, star formation rates and emission line width (σ) of the studied sample. The first 14 entries are DEEP2 sources. The last 3 entries are TKRS galaxies. In this table, redshifts marked with asterisks denote galaxies for which all emission lines from [OII]λ3727 to [OIII]λ5007 could be measured.

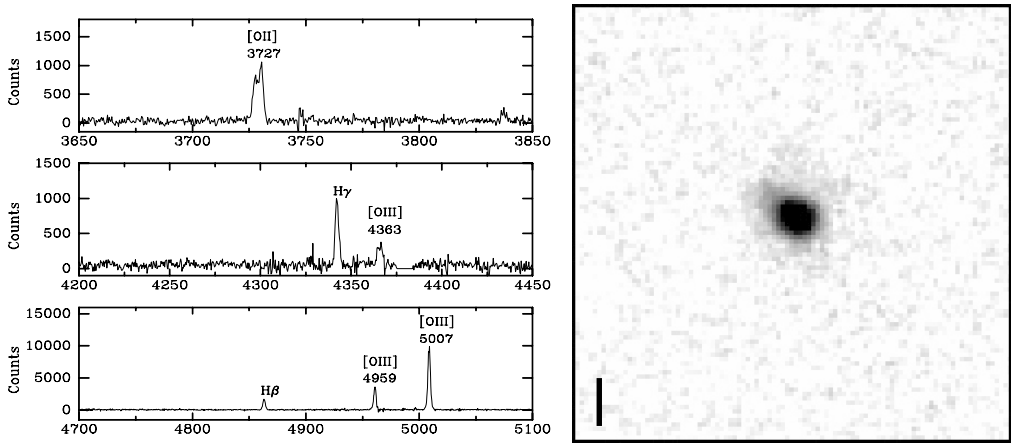

Figure 6.1: Spectrum of a low-metallicity (1/10 solar) galaxy at redshift $z = 0.68$ (TK-2 in Table 1) showing the temperature-sensitive [OIII]λ4363 line used to identify the sample and the other lines used to measure the gas phase abundance [O/H]. From top to bottom, (i) the [OII]λ3727 line, (ii) the Hγ and [OIII]λ4363 lines, and (iii) the H_β and [OIII]λ, λ4959,5007 lines. The *HST* ACS image is taken in the $F814W$ filter (close to rest frame B); North is up, and East is to the left. The image is 3 $''\times$ 3$''$(18 kpc $\times$ 18 kpc). The half-light radius of this galaxy is 0.7 kpc. The thick, dark line shown represents 2 kpc.

It is also the case (see Table 6.1) that TKRS sources present higher velocity dispersions, lower EW(Hβ) and redder $U-B$ colors than DEEP2 sources. This suggests that TKRS sources might be more evolved, since they would be more massive and their older populations would be more important.

6.3 The Luminosity-Metallicity Relation (LZR). The nature of the O-4363 sample.

The oxygen abundances here are the first using the temperature-sensitive method based in the [OIII]λ4363 line for star-forming regions at $z \sim 0.7$. It can be seen in table 6.1 that these galaxies are low-metallicity objects. The oxygen abundance of the most metal-rich target in this sample is only 40% that of the sun.

Three sets of intermediate-redshift galaxies are available for comparison. The first consists of the 25 more distant star forming galaxies (as opposed to being Active Galactic Nuclei) from the K03 sample with redshifts from 0.60 to 0.81. These galaxies are DEEP1 sources (Vogt et al., 2005) in the Groth Strip Survey (GSS), and were observed with the Low Resolution Imaging Spectrometer (LRIS;Oke et al. (1995)). They all have the strong oxygen lines [OIII]λ, λ4959, 5007 and [OII]λ3727, and the S/N of the Hβ emission line is greater than 8

(the minimum recommended for reliable chemical determinations via empirical calibrations, see Kobulnicky, Kennicutt, & Pizagno (1999)). This selection favors galaxies of lower star formation rates. $B-V$colors range from 0.30 to 0.50, and half-light radii range from 1.1 kpc to 7.0 kpc. The second set includes the 55 galaxies with actual measurements of the bright nebular [OIII] and Hβ lines, rather than upper limits, from the L03 sample. Their redshifts range from 0.48 to 0.91. These galaxies were observed with the Multi Object Spectrograph (MOS) instrument on the CFHT. These galaxies are compact ($R_e \leq$ 1.0kpc, when available), bright (M_B brighter than -19.6) and have an observed [OII]λ3727 flux greater than 3×10^{-16}erg s^{-1}. The third set consists on the 102 galaxies from the KK04 sample with redshifts between 0.55 and 0.85 and whose oxygen abundances were determined in that work using various "bright-line" calibrations as being greater than 8.4. These galaxies were also observed in the TKRS survey. They are all located in the Great Observatories Origins Deep Survey-North (GOODS-N;Giavalisco et al. (2004)) field. These sources are bright (M_B typically less than -19.0) and their $U-B$ color is bluer than that of the majority of the objects observed in the TKRS survey. They all show the strong oxygen lines [OIII]λ5007 and [OII]λ3727, and the S/N of their Hβ emission lines is also greater than 8.0. AGNs were filtered out from this sample too.

These three samples are, to our knowledge, the largest samples of intermediate-z star-forming galaxies whose gas-phase oxygen abundances have been calculated by means of the bright emission lines [OIII]$\lambda, \lambda 4959, 5007$ and [OII]λ3727. The oxygen abundances of these objects have been derived through empirical calibrations, then. This makes them ideally suited to be compared with the objects present here. The metallicities from K03 were derived using a modification of the prescription given in McGaugh (1991) for the metal-rich branch of the R_{23} to $12 + \log(\mathrm{O/H})$ calibration, namely using equivalent widths to estimate line ratios instead of line intensities (Kobulnicky & Phillips, 2003). Its systematic error decreases with increasing equivalent widths. The oxygen abundances given in L03 were calculated according to the McGaugh (1991) calibration for the metal-rich branch of the R_{23} to $12 + \log(\mathrm{O/H})$ diagram, assuming an uniform $B-V$color excess of 0.15. The oxygen abundances given in KK04 were calculated using a variety of "bright-line" calibrations. It is also interesting to compare the intermediate-redshift galaxies with [OIII]λ4363 introduced here with other star-forming high-redshift objects. The galaxy sample given in Kobulnicky & Koo (2000, table 4 of,) and the high-redshift HII galaxy known as the Lynx arc (Villar-Martín, Cerviño, & González Delgado, 2004; Fosbury et al., 2003) were chosen. The galaxies from Kobulnicky

& Koo (2000) are Lyman Break Galaxies (LBGs). This sample was assembled from infrared spectroscopic observations of LBGs. It includes objects from Teplitz et al. (2000a,b); Pettini et al. (1998). LBGs are high-redshift ($z \geq 2.0$), rather massive ($M_{\rm virial} \sim 10^{11}$), vigorously star-forming systems (SFR$\geq 20 M_{\odot}$). Their ionization degree suggests that they are ionized by very young starbursts. The Lynx arc is a gravitationally lensed HII galaxy at z=3.357. This is an extreme system in many respects, probably undergoing the Wolf-Rayet phase of the evolution of its ionizing star cluster. Its oxygen abundance is 10% solar. The star formation rate is around 6 solar masses per year and its continuum is mostly nebular.

In order to place all the different samples in the same system, the oxygen abundances of the L03 and K03 comparison sets were rederived using the calibration of Pilyugin (2000), assuming the upper branch of the calibration. In the case of the L03 objects, a uniform extinction of $c(H\beta) = 0.50$ was assumed. This value was adopted since this is the average extinction found for emission-line galaxies in the Nearby Field Galaxy Survey of similar luminosity (Lilly, Carollo, & Stockton, 2003). For both K03 sources, line equivalent widths were used as surrogates for line strengths. No extinction correction was applied to K03 objects. The metallicity values listed in KK04 were accepted.

The uncertainties in these metallicity estimates are around 0.3–0.4 dex. Besides the intrinsic scatter of the empirical calibrations used, the main contributors to the final error budget are the use of line equivalent widths as surrogates to line strengths and the use of a uniform extinction for the L03 sample. For some L03 and K03 sources, the calculated metallicities fell below 8.35, which is approximately the mid-point between the high metallicity branch and the lower metalicity branch. However, given the huge scatter of the $12+\log({\rm O/H}) - R_{23}$ relationship in this regime (0.4–0.5dex), they might still be compatible with the use of the upper branch. For this reason, their oxygen abundance is fixed at 8.35.

As a quick sanity check, and to briefly test the use of equivalent widths instead of line strengths to derive metallicities, the oxygen abundances of the 7 objects that show [OII]$\lambda, \lambda 3726, 3729$ in the DEEP2 and TKRS surveys were rederived using two different calibrations. The first one was the calibration from McGaugh (1991) for the metal poor branch of the R_{23}–$12+\log({\rm O/H})$ relation, and the other one was the calibration from Pilyugin (2000) and Pilyugin (2001), again for the metal poor branch. In both cases, equivalent widths were used instead of line strengths. For the first one the *rms* value of the difference between the temperature-sensitive method and the modified calibration is 0.1 dex, whereas for the second calibration, the *rms* value of this difference is 0.2 dex. Both values are of the order of magni-

tude of the expected errors, indicating that the use of equivalent widths might be appropriate for objects showing [OIII]λ4363. However, the use of line equivalent widths should not become standard practice and real line strengths measured from flux calibrated spectra should be used whenever possible. This alteration of the empirical methods effectively enlarges the turnaround region of the metallicity–R_{23} relationship where the statistical error in the metallicity is very large. Unfortunately, it is in this region where the majority of the luminous intermediate-redshift sources lie. This alteration of the empirical methods can however be used to *sort* metallicities, but the oxygen abundance of a particular source obtained by this method should not be taken too seriously.

Several samples of star-forming local galaxies can also be compared to the metal-poor intermediate-redshift galaxies presented here. The position in the luminosity–metallicity diagram of local samples of star-forming galaxies with respect to distant galaxies can help understand the possible evolution of the LZ relationship over cosmic time. The first of such samples is made of eXtreme Blue Compact Galaxies (XBCGs). XBCGs are defined in Kunth & Östlin (2000) as Blue Compact Galaxies which are more metal-poor at a given luminosity than the dIrrs that consitute the backbone of the luminosity–metallicity diagram. The three most metal-poor local BCDGs are included too. They fall in the XBCGs luminosity–metallicity relationship. Figure 6.2 also shows the dIrrs luminosity–metallicity relationships from Skillman, Kennicutt, & Hodge (1989) and Richer & McCall (1995). They represent the "average" luminosity–metallicity plot for the local universe. As a third local sample, the subsample drawn from the emission-line selected galaxies from the Kitt Peak National Observatory Spectroscopic Survey (Salzer et al., 2000, KISS) presented in Melbourne & Salzer (2002) was chosen. KISS is a large-area, objective prism survey of local ($z \leq 0.09$) galaxies selected on the basis of strong HII emission lines. This sample spans a wide range in luminosity. ($-13 \geq M_B \geq -22$). The last local sample used is that from Lamareille et al. (2004). This sample was extracted from the 2dF survey, choosing star-forming objects (i.e. AGNs were excluded from this sample) with high-quality spectra showing [OII]$\lambda, \lambda 3726, 3729$, H$\beta$, [OIII]$\lambda, \lambda 4959, 5007$, H$\alpha$, [NII]$\lambda 6584$ and [SII]$\lambda, \lambda 6717, 6731$. This sample spans a wide range in luminosity too.

The key result is seen in the [O/H] *vs.* M_B relation in figure 6.2, which shows that [O/H] for the 17 galaxies in our O-4363 sample is 1/3 to 1/10 the solar value of $[\mathrm{O/H}]_\odot = 8.69$ (Allende Prieto, Lambert, & Asplund, 2001). While the O-4363 galaxies have luminosities close to L^* ($M_B \sim -20.4$ locally), they are offset to lower metallicities by about 0.6 dex

in [O/H] when compared to the 182 other $z \sim 0.7$ field galaxies studied by K03, L03, and KK04. All these studies used empirical calibrations, such as R_{23}, and adopted the upper, metal-rich branch[3]. This discovery of luminous galaxies with low [O/H] gas metallicities suggests that adopting the metal-rich branch when using, e.g., the R_{23} method should be made with much caution. Such an assumption precludes finding [O/H] below ∼8.4. If the empirical R_{23} method and upper branch assumption were to be applied to the O-4363 sample, [O/H] would be greater by about 0.4 ± 0.2 dex, nearly enough to place the O-4363 points atop the mean LZR of the $z \sim 0.7$ field galaxies, as can be seen in figure 6.2.

The metallicity range spanned by all the galaxy samples goes from 7.70 to 9.25. This range is virtually the same range spanned by local HII galaxies (see Terlevich et al. (1991); Hoyos & Díaz (2006)). The observed luminosities are found in the local universe, too. However, DEEP2 and TKRS sources as well as a fraction of objects from the DGSS and CFRS comparison samples (as indicated by the black square in figure 6.2) are clearly over-luminous for their metallicity, lying along the XBCG luminosity-metallicity relationship. A few of the DEEP2 and TKRS sources are rather extreme in this respect, falling below the XBCG luminosity-metallicity relationship. On the other hand, KK04 sources lie along the LZ relationships derived from dIrrs data (Richer & McCall, 1995; Skillman, Kennicutt, & Hodge, 1989), but slightly below the LZ relationships derived from KISS or 2dF data. It can also be seen that the LZ relationship derived from this comparison sample, shown in figure 6.2 as a double dotted line is much flatter than the rest of the relationships shown, maybe suggesting some cosmic evolution of the LZ relationship with cosmic epoch. Its expression is:

$$12 + \log(\mathrm{O/H}) = 6.7 \pm 0.3 - 0.09 \pm 0.02 \times M_B \tag{6.2}$$

The position of three most metal-poor BCDGs in the local universe, as well as the location of the Lynx arc and the average position of LBGs can also be seen in figure 6.2. It is interesting to note that the most metal-poor objects in the local universe, DEEP2 and TKRS sources with [OIII]λ4363 and LBGs lie along the XBCG LZ line, suggesting that the population of metal-poor objects at intermediate-z presented here is a link of the most metal-poor objects in the local universe with the more distant LBGs. Finally, the position of the Lynx arc in this diagram is the most extreme of all objects presented here. Deviating from the XBCG

[3]The K03 sample had 25 galaxies in the redshift range $0.60 < z < 0.81$; L03 had 55 galaxies between 0.48 and 0.91; and KK04 had 102 between 0.55 and 0.85.

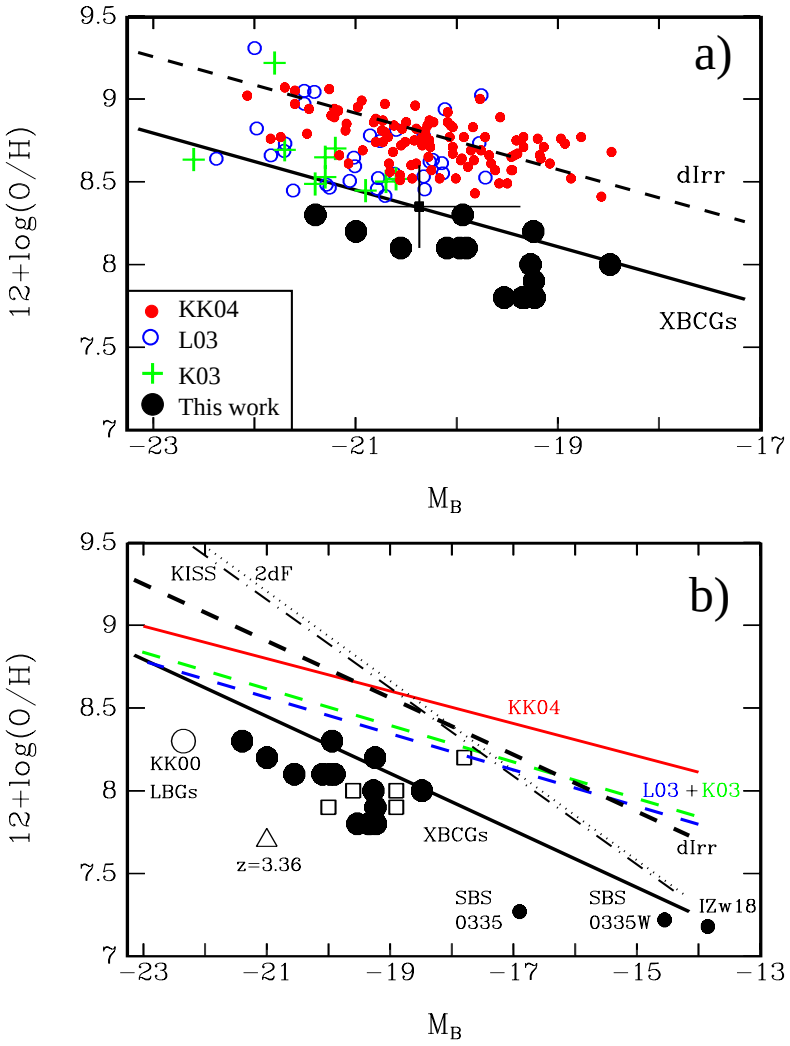

Figure 6.2: (a) LZR diagram showing the intermediate-redshift samples as marked in the inset. The [O/H] values for K03 and L03 were rederived using the Pilyugin (2000) calibration, placing all surveys on the same system. We estimate the errors to be about 0.3-0.4dex for these data. In some fraction of cases, the resulting metallicities fell below 8.35, which is approximately the limit between the high metallicity branch and the lower metalicity branch. However, given the huge scatter of the $12+\log$ O/H-R_{23} relationship in this regime ($\sim$0.4dex), they might still be compatible with the use of the upper branch. For this reason, their oxygen abundance is fixed at 8.35. The average position of these sources is given by the black solid square with error bars. The dashed dIrr line is the average LZR found for local dIrr (Skillman, Kennicutt, & Hodge, 1989; Richer & McCall, 1995) while the solid XBCG line is the LZR for local, metal-poor, blue compact galaxies (Kunth & Östlin, 2000). (b) LZ diagram showing possible local or high-redshift counterparts to the O-4363 sample. The three most metal-poor galaxies known are identified by name. Besides keeping the LZRs from panel (a) of dIrr and XBCGs, we show the LZR of two local, emission-line galaxy samples: one from KISS (Melbourne & Salzer, 2002) and the other from 2dF (Lamareille et al., 2004). The big, open triangle is for the $z = 3.36$ lensed galaxy (Villar-Martín, Cerviño, & González Delgado, 2004) and the big open circle is the average position of LBGs at $z \sim 3$ (KK00). Five local XBCGs from Bergvall & Östlin (2002) are shown as open squares.

LZ relationship by a large amount. This is the most distant object included in this work, lending at least an additional drop of support to the idea of a cosmic evolution of the LZR.

It would be interesting to detect any dependence of the metallicity offsets of the OI-4363 sample with respect to the XBCG LZR. Figure 6.3 shows the metallicity residuals of the intermediate-redshift samples with [OIII]λ4363 from the LZR given by the LZ relationship for local XBCGs. The two LBGs from Kobulnicky & Koo (2000) are also included as open circles.

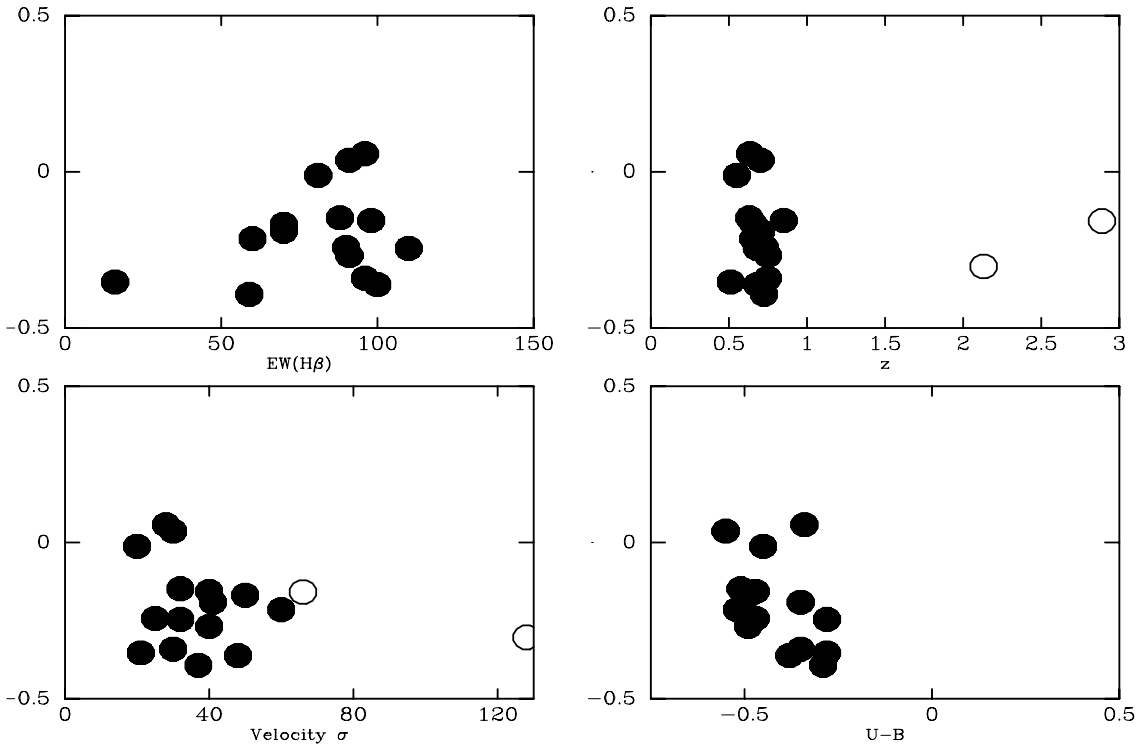

Figure 6.3: Metallicity residuals (Actual-XBCG LZ value) for intermediate-redshift star-forming galaxies showing [OIII]λ4363 plotted against (i) velocity dispersion (in km s^{-1}), (ii) $U-B$ color, (iii) EW(Hβ) (in Å) and (iv) redshift. Symbols as in figure 6.2, except for open circles, which represent the two individual LBGs from Kobulnicky & Koo (2000). It is seen that no clear correlation is found.

It can be seen in figure 6.3 that the metallicity residuals of DEEP2 and TKRS sources do not have a clear-cut correlation with redshift, EW(Hβ), $U-B$ color or velocity dispersion.

What is the nature of our O-4363 sample, and do such galaxies exist locally or at higher redshifts? Figure 6.2 shows several relevant LZRs from local to distant samples. It is seen that relatively common samples of emission line galaxies, such as those of local dIrr, the $z \sim 0.7$ galaxies from K03, L03, and KK04 and the local emission line galaxies from 2dF or KISS surveys all have LZRs that are offset to metallicities higher than that of the O-4363

sample[4].

On the other hand, the O-4363 galaxies are far better matches to local XBCG's and even to the luminous Lyman Break Galaxies (LBG) at redshifts $z \sim 2.5$ (KK00), or to the gravitationally-lensed galaxy at redshift $z = 3.36$, which has a metallicity of 1/10 solar, a blue absolute magnitude of -21.0 and a SFR of 6 $M_{\odot}\mathrm{yr}^{-1}$ (Villar-Martín, Cerviño, & González Delgado, 2004)[5]. As it is said above, we do not find any correlation between the residuals of the O-4363 sample with respect to the LZR of local Extreme Blue Compact Galaxies (XBCG) (Kunth & Östlin, 2000) with $U-B$ color, strength of H_{β}, and internal velocity dispersion (see table 6.1).

6.3.1 The Search for Metal-Poor Objects in the Other Intermediate-z Samples.

What fraction of the three other moderate-redshift samples are actually metal-poor? One estimate adopts two criteria suggested in L03 to identify metal-poor galaxies. The first is based on calculating $R_{23,0}$[6]. The idea here is that O-4363 galaxies have $R_{23,0} > 5$. This places them near the turnaround region of the R_{23}–[O/H] relation, where a small range in R_{23} spans a wide range in metallicity. Our discovery of distant, luminous, metal-poor galaxies in this region implies that the other distant samples may also have such metal-poor galaxies. The second criterion is based on large line equivalent widths. The O-4363 galaxies yield equivalent widths greater than 40 Å for all but one object [7]. This additional criterion selects those galaxies in the turnaround region that were most likely to be metal-poor (Hoyos & Díaz, 2006).

With the preceeding considerations in mind, in order to look for high-luminosity metal-poor candidates in the three comparison sets at intermediate-redshift, the $\log R_{23,0}$ to M_B and $EW(H\beta)$ to M_B diagrams are jointly investigated. Here, the analysis presented in Lilly,

[4]The comparison with the latter samples of local galaxies should not be taken beyond [O/H] = 9.0, because the KISS and 2dF abundances at high luminosities are clearly too high (Pettini & Pagel, 2004). It is then only below [O/H] = 9.0 ($M_B \geq -20.5$) that valid comparisons can be made between our O-4363 sample and the KISS or 2DF samples. Fortunately, most of the $z \sim 0.7$ O-4363 objects are less luminous than this limit.

[5]This object is rather extreme, being 1.0 dex below L03, K03 and KK04 objects of similar luminosity.

[6]Defined as the R_{23} value that an ionized HII region would show if the reddening-corrected ionization ratio [OIII]$\lambda, \lambda 4959, 5007$/[OII]$\lambda 3727$ were equal to one, leaving the oxygen content unchanged.

[7]TK-3 with TKRS catalogue ID-3653 has an unusually low EW(H_{β}) of about 20 Å. Its ionization ratio [OIII]$\lambda, \lambda 4959+5007$/[OII]$\lambda 3727$ is approximately 0.7, and the ratio EW([OII]$\lambda 3727$)/EW(H_{β}) is 5 ± 1. These values indicate that this object is probably a Seyfert 2 galaxy, according to Rola, Terlevich, & Terlevich (1997). For all other objects for which the Rola, Terlevich, & Terlevich (1997) diagnostics could be calculated, all tests indicate that they are normal star-forming galaxies.

Carollo, & Stockton (2003) is roughly followed. Both plots are gathered in figure 6.4.

We used the Pilyugin (2000) calibration for the upper branch. In the case of the L03 objects, a uniform extinction of $c(H\beta) = 0.50$ was used. This value was adopted since this is the average extinction found for emission-line galaxies in the Nearby Field Galaxy Survey of similar luminosity (Lilly, Carollo, & Stockton, 2003). For both K03 and KK04 sources, line equivalent widths were used as surrogates for line strengths, but with no extinction corrections for K03 and a uniform extinction of $c(H\beta) = 0.40$ for KK04. In this latter case, we have used the mean value of a very large sample of bright local HII galaxies from Hoyos & Díaz (2006). for all galaxies. Thus, according to the Pilyugin (2000) calibration for the upper branch, the expression for $\log R_{23,0}$ is:

$$\log R_{23,0} = 0.072 + 0.76 \times \log R_{23} + 0.24 \times \log \frac{[\mathrm{OII}]\lambda 3727}{H\beta} \tag{6.3}$$

The three most metal-poor galaxies in the local universe are included in this comparison, too. For these systems, however, $\log R_{23,0}$ is calculated as[8]:

$$\log R_{23,0} = 5.75 - 0.595 \times (12 + \log(\mathrm{O/H})) \tag{6.4}$$

The first panel of figure 6.4 presents the $\log R_{23,0}$–M_B plot. This plot shows that DEEP2 and TKRS sources, LBGs, local eXtremely Metal Poor Galaxies (XMPGs) and local XBCGs, as well as some members of the intermediate-redshift comparison samples have a $\log R_{23,0}$ value greater than 0.75. This corresponds to a metallicity lower than ∼8.4, if one insists on using the upper branch of the Pilyugin (2000) empirical calibration. Since $12 + \log(\mathrm{O/H}) = 8.4$ approximately marks the mid-point of the turnaround region of the R_{23}–$12 + \log(\mathrm{O/H})$ relation, these galaxies could well have metallicities anywhere in the ellbow region, opening the possibility that at least some fraction of the comparison samples could indeed be of lower metallicity. This panel also shows that luminosity alone can not be used to discriminate between high and low oxygen abundances. Panel (b) in figure 6.4 shows the distribution of the intermediate-redshift galaxies studied in this paper in the M_B–$EW(H\beta)$ plane. This plot shows that genuine lower metallicity sources have larger equivalent widths than the majority of galaxies for which the oxygen abundance had to be derived from empirical calibrations. There are metal-poor objects with equivalent widths as low as 40Å . Therefore, L03, K03

[8]This expression also originates from the upper branch of the Pilyugin (2000) calibration.

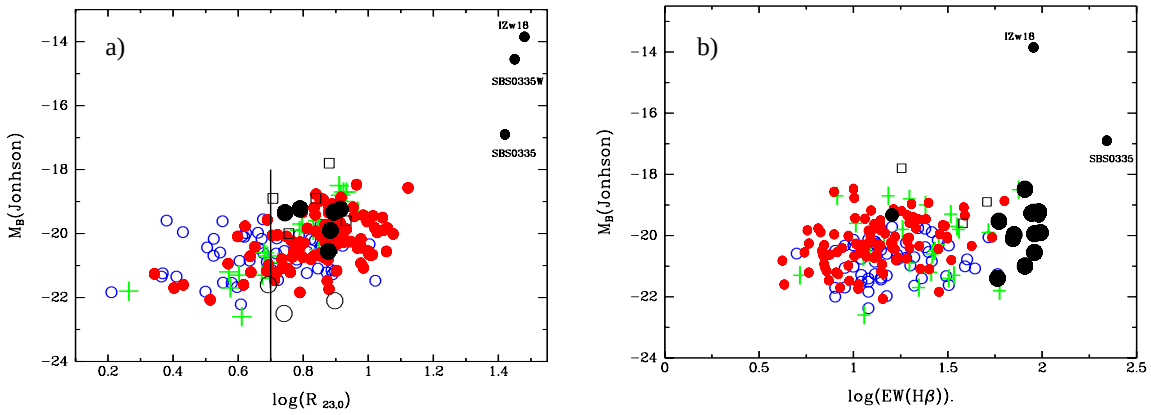

Figure 6.4: The search for metal-poor galaxies at intermediate redshift. Symbols as in figure 6.2. Open circles, however, represent individual LBGs from KK00. (a) M_B *vs.* $\log R_{23,0}$ plot. This diagram shows that most of the intermediate redshift objects whose oxygen abundance has been determined using empirical methods fall in the turnaround region of the calibration, where the oxygen abundance is ill-determined. The fact that the O-4363 sources have similar luminosities implies that some fraction of the L03, K03 and KK04 might indeed be of lower metallicity, and that lumninosity alone can not be used to discriminate between high and low oxygen abundances. (b) M_B *vs.* $\log EW(H\beta)$diagram. This plot shows that systems showing the [OIII]λ4363 line present high equivalent widths. There are two metal-poor objects with equivalent widths as low as $\sim$30Å . L03, K03 and KK04 sources with larger equivalent widths could turn out to be metal-poor galaxies (Hoyos & Díaz, 2006).

and KK04 sources with larger equivalent widths have a non zero probability of being metal-poor galaxies, as was shown in Hoyos & Díaz (2006). Figure 6.4 therefore suggests that, in the absence of other ancillary data such as [NII]λ6584, or an estimate of the S/N of the spectra used, very luminous, intermediate-redshift sources with large $\log R_{23,0}$ and rest frame $EW(H\beta)$ greater than $\sim$40 Å can indeed be metal-poor sources. In the other distant galaxy surveys, we found 13 galaxies (7%) with high H_β equivalent widths and $R_{23,0}$, that together suggest low-metallicities. However, this small percentage is misleading, since it is clearly a lower limit to the real fraction for several reasons. First of all, the cosmological dimming factor $(1+z)^4$ dillutes the weak auroral line. This factor is ~ 8 at $z = 0.7$, implying that we are bound to miss the auroral line in the majority of objects with lower line luminosities or lower equivalent widths. Second, the [OIII]λ4363 line is preferentially observed during the earliest stages of the starburst, as it fades away as the starburst is less able to keep the oxygen atoms doubly ionized. Finally, intermediate-redshift surveys naturally detect very bright objects, equipped with very luminous underlying stellar populations. The enhanced continuum of these old stellar populations is likely to wash away the weak auroral line amidst their higher *absolute* noise, or swallow it in the absorption wings of Hγ. In addition, some

metal-poor galaxies may be outside the turnaround region or may have smaller H_β equivalent widths. Furthermore, if the statistics presented in Hoyos & Díaz (2006) are to be extended all the way to $z \sim 0.7$, the fraction of metal-poor galaxies in the L03, K03 and KK04 samples could be up to 50%. In any case, independent tests are critical to assess the true fraction of intermediate redshift galaxies that have abundances below the upper branch, e.g., by observing [NII]/H_α in the near-infrared at our redshifts as suggested by Pérez-Montero & Díaz (2005) and Denicoló, Terlevich, & Terlevich (2002). In this context, it is interesting to rederive the oxygen abundance of the DEEP2 and TKRS sources using the upper branch of the Pilyugin (2000) calibration for the objects for which [OII]λ3727 can be measured. The resulting oxygen abundances are 0.4 ± 0.2(rms)dex higher than the oxygen abundances determined using the direct method. They would fall between the Skillman, Kennicutt, & Hodge (1989) and the XBCG LZ relationships, and their position in figure 6.2 would then be compatible with the location of L03, K03 and KK04 galaxies. The point here is that these systems would have been assigned metallicities typical of those of the upper branch of the R_{23}–$12 + \log(\mathrm{O/H})$, while in reality their oxygen abundance is lower. On the other hand, objects presenting high equivalent widths, being more likely to present the [OIII]λ4363 line, have a higher probability of harbouring metal-poor starbursts.

Figures 6.2 and 6.4 can be used together to shed more light on the nature of the O-4363 sample. Figure 6.2 shows that DEEP2 and TKRS galaxies fall at around the same place as the Bergvall & Östlin (2002) XBCGs. However (see panel (b) of figure 6.4), the Hβ equivalent widths of the DEEP2 and TKRS samples are larger than those of this XBCG set, which range from 20 to 70. This latter interval is similar to the Hβ equivalent widths found in L03, K03 and KK04. First, this suggests that the ionizing star clusters of DEEP2 and TKRS objects are younger than the ionizing sources of the other works, or that their underlying stellar population is less important. Second, it is seen in figure 6.2 that LBGs and the most metal-poor objects in the local universe lie along, or below the XBCG LZR. Since XMPGs and LBGs have very high $EW(H\beta)$[9] This suggests that the DEEP2 and TKRS populations could be considered to be higher luminosity distant counterparts of the most metal poor objects in the local universe, or lower luminosity, intermediate-redshift counterparts of LBGs, defining, together with the Lynx arc an "extreme" LZ sequence of high equivalent width, metal-poor

[9] $EW(H\beta)_{SBS0335}$ = 220 Å and $EW(H\beta)_{IZw18}$ = 90Å (Izotov & Thuan, 1998; Skillman & Kennicutt, 1993). These numbers are even larger than the equivalent widths measured for the DEEP2 or TKRS objects presenting [OIII]λ4363.

galaxies.

6.3.2 The Search for eXtremely Metal Poor Galaxies in the Distant Universe.

The oxygen abundances presented in table 6.1 for the O-4363 objects are not uncommon in the local universe, although they definitely lie in the high-luminosity end for their $12+\log(\mathrm{O/H})$ value. However, in spite of the high redshifts explored, no galaxy with an oxygen abundance lower than 7.65 has been found. Just to remind the reader, we recall that the blue absolute magnitude for compact and dwarf galaxies in the local universe with $12+\log(\mathrm{O/H}) \sim 8.0$ ranges from -13.0 to -21.0, see Kunth & Östlin (2000, fig 10 of,). We can interpret these facts in the light of a S/N analysis, with the aim of studying the feasibility of detecting an XMPG in the DEEP2 or TKRS surveys. The S/N ratio of the Hγ line, snr_γ, is used here to classify the spectra. The S/N of the [OIII]λ4363 line can then be calculated from the oxygen abundance and the electron temperature assuming that the continuum noise that affects both lines is the same, a very reasonable assumption. In the case of average spectra (snr_γ around 10) it is only possible to measure metallicities of $12+\log(\mathrm{O/H}) = 7.7$, the lowest oxygen abundance found in the objects presented in this work if and only if the electron temperature of the O^{++} shell is greater than 16000K. Such temperatures are detected in the local universe and then, it is not strange that they can be detected in the DEEP2 or TKRS samples. Lower metallicities require much higher electron temperatures to reign in the nebula making them very unlikely. For instance, with spectra of average quality, it is possible to observe objects with an oxygen abundance of around 7.4, but the electron temperature has to be greater than 20000K. Such temperatures require ionizing clusters with plenty of very hot stars, or special geometries. In any case, such conditions can not be maintained for long. On the other hand, luminous (M_B =-21.5) and nearby ($z = 0.50$) objects could produce a spectrum with very high snr_γ. With a spectrum of this kind, it would be possible to detect objects with an oxygen content of 7.2, the oxygen abundance of the most metal poor galaxy known IZw18. The electron temperature has to be greater than 17000K though. This temperature has been measured in other objects in the local universe too. It is therefore concluded that a very bright XMPG could, in principle, be found in the DEEP2 or TKRS surveys. These calculations have been carried out assuming that most of the oxygen is doubly ionized. This approximation is reasonable in the framework of the objects under consideration.

6.4 Photometric Properties of O-4363 Galaxies.

The results presented so far lead to think that this family of DEEP2 and TKRS objects with [OIII]λ4363 can be considered as intermediate-redshift XBCGs. They are also a bridge between LBGs and XMPGs in the LZ diagram. For this reason, it is important to investigate their properties in more detail. In this section, the morphology of the TKRS sources are presented and compared with the properties of the XBCGs from the Bergvall & Östlin (2002) sample. Fortunately, the galaxies in the TKRS survey have been observed with the Advanced Camera for Surveys (ACS) on board the Hubble Space Telescope (HST) as a part of the Great Observatories Origins Deep Survey (GOODS). The assumption here is that the morphology of DEEP2 sources will be similar to that of the TKRS sources. The HST/ACS data available consist of very deep images in the F435W, F606W, F775W and F850LP bands. Figure 6.5 presents images of the TKRS objects TK-2 and TK-3, together with two other objects in the TKRS survey that also show the [OIII]λ4363 but are too close to be considered as intermediate redshift sources, in the filter that best matches rest-frame B, which is indicated in the figure. The code is B=F435W, V=F606W and I=F707W. Figure 6.6 presents the luminosity profiles of the selected TKRS galaxies, again in the filter that best matches rest-frame B. These luminosity profiles were calculated by fitting simple circular apertures to the surface brightness distribution. All circular apertures share the same center, which is the centroid of each galaxy. TK-1 is not included in these plots because it is very faint.

Finally, table 6.2 gathers the more relevant photometric data for TK objects 2 through 5. It can be seen that all objects are compact, having half-light radii of less than 1kpc. These half-light radii, R_e, were estimated from curve-of-growth profiles derived from multi-aperture photometry of the *HST ACS* image taken with the filter that yielded the closest match to restframe B at the target's redshift. It is also noteworthy that the more distant objects TK-2 and TK-3 have effective surface brightnesses, blue absolute magnitudes and $B-V$colors that make them full-fledged LCBGs. Since the DEEP2 objects are also blue (in fact bluer than the TKRS sources in $U-B$), distant ($z \sim 0.7$), and even more luminous than the TKRS galaxies, it is very likely that they are also LCBGs by their own right[10].

Even though the observational data is limited to only four objects, and hence the statistics are very uncertain, figure 6.5 and table 6.2 shows that these galaxies come in two flavors.

[10]The mere fact that the DEEP2 galaxies are observed indicates that their surface brightness have to be correspondingly high, otherwise the $(1+z)^4$ cosmic dimming would render them unobservable.

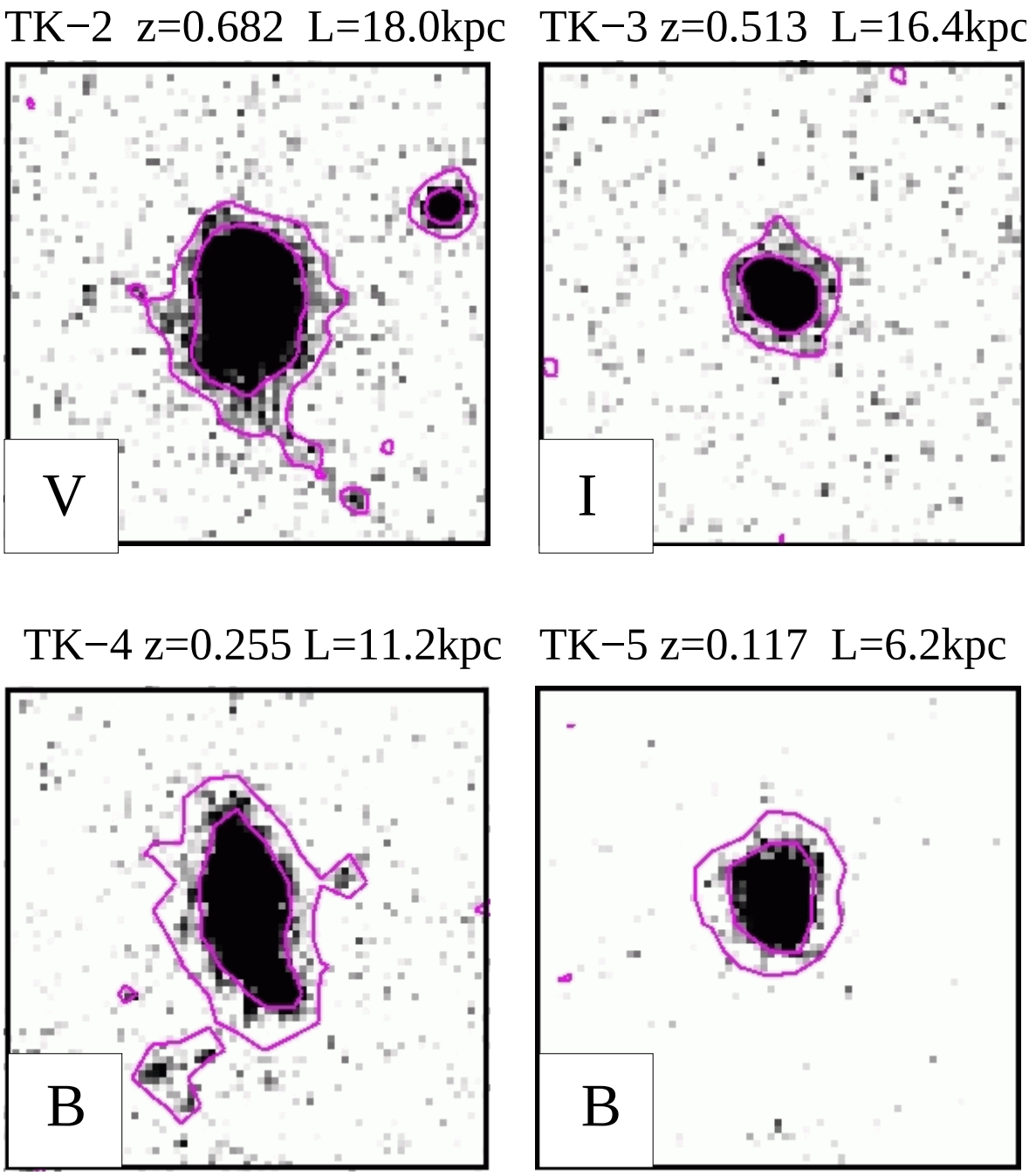

Figure 6.5: TKRS sources with [OIII]λ4363 ACS images. All frames are 3″on a side. Redshifts and linear scales are indicated for each object. Arbitrary but appropriate contours are also shown for each galaxy in magenta. These contours help visualize the outer regions of the presented galaxies. The tail seen in the V image is caused by a nearby luminous star, it is not related to TK-2.

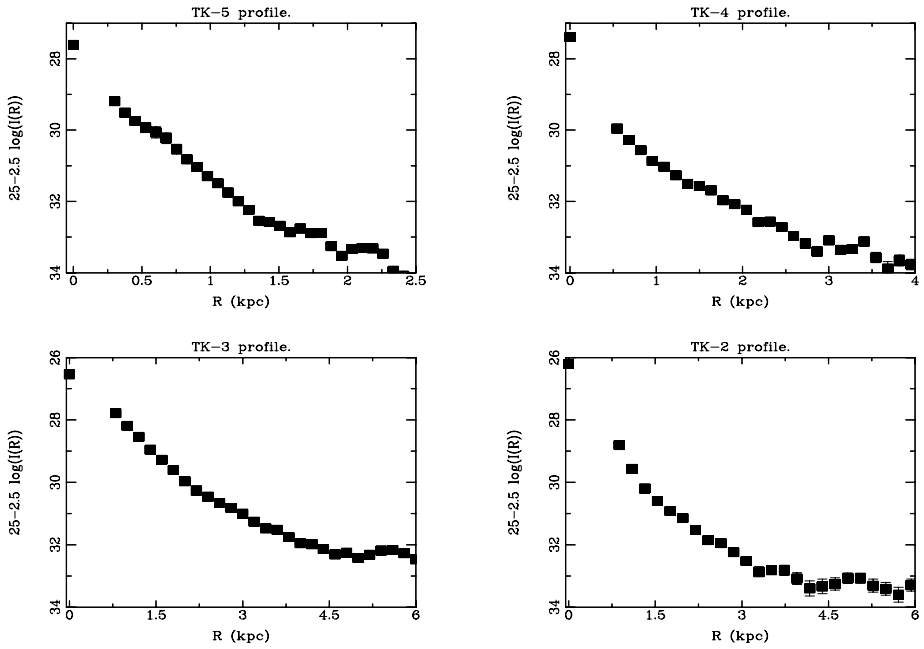

Figure 6.6: Luminosity profiles of selected galaxies. The vertical axis is arbitrary. It does not represent the surface brightness in any magnitude system. This plot presents the luminosity profiles of the selected TKRS galaxies in the filter that best matches rest-frame B.

ID.	R.A. (J2000)	DEC. (J2000)	M_B	$U-B$	$B-V$	R_e (kpc)	SB_e (mag $''^{-2}$)	$\log(M/M_\odot)$
TK-2	12 36 33.02	62 15 37.52	-19.30	-0.382	0.264	0.68	18.432	9.27±0.07
TK-3	12 36 50.22	62 17 17.91	-19.14	-0.276	0.397	1.56	20.400	8.9±0.3
TK-4	12 37 21.12	62 20 19.28	-17.36	-0.285	0.366	1.28	21.747	9.2±0.4
TK-5	12 37 21.93	62 18 06 17	-15.74	-0.385	0.370	0.69	22.03	8.2±1.0

Table 6.2: Coordinates, blue absolute magnitudes, colors, half-light radii, effective surface brightnesses and dynamical masses for selected TKRS objects. Photometric data kindly provided by Jason Melbourne.

Objects TK-3 and TK-5 are more compact sources, as opposed to TK-2 and TK-4 that are more extended. In particular, the appearance of TK-4 might expose the presence of a disky structure. The rest of the sources have a rounder shape. Furthermore, the luminosity profiles shown in figure 6.6 show that the light distribution of these galaxies can be fairly well approximated by an exponential profile, with the possible exception of TK-5, which shows a bump around $R = 0.75$kpc. These luminosity profiles have been observed in local HII galaxies (Telles, Melnick, & Terlevich, 1997). However, it has to be kept in mind that studies based on luminosity profiles can be very tracherous, since their results depend critically on the depth and photmetric pass band of the images used. For this reason, and given the

fact that the images used here were obtained using several filters and the observed objects were located at different distances, a more detailed analysis is clearly needed before taking this latter suggestion too seriously. However, if it is safer to say, as outlined above, that the DEEP2 and TKRS O-4363 galaxies are real LCBGs. These galaxies can be regarded as distant XBCGs, although the differences in equivalent widths between the local XBCGs and the O-4363 sample presented here indicates that either the star formation rate of the DEEP2 and TKRS sources is higher or that the underlying population of the local sources is more important relative to the observed starburst, or a combination of both effects.

6.5 The Hβ Luminosity and the Star Formation Rate.

The relationship between the Hβ luminosity and velocity dispersion for local HII galaxies has been discussed extensively. This relationship has been investigated in Terlevich & Melnick (1981), Melnick, Terlevich, & Moles (1988) and Melnick, Terlevich, & Terlevich (2000). The results shown in those works indicate that the emission-line profile widths of HII measures the mass of these systems within the line-emitting region, while other authors have supported the idea that gas motions are caused by stellar winds from massive stars (Melnick, Tenorio-Tagle, & Terlevich, 1999, for a review,). The scatter in the L(Hβ) *vs.* velocity dispersion relationship therefore arises from a second parameter, or from other possible issues such as rotation, environment, age, or variations in the initial mass function (IMF) which would alter the time evolution of the ionizing radiation properties. It was concluded in Terlevich & Melnick (1981) that metallicity is the most important second parameter and it is shown in Melnick, Terlevich, & Moles (1988), later updated in Melnick, Terlevich, & Terlevich (2000), that the expression:

$$\log L(H\beta) = (1.00 \pm 0.04) \log \frac{\sigma^5}{(O/H)} + 41.32 \pm 0.08 \tag{6.5}$$

can be used to estimate Hβ luminosities of HII galaxies to within the observational errors. This fact encouraged Melnick, Terlevich, & Moles (1988) to determine the value of H_0 from observations of HII galaxies using this expression. This work was further developed in Melnick, Terlevich, & Terlevich (2000). This expression is best suited for objects of high equivalent width, since it was obtained in Melnick, Terlevich, & Moles (1988) using galaxies with EW(H_β) $\geq$ 25.0. This restriction has the two-folded aim of selecting the youngest starbursts and eliminating those with significant underlying stellar populations. This latter

issue is critical since the emission line widths can be widened by the old stellar generation. The scatter of this relationship is minimized by selecting objects whose velocity dispersion is lower than 65km s^{-1}. This was also noted in Koo et al. (1995).

Although equation 6.5 was calibrated using *local* HII galaxies. It is plausible to assume that it holds for more distant objects too. We are assuming that the ionizing properties and environment of the young stellar populations of the DEEP2 and TKRS objects studied are similar to those of local HII galaxies, an assumption that seems reasonable given the similarities we have found between LCBGs and local HII galaxies.

Once the line luminosities have been calculated, the star formation rates can be derived from the Hβ luminosity as in Kennicutt, Tamblyn, & Congdon (1994), valid for $T_e = 10^4 K$ and case B recombination (all the ionizing photons are processed by the nebular gas). The expression is:

$$\mathrm{SFR}(M_\odot \mathrm{yr}^{-1}) = 2.26 \times 10^{-41} L_{H\beta}(\mathrm{erg\ s}^{-1}) \tag{6.6}$$

These two expressions 6.5 and 6.6 can be used to determine the star formation rates (SFR) of the O-4363 sources. The obtained SFR are gathered in table 1. Unfortunately, the uncertainties in the measured velocity sigmas translate into very large errors in the derived star formation rates. All that can be said is that the SFR of the O-4363 galaxies is between 1 and 30 solar masses per year, the average value being $6 \pm 8 \mathrm{M}_\odot \mathrm{yr}^{-1}$. This star formation rate is very similar to the star formation rates of the most luminous HII galaxies in the local universe and to the LCBGs presented in Hoyos et al. (2004). For an additional reference, the SFR of 30-Dor, the largest star forming region in the LMC, is only $0.1 M_\odot \mathrm{yr}^{-1}$.

In order to further highlight the nature of the O-4363 sample, the dynamical masses of the TKRS objects with the auroral line are derived using the half-light radii and velocity sigmas as measures of galaxy size and gravitational potential[11]. The resulting masses are given in table 6.2.They are lower than the masses presented in Hoyos et al. (2004) by one order of magnitude, although the errors are rather large. The large errors in the masses again arise from the uncertainties in the velocity dispersions caused by the instrumental broadening.

[11]The expression used arises from $M = 3kG^{-1}R_e\sigma^2$, where the structural constant k varies with different galaxy surface density profiles. Since the surface brightness profile of the observed galaxies is consistent with an exponential law, we adopt $k = 1.7$, following Bender, Burstein, & Faber (1992).

$$\log M/M_{\odot} = 6.08 + \log R_e(\mathrm{kpc}) + 2 \times \log \sigma(\mathrm{km\ s^{-1}}) \tag{6.7}$$

Although the uncertainties in these calculations are rather large, it can be said that the star formation properties of the O-4363 LCBGs are qualitatively similar to the star formation properties of the LCBGs presented in Hoyos et al. (2004) and Guzmán et al. (1997). However, the lower mases and sizes of the TKRS objects lead to think that the star formation episode of the O-4363 galaxies is somewhat more concentrated, or that its efficiency is larger. Of course, no firm conclusion can be reached with the available data.

As an additional item on this study of the star formation properties of the O-4363 sample, the effective temperatures of the ionizing star cluster of the objects for which the [OII]λ3727 was observed can be calculated following Díaz (unpublished). Assuming a solar abundance of 8.69 (Allende Prieto, Lambert, & Asplund, 2001), the effective temperatures range from 42000K to 50000K. These temperatures are typical of O4 to O6 stars, hinting towards a very young starburst.

The expressions used to derive the effective temperatures are:

- For metallicities near $Z = Z_{\odot}/10$

$$\log T_{eff} = 0.229 \log [\mathrm{OII}]/\mathrm{H}\beta - 0.387 \log [\mathrm{OIII}]/\mathrm{H}\beta + 1.97459 \log R_{23} + 3.1650 \tag{6.8}$$

  The standard deviation of this temperature estimator is 10%.

- For metallicities near $Z = Z_{\odot}/5$

$$\log T_{eff} = 0.124 \log [\mathrm{OII}]/\mathrm{H}\beta - 0.017 \log [\mathrm{OIII}]/\mathrm{H}\beta + 1.168 \log R_{23} + 3.594 \tag{6.9}$$

  The standard deviation of this latter expression is 5%.

It should be said that these estimates were derived using specific atmosphere models. They are not meant to be an absolute scale. The previous identification of these temperatures with specific stellar types can be considered to be bold. However, the conclusion that these galaxies harbor very young starbursts is robust.

In summary, the SFR of the O-4363 galaxies are not uncommon for local or intermediate redshift objects of their kind, although the star forming episode might be more intense than

that of other objects studied at similar distances. It has also been found that the ionizing clusters powering the O-4363 galaxies are likely to be very young.

6.6 Summary.

Based on a search for the [OIII]λ4363 emission line in the TKRS and initial DEEP2 surveys of field galaxies, we have discovered 17 galaxies at redshift $z \sim 0.7$ that are luminous, very blue, compact, and metal poor, roughly 1/3 to 1/10 solar in [O/H]. Though rare, such metal-poor galaxies highlight the diversity among galaxies with similar luminosities and serve as important laboratories to study galaxy evolution (Kunth & Östlin, 2000). This sample is lower in [O/H] by 0.6 dex on average in the LZR when compared to prior studies at these redshift, which used empirical calibrations, such as R_{23}. The previous studies, however, assumed the metal-rich branch of the calibration, while our results show that this assumption may not apply, even for luminous galaxies, especially when high values of EW(H_β) and R_{23} are found (roughly 7% of the other samples, although this percentage is clearly a lower limit). Based on comparisons to local and high redshift samples, we speculate that our metal-poor, luminous galaxies at $z \sim 0.7$ provide an important bridge between local Extreme Blue Compact Galaxies (XBCGs) and Lyman Break Galaxies (LBGs) at redshifts $z \sim 3$. All three samples share the property of being overluminous for their metallicities, when compared to local galaxy samples, and of having very high EWs of H_β, typically above 40 Å and up to 150 Å and, thus, similar to that found for some local HII galaxies (Terlevich et al., 1991; Hoyos & Díaz, 2006). Overall, the trend suggested by figure 6.2 is that the most luminous, metal-poor galaxies are getting fainter with time. Much like the XBCG and LBG, the O-4363 galaxies may belong to the compact class of galaxies. But this suggestion is based presently on the small 1–2 kpc sizes and high surface brightnesses seen in the three $z \sim 0.7$ TKRS galaxies with *HST* images. Moreover, the emission-line velocity widths (see table 6.1) are narrow and suggest that the O-4363 galaxies are more likely to be galaxies with small dynamical masses, probably lower than similar systems both in the local universe and at intermediate redshift. The calculated star formation rates of the O-4363 galaxies are mostly from 1 to 20 $M_\odot \mathrm{yr}^{-1}$, indicating that the star-forming activity is very strong (c.f., the SFR of 30 Doradus is 0.1 $M_\odot \mathrm{yr}^{-1}$) and thus lying roughly between that of local metal-poor, blue compact galaxies and distant Lyman Break Galaxies. The very blue colors, high equivalent widths and high star formation rates suggest a recent, strong burst of star formation.

When DEEP2 is complete, a sample nearly 10× larger will be available, many with *HST* images. The resulting data set should thus provide vastly improved probes of their nature, enable us to understand their relationship to other classes of galaxies at different epochs, and yield constraints on the physical processes involved in chemical and galaxy evolution.

Bibliography

Allende Prieto C., Lambert D. L., Asplund M., 2001, ApJ, 556, L63

Bender R., Burstein D., Faber S. M., 1992, ApJ, 399, 462

Bergvall N., Östlin G., 2002, A&A, 390, 891

Campos-Aguilar A., Moles M., Masegosa J., 1993, AJ, 106, 1784

Caon N., Cairós L. M., Aguerri J. A. L., Muñoz-Tuñón C., 2005, ApJS, 157, 218

Cen R., Ostriker J. P., 1999, ApJ, 519, L109

Coil A. L., Newman J. A., Kaiser N., Davis M., Ma C.-P., Kocevski D. D., Koo D. C., 2004, ApJ, 617, 765

Davis M., et al., 2003, SPIE, 4834, 161

Denicoló G., Terlevich R., Terlevich E., 2002, MNRAS, 330, 69

Díaz A. I., unpublished.

Faber S. M., et al., 2003, SPIE, 4841, 1657

Fall S. M., Pei Y. C., 1993, ApJ, 402, 479

Fosbury R. A. E., et al., 2003, ApJ, 596, 797

Giavalisco M., et al., 2004, ApJ, 600, L93

Guzmán R., Gallego J., Koo D. C., Phillips A. C., Lowenthal J. D., Faber S. M., Illingworth G. D., Vogt N. P., 1997, ApJ, 489, 559

Hoyos C., Guzmán R., Bershady M. A., Koo D. C., Díaz A. I., 2004, AJ, 128, 1541

Hoyos C., Díaz A. I., 2006, MNRAS, 365, 454

Izotov Y. I., Thuan T. X., 1998, ApJ, 500, 188

Kennicutt R. C., Tamblyn P., Congdon C. E., 1994, ApJ, 435, 22

Kobulnicky H. A., Kennicutt R. C., Pizagno J. L., 1999, ApJ, 514, 544

Kewley L. J., Dopita M. A., 2002, ApJS, 142, 35

Kinman T. D., Davidson K., 1981, ApJ, 243, 127

Kobulnicky H. A., Kewley L. J., 2004, ApJ, 617, 240 (KK04)

Kobulnicky H. A., Koo D. C., 2000, ApJ, 545, 712 (KK00)

Kobulnicky H. A., Phillips A. C., 2003, ApJ, 599, 1031

Kobulnicky H. A., et al., 2003, ApJ, 599, 1006 (K03)

Koo D. C., Guzmán R., Faber S. M., Illingworth G. D., Bershady M. A., Kron R. G., Takamiya M., 1995, ApJ, 440, L49

Kunth D., Östlin G., 2000, A&ARv, 10, 1

Lamareille F., Mouhcine M., Contini T., Lewis I., Maddox S., 2004, MNRAS, 350, 396

Lequeux J., Peimbert M., Rayo J. F., Serrano A., Torres-Peimbert S., 1979, A&A, 80, 155

Lilly S. J., Carollo C. M., Stockton A. N., 2003, ApJ, 597, 730 (L03)

Star-forming Dwarf Galaxies and Related Objects, ed. D. Kunth T.X. Thuan, & J. T. T. Van.(Gif-sur-Yvette: Editions Frontières), 73

Loose H.-H., Thuan T. X., 1986, ApJ, 309, 59

McGaugh S. S., 1991, ApJ, 380, 140

Melbourne J., Salzer J. J., 2002, AJ, 123, 2302

Melnick J., Terlevich R., Moles M., 1988, MNRAS, 235, 297

Melnick J., Tenorio-Tagle G., Terlevich R., 1999, MNRAS, 302, 677

Melnick J., Terlevich R., Terlevich E., 2000, MNRAS, 311, 629

Oke J. B., et al., 1995, PASP, 107, 375

Osterbrock, D. E. 1989, Astrophysics of Gaseous Nebulae and Active Galactic Nuclei (Mill Valley:Univ. Science Books)

Pagel B. E. J., Edmunds M. G., Blackwell D. E., Chun M. S., Smith G., 1979, MNRAS , 189, 95

Pagel B. E. J., Simonson E. A., Terlevich R. J., Edmunds M. G., 1992, MNRAS, 255, 325

Pagel, B. E. J. 1997, Nucleosynthesis and chemical evolution of galaxies (Cambridge: Cambridge Univ. Press)

Papaderos P., Loose H.-H., Thuan T. X., Fricke K. J., 1996, A&AS, 120, 207

Papaderos P., Loose H.-H., Fricke K. J., Thuan T. X., 1996, A&A, 314, 59

Pérez-Montero E., Díaz A. I., 2003, MNRAS, 346, 105

Pérez-Montero E., Díaz A. I., 2005, MNRAS, 361, 1063

Pettini M., Kellogg M., Steidel C. C., Dickinson M., Adelberger K. L., Giavalisco M., 1998, ApJ, 508, 539

Pettini M., Pagel B. E. J., 2004, MNRAS, 348, L59

Pettini M., Shapley A. E., Steidel C. C., Cuby J.-G., Dickinson M., Moorwood A. F. M., Adelberger K. L., Giavalisco M., 2001, ApJ, 554, 981

Pilyugin L. S., 2000, A&A, 362, 325

Pilyugin L. S. 2001, A&A, 369, 594

Richer M. G., McCall M. L., 1995, ApJ, 445, 642

Rola C. S., Terlevich E., Terlevich R. J., 1997, MNRAS, 289, 419

Salzer, J. J., et al. 2000, AJ, 120, 80

Sargent W. L. W., Searle L., 1970, ApJ, 162, L155

Searle L., Sargent W. L. W., 1972, ApJ, 173, 25

Skillman E. D., Kennicutt R. C., Hodge P. W., 1989, ApJ, 347, 875

Skillman E. D., Kennicutt R. C., 1993, ApJ, 411, 655

Telles E., Melnick J., Terlevich R., 1997, MNRAS, 288, 78

Telles E., Terlevich R., 1997, MNRAS, 286, 183

Teplitz H. I., et al., 2000, ApJ, 542, 18

Teplitz H. I., et al., 2000, ApJ, 533, L65

Terlevich R., Melnick J., 1981, MNRAS, 195, 839

Terlevich R., Melnick J., Masegosa J., Moles M., Copetti M. V. F., 1991, A&AS, 91, 285

Villar-Martín M., Cerviño M., González Delgado R. M., 2004, MNRAS, 355, 1132

Vogt N. P., et al., 2005, ApJS, 159, 41

Willmer C.N.A., et al., 2005, ApJ, submitted.

Wirth G. D., et al., 2004, AJ, 127, 3121

Global Summary and Main Conclusions.

In this chapter, the most relevant conclusions derived from this thesis are summarized. Since most of this work has been devoted to describe and characterize the nature of intermediate-redshift HII-like LCBGs many of the following conclusions will go in this sense. This work has also contributed to study their relationship with local galaxies.

Most of the presented conclusions have already been shown in the closing section of each chapter.

- The Hβ luminosities of LCBG-like HII galaxies are much greater than the line luminosities of the rest of HII galaxies. This is a very important difference between the two subsamples. We have also found that their ionizing star clusters are more massive than those of lower luminosity HII galaxies. LCBG-like HII galaxies have been found to posses larger (and hence probably older) underlying populations, and their ionizing star clusters are also more evolved. LCBG-like HII galaxies are marginally more metal-rich than the average HII galaxy, but not enough to explain the observed differences in the ionization ratio [OIII]/[OII] between the two subsamples. In addition, LCBG-like HII sources are clearly further away than the average local HII galaxy.

- It has been found that Hβ fluxes are larger for HII galaxies showing the [OIII]λ4363 line, even though the Hβ luminosity distributions for local HII galaxies with and without the auroral line are very similar. This is in part because objects not showing the auroral line are more distant and their extinction is higher. However, it has been shown that the non-detection of the [OIII]λ4363 line in local HII galaxies is a real metallicity effect for at least some cases. The galaxies without the auroral line are about 0.4dex more

metal rich than objects from the other subsample. The analysis of the [OIII]/[OII] to $12 + \log(O/H)$ relationship reveals the existence of high-ionization, metal rich objects without the auroral line. Objects from the subsample without the auroral line are found to harbour more massive star clusters, although the differences in excitation between the two subsamples indicates that the galaxies without the [OIII]λ4363 line are probably powered by somewhat older star clusters.

- The two preceeding points imply that LCBG-like sources are more similar to objects without the auroral line [OIII]λ4363, meaning that any local control sample designed to study more distant LCBGs is to be made of galaxies not showing the [OIII]λ4363 line. If one observes a distant LCBG and is unable to detect the [OIII]λ4363 line, it is likely that this object will present a massive underlying stellar population, high metallicity and low ionization. This is not in contradiction with the fact that the DEEP2 and TKRS sources with [OIII]λ4363 are LCBGs, since this latter sample was selected using the presence of the auroral line as the sole crterium. There are many other LCBGs in the DEEP2 and TKRS surveys that do not present this line.

- The distributions of the continuum and emission lines in HII-like LCBGs studied using high resolution spectra indicate that the starburst usually occupies more than 50 % of the continuum emitting region, rather than being a local phenomenon. The starburst is not necessarily centered in the object. The star formation properties of HII-like LCBGs are very similar to those of high luminosity HII galaxies. Other vigorous starburst galaxies have star formation properites very different from those of the observed intermediate redshift LCBGs. It has also been found that the LCBGs at intermediate redshift presented do not show unusually high star formation rates per unit area, although they are more massive than the average local HII galaxy of similar areal star formation rate. This supports the idea of a "downsizing" or "downdimming" in the evolution of starbursts in the Universe.

- There is evidence for a massive underlying stellar population in intermediate redshift LCBGs. This population was formed at around $z = 0.7$. It has also been found that, should these LCBGs finally evolve into dwarf elliptical galaxies, their metal content should be in the higher end of the interval allowed by their observed line ratios. Furthermore, their Sph descendants can only be the more luminous, massive and redder ones. The comparison of the LCBG models with the underlying population of lumi-

nous and local HII galaxies indicates that, even though both galaxy types could be considered to be similar, LCBGs might have a lower number of red giants.

- The kinematic data presented is against bulge formation in disk systems and in favor of a dE-like descendant scenario for most of the observed HII-like LCBG sample (6 out of 7). However, the disturbed morphology and kinematics makes clean interpretations difficult. In particular, it is not clear whether or not these systems are in dynamic equilibrium. While their morphology and resolved kinematics would argue otherwise, the agreement between integrated velocity dispersions and resolved profiles indicates the systems cannot be too far out of equilibrium. Moreover, it is not clear what is the gas really telling us about dynamics. The bulk of the observed random motions is probably of gravitational origin, although it will certainly have a turbulent component caused by local phenomena such as supernovae or winds from massive stars. Stellar velocity and dispersion profiles would provide a much clearer dynamical picture.

- One of the LCBGs studied, H1-13385, is very similar to the Large Magellanic Cloud. The mass distribution of this objects is very peaked towards its center and mainly supported by rotation, as evidenced by its steep rotation curve. The derived Mass-to-Light ratio shown by this object implies that it is not a young system. The observed starburst is not likely to contribute to a large extent to the stellar mass already built in this system. The discovery of this object is very interesting, since it means that LMC-like systems existed in isolation (as opposed to being a satellite of a much larger and luminous system) 2Gyr ago. This fact can not be explained in the hierarchical clustering model. On the other hand, the other LCBG kinematically studied in detail, SA68-6134, is a much younger object, mainly supported by random motions. This is a very luminous irregular system very similar to the most luminous HII galaxies in the local universe.

- Based on a search for the [OIII]λ4363 emission line in the TKRS and initial DEEP2 surveys of field galaxies, it's been possible to identify 17 galaxies at redshift $z \sim 0.7$ that are luminous, very blue, compact, and metal poor, roughly 1/3 to 1/10 solar in $12 + \log(\mathrm{O/H})$. Though rare, such metal-poor galaxies highlight the diversity among distant, star forming galaxies with high luminosities and serve as important laboratories to study galaxy evolution. This sample is lower in 12+log (O/H) by 0.6 dex on average in the luminosity–metallicity relationship when compared to prior studies at these redshift,

which used empirical calibrations, such as the R_{23} method. These previous studies, however, assumed the metal-rich branch of the calibrations used. Our results show that this assumption is sometimes invalid, even for luminous galaxies particularly when high values of EW(H_β) and moderate to high R_{23} are found. Based on comparisons with local and high redshift samples, we speculate that our metal-poor, luminous galaxies at $z \sim 0.7$ provide an important bridge between local Extreme Blue Compact Galaxies and Lyman Break Galaxies at redshifts $z \sim 3$. All three samples share the property of being overluminous for their metallicities, when compared to local galaxy samples. The three samples also have very high H_β equivalent widths, typically above 40 Å and up to 150 Å . They are similar to some local HII galaxies in this respect. Overall, the observed trend is that the most luminous, metal-poor compact emission-line galaxies are getting fainter with time.

- Much like the local Extreme Blue Compact Galaxies or the distant Lyman Break Galaxies, the O-4363 galaxies may belong to the compact class of galaxies. But this suggestion is based presently on the small 1–2 kpc sizes and high surface brightnesses seen in the four TKRS galaxies with [OIII]λ4363 observed with *ACS/HST*. Moreover, the emission-line velocity widths are narrow and suggest that the O-4363 galaxies are more likely to be galaxies with small dynamical masses, probably lower than similar systems both in the local universe and at intermediate redshift. The small sizes and velocity dispersions of the TKRS [OIII]λ4363 sources lead to think that the O-4363 sample belongs to the HII-like LCBG subtype. The calculated star formation rates of the O-4363 galaxies are mostly from 1 to 20 $M_\odot \mathrm{yr}^{-1}$, indicating that the star-forming activity is very strong (c.f., the SFR of 30 Doradus is 0.1 $M_\odot \mathrm{yr}^{-1}$) and thus lying roughly between that of local metal-poor, blue compact galaxies and distant Lyman Break Galaxies. The very blue colors, high equivalent widths and high star formation rates suggest that the strong burst of star formation has to be very recent.

- Finally, a short note about environment. Is NGC 205 a good example of a faded descendant of some LCBG that existed several Gyr ago? If so, where are the M31-like neighbors we do not see in the images of the distant objects? Are there field dEs? If dSphs are the low-mass end of the dEs population, the presence of isolated dSphs such as Tucana, Cetus, and the recently discovered Apples 1 galaxy should make us to approach with caution assertions in the sense that dEs do not exist outside of

rich environments or far from massive galaxies. The space density of the intermediate-redshift LCBGs we have observed with HST is $1.25\pm0.15\times10^{-5}$ Mpc^{-3} (for $M_B \leq -20$) between $0.3 < z < 0.7$. Even allowing for a factor of ~ 20 higher relic density, calculated using the time interval in this redshift slice and assuming the LCBG phase lasts for a few$\times10^8$ yr (~ 10 dynamical time-scales), an all-sky local survey volume reaching out to $\sim$10 Mpc is required to find even one single evolved descendant. At this distance the half-light radius of NGC 205 is only $\sim 12''$. Are the available local surveys this complete?

Sumario General y Conclusiones Principales.

En este capítulo final se resumen las conclusiones más importantes que se derivan de este trabajo. Dado que la mayor parte de este estudio se ha dedicado a la descripción y caracterización de las GLCA parecidas a las galaxias HII a desplazamientos al rojo intermedios, muchas de las conclusiones que se exponen van en este sentido. Tambieén se ha explorado la relacion de las GLCA con objetos del Universo cercano.

La mayor parte de las conclusiones que se resumen aquí se han expuesto ya en el sumario de cada capítulo.

- La luminosidad de Hβ de las galaxias HII más parecidas a las GLCA es muy superior a la luminosidad de Hβ del resto de galaxias HII. Esta es una diferencia muy importante entre estas dos submuestras. También se encuentra que los cúmulos ionizantes de las galaxias HII más similares a las GLCA son más masivos y viejos que los del resto de galaxias HII. Sus poblaciones subyacentes son también más importantes y por ello quizás también más viejas. Las galaxias HII con propiedades similares a las de las GLCA son un poco más metálicas que el promedio para todas las galaxias HII, pero no lo suficiente como para explicar las diferencias que se observan en el cociente de ionización [OIII]/[OII] entre las dos submuestras. Además, las fuentes parecidas a las GLCA están declaradamente más lejos que la galaxia HII promedio.

- Se ha encontrado además que los flujos observados son mayores en el caso de las galaxias que muestran la línea auroral [OIII]λ4363, a pesar de que las distribuciones de luminosidad en Hβ son muy parecidas. Esto se debe, en parte, a que las galaxias que no muestran esta característica en su espectro están más lejos y su extinción es más

elevada. Sin embargo, se ha demostrado que para algunos casos, la no observación de esta línea está causada por su mayor metalicidad. Las galaxias HII sin esta característica línea auroral son 0.4dex más ricas en metales que las galaxias de la otra submuestra. Además, el análisis de la relación [OIII]/[OII]—$12 + \log(O/H)$ demuestra la existencia de objetos ricos en metales con alta ionización que no presentan esta línea espectral. Finalmente, los objetos sin la línea auroral poseen cúmulos estelares más masivos aunque las diferencias de ionización entre las dos submuestras indican que las galaxia sin [OIII]λ4363 poseen cúmulos algo más evolucionados.

- Los dos puntos anteriores implican que las GLCA son más parecidas a las galaxias HII sin la línea [OIII]λ4363 que a aquellas galaxias HII que la muestran. Esto significa que cualquier muestra de control de galaxias compactas locales con formación estelar debe contener una mayoría de objetos sin la línea [OIII]λ4363. Si se observa una GLCA en el universo remoto y no se detecta esta característica en su espectro, es probable que ese objeto tenga una población ionizante masiva, alta metalicidad y baja ionización. Esto no está en contradicción con el hecho de que las fuentes con la línea [OIII]λ4363 de las muestras DEEP2 y TKRS sean GLCA, dado que esta muestra se ha seleccionado usando la presencia de esta línea como único cirterio. Hay muchas otras GLCA en las muestras DEEP2 y TKRS que no presentan [OIII]λ4363.

- Las distribuciones espaciales de las líneas de emisión y del contínuo de las GLCA parecidas a galaxias HII estudiadas gracias a los espectros de alta resolución espacial muestran que el episodio de formación estelar ioniza el gas presente en al menos el 50% de la extensión espacial del contínuo en los objetos observados. Los brotes de formación estelar no tienen porqué estar situados en el centro de los objetos. Las propiedades relativas a la formación estelar de las GLCA son muy parecidas a las de las galaxias HII más luminosas y masivas. Otros sistemas con formación estelar vigorosa tienen propiedades relativas a la formación estelar muy diferentes a las de las GLCA. Las tasas de formación estelar areolares de las GLCA no son inusuales en el Universo local, aunque las GLCA son más masivas que las galaxias HII cercanas de tasas de formación estelar areolares parejas. Esto apoya un escenario en el cual los brotes de formación estelar mas poderosos se producen en galaxias cada vez más masivas a altos desplazamientos al rojo.

- Se han encontrado pruebas de la existencia de una importante población subyacente en

las GLCA a desplazamientos al rojo intermedios. Esta generación de estrellas se formó a aproximadamente $z = 0.7$. Además, para que las GLCA observadas puedan evolucionar hacia sistemas esferoidales su metalicidad debe estar en el intervalo superior que permiten los cocientes de líneas observados. Además deben evolucionar a los sistemas más luminosos y rojos, de entre la población de galaxias esferoidales. Es así mismo el caso que las GLCA tienen probablemente también un número mayor de estrellas gigantes rojas que las galaxias HII locales más luminosas.

- Los datos cinemáticos que se presentan van en contra de que las GLCA parecidas a galaxias HII observadas (6 de 7) sean un bulbo en formación en objetos dominados por un disco. Esto favorece la visión según la cual las GLCA a desplazamientos al rojo intermedios se convertirían en sistemas esferoidales. Sin embargo, el aspecto perturbado impide llegar a conclusiones claras. No está claro, por ejemplo, si estos sistemas están en equilibrio dinámico. Aunque el aspecto de estas galaxias invita a pensar que no, el acuerdo entre las dispersiones de velocidades integradas y los perfiles de velocidades resueltos indican que tampoco pueden estar muy lejos del equilibrio. Tampoco está claro que fracción de las dispersiones de velocidades medidas tiene un origen gravitatorio, puesto que seguramente alguna parte de los velocidades medidas tienen un origen turbulento causado por supernovas u otros fenómenos locales. Sería necesario disponer de la cinemática de la componente estelar para poder responder a estas cuestiones.

- Una de las GLCA estudiadas cinemáticamente en detalle, H1-13385, es muy parecida a la gran nube de Magallanes. La distribución de masa de este objeto está muy picada hacia el centro y está principalmente soportada por la rotación, como demuestra la curva posición-velocidad presentada. El cociente entre la masa y la luminosidad de este objeto implica que no se trata de un objeto muy joven. El brote de formación estelar observado probablemente no contribuya en gran medida a la masa de la galaxia. El descubrimiento de este objeto es muy interesante, ya que significa que sistemas parecidos a la gran nube de Magallanes existían aislados hace ya 2 Gyr. Esto no puede ser explicado fácilmente por los modelos jerárquicos de formación de estructura. Por otra parte, el otro objeto estudiado en detalle, SA68-6134, es un objeto mucho más joven cuya cinemática está basada en movimientos aleatorios. Es un sistema irregular muy luminoso, muy parecido a las galaxias HII del Universo local.

- Basándonos en una búsqueda de la línea [OIII]λ4363 en las exploraciones DEEP2 y

TKRS de galaxias de campo ha sido posible identificar 17 galaxias luminosas y pobres en metales (entre un tercio y un décimo del valor solar) a desplazamientos al rojo $z \sim 0.7$. Aunque estas galaxias son poco comunes, estos objetos muestran la gran diversidad de objetos luminosos a alto desplazamiento al rojo, y también sirven como laboratorios para investigar la evolución de galaxias. Esta muestra es en promedio 0.6dex más pobre en oxígeno que otras muestras de galaxias de luminosidad parecida a estos desplazamientos al rojo. Sin embargo, las metalicidades de las otras muestras fueron calculadas con métodos empíricos, asumiendo que las metalicidades de esos objetos no son bajas. Los resultados de este estudio indican que esta suposición es inválida en algunos casos, especialmente si los anchos equivalentes son altos o si la intensidad de las líneas de oxígeno son moderadas o elevadas en comparación con la intensidad de Hβ. Proponemos que estas galaxias son un puente entre la población de galaxias compactas azules extrema y las galaxias a altos desplazamientos al rojo ($z = 3.0$) en las cuales se puede ver la discontinuidad de Lyman. Todas estas galaxias son más luminosas que las galaxias típicas del Universo local con metalicidades parecidas. Las tres muestras tienen también altos anchos equivalentes de Hβ, mayores de 40 Åy hasta 150Å. Estos valores son parecidos a los encontrados en galaxias HII locales y permiten avanzar que el brote de formación estelar de estos objetos es joven. La tendencia observada es que los sistemas compactos con líneas de emisión más luminosos y pobres en metales se van haciendo más débiles on el tiempo.

- Como las galaxias compactas azules extremas locales y las galaxias a altos desplazamientos al rojo en las cuales se puede ver la discontinuidad de Lyman, los objetos de la muestra O-4363 podrían ser objetos compactos. Por ahora, esta afirmación se basa en las tamaños observados (1–2 kpc) y altos brillos superficiales que se ven para las cuatro galaxias de la exploración TKRS observadas con el instrumento ACS en el telescopio espacial. Las dispersiones de velocidades medidas para los objetos O-4363 son pequeñas, implicando que estas galaxias probablemente tengan masas pequeñas, algo menores que las de sistemas parecidos del Universo local o a desplazamientos al rojo intermedios. Los pequeños tamaños y dispersiones de velocidades de las galaxias de la muestra TKRS con [OIII]λ4363 invitan a pensar que las galaxias distantes con [OIII]λ4363 pertenecen al subtipo más similar a las galaxias HII. Las tasas de formación estelar que se miden están comprendidas entre una y veinte masas solares por

año, indicando que son sistemas en los cuales la formación estelar está muy activa (esta tasa tiene un valor de 0.1 $M_{\odot}\mathrm{yr}^{-1}$ en el complejo de formación estelar 30 Doradus, en la gran nube de Magallanes). Estos valores se encuentran entre los de las galaxias compactas locales pobres en metales y las galaxias a alto desplazamiento al rojo en las cuales se puede ver la discontinuidad de Lyman.

- Para terminar, es necesaria una breve mención acerca del entorno. ¿ Es NGC205 un buen ejemplo de una galaxia esferoidal descendiente de alguna GLCA? ¿ Dónde estarían, en este caso, los objetos parecidos a M31 que no se ven en las imágenes de los objetos distantes? ¿ Existen las galaxias esferoidales en el campo? Si las esferoidales enanas son el límite inferior de la distribución de masas de las galaxias elípticas enanas, el descubrimiento de esferoidales enanas tales como los objetos en Tucana, Cetus o el sistema Apples 1, recientemente descubierto, debiera hacernos reflexionar antes de aceptar que las galaxias esferoidales sólo existen en cúmulos. La densidad espacial de las GLCA observadas con HST presentadas en este trabajo es $1.25\pm0.15\times10^{-5}$ Mpc^{-3} (para $\mathrm{M}_B \leq -20$ y $0.3 < z < 0.7$). Incluso si la densidad de descendientes fuese un factor 20 mayor, calculado usando el intervalo de tiempos entre estos dos desplazamientos al rojo y estimando que una galaxia subsiste como una GLCA durante unos cientos de millones de años (10 veces un tiempo dinámico), sería necesaria una exploración completa del cielo hasta 10Mpc. A esta distancia, NGC205 sólo subtiende 12 segundos de arco. ¿ Son las exploraciones locales del cielo tan profundas?